



Theses and Dissertations

1996

Combustion Modeling of RDX, HMX and GAP with Detailed Kinetics

Jeffrey E. Davidson
Brigham Young University

Follow this and additional works at: <https://scholarsarchive.byu.edu/etd>



Part of the [Chemical Engineering Commons](#)

BYU ScholarsArchive Citation

Davidson, Jeffrey E., "Combustion Modeling of RDX, HMX and GAP with Detailed Kinetics" (1996). *Theses and Dissertations*. 6531.

<https://scholarsarchive.byu.edu/etd/6531>

This Dissertation is brought to you for free and open access by BYU ScholarsArchive. It has been accepted for inclusion in Theses and Dissertations by an authorized administrator of BYU ScholarsArchive. For more information, please contact scholarsarchive@byu.edu, ellen_amatangelo@byu.edu.

Combustion Modeling of RDX, HMX and GAP with Detailed Kinetics

A Dissertation

Presented to the

Department of Chemical Engineering

Brigham Young University

In Partial Fulfillment

of the Requirements for the Degree

Doctor of Philosophy

©Jeffrey Davidson 1997

by

Jeffrey Edward Davidson

April 1996

ACCEPTANCE

This dissertation, by Jeffrey E. Davidson is accepted in its present form by the Department of Chemical Engineering of Brigham Young University as satisfying the dissertation requirement of the degree of Doctor of Philosophy.

Merrill W. Beckstead, Committee Chair

John L. Oscarson, Committee Member

Thomas H. Fletcher, Committee Member

Ronald E. Terry, Committee Member

Paul O. Hedman, Committee Member

Date

William G. Pitt, Graduate Coordinator

TABLE OF CONTENTS

Combustion Modeling of RDX, HMX and GAP with Detailed Kinetics.....	i
ACCEPTANCE	ii
TABLE OF CONTENTS	iii
LIST OF TABLES	vi
LIST OF FIGURES	vii
ACKNOWLEDGMENTS	ix
GLOSSARY.....	x
NOMENCLATURE	xi
COMBUSTION MODELING OF RDX, HMX AND GAP WITH DETAILED KINETICS	1
Introduction.....	1
Nature of Research Contract.....	4
My Contribution.....	5
CHAPTER 1: OVERVIEW OF SOLID PROPELLANT COMBUSTION	6
Combustion of a Homogenous Propellant.....	6
Solid Region	7
Two-Phase Region	7
Gas-Phase Region	8
Composite Propellant Combustion.....	9
CHAPTER 2 : THE CONSERVATION EQUATIONS.....	13
The Conservation Equations.....	13
Simplifying Assumptions.....	15
CHAPTER 3 : MODELS FOUND IN THE LITERATURE	17
Previous Modeling Efforts	18
Global Kinetic Models	18
Semi-Global Models	21
Development of Detailed Kinetic Mechanisms	25
Multi-Phase Models with Detailed Reactions	27
Data for Model Validation.....	30
Most Recent Propellant Combustion Models.....	31
Future Modeling Directions.....	32
CHAPTER 4: DESCRIPTION OF MODEL	35
Solid Region.....	35
Liquid-Gas Two-Phase Region	35
Gas Region.....	39
Determination of the Mass Burning Rate.....	40
Model Inputs/Outputs	41
CHAPTER 5: DECOMPOSITION STUDIES OF RDX AND HMX.....	43

CHAPTER 6: MODEL CALCULATIONS FOR RDX.....	47
Properties of RDX	47
Kinetics of RDX Combustion	50
Liquid RDX Decomposition Mechanism	50
Gas-Phase Reaction Mechanism.....	51
Comparison with Experimental Data	52
Burning Rate.....	52
Self-Deflagration Temperature Profiles	54
Surface Conditions.....	56
Species Concentration Profiles	57
Laser-Assisted Combustion Experiments.....	63
Summary of RDX Model Comparison with Experimental Data	72
 CHAPTER 7: ANALYSIS AND REDUCTION OF THE MELIUS-YETTER RDX MECHANISM	 73
Introduction.....	73
Integral Reaction Flow Analysis	73
Explanations for Discrepancies in Species Profiles	75
CH ₂ O.....	75
NO.....	76
Mechanism Reduction	81
Background.....	81
Skeletal Mechanism.....	82
Global Mechanism.....	85
Comparison of Reduced Mechanisms with Experiment and Full Mechanism Calculations	86
CPU Time Savings.....	91
Conclusions.....	92
 CHAPTER 8: SENSITIVITY ANALYSIS OF RDX/HMX MODEL	 94
Factors Affecting the Burning Rate.....	95
Factors Affecting Temperature Sensitivity (σ_p)	97
Factors Affecting the Final Flame Temperature	98
Factors Affecting the Surface Temperature	99
Factors Affecting the Melt-Layer Thickness.....	99
Summary	100
 CHAPTER 9: THE HMX MODEL WITH COMPARISONS TO THE RDX MODEL	 101
Introduction.....	101
Observed Differences in the Combustion of HMX and RDX	101
Properties of RDX and HMX	101
Kinetic Mechanisms	104
Condensed-Phase Mechanism	104
Gas Mechanism	104
Comparisons with Experimental Data.....	105
Burning Rate.....	105
Temperature Sensitivity	107
Adiabatic Flame Temperature	108
Surface Temperature.....	108
Melt-Layer Thickness	110
Experimental Data Unique to HMX	111
Summary	112

CHAPTER 10: PRELIMINARY MODELING OF GAP	114
Introduction.....	114
Thermophysical Properties	115
Decomposition Studies of GAP.....	115
Combustion Characteristics of GAP.....	119
Modeling.....	120
Comparison with Experimental Data.....	123
Burning Rate.....	123
Surface Temperature.....	125
Final Flame Temperature	125
Sensitivity Analysis	126
Conclusion	128
CHAPTER 11: SUMMARY AND CONCLUSIONS	130
Summary of Work	130
Originality of Work	131
RDX Modeling	133
HMX Modeling	133
GAP Modeling.....	133
Development of Modeling Tools.....	133
Phase3: The 1D, SS Propellant Combustion Code.....	134
Standard Calculations	134
Sensitivity Analysis	134
Reduced Mechanisms	135
Mechanism Manager.....	135
Foundation for Future Work	135
Modeling of Other Propellants	136
Extension to Multi-Dimensional and Unsteady Models.....	136
Publications.....	114
Peer-Reviewed.....	136
JANNAF.....	137
REFERENCES.....	138
APPENDIX: THE MELIUS-YETTER RDX GAS-PHASE MECHANISM.....	149
APPENDIX: DESCRIPTION OF MECHANISM REDUCTION METHODS	155
Reaction Flow Analysis	155
Time-Scale Analysis.....	155
Fitted Kinetic Mechanisms	156
APPENDIX: SKELETAL RDX MECHANISM S18-39	157
APPENDIX: BURNING RATE SENSITIVITY TO INITIAL TEMPERATURE.....	159
Determining σ_p from Experimental Data.....	159
Reconciling Predicted and Calculated Values of σ_p for HMX.....	162
The Difference in Temperature Sensitivity of RDX and GAP.....	163
Summary	166
APPENDIX: STATISTICAL ANALYSIS OF BOGGS' HMX TEMPERATURE SENSITIVITY DATA.....	167

LIST OF TABLES

Table 1: Tasks as Specified in the Research Contract.....	5
Table 2: General Differences between Categories of Models.....	18
Table 3: Global Kinetic Models.....	20
Table 4: Elementary-Step Mechanisms for Propellant Combustion.....	28
Table 5: Experimental Studies Available for Model Validation.....	31
Table 6: Comparison of Propellant Combustion Models.....	34
Table 7: Model Inputs and Outputs.....	42
Table 8: Nitramine Decomposition Mechanisms.....	44
Table 9: RDX Property Values Found in the Literature.....	48
Table 10: Thermodynamic and Physical Properties of RDX Solid and Liquid Used in Model.....	50
Table 11: RDX Condensed-Phase Mechanism.....	51
Table 12: NO and NO ₂ Peak Mole Fractions.....	70
Table 13: Reactions Producing CH ₂ O.....	76
Table 14: Reactions Producing NO.....	77
Table 15: Reactions Destroying NO.....	77
Table 16: Proposed Modifications to Melius-Yetter to Reduce Peak NO Concentration.....	80
Table 17: Full Molecular RDX Decomposition.....	82
Table 18: Skeletal Molecular RDX Decomposition.....	82
Table 19: Global Molecular RDX Decomposition.....	84
Table 20: RDX Gas-Phase Global Mechanism.....	86
Table 21: Comparison of Calculations using Full, Skeletal and Global Mechanisms at 20 and 70 atm.	93
Table 22: Thermophysical Properties of RDX and HMX.....	103
Table 23: Condensed Phase Decomposition Mechanisms of RDX and HMX.....	104
Table 24: Differences in the Gas-Phase Mechanisms of RDX and HMX.....	105
Table 25: Reasons for the Similarities and Differences in HMX and RDX Combustion.....	113
Table 26: Thermophysical Properties of GAP.....	115
Table 27: GAP Properties used in Model.....	121
Table 28: Proposed Condensed-phase Reaction Mechanisms for GAP.....	122
Table 29: Key Characteristics of Three Proposed GAP Mechanisms.....	123
Table 30: Sensitivity to Production of Species Analysis (Mechanism C, GAP).....	127
Table 31: Comparison of RDX Multi-Phase Models of BYU, PSU and Yale.....	132

LIST OF FIGURES

Figure 1: Propellant Formulation and Configuration.....	2
Figure 2: Feedback Relationship between Experiment and Modeling	4
Figure 3: Effect of Pressure on Temperature Profile	7
Figure 4: Physicochemical Processes Occurring in the Melt Layer	8
Figure 5: Multiple Flames in Composite Propellant Combustion.....	10
Figure 6: Pressure Effects on Flame Structure.....	11
Figure 7: Composite Flame Structure as a Function of Geometry.....	12
Figure 8: HMX Burning Rate Data	22
Figure 9: Schematic of Williams Nitramine Model	23
Figure 10: The Multiple Phases of a Burning Propellant	28
Figure 11: Convergence Scheme for Numerical Model.....	41
Figure 12: Chemical Structure of RDX and HMX.....	44
Figure 13: Nitramine Surface Species Concentrations from Litzinger et al.....	46
Figure 14: RDX Thermal Conductivity	49
Figure 15: RDX Vapor Pressure Correlations.....	49
Figure 16: RDX Condensed Phase Kinetics	51
Figure 17: RDX Burning Rate for $T_{init}=298$ K.....	53
Figure 18: RDX Burning Rate for $T_{init}=223$ K.....	53
Figure 19: RDX Burning Rate for $T_{init}=373$ K.....	53
Figure 20: RDX Self-Deflagration Temperature Profile 1 atm (Parr).....	54
Figure 21: RDX Temperature Profiles at 1, 5, 20 and 90 atm (Zenin).....	55
Figure 22: Calculated RDX Temperature Profiles at 10 and 70 atm.....	56
Figure 23: RDX Surface Temperature at 1 to 90 atm (Zenin).....	56
Figure 24: RDX Melt Layer Thickness at 1 to 90 atm (Zenin, Brewster).....	57
Figure 25: RDX CO, H ₂ , NO, and HCN Profiles at 0.5 atm (Ermolin).....	57
Figure 26: RDX CO ₂ , H ₂ O and N ₂ Profiles at 0.5 atm (Ermolin).....	58
Figure 27: RDX NO ₂ , HNCO and N ₂ O Profiles at 0.5 atm (Ermolin).....	58
Figure 28: RDX Mass 28 Profile at 1 atm (Korobeinichev).....	59
Figure 29: RDX Mass 30 Profile at 1 atm (Korobeinichev).....	60
Figure 30: RDX Mass 27 Profile at 1 atm (Korobeinichev).....	60
Figure 31: RDX Mass 44 Profile at 1 atm (Korobeinichev).....	60
Figure 32: RDX Mass 27 Profile at 2 atm (Korobeinichev).....	61
Figure 33: RDX Mass 30 Profile at 2 atm (Korobeinichev).....	61
Figure 34: RDX NO and OH Profiles at 1 atm (Parr).....	62
Figure 35: RDX NH and CN Profiles at 1 atm (Parr).....	63
Figure 36: Model of Parrs' Experiment.....	64
Figure 37: RDX Laser-assisted Temperature Profile at 1 atm (Parr).....	66
Figure 38: Calculated RDX Laser-assisted Two-Stage Flame Structure at 1 atm.....	67
Figure 39: RDX Laser-assisted CN Profile 1 atm (Parr).....	67
Figure 40: RDX Laser-assisted NH Profile at 1 atm (Parr).....	68
Figure 41: RDX Laser-assisted OH Profile at 1 atm (Parr).....	68
Figure 42: RDX Laser-assisted NO and NO ₂ Mole Fractions at 1 atm (Parr).....	69
Figure 43: RDX Laser-assisted N-Containing Species Profiles at 1 atm (Litzinger).....	70
Figure 44: RDX Laser-assisted C-Containing Species Profiles at 1 atm (Litzinger).....	71

Figure 45: RDX Laser-Assisted Burning Rate at 1 atm (Brewster, Litzinger, Parr)	72
Figure 46: Integral Reaction Flow Analysis for RDX at 20 atm.....	74
Figure 47: NO Sensitivity Analysis for RDX at 10 atm.	78
Figure 48: Modified Melius-Yetter NO and OH Concentration Profiles at 1 atm (Parr).....	80
Figure 49: Modified Melius-Yetter NH and CN Concentration Profiles at 1 atm (Parr).....	80
Figure 50: Skeletal RDX Mechanism S18-39.....	84
Figure 51: RDX Calculated Burning Rate using Reduced Mechanisms	87
Figure 52: RDX Calculated Surface Temperature using Reduced Mechanisms.....	87
Figure 53: RDX Calculated Melt Layer Thickness using Reduced Mechanism.....	88
Figure 54: Calculated Adiabatic Flame Temperature using Reduced Mechanisms.....	88
Figure 55: RDX Adiabatic Flame Species Concentrations at 20 atm.	88
Figure 56: Calculated Temperature Profiles using Reduced Mechanisms at 20 atm.....	89
Figure 57: H ₂ , N ₂ , CO, RDX Concentration Profiles (Symbols=F45-232, Line=S18-39)	90
Figure 58: HCN, H ₂ , CO ₂ Concentration Profiles (Symbol=F45-232, Line=S18-39).....	90
Figure 59: N ₂ O, NO ₂ and CH ₂ O Concentration Profiles (Symbols=F45-232, Line=S19-39)	90
Figure 60: CPU Time for Standard Test.....	91
Figure 61: Increase in Speed by Dropping Species.	92
Figure 62: RDX Burning Rate Sensitivity at 10 atm, T _{init} =298.....	96
Figure 63: Top Reactions Influencing Burning Rate of RDX at 10 atm.	96
Figure 64: RDX σ_p Sensitivity at 10 atm.....	97
Figure 65: RDX Final Flame Temperature Sensitivity at 10 atm.	98
Figure 66: Top Reactions Influencing Final Flame Temperature of RDX at 10 atm.....	98
Figure 67: RDX Surface Temperature Sensitivity at 10 atm.	99
Figure 68: RDX Melt-Layer Thickness Sensitivity at 10 atm.....	100
Figure 69: Sublimation Pressures of RDX and HMX.....	102
Figure 70: HMX and RDX Burning Rate Data (T _{init} =298 K).....	106
Figure 71: HMX and RDX Burning Rate Data (T _{init} =223 K).....	106
Figure 72: HMX and RDX Burning Rate Data (T _{init} =373 K).....	106
Figure 73: HMX Temperature Sensitivity (173 K to 423 K).....	108
Figure 74: RDX and HMX Surface Temperature	109
Figure 75: Calculated Percent of RDX and HMX Evaporating	109
Figure 76: RDX and HMX Melt-Layer Thickness.....	110
Figure 77: HMX Self-Deflagration Species Profiles at 1 atm (Parr).....	111
Figure 78: HMX CN Peak Location at 1 to 12 atm (Parr).....	112
Figure 79: Reported Mole Fractions for GAP Decomposition.....	117
Figure 80: Comparison of Species from Decomposition Studies	117
Figure 81: NASA-Lewis ¹¹⁴ Calculated GAP Equilibrium Products at 40 atm	118
Figure 82: Comparison of Condensed Phase Decomposition Products	123
Figure 83: GAP Burning Rate with Pressure.....	124
Figure 84: GAP Temperature Sensitivity of Burning Rate (Mechanism A).....	124
Figure 85: GAP Surface Temperature with Pressure.	125
Figure 86: GAP Adiabatic Flame Temperature	126
Figure 87: Simple σ_p Analysis (HMX, P=54.53 atm).	160
Figure 88: Temperature Sensitivity from Bogg's Data using Simple Analysis.....	160
Figure 89: σ_p Calculation from Bogg's Smoothed HMX Data	161
Figure 90: RDX and HMX Temperature Sensitivity (298 K).....	162
Figure 91: GAP Temperature Sensitivity.....	163
Figure 92: Effect of Q _s on Burning Rate and Temperature Sensitivity (RDX).....	164
Figure 93: Energy Balance at the Surface of RDX and GAP (10 atm) (C for Condensed).....	165

ACKNOWLEDGMENTS

I have many people to thank for contributing to this research. Those who have contributed in a technical manor are listed in the references. Though non-technical, the contributions listed here, have played an even more important role.

I would like to thank my advisor, Dr. Merrill W. Beckstead. His dedication to his students has enabled me to complete this degree in just four years. Dr. Beckstead arranged for me to have the latest literature, computers, software, and funding necessary for my research. He enabled me to travel to California, Alabama, Nevada and Italy to attend technical conferences. Most importantly, he has advised me and given helpful evaluations of my work. It has been a pleasure to work for and *with* Dr. Beckstead.

I would like to thank the Chemical Engineering Department, Brigham Young University, and the Church of Jesus Christ of Latter-day Saints for giving me the opportunity for such a excellent education. Because of their scholarships and a fellowship from Kodak Eastman Company, I have never had to pay tuition. I am truly grateful.

I would like to thank my parents for teaching me the value of hard work, to work until the job is done, and to do it right the first time. I would like to thank all the relatives who have helped financially. At the request of some, they will remain anonymous.

I am very grateful to my wife for knowing me well enough, to insist on me going to graduate school for a Ph. D. Despite serious illness, and the financial concerns that come with graduate school, she has never waned in her support.

I am eternally grateful to my Heavenly Father and his Son, Jesus Christ for healing my wife, and for the talents they have given me. I have felt their inspiration in this research and in many other aspects of my life.

Jeffrey E. Davidson

GLOSSARY

Note: This glossary is not intended to be comprehensive, but rather provide a few brief definitions for readers not familiar with this field.

AP- (Ammonium perchlorate, NH_4ClO_4), an oxygen rich energetic crystalline material.

BAMO- (bisazidomethyl oxetane) an energetic binder.

BDP- Refers to a composite propellant model developed by Beckstead, Derr and Price. (Ref. 13)

Binder- a matrix material used to support the various ingredients in a propellant.

Burning rate- in this dissertation, this refers to the surface regression rate (cm/sec).

Composite propellant- a propellant composed of two or more ingredients

Condensed phase- refers to either the solid or liquid regions.

Dark zone- the region in a two-stage flame where reaction rates are slow, characterized as a having low emission of light, and small temperature rise.

DB- Double Base, a energetic material composed mostly of nitrocellulose and nitroglycerin. This propellant has a two-stage flame separated by a dark zone.

GAP- (glycidyl azide polymer, $(\text{C}_3\text{H}_5\text{ON}_3)_n$), an energetic fuel rich binder.

HMX- (cyclotetramethylenetetranitramine, $\text{C}_4\text{H}_8\text{N}_8\text{O}_8$, octogen) a nitramine energetic material similar to RDX. Properties are listed in Table 22, page 103.

HMXR- HMX minus an NO_2 group.

HMXRO- an isomer of HMXR.

HTPB- (hydroxyl-terminated polybutadiene), a non-energetic binder.

Monopropellant- a single ingredient propellant.

NG- Nitroglycerin.

RDX- (cyclotrimethylenetrinitramine, $\text{C}_3\text{H}_6\text{N}_6\text{O}_6$, hexogen), a nitramine energetic material similar to HMX. Properties are listed in Table 22, page 103.

RDXR- RDX minus an NO_2 group.

RDXRO- an isomer of RDXR.

Surface- in this dissertation, the interface between the gas and two-phase region.

Temperature Sensitivity- (σ_p) a parameter used in unsteady combustion analysis, defined as $\partial \ln(r_b) / \partial T_{\text{init}}$ at constant pressure.

COMBUSTION MODELING OF RDX, HMX AND GAP WITH DETAILED KINETICS

Introduction

Solid propellants are widely used in many industries today. Solid propellants are found in the solid rocket boosters that help provide the thrust to launch the Space Shuttle into orbit and in automotive air bags where they rapidly generate gas to inflate the bags. Solid-fueled rockets launch satellites into orbit, eject pilots to safety from disabled aircraft, launch dazzling firework displays and are one of the main delivery mechanisms for military weapons. Compared to liquid-fueled rockets, solid rocket motors have very few, if any, moving parts. Solid rocket motors do not require pumps to bring the reactants up to chamber pressure. The solid fuel can generally be stored for long periods of time under ambient conditions with little change in performance, whereas some liquid propellants must be stored in cryogenic conditions and others can be corrosive to their storage vessels. Solid propellants can be launched in a fraction of a second, but liquid-fueled rocket motors require some preparation time before launch. In the Gulf War, the Iraqis were often detected fueling their liquid-fueled SCUD missiles before they could launch their missiles. Almost all aircraft-launched missiles are solid-fueled because of their simplicity, quick response time, and reliability.

For in-flight-performance control, the liquid-fueled motors have a definite advantage. For liquid-fueled rockets, the chamber pressure (which determines the thrust) can be controlled by the pumps. For solid-fueled rockets, their performance over time is determined by their design, namely the propellant formulation and configuration. The formulation deals with small scale (microns to cm) effects and the configuration deals with the large scale (cm to m) (physical grain design). (Figure 1 clarifies this distinction). The formulation and configuration of a rocket propellant is chosen to give the desired solid rocket motor performance.

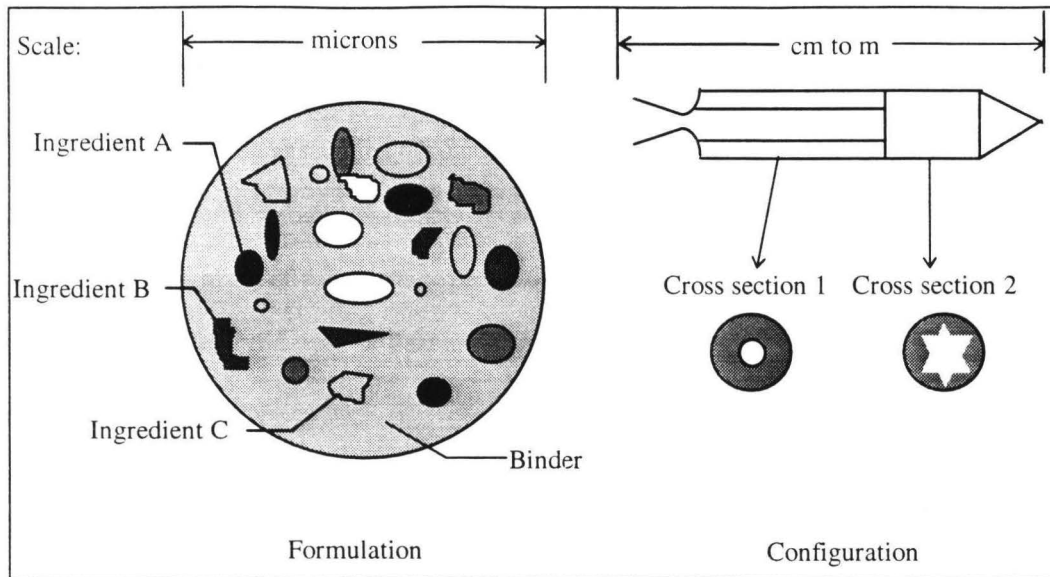


Figure 1: Propellant Formulation and Configuration

The difficulty in designing a rocket motor is compounded by acoustic pressure oscillations which occur in the combustion chamber. Because the burning rate of a propellant is generally a strong function of pressure, and the pressure of the combustion chamber is a function of the burning rate, positive feedback can occur leading to catastrophic failure of the rocket motor. The effect of propellant formulation on combustion instability is not well understood. Understanding and predicting the relationship of propellant formulation and pressure oscillations is the objective of the contract from which my research has been funded.

Most solid propellants are a heterogeneous mixture of several ingredients. These multi-ingredient propellants are referred to as composite propellants; whereas, single-ingredient propellants are called monopropellants. The various ingredients often include oxidizers (or energetic compounds), fuel (or binder), plasticizer, stabilizer, curing agents, cross-linking agents, bonding agents, burning rate catalysts, anti-aging agents, opacifier, flame suppressant, and combustion instability suppressant.¹ The weight fractions and particle sizes of the different components are varied to achieve the desired combustion characteristics. Experimentally determining the optimum mixture can be very costly; therefore, developing a model that could *a priori* predict composite propellant combustion would be extremely valuable. But the chemical and physical interactions between the different ingredients are very complex. The first step in developing such a model would be to understand thoroughly and accurately model the

steady-state combustion of the individual ingredients. Much of the initial understanding comes from experimental observations.

The level of understanding of combustion and combustion related processes has rapidly increased over the past several decades. Advances in experimental techniques now allow scientists to measure concentrations of many of the reacting species on the parts per million level with a spatial resolution of about 4 microns (e.g. the work of Parr and Hanson-Parr²). Advances in computers, quantum mechanics and statistical mechanics have enabled scientists to estimate within reasonable accuracy, the thermophysical properties and reaction kinetics of short-lived combustion intermediates (e.g. the work of Melius³). Progress has also been made in measuring some of the heterogeneous processes involved in propellant combustion.^{4,5,6}

Experimental data are like pieces of a complicated jigsaw puzzle. Some of the pieces are still missing (experiments that have not been done); some of the pieces that are available do not fit together perfectly (variations in experimental technique and scatter in experimental data); and the complete picture is still unknown (incomplete understanding of the combustion process). As pieces of the puzzle come together, a blurry and incomplete picture forms. Scientists propose what the picture could look like by developing a model. The complexity of the model is constrained by lack of understanding of the process (missing pieces of the puzzle), but the model will often make an assumption as to the form of the missing pieces. Once complete, the model is compared to experimental data. How well the model puts together the pieces of the puzzle (agrees with experimental data) will depend on the assumptions upon which the model is based and the input parameters of the model. This comparison of the model's picture with reality not only will indicate what pieces of the puzzle are still missing but what experimental data should be reevaluated. More experimental data helps refine the model. Models help scientists interpret their experiments and experiments help validate models (see Figure 2). By iterating between experiment and modeling, the pieces of the puzzle begin to line up and the picture becomes clearer. The process is greatly enhanced if there is close interaction between those performing the experiments and those developing the models.

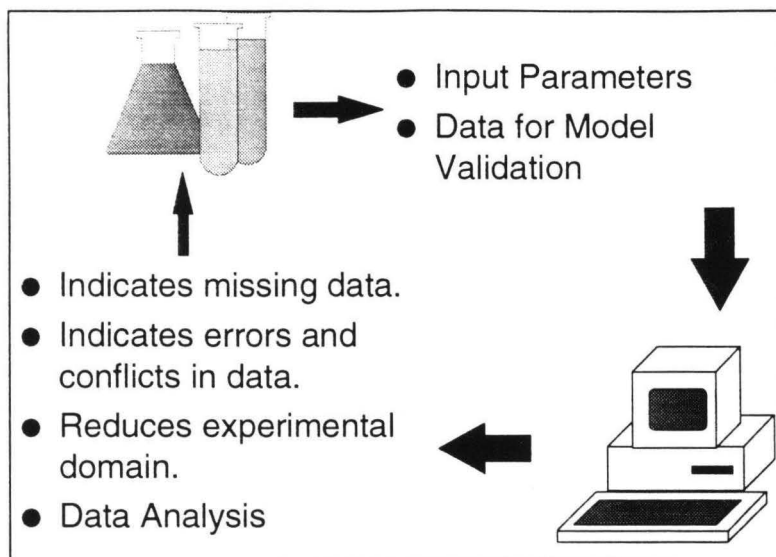


Figure 2: Feedback Relationship between Experiment and Modeling

Nature of Research Contract

To better facilitate the interaction between those doing experiments and those developing models, a multi-university research project was proposed. This research involves six principle investigators* at five universities and is funded by the Air Force Office of Scientific Research under contract AFOSR F496209-93-1-0430.⁷ The objective of this research is to develop models of fundamental mechanisms of combustion instability which can be applied to a variety of energetic materials. The responsibilities of each principle investigator are summarized in Table 1.

The first three investigators in Table 1 focus on obtaining the experimental data and the last three investigators are involved in modeling. The experiments of Brill, Branch, and Litzinger provide data for development of chemical reaction mechanisms and for model validation. The research group headed by Smooke focuses on the development of the gas-phase reaction chemistry. Beckstead's group is responsible for developing simplified models which would be used by Yang's group in modeling the reacting flow in a rocket motor.

* M. W. Beckstead (Brigham Young University), M. C. Branch (University of Colorado), T. B. Brill (University of Delaware), T. A. Litzinger (Pennsylvania State University), M. D. Smooke (Yale University), and V. H. Yang (Pennsylvania State University).

Table 1: Tasks as Specified in the Research Contract.

Brill	T-Jump and SMATCH/FTIR experiments to evaluate the effect of unsteady temperature and pressure fields
Litzinger	Microprobe mass spectroscopy to characterize dynamic combustion phenomena under a varying laser heat flux.
Branch	Measure the structure of two-dimensional laminar diffusion flames, diffusion flames with cross flow, and counter flow diffusion flames.
Smooke	Modeling of flame structure with full chemistry.
Yang	Modeling of flow field in a rocket motor with simplified chemistry and pressure oscillations.
Beckstead	Integration of the above studies into a propellant/diffusion flame model which includes decomposition kinetics and simplified chemistry.

My Contribution

As stated above, prior to modeling the unsteady combustion of several ingredients, one must first model the steady-state combustion of the individual ingredients. My contribution to the research has been the development, testing and use of a model for the steady-state combustion of homogeneous propellants for pressures typical of solid rocket motors (less than 100 atm). In the development and application of this model to several ingredients, key thermophysical properties and reaction mechanisms have been identified. Additionally, a reduced chemical reaction mechanism has been developed. My work serves as a necessary precursor in the development of unsteady and multidimensional models.

The outline of this dissertation is as follows. First, the physical and chemical processes that occur in the combustion of solid propellants are introduced. Then, the general conservation equations are presented along with a discussion of common simplifying assumptions. A review of steady-state propellant combustion models found in the literature is presented. The rest of the dissertation is a description of the combustion model and its application to the monopropellants RDX (Chapter 6), HMX (Chapter 9) and GAP (Chapter 10). Various acronyms commonly used in this area of research are defined in the Glossary.

CHAPTER 1: OVERVIEW OF SOLID PROPELLANT COMBUSTION

As described above, propellants found in practical applications are composed of a variety of ingredients. To understand how a propellant burns, the combustion of a pure ingredient is discussed first, followed by a brief discussion of the complexities of the combustion of heterogeneous propellants.

Combustion of a Homogenous Propellant

As a propellant burns there are complex interactions between the gas-phase flame, the liquid layer on the surface and the un-reacted solid. The heat released in the flame provides a heat flux to the surface. This energy causes the propellant to melt, evaporate and/or decompose, providing reacting species to the gas flame. This fuel reacts, providing more energy back to the surface. The increase in heat flux to the condensed propellant causes an increased mass flux away from the surface. The increased mass flux has the effect of "blowing" the gas-phase reactions away from the surface which reduces the heat flux to the surface. Steady-state deflagration occurs when the heat flux from the gas flame is in balance with the mass flux away from the surface.

Pressure has a strong effect on the burning rate. As pressure increases, the reaction rates in the gas-phase increase. This increases the temperature gradient (heat flux) near the surface which leads to an increase in burning rate. This effect is illustrated in Figure 3.⁸

Combustion of a propellant can be broken into three regions: solid, liquid-gas two-phase region, and the gas region. Each of these three regions is discussed below.

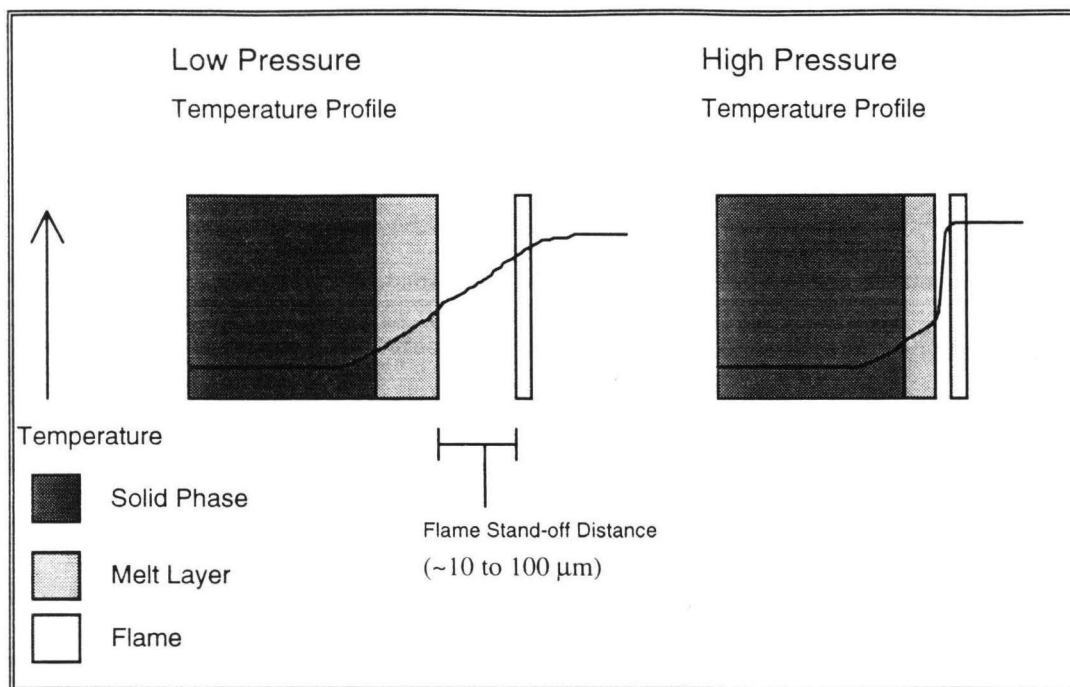


Figure 3: Effect of Pressure on Temperature Profile

Solid Region

The solid phase of many monopropellants (RDX, HMX, AP) is crystalline, though there are numerous polymer propellants (GAP, BAMO, DB). Depending upon the specific ingredient, there can be several phase transitions (with their respective density changes and heats of phase change) to consider between the initial temperature and the melting temperature. Some propellants can sublime and/or decompose while in their solid form, but the rates associated with these processes are small compared to the decomposition and evaporation rates after the propellant has melted. For certain propellants, it is uncertain whether the solid to liquid transition occurs via melting or decomposition.⁹ For these reasons, it is often difficult to find experimental values for ΔH_{melt} in the literature.

Two-Phase Region

The two-phase region consists of liquid and gaseous species resulting from the melting and/or decomposition of the solid phase. The initial decomposition reactions are probably the least understood part of the monopropellant flame. Many of these propellants are complex molecules which can break down by several pathways, some of which are exothermic and others endothermic. The molten phase has

been difficult to understand because of the many processes occurring (see Figure 4). Decomposition, evaporation and heterogeneous reactions (liquid-gas, liquid-solid, and gas-solid) generate gas-phase molecules. These gas-phase molecules can nucleate to form bubbles. Gas-phase reactions can occur inside the bubbles and liquid-gas reactions can occur at the bubble surfaces. Gases can dissolve into the liquid, and liquid can evaporate into the bubbles.¹⁰ The void fraction of bubbles is a function of both heat flux and pressure. At high pressures, the burning rate is sufficiently fast that bubble formation appears to have less effect on the combustion process than at low pressure.¹¹

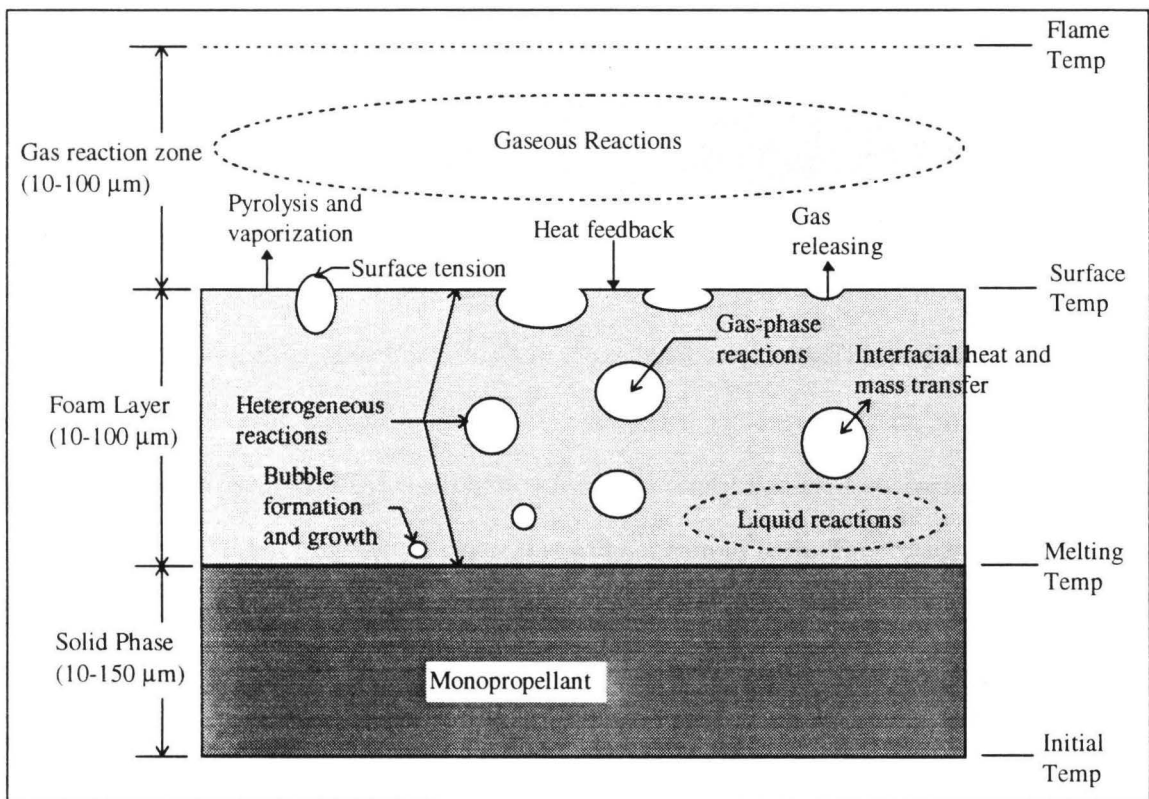


Figure 4: Physicochemical Processes Occurring in the Melt Layer (adapted from Ref. 10)

Gas-Phase Region

As with the division between the solid and two-phase regions, the division between the two-phase and gas-phase region is not well defined due to chemical reactions, bubbles, and condensed material being advected away from the surface. In the gas-phase region of a monopropellant, the flame is essentially premixed. The species coming from the surface react with each other and/or decompose to form other species. The reactions continue until equilibrium is reached. As discussed above, energy from these

reactions is conducted back to the surface. Species are advected away from the surface by the net mass flux, but mass diffusion has the effect of transporting species to and from the surface. Thousands of reactions involving hundreds of species can be occurring in the gas flame.¹²

Composite Propellant Combustion

The heterogeneous nature of composite propellants make the combustion of composite propellants multidimensional. All of the complexities of the combustion of homogenous propellants are compounded by interactions between the different ingredients. For example, in the combustion of heterogeneous propellants, the coupling between the heat flux from the gas phase and the burning rate is complicated by varying flame structure on the burning surface. These concepts can be largely attributed to the work of Beckstead, Derr and Price (i.e. the BDP model).¹³ (See Figure 5).

While the flame structure shown in Figure 5 has more of an effect in certain propellants than in others, it is still present, at least to some degree, in all composite propellants and should be considered. Due to the dominating effect of multiple flames in the combustion of AP/HTPB propellants, this type of propellant will serve as the example in the following discussion on composite propellant combustion. AP (ammonium perchlorate, NH_4ClO_4) is oxygen rich (i.e. its combustion products contain approximately 30% O_2), while HTPB is a hydrocarbon binder that will not burn by itself. The monopropellant flame in Figure 5 is the same type of premixed flame as illustrated in

Figure 3. It is the result of reactions between species coming from the oxidizer. Near the boundaries of the AP crystal, the decomposition species coming from the oxidizer diffuse and react with the species pyrolyzing from the fuel binder. This forms the primary diffusion flame. This flame is not only more energetic than the AP monopropellant flame, but occurs closer to the surface (Note: This is true at intermediate pressures (~34 atm). See the discussion below of the effect of pressure on the composite flame structure). This causes the surface to regress faster at the interface between the binder and oxidizer. The final diffusion flame is a result of reactions between the products of the monopropellant flame with those of the primary diffusion flame and unreacted binder species.

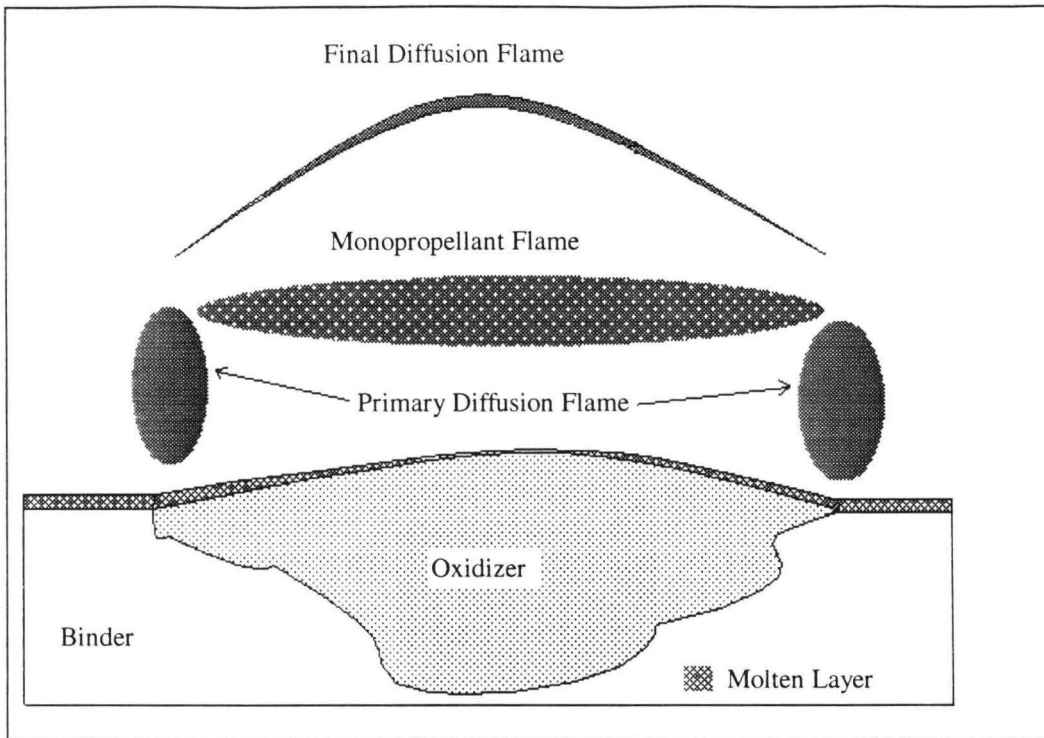


Figure 5: Multiple Flames in Composite Propellant Combustion. (adapted from Ref. 8)

The relative effect of these three flames to the burning rate is a function of pressure, as illustrated in Figure 6. At low pressures (≤ 20 atm), the diffusion flame dominates and the monopropellant flame is not well established due to slower kinetics. The location of the monopropellant flame is a stronger function of pressure than is the location of the diffusion flame and as the pressure increases it moves closer to the surface than the final diffusion flame. At moderate pressures (~ 20 - 40 atm), the monopropellant flame and primary diffusion flame compete for control of the heat flux to the surface. At high pressures (> 40 atm), the monopropellant flame is next to the surface and there is only one diffusion flame. The contribution of heat flux to the surface from the diffusion flame can still be important, but the monopropellant flame dominates.⁸

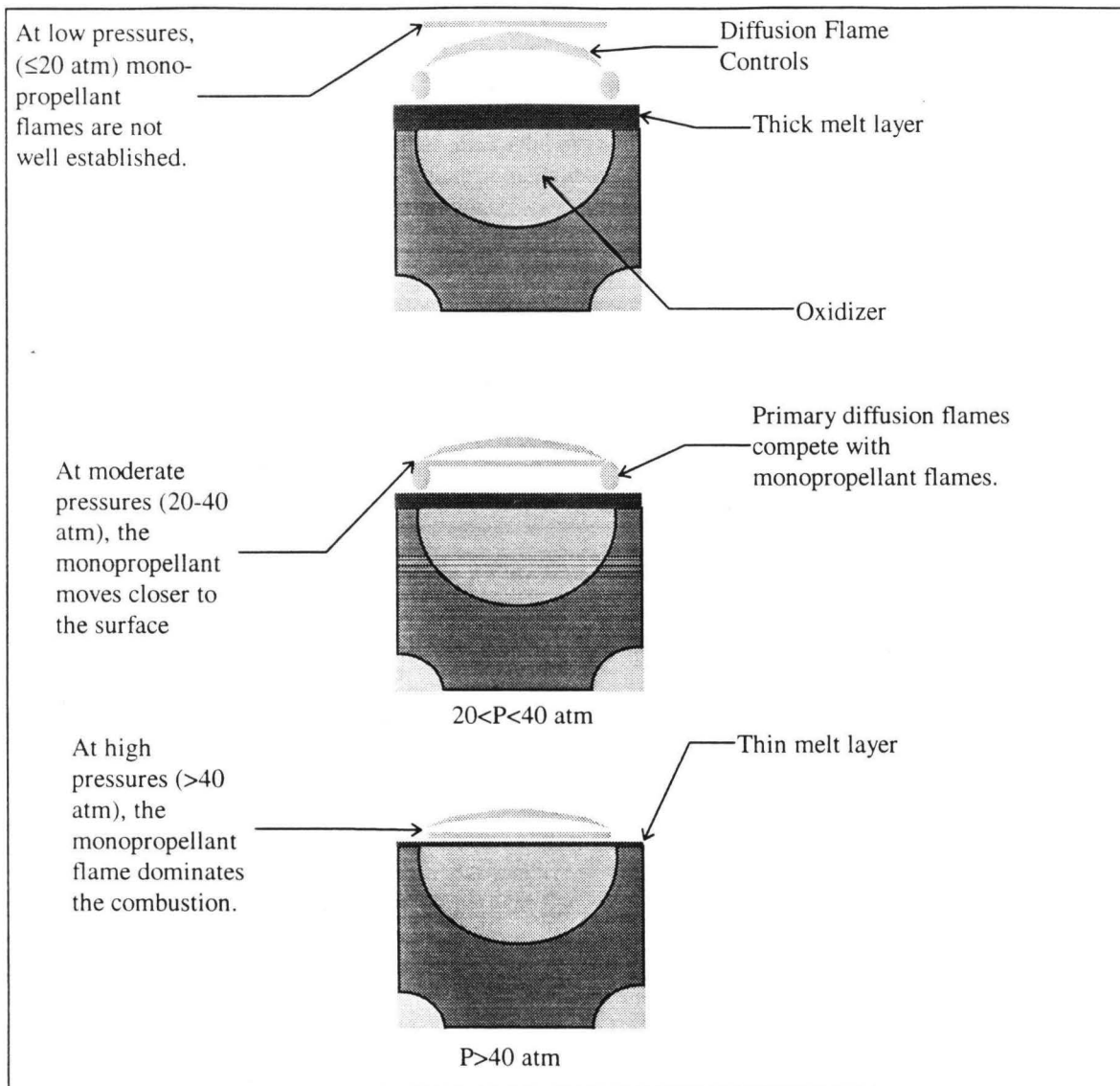


Figure 6: Pressure Effects on Flame Structure (adapted from Ref. 8).

The flame structure is also a function of geometry. As the binder and oxidizer crystal burn, the initial diffusion distances are relatively small but increase with the diameter of the exposed crystal. The flame structure above the oxidizer crystal changes with the diffusion distances.⁸ (See Figure 7).

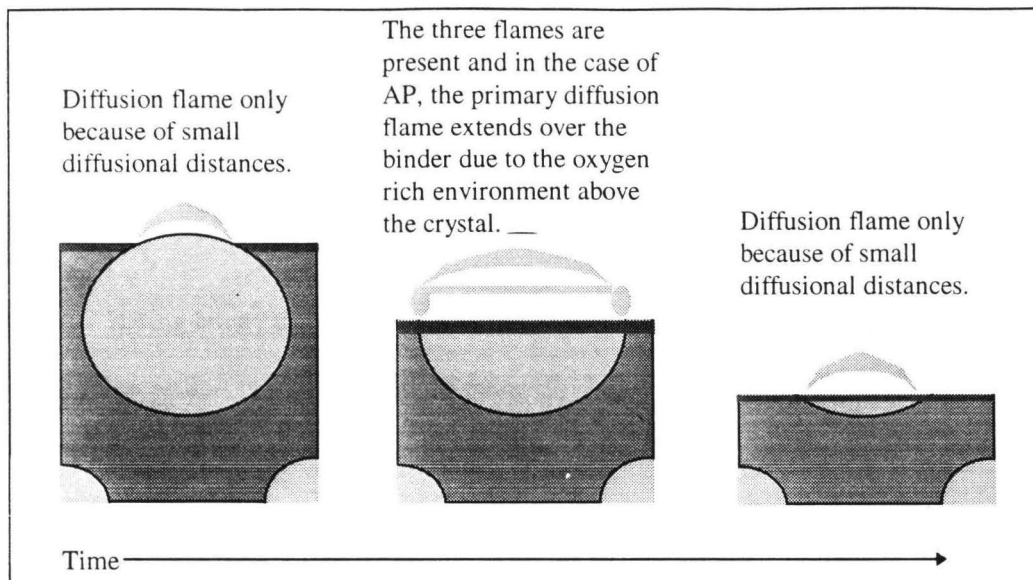


Figure 7: Composite Flame Structure as a Function of Geometry. (adapted from Ref. 8).

The relative significance of diffusion flames in the combustion of a propellant is largely determined by the chemical composition of the individual ingredients. For example, the pure nitramines, RDX and HMX, burn faster than pure AP, but a composite AP propellant will burn faster than a composite nitramine propellant (assuming a non-energetic binder).⁸ Characteristics of composite propellant combustion are dependent on particle size, pressure, mass percentages of binder and oxidizer, initial temperature and chemical composition. The ultimate goal of modeling efforts is to predict accurately this functionality. To do so, a model must be able to predict the correct temperature and species concentrations in three dimensions. A one-dimensional model which accurately predicts temperature and species profiles is a necessary precursor for multi-dimensional models with detailed chemistry.

The following two chapters address how various models found in the literature address these issues.

CHAPTER 2 : THE CONSERVATION EQUATIONS

Having briefly discussed in words the state of understanding of the combustion of propellants in the previous section, this chapter and the following chapter will discuss how scientists and engineers have attempted to describe the above processes mathematically. In doing so, the general conservation equations will first be presented without any simplifying assumptions. These equations, after applying the simplifying assumptions that are common among almost all propellant combustion models (i.e. Fourier's law of heat transfer, Newtonian fluid, and ideal gas), will serve as the basis for comparison for the various propellant combustion models found in the literature (Chapter 3).

The Conservation Equations

The combustion of solid propellants can be described by the general conservation equations of mass, momentum, and energy. Even though some of the terms in the following equations are generally set to zero for solid and liquid phases, they are included here for completeness because they can become important in the gas phase.¹⁴

$$\text{Continuity Eq.:} \quad \frac{\partial \rho}{\partial t} + \nabla \cdot (\rho u) = 0 \quad (1)$$

$$\text{Momentum Eq. :} \quad \rho \left[\frac{\partial u_i}{\partial t} + u_j \frac{\partial u_i}{\partial x_j} \right] = \frac{\partial \sigma_{ji}}{\partial x_j} + \rho \sum_{k=1}^{kk} (Y_k f_k)_i \quad (2)$$

$$\begin{aligned} \text{Energy Eq.:} \quad & \rho \frac{\partial h_t}{\partial t} + \rho u_i \frac{\partial h_t}{\partial x_i} = \\ & - \nabla \cdot q + \dot{Q} + \frac{\partial \sigma_{ji} u_i}{\partial x_j} + \rho \sum_{k=1}^{kk} Y_k f_{(k)i} (u_i + V_{(k)i}) + \frac{\partial p}{\partial t} + u_i \frac{\partial p}{\partial x_i} \end{aligned} \quad (3)$$

The continuity equation is sum of all the individual species equations:

Species Eq:
$$\rho \frac{\partial Y_k}{\partial t} + \rho \underline{v} \cdot \nabla Y_k + \nabla \cdot \left(\rho Y_k \underline{V}_k \right) = \omega_k \quad (4)$$

No assumptions are made in Eqs.s 1-4, but many of the terms require further definition. (Note: \underline{V}_k is the velocity of species k due to diffusion with respect to the bulk velocity u .) Assuming an isotropic Newtonian fluid, and employing the hypothesis made by Stokes, the total stress tensor can be defined as:

$$\sigma_{ij} = -p\delta_{ij} + \mu \left[\frac{\partial u_i}{\partial x_j} + \frac{\partial u_j}{\partial x_i} \right] - \frac{2}{3}\mu \left[\delta_{ij} \frac{\partial u_k}{\partial x_k} \right] \quad (5)$$

where p is the hydrostatic pressure and μ is the dynamic viscosity.

In the energy equation, the heat flux \mathbf{q} is defined as the sum of the heat flux due to conduction (Fick's law), diffusion and Dufour effect, but the Dufour effect is so small that it is generally assumed to be negligible. Thus \mathbf{q} is defined by:

$$\mathbf{q} = -\lambda \nabla T + \rho \sum_{k=1}^{kk} h_k Y_k \underline{V}_k \quad (6)$$

The heat input term, \dot{Q} includes energy from chemical reactions, radiation and any heat loss from the system (i.e. laser heat flux or a non-adiabatic system). \dot{Q} is defined as:

$$\dot{Q} = -\sum_{k=1}^{kk} \omega_k \Delta h_{f,k}^\circ + \dot{Q}_{loss} + \dot{Q}_{radiation} \quad (7)$$

where ω_k is the mass production rate of species k and is defined in terms of the chemical reactions:

$$\omega_k = W_k \sum_{i=1}^{ii} (v''_{k,i} - v'_{k,i}) A_i T^i \exp\left(-E_{a,i}/RT\right) \prod_{j=1}^{kk} \left(\frac{X_j P}{RT}\right)^{v'_{j,i}} \quad (8)$$

The diffusion velocity V_k for a multi-component system, assuming that thermal diffusion, body forces, ideal gas and pressure-induced diffusions are negligible can be found by solving:¹⁴

$$\Delta X_k = \sum_{j=1}^{kk} \frac{X_k X_j}{D_{kj}} (V_j - V_k) \quad (9)$$

Finally, in propellant combustion, body forces ($f_{(k)}$) can usually be neglected. With these assumptions, constitutive relations, and definitions, Eqs.s 1-4 are very difficult to completely specify and solve. Almost all of the models discussed in subsequent chapters make the assumption that the combustion

can be treated as one-dimensional. With the assumptions discussed above the one-dimensional versions of Eqs.s 1-4 are:

$$\text{1-D Continuity:} \quad \frac{\partial \rho}{\partial t} + \frac{\partial}{\partial x}(\rho u) = 0 \quad (10)$$

$$\text{1-D Momentum Eq. :} \quad \rho \left[\frac{\partial u}{\partial t} + u \frac{\partial u}{\partial x} \right] = -\frac{\partial p}{\partial x} + \frac{4}{3} \frac{\partial}{\partial x} \left(\mu \frac{\partial u}{\partial x} \right) \quad (11)$$

$$\begin{aligned} \text{1-D Energy Eq.:} \quad & \rho C_p \frac{\partial T}{\partial t} + \rho u C_p \frac{\partial T}{\partial x} - \frac{\partial p}{\partial t} - u \frac{\partial p}{\partial x} = \\ & \frac{\partial}{\partial x} \lambda \frac{\partial T}{\partial x} - \frac{\partial}{\partial x} \left(\rho T \sum_{k=1}^{kk} C_{p(k)} Y_k V_k \right) \\ & + \dot{Q}_{radiation} + \dot{Q}_{loss} + \sum_{k=1}^{kk} \omega_k \Delta h_{f(k)}^\circ + \mu \frac{4}{3} \left(\frac{\partial u}{\partial x} \right)^2 \end{aligned} \quad (12)$$

$$\text{1-D Species Eq:} \quad \rho \frac{\partial Y_k}{\partial t} + \rho u \cdot \frac{\partial}{\partial x} Y_k + \frac{\partial}{\partial x} (\rho Y_k V_k) = \omega_k \quad (13)$$

Simplifying Assumptions

For steady-state problems, not only do the time-dependent terms disappear, but the viscous effects are usually assumed negligible. By assuming constant pressure, the pressure gradient terms in the momentum and energy equations are dropped. This effectively eliminates the need for the momentum equation. Applying these additional assumptions to Eqs.s 10-13 yields:

$$\text{1-D SS Continuity:} \quad \frac{\partial}{\partial x}(\rho u) = 0, \quad \rho u = \text{constant} \quad (14)$$

$$\begin{aligned} \text{1-D SS Energy Eq.:} \quad & \rho u C_p \frac{\partial T}{\partial x} = \frac{\partial}{\partial x} \lambda \frac{\partial T}{\partial x} - \frac{\partial}{\partial x} \left(\rho T \sum_{k=1}^{kk} C_{p(k)} Y_k V_k \right) \\ & + \dot{Q}_{radiation} + \dot{Q}_{loss} + \sum_{k=1}^{kk} \omega_k \Delta h_{f(k)}^\circ \end{aligned} \quad (15)$$

$$\text{1-D SS Species Eq:} \quad \rho u \frac{\partial}{\partial x} Y_k + \frac{\partial}{\partial x} (\rho Y_k V_k) = \omega_k \quad (16)$$

The above set of equations (14,15,16) are still difficult to solve when considering the many species and reactions that can be involved in three phases (solid, liquid and gas). Steady-state propellant combustion models are generally developed by making further simplifications to these equations. Many of these assumptions are discussed in the next chapter.

CHAPTER 3 : MODELS FOUND IN THE LITERATURE

In this chapter, a review of the steady-state propellant combustion models from the past 30 years is presented. Many of the models developed prior to 1970 were summarized by Beckstead and McCarty.¹⁵

Though there are a variety of levels of assumptions made, the evolution of steady-state propellant combustion modeling can be divided into four categories:

1. Global Kinetic Models.
2. Semi-Global Models
3. Development of Detailed Kinetic Mechanisms.
4. Multi-Phase Models with Reactions.

Naturally, some models will overlap two of the categories. The general differences are highlighted in Table 2. As the name implies, the global kinetic models use global kinetics and, in general, only solve the energy equation assuming a surface reaction and flame sheet. The semi-global models relax the surface reaction and flame sheet assumptions, solve both the energy and species equations, and generally have at least two competing global reaction steps. The next step in the evolution of propellant combustion models was the development of elementary-step reaction mechanisms. The simplest of these mechanisms generally include more than 15 species involved in more than 30 reactions. The most recent models include the detailed reaction mechanisms in the gas phase coupled with reacting condensed phases. The progression in the complexity and power of the models can be attributed to more and better experimental data, better computers, and better numerical algorithms.

Table 2: General Differences between Categories of Models.

Characteristic	Global	Semi-Global	Detailed Kinetics	Multi-Phase
Solid region	*	*		*
Liquid region		?		*
Gas region		*	*	*
Energy equation	*	*	*	*
Species equation		*	*	*
Surface reaction	*		?	
Flame sheet/standoff	*			
Elementary gas reactions			*	?
In-depth condensed reactions		*		?

* indicates incorporation of characteristic in model category.

Previous Modeling Efforts

Global Kinetic Models

In 1970, Beckstead, Derr and Price¹³ published their BDP model for composite solid-propellant combustion. This model served as a starting point for many subsequent models of both monopropellant and composite propellant combustion. The application of this model to a monopropellant will first be described.

For the BDP type of model, the combustion processes are described by a one-dimensional energy equation spanning a condensed (generally assumed to be solid) and gas region. The species continuity equations are neglected and the reactions are represented by heat releases due to a surface reaction and a flame sheet approximation at some flame stand-off distance from the surface. The energy equation is solved for the surface temperature, which is then used to calculate the burning rate from an Arrhenius expression. The equations, as presented by Beckstead in his application of the BDP model to a double base propellant, are:¹⁶

The burning rate:

$$m_s = A_s \exp\left(\frac{-E_s}{RT_s}\right) \quad (17)$$

Energy Equations:

$$T_s = T_o - \frac{Q_L}{c_p} + \frac{Q_f}{c_p} \exp(-\zeta^*) \quad (18)$$

$$Q_f = c_p \cdot (T_f - T_o) - Q_L \quad (19)$$

Flame stand-off distance:
$$\zeta^* = \frac{c_p m_s^2}{\lambda k P^\delta}, \quad k = A_f \exp\left(\frac{-E_f}{RT_f}\right) \quad (20)$$

where f refers to the gas flame, s for the surface, and L the liquid. To use this model, the adiabatic flame temperature (T_f) is calculated by a thermo-equilibrium code for a given pressure (P) and initial temperature (T_o). Equations 18, 19, and 20 can be substituted into Eq. 17, yielding a single equation, implicit in the burning rate (m_s), with eight remaining parameters to be specified (E_f , A_f , c_p , λ , δ , Q_L , E_s and A_s). Since all eight parameters are either global and/or independent of local temperature and composition, they tend to represent averages. Therefore, they generally have large levels of uncertainty. Whenever this or similar models have been presented in the literature for specific propellants, much of the discussion has dwelt upon the choice of the parameters. In almost every case, at least one or two of the parameters are chosen (usually the gas-phase reaction prefactor, A_f) by optimization so that Eq. 17 accurately predicts the burning rate.

As stated above, the BDP model was originally developed for composite propellants with combustion occurring in three flames. (See Figure 5, page 10). This was accomplished by including two extra flame terms in Eq. 18 and describing their flame stand-off distance in terms of diffusional lengths. These diffusional lengths were determined by a Burke-Schumann analysis using the surface geometry to determine the mixture ratio. (For further details see Ref. 13). In the years following its development, the BDP model (or models based on similar assumptions) has been applied to many mono- and composite propellants. In the case of composite propellant models, the differences in the models mainly arise in the method of determining the surface conditions (the fuel to oxidizer surface area ratio, surface temperatures for the different components and treatment of the distribution of particle sizes). Despite the differing assumptions made, most of these composite models correlate experimental data to nearly the same accuracy. Several of the composite global kinetic models are reviewed by Cohen¹⁷ and will not be repeated here. Many of the global-kinetic models are summarized in Table 3.

Table 3: Global Kinetic Models

Year	Researchers	Ingredient(s)	Assumptions
1970	Beckstead, Derr & Price ¹³	AP/HTPB	<ol style="list-style-type: none"> 1. Area of AP crystal calculated assuming spherical crystal in constant contact with planer binder surface. 2. Surface temperature of binder equals surface temperature of oxidizer. 3. Composite propellant represented by average crystal size.
1971	Beckstead, Derr & Price ¹⁸	AP, HMX, KP	<ol style="list-style-type: none"> 1. Studies of these ingredients as monopropellants and composite propellants. 2. Other assumptions similar to 1970 paper.
1971	Guirao & William ¹⁹	AP	<ol style="list-style-type: none"> 1. Although the equations and solution method are somewhat different from the traditional BDP approach, the approach is very similar. 2. Develop rate constants for a one-step gas reaction, by fitting constants to data generated from a nine-step mechanism. 3. In surface reaction, 70% of AP forms final products. 30% forms NH₃, HClO₄. 4. Instead of solving for T_s, they calculate Y_s from which the burning rate is calculated.
1976	Beckstead & McCarty ¹⁵	HMX	<ol style="list-style-type: none"> 1. Determined parameters via optimization to experimental data.
1980	Beckstead ¹⁶	DB	<ol style="list-style-type: none"> 1. Studies the effect of propellant energy on model predictions.
1981	Beckstead & McCarty ^{20,21}	HMX/HTPB	<ol style="list-style-type: none"> 1. Burning rate averaged as burning surface regresses linearly. 2. Two types of oxidizers, three sizes possible. 3. Binder and oxidizer can have different surface temperatures. 4. Incorporation of ignition delay time for oxidizer crystal.
1986	Mitani and Williams ²²	HMX	<ol style="list-style-type: none"> 1. 20 to 40 % of HMX decomposed in the condensed phase. 2. Allowed for evaporation at surface. 3. Activation-energy asymptotics.
1989	Beckstead ²³	AN, AP, HMX, DB	<ol style="list-style-type: none"> 1. Same assumptions as Beckstead 1971 except for DB. The dark zone temperature was chosen as the flame temperature.
After 1970	Summary by Cohen. ¹⁶ Cor ²⁴ Glick, ²⁵ others.	AP/Binder Composites	<p>These models differ in the determination of the ratio of fuel surface area oxidizer surface area, and non-uniform surface conditions. Despite the many differences, the ability of these models to correlate with experimental data is nearly the same. Cohen did an extensive review of the main composite propellant models and will not be repeated here.</p>

The model of Guirao and Williams¹⁹ could be categorized as either a global or semi-global model. Guirao and Williams began with a fourteen-step mechanism but reduced it down to one global step in the final model. Instead of solving for the surface temperature by the energy equation, they used the species equation.

Semi-Global Models

In order to develop more realistic models, researchers began including more reactions and relaxing surface-reaction and flame-sheet assumptions. In 1976, BenReuven et al.²⁶ were the first to include an in-depth condensed reaction zone in their modeling of RDX and HMX. Their RDX model (similar to their HMX model) is described here. They assumed that RDX decomposition began after melting and described it by a single first-order reaction. The gaseous species formed by this reaction were assumed to be dissolved in the liquid, thus bubble formation was neglected. The gas phase was described essentially by Eqs. 14, 15 and 16 with the Lewis number[†] for the individual species and the mixture assumed to be unity. The gases from the RDX decomposition occurring in the liquid region plus the RDX evaporating at the surface provide the boundary conditions for the gas phase. Evaporation is calculated using a Clausius-Clapeyron expression assuming vapor-liquid equilibrium. In addition to the RDX_{vapor} decomposition, one reaction between the decomposition products was considered in the gas phase. The gas-phase calculations continue away from the surface until all the RDX vapor decomposes, at which point the authors assume that the effect the remaining portion of the flame has on the surface is negligible. The surface temperature and burning rate are determined by matching the energy gradient and evaporation mass flux at the surface. In addition to burning rate and surface temperature, the model also predicts the melt-layer thickness, temperature profile and the species profiles. For RDX, the model accurately predicts the burning rate over the pressure range of 10-40 atm, but for HMX,²⁷ the authors had to specify the burning rate. Based on the behavior of the HMX model, the authors speculated that bubble formation is an important factor that should be considered. The major contributions that BenReuven et al. made to propellant combustion modeling were the inclusion of the in-depth liquid reaction and solving the species equation albeit for a limited number of species involved in a very global mechanism.

In 1985, Cohen et al.²⁸ updated the chemistry of BenReuven's HMX model (but it was still global) and the model was able to match experimental burning rates. Contrary to Ermolin's conclusion,²⁹

[†] $Le = \alpha / D_{ab}$, the ratio of thermal and mass diffusivities.

Cohen felt that mass diffusion could be neglected in the species equations for the gas phase. The differing opinions can likely be attributed to the differences in mechanisms.

In 1988, Bizot and Beckstead modeled double base³⁰ (DB) and HMX³¹ monopropellants by dividing the combustion process into two regions (condensed and gas). In both regions, their reactions were global and the products were not specified. They neglected mass diffusion, phase changes, and assumed constant properties. After adjusting kinetic parameters, the calculations agreed fairly well with experimental data for burning rate, surface temperature, and dark zone length.. While more correlative than predictive, this model requires much less computer time than the more complex models and has been incorporated in models of multidimensional, unsteady combustion in rocket motors.³²

Beginning in the mid-1980's, Williams and co-workers developed numerical models of the combustion of RDX and HMX. Based on thermocouple data for HMX, Williams and Mitani³³ concluded that 20 to 40 percent of the HMX must decompose in the condensed phases via exothermic reactions. They noted that below 67 atm, the flame of HMX is blue with white smoke and above 134 atm the flame is bright orange. Yet according to them, there is no apparent change in the burning rate curve. From this observation they assume that the burning rate of HMX is controlled by processes occurring in a very thin layer close to the surface and that the later stages of the flame have very little influence over the burning rate. Not only is this a large extrapolation to make, but as seen in Figure 8, this observation is very questionable.

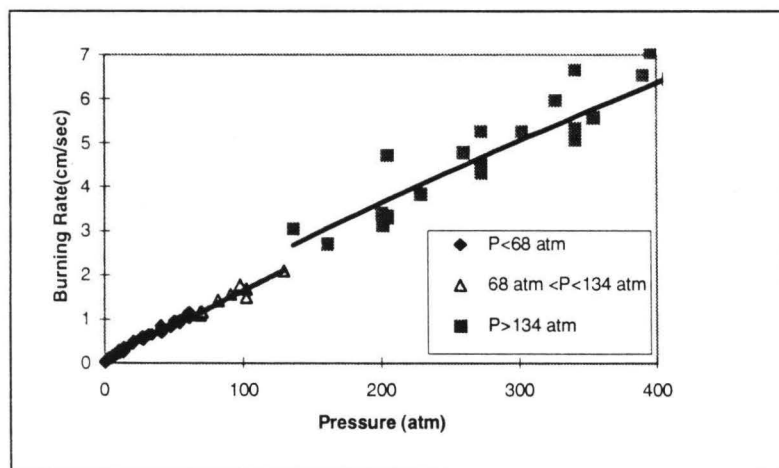


Figure 8: HMX Burning Rate Data^{34,35}

The Williams nitramine model divides the combustion process into seven regions.³⁶ (See Figure 9). The solid is heated via conduction from the initial temperature (T_{init}) to the melting temperature (T_{melt}). The liquid continues to preheat until the evaporative equilibrium region is reached where, as the name suggests, evaporative equilibrium is maintained.

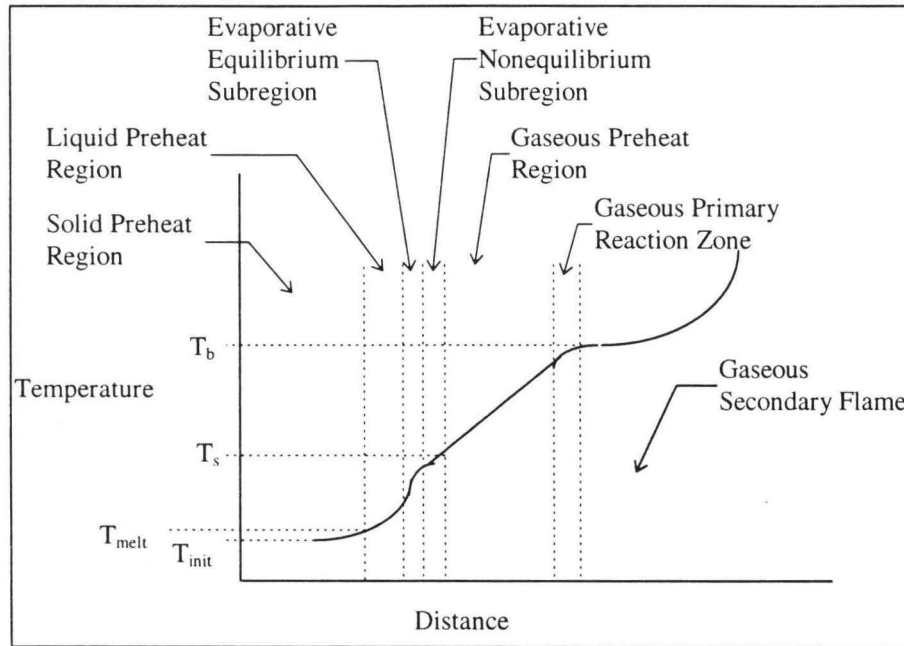


Figure 9: Schematic of Williams Nitramine Model (adapted from Ref. 36)

In the evaporative equilibrium and non-equilibrium regions, two phases exist: liquid and gas. The effect of two-phase flow on the deflagration of solids was studied theoretically by Margolis, Williams and Armstrong.³⁷ After considering pressure-gradient effects, surface-tension-gradient effects, momentum transfer associated with mass transfer, and viscous drag of the gas on the condensed phase, the authors concluded that the velocity of the bubbles is greater than that of the surrounding liquid. This order-of-magnitude analysis failed to quantify the differences in the velocity of the two phases. In the full model,³⁶ the authors used the overall conservation equation:

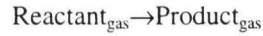
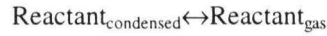
$$\rho_c u_c (1 - \phi) + \rho_g u_g \phi = \dot{m} = \text{constant} \quad (21)$$

with

$$u_c = \frac{\dot{m}}{\rho_c}(1 - s\phi) \quad \text{and} \quad u_g = \frac{\dot{m}}{\rho_g}(1 + s(1 - \phi)) \quad (22)$$

where the parameter s can be used to take into account the possibility that u_c might be less than \dot{m}/ρ_c because of gradients in surface tension. For the nitramines, the authors use $s=0$ and therefore $u_c = \dot{m}/\rho_c$ and $u_g = \dot{m}/\rho_g$.

The reaction mechanism in this model is global. Three reactions are considered:



The authors assumed the products in the first and third reactions are $n\text{CH}_2\text{O} + (n/3)(\text{NO}_2 + \text{N}_2\text{O}) + (n/2)\text{N}_2$, where $n=4$ for HMX and 3 for RDX.³³ These products are not the final flame products but those considered by the authors as being produced very near the surface and thus controlling the burning rate. The reactions in what the authors called the secondary flame are neglected.

Williams et al. applied methods of asymptotic analysis to obtain a solution to the energy and species equations.³⁶ Constant property values were estimated and global kinetic parameters were optimized so as to allow the model to correlate well with experimentally determined burning rate data for several initial temperatures. Based on sensitivity analysis of their model, the authors predicted RDX to have a lower surface temperature than HMX because of the higher vapor pressure of RDX. They also concluded that RDX decomposition in the two-phase region is negligible as their model indicates that 99.5 percent of the $\text{RDX}_{\text{liquid}}$ evaporates. The authors stated that the next step in refining their model was to use detailed chemical-kinetic parameters.

Recently, Li and Williams³⁸ proposed an elementary-step reaction mechanism for RDX in the primary flame zone, but failed to provide kinetic rate parameters. After devoting most of their paper to a discussion of possible important elementary-step reactions, the authors reverted back to their global, two-step mechanism.

With both the global and semi-global models, there are always unknown model inputs (usually global reaction rate constants) that could be adjusted (optimized) to enable these models to correctly

predict burning rate or some other parameter. To make the models more fundamental, elementary kinetics with experimentally determined rate constants are needed. In reality, there are at least hundreds of different reactions occurring simultaneously. The next step in the evolution of combustion modeling is to incorporate detailed kinetics.

Development of Detailed Kinetic Mechanisms

One of the difficulties faced by Guirao and Williams¹⁹ in developing the 14-step mechanism for AP was determining the kinetic parameters. With the progress that has been made in both experimental and theoretical determination of reaction rates, reaction paths, and thermophysical properties, the species equation has become an important part of the propellant combustion model. In this section, work that has led to the development of complex elementary-step mechanisms in propellant combustion models is discussed. The development of these propellant combustion mechanisms has been greatly aided by research in hydrocarbon combustion, but this contribution will not be discussed here.

In 1982, Korobeinichev et al.³⁹ measured concentration profiles in perchloric acid/methane flames. They proposed an 18-step mechanism for this system. In subsequent work, Ermolin et al.¹² measured concentration profiles for AP and proposed an elementary mechanism composed of 80 steps and 24 species. They modeled the gaseous flame using Eqs. 14, 15 and 16 (page 15) neglecting heat and mass diffusion. The agreement between the model and their experimental data was fair but their model did indicate which reactions needed further review. In 1984,²⁹ they included thermal and mass diffusion in their equations and concluded that thermal and mass diffusion play an important role in the overall flame structure. Later they developed a 90-step mechanism for RDX combustion and were able to match their experimental species profiles to within 10% at 0.5 atm.⁴⁰ The focus of their work has been on the gas-phase chemistry at low pressures. They have neglected any condensed-phase interaction other than assuming the feed concentrations going into their gas-phase model came from the decomposition of AP or RDX.

The development of gas phase mechanisms was greatly advanced by the work of Kee et al.^{41,42,43,44} at Sandia National Laboratories. Beginning in the 1980's, researchers at Sandia developed a

subroutine library (CHEMKIN) which performs many of the calculations necessary for reacting gaseous mixtures. With this library, workers at Sandia developed computer codes to model premixed laminar flames (PREMIX),⁴⁵ perfectly stirred reactors (PSR),⁴⁶ and other systems. Given the system conditions, thermophysical properties of all of the species and a reaction mechanism, PREMIX can solve Equations 14, 15 and 16 for the temperature profile, species profiles and laminar flame speed of gas mixtures. The majority of propellant combustion models that have been developed since the release of PREMIX have used PREMIX to model the gas region.

Also during this time, Melius et al.^{47,48} calculated thermodynamic properties and reaction rate constants for the decomposition of RDX_{vapor}. This was done via the theoretical procedure Bond-Additivity-Corrected Moller-Plesset 4th order perturbation theory method (BAC-MP4). With the computers that he had available, he was able to calculate thermochemical properties, vibrational frequencies and bond energies for species containing up to nine heavy atoms. From calculations made for smaller "model" molecules, he estimated the thermochemical properties and rate constants for heavier molecules such as RDX_{vapor} (15 heavy atoms). He proposed 158 reactions involving 38 species to describe the ignition of RDX. The model is described below.⁴⁹

Many improvements have been made to the original Melius-RDX mechanism. Yetter et al.⁵⁰ with the input of other workers (Lin et al.⁵¹ and Politzer et al.⁵² etc.) are systematically improving upon the Melius-RDX mechanism. They have divided the large mechanism into smaller groupings to limit the number of species and reactions that can occur within a sub-mechanism. Then, they study the elementary reactions, both experimentally and theoretically, to determine rate constants. The sub-mechanisms are tested by comparing calculated results to measured results from shock tube, PSR, premixed flames and diffusion flames. Once the sub-mechanisms are validated, they are combined to determine cross interactions. Yetter's changes to the RDX mechanism have greatly improved its predictive power. The version of the Melius-Yetter mechanism used in this dissertation work has 232 reactions and 45 species.⁵³

Cohen⁵⁴ recently reviewed several AP mechanisms. He compared those developed by Guirao and Williams,¹⁹ Jacob and Pearson⁵⁵, Sahu et al.⁵⁶ and Ermolin.¹² After pointing out several obvious mistakes in the previous mechanisms, Cohen proposed a new mechanism but conceded, "It is entirely possible that

no model consisting only of homogeneous gas-phase reactions will give realistic predictions of reaction time, apparent activation energy, stoichiometry, and temporal behavior of selected intermediates—the principal observable quantities." While proposing several steps that he felt were important, he did not provide rate constants for them. Unlike the nitramines (RDX and HMX), AP has chlorine instead of carbon. Because the chlorine gas-phase chemistry has not been studied as extensively as the carbon chemistry, the AP mechanism is less complete when compared with the RDX mechanism.

Other researchers have compiled elementary step mechanisms for the combustion of monopropellants. These other compilations are summarized in Table 4.

Multi-Phase Models with Detailed Reactions

The most successful models being developed today have abandoned the surface-reaction and flame-sheet assumptions, include a condensed phase reaction zone, and solve the species equation in both the condensed and gas regions. The use of an elementary-step mechanism for at least the gas phase distinguishes this category from the semi-global category. Most of these models include solid, liquid (or two-phase) and gas regions as demonstrated in Figure 10, but some models combine the solid and liquid regions into a single "condensed" region.

In 1984, Narahari et al.⁵⁸ were the first to link a condensed phase to a gas-phase model that includes complex kinetics with thermal and mass diffusion. For AP, the gas-phase mechanism included 17 species involved in 14 reactions. The condensed-phase calculations included solving the energy equation for both the solid and liquid regions, but no condensed-phase reactions were considered except at the liquid/gas interface. The predictions by their model did not agree well with experimental data. The authors attributed the lack of agreement to their abbreviated mechanism.

Table 4: Elementary-Step Mechanisms for Propellant Combustion

Year	Researchers	Ingredient	# of Species	# of rxns	Comments
1969	Jacobs & Pearson ⁵⁵	AP	19	17	Gave only a possible path but no kinetics constants.
1971	Guirao & Williams ¹⁹	AP	19	14	Developed one global step from calculations made 14-step mechanism under iso-thermal conditions.
1982	Ermolin et al. ⁵⁷	AP	24	80	Qualitative agreement with mass spec. data at 0.58 atm
1984	Narahari et al. ⁵⁸	AP	14	17	
1986	Hatch ⁵⁹	NG/binder	21	60	Indicates presence of a dark zone.
1986	Ermolin et al. ⁴⁰	RDX	23	90	Mechanism produced reasonable agreement with experiment at 0.5 atm.
1987	Hatch ⁶⁰	HMX	25	77	Assumed HMX decomposed to CH ₂ O, NO ₂ , N ₂ O and HCN in condensed phase.
1990	Sahu et al. ⁵⁶	AP	18	22	ClO, a species considered by many to be important is not included. Some rate constants are not reasonable.
1990	Melius ^{17,48,49}	RDX	38	158	Calculated properties and kinetics from BAC-MP4
1992	Cohen ¹⁷	AP	35	136	Reviewed several other AP mechanisms and proposes his own, but does not provide rate constants for several reactions he considers to be important.
1994	Li & Williams ³⁸	RDX		15	Describe a primary flame mechanism but do not provide any rate constants.
1995	Anderson et al. ⁶¹	Double Base	41	189	Mechanism for predicting the chemistry of the dark zone (1-30 atm)
1995	Yetter et al. ⁵⁰	RDX	45	232	Improvements on Melius Mechanism

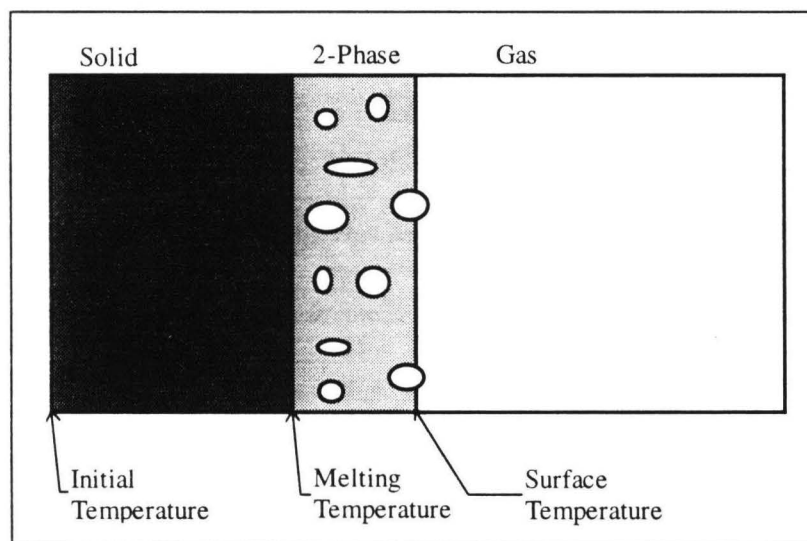


Figure 10: The Multiple Phases of a Burning Propellant.

In 1986, Hatch⁵⁹ developed a model for NG/binder combustion similar to the one developed by BenReuven et al.²⁶ for RDX ten years before. There are three major differences. Hatch assumed that:

1. The gas formed in the liquid region is **not** dissolved in the liquid but forms voids in the liquid. The gas in these voids is allowed to react.
2. The gas-phase mechanism is elementary in nature compared to the two global reactions of BenReuven.
3. The gas-phase calculations proceed to the final flame products.

There were no free parameters in Hatch's model, and although it failed to accurately predict experimentally determined burning rates, sensitivity analysis indicated which parameters were affecting the burning rate significantly. His model also predicted a dark zone, characteristic of NG and DB combustion.

The following year, Hatch applied his model to HMX⁶⁰ and again failed to match burning rate measurements. Hatch's major contribution to the modeling effort was allowing for the formation of voids (or bubbles) in the liquid/two-phase region. In Hatch's model, the continuity equation in the two-phase region is written as:

$$\rho_l u_l (1 - \phi) + \rho_g u_g \phi = \dot{m} \quad (23)$$

An additional relation between the liquid and gas velocity is required to specify the system. Using the momentum equation for this relation introduces several poorly characterized parameters to the problem (i.e. surface tension, viscosity, etc.). To avoid this, Hatch assumed an inviscid flow; thus, the voids are detached from the liquid. With this assumption, the liquid and gas velocities can then be calculated by: $u_l = \dot{m} / \rho_l$, $u_g = \dot{m} / \rho_g$. This leads to void velocities a couple orders of magnitude higher than the liquid velocity. The other extreme is to assume $u_l = u_g$, which means that as the voids expand in the two-phase region, the liquid and gas accelerate together. Margolis and Williams theoretically investigated these various assumptions (discussed in Ref. 37 and on page 23) and concluded that the former assumption is more accurate.

One of the major contributions of Melius to the propellant modeling was the development of the RDX gas-phase mechanism described above.⁴⁸ While the gas flame chemistry was the major focus, he also developed a one-dimensional, premixed RDX ignition model.⁴⁹ The model consisted of a simple condensed model supplying the cold boundary conditions to the PREMIX⁴⁵ code described above. He allowed for one decomposition reaction and an evaporation/condensation relation at the surface. The model under-predicted the burning rate and surface temperature at 1 and 20 atmospheres and has been criticized for how the burning rate is calculated.⁶² The burning rate is largely controlled by the evaporation/condensation relation. The net mass flux becomes the difference between two very large numbers, neither of which is known very accurately.

Data for Model Validation

At this point in time, modeling efforts had gone beyond the available experimental data. After the demonstration of the calculations of Melius,⁴⁹ many researchers turned their focus to improving and verifying his mechanism and model. In order to do this, a more quantitative description of the flame structure (species and temperature profiles) of RDX was needed. Litzinger et al.,^{63,64,65} Brewster et al.⁶⁶ and Hanson-Parr and Parr^{67,68,69} have used mass spectrometers and UV-Visible absorption measurements to quantify the gas phase flame structure. Kuo et al.^{6,70} and Brill⁴ have focused on the initial decomposition mechanism and melt region of RDX using mass spectrometry and T-Jump experiments. Using thermocouples, Zenin⁷¹ measured temperature profiles, surface temperature, and melt-layer thickness. Examples of the experimental data available for model validation for RDX and other energetic materials is summarized in Table 5.

In attempting to validate a model with experimental data, one must either model the experiment or develop an experiment that corresponds to the model. In a self-deflagrating RDX flame, the reactions occur too close to the surface to measure concentration profiles for several species. To overcome this difficulty, Litzinger⁶⁴ and Parr⁶⁷ used a laser heat flux on the burning propellant surface to increase the burning rate and spread out the flame. With the added heat flux a two-stage flame developed similar to that seen in double base (DB) combustion. (Refer to Figure 37, page 66). At this point, none of the models

were modeling a laser flux or seeing a dark zone. (Note: No dark zone is observed when there is no additional laser flux). In order to validate the models with experimental data, the effect of the laser flux on the burning rate had to be included within the models. The experimental data indicated that the Melius mechanism and model needed refinement. These data and other data shown in Table 5 is discussed in more detail below.

Table 5: Experimental Studies Available for Model Validation.

Researchers	Propellant	Type of Data	Comments
Ermolin et al. ¹²	AP	X(H ₂ O, HCl, O ₂ , HClO ₄ , Cl ₂ , ClOH, NO, NO ₂ , N ₂ O, ClO ₂)	0.5 atm
Brewster & Schroeder ⁶⁶	RDX	T _s , r _b (Laser)	
Ermolin ⁴⁰ et al. Korobeinichev ⁷² et al.	RDX, HMX	X(CO, H ₂ CO, NO ₂ , HCN, CO ₂ , N ₂ O, H ₂ O, NO, N ₂ , H ₂)	0.5 atm. Species concentrations do not approach equilibrium values.
Zenin ⁷¹	HMX, RDX	T(x), r _b , I _{melt}	1-90 atm
Parr & Hanson-Parr ^{67,68,69,73}	RDX, HMX, XM39, HNF	T(x), X(NO, CN, OH, NH, NO ₂ , H ₂ CO), r _b (laser)	With and without laser augmentation at 1 atm.
Litzinger et al. ^{63,64,65,74}	RDX, HMX, XM39, M43, BAMO, GAP	T(x), X(H ₂ O, HCN, CO, N ₂ , NO ₂ , CO ₂ , H ₂ , N ₂ O, CH ₂ O, NO) r _b (laser)	With high laser flux, elemental balance not closed.
Boggs ³⁴	HMX, RDX, AP, ADN, CL-20	r _b (P, T _{init})	
Brill ⁴	RDX, HMX	Relative initial decomposition species concentrations.	Limited number of species. 1 atm.

(X in this table refers to mole fraction profile data in the gas phase region.)

Most Recent Propellant Combustion Models

During the past few years, three models (Liau and Yang⁷⁵, Prasad, Smooke and Yetter,⁶² and Davidson and Beckstead⁷⁶)[‡] have been developed for the one-dimensional steady-state combustion of RDX. These models solve Eqs. 14-16 (page 15) in the three regions (see Figure 10, page 28), neglecting mass diffusion in the condensed regions and the radiation term in the energy equation. There has been a significant amount of communication and sharing of ideas between the three modeling groups and between those developing the models and those doing experiments. This has resulted in unprecedented agreement between experiment and model predictions for a wide variety of conditions.

The next chapter describes the details of the Davidson-Beckstead model. Differences and similarities in the three models is noted.

Future Modeling Directions

The Davidson-Beckstead,⁷⁶ Liao-Yang⁷⁵ and Prasad-Smooke⁶² models require thermophysical properties of the liquid propellant as inputs, but because of the reactions that start occurring after melting, these values are very difficult to determine experimentally. A future step in the development of a more complex model (more detail in the two-phase region) would be difficult without additional experimental studies to supply the liquid phase properties. Such a model was outlined by Kuo et al. in 1993.¹⁰ In a complete formulation, a model would consider all of the processes shown in Figure 4 (page 8). These would include bubble formation, expansion, and dynamics in the two-phase region due to decomposition, evaporation and chemical reaction in both the liquid and bubble phases. Because of a lack of knowledge about these physical constants, the full model has not been solved. In 1995, a much simplified version of Kuo's model,⁷⁷ considering the life of one bubble from nucleation to reaching the burning surface, was solved after making the following assumptions:

1. The velocity of the bubble is equal to the velocity of the surrounding liquid (contrary to Hatch's,⁵⁹ Davidson's,⁷⁶ and Liao's⁷⁵ assumption and Li's³⁸ conclusion.)
2. A temperature profile in the liquid was specified as input.
3. An initial bubble diameter of 2 microns was arbitrarily assumed.
4. Pressure in the bubble was the same as the system pressure. (Neglecting the contribution of surface tension).
5. No decomposition of liquid RDX occurs, only evaporation.
6. In the bubble, evaporation, two decomposition reactions, and one gas reaction between decomposition products were considered.

‡ All three modeling groups have been funded under the AFOSR contract discussed in the introduction on Page 4.

7. The analysis was extended to many bubbles through statistics, but this introduced additional parameters with large uncertainty.

The authors concluded that the reaction between decomposition products in the bubble is negligible. This was also concluded from the Davidson-Beckstead model. Kuo also concluded that the temperature in the gas bubble is largely governed by the liquid temperature. This supports the assumption that $T_g = T_l$ made by Davidson,⁷⁶ Liao,⁷⁵ and Hatch^{59,60} in their models. Further development with the detailed Kuo model will have to wait until the required experimental data become available.

The assumptions and details of the various multi-phase models with reactions are summarized in Table 6. In the rows of predictions, if the model was able to predict the characteristic, an * was placed in the column. If those predictions were presented in comparison to experimental data, a quality of correlation (G=good, F= fair, P=poor) was assigned (based on my judgment). If a model did not distinguish between solid and liquid phases, the condensed region was tabulated under the liquid columns. As shown, almost all of the effort has been directed at the nitramines, RDX and HMX. Double Base and AP were also considered, but showed poor correlation with experimental data or used simplified kinetics. All have neglected radiation effects which may become important for certain propellants. In summary, the most recent models of RDX and HMX are able to calculate most measurable quantities (burning rate, temperature and species profiles, and melt layer thickness) with reasonable accuracy.

Table 6: Comparison of Propellant Combustion Models

Year	1976	1979	1984	1985	1986	1987	1987	1987	1989	1993	1995	1995	1995	1995	1996
Researchers	BenReuven, et. al.	BenReuven, et. al.	Narahari, Mukunda & Jain	Cohen, Lo, and Crowley	Hatch	Hatch	Margolis & Williams	Bizot & Beckstead	Melius	Kuo & Lu	Liau&Yang	Davidson & Beckstead	Smooke &Prasad	Laxton, Kuo & Lu	Davidson & Beckstead
System	RDX	HMX	AP	HMX	NG	HMX	Gen.	DB	RDX	RDX	RDX	RDX	RDX	RDX	HMX
Pressure Range (atm)	10-40	10-40	45-80	1-100	7-700	7-700	N/A		1-20	N/A	1-200	1-400	1-200	5	1-200
SS, Ignition, Osciltory	SS	SS	SS	SS	SS	SS	SS	SS	IG	SS	IG	SS	SS	SS	SS
Solid	Energy Eq.	*	*	*	*	*	*	*	*	*	*	*	*	*	*
	Species Eq.														
	Phase Changes					*				*					*
	Melting	*	*	*	*					*	*	*	*	*	*
	Properties (T,Y)					*				*	*	*	*	*	*
	Decomposition														
Liquid or 2-Phase	Energy Species	*	*	*	*	*	*	*	*	*	*	*	*	*	*
	Thermal Diffusion	*	*	*	*	*	*	*	*	*	*	*	*	*	*
	Mass diffusion														
	Bubbles/Void Fraction					*	*	*		*	*	*	*	*	*
	Viscous Effects						*	*		*	*	*	*	*	*
	2-phase flow						*	*		*	*	*	*	*	*
	Properties (T,Y)	*	*	*	*	*	*	*	*	*	*	*	*	*	*
	Liquid Decomp. rxn	*	*	*	*	*	*	*		7	*	*	*	*	*
	Liquid-Gas Reaction														
	Gas Reactions				*			*		27	*	*	*	3	*
	Evaporation									5	*	*	*	*	*
Surface	Surface rxn			*					*						
	Evaporation	*	*	*	*	*	*	*	*	*	*	*	*	*	*
Gas	Energy Equation	*	*	*	*	*	*	*	*	*	*	*	*	*	*
	Species Equation	*	*	*	*	*	*	*	*	*	*	*	*	*	*
	Momentum Equation														
	Heat Diffusion	*	*	*	*	*	*	*	*	*	*	*	*	*	*
	Mass diffusion	*	*	*	*	*	*	*	*	*	*	*	*	*	*
	Radiation														
	Viscous Effects														
	# of Species	7	7	14	10	21	25		38	38	44	45	45		45
	# of Reactions	2	2	17	5	60	77		158	158	185	232	232		232
	Properties (T,Y)	*	*	*	*	*	*	*	*	*	*	*	*	*	*
	dP/dx=0	*	*	*	*	*	*	*	*	*	*	*	*	*	*
	Ideal Gas	*	*	*	*	*	*	*	*	*	*	*	*	*	*
Predictions:	Burnrate (P)	G		P	G	P	P	F	P	*	F	G	G		G
	Burnrate (Tinit)	*		*	*			F		*	P	F	F		F
	Temp Profile (solid)	*	*	*	*					*	*	*	*	*	*
	Temp Profile (liquid)	*	*	*	*	*	*	*	*	*	*	*	*	*	*
	Temp Profile (gas)	*	*	*	*	*	*	*	*	*	*	*	*	*	*
	Species Profile (liquid)	*	*	*	*	*	*	*	*	*	*	*	*	*	*
	Species Profile (gas)	*	*	*	*	*	*	*	*	*	F	G	G		F
	Surface Temperature	G	*	*	*	*	*	*	P	*	P	G			G
	Melt Layer Thickness	*	*	*	*	*	*	*	*	*	G	G	*		G
	Void Fraction Profile					*	*			*	*	*	*	*	*

(* - indicates that the model made this particular assumption or was able to calculate this particular characteristic. G, F, P (Good, Fair, Poor) correspond to my judgment as to how well the predictions of a particular model correlates with experimental data.)

CHAPTER 4: DESCRIPTION OF MODEL

The focus of my research has been the development and use of the numerical model presented in this chapter. It was written to handle any propellant that burns as a homogenous substance. The model divides the combustion process into three regions: solid, melt layer (liquid and gas) and gas. (See Figure 10, page 28). The mass flux \dot{m} is an eigenvalue of the problem and is determined by matching boundary conditions at the liquid-gas interface. The treatment of each of the three regions is described.

Solid Region

In the solid region, it is assumed that the propellant does not decompose. This is an assumption made in most models to date.^{33,59,60,75} Only the energy equation is solved for this region:

$$\rho r_b c_p \frac{dT}{dx} - \lambda_s \frac{d^2T}{dx^2} = 0 \quad (24)$$

with boundary conditions:

$$T(-\infty) = T_{init}, \quad T(0) = T_{melt} \quad (25)$$

Assuming constant c_p and λ , this equation can be solved:

$$T(x_s) = T_{init} + (T_{melt} - T_{init}) e^{\left(\frac{\rho r_b c_p}{\lambda_s}\right) x_s} \quad (26)$$

Because r_b is part of the eigenvalue of the problem, the solid region cannot be solved until the rest of the problem is converged; therefore, the solid region calculations and their results do not affect the calculations in the rest of the model.

Liquid-Gas Two-Phase Region

Once the propellant melts, several things start happening. The propellant can evaporate or decompose into gas and/or liquid fragments creating a frothy melt layer. As a gas-phase develops in this

two-phase region, bubbles form. The bubbles are represented by the void fraction (ϕ , the fraction of the original propellant liquid volume that has been converted to gas by either evaporation or decomposition). As in many models^{56,59,62,75} mass diffusion is neglected in this two-phase region. Because the melt-layer thickness and the right boundary conditions are unknown until the solution is complete, the energy and species equations are treated as a system of initial boundary value problems and solved using DVODE⁷⁸ (a variable coefficient ordinary differential equation solver subroutine). The second-order energy equation:

$$\dot{m} \frac{dT}{dx} - \frac{1}{c_{p,gl}} \frac{d}{dx} \left(\lambda A_c \frac{dT}{dx} \right) + \frac{A_c}{c_{p,gl}} \sum_{k=1}^{\# \text{ of species}} \dot{w}_k H_k = 0 \quad (27)$$

is treated as two first-order ordinary differential equations:

$$\begin{aligned} \frac{d}{dx} (\lambda \tau A_c) &= \dot{m} \tau c_{p,gl} + A_c \sum_{k=1}^{\# \text{ of species}} \dot{w}_k H_k \\ \frac{dT}{dx} &= \tau \end{aligned} \quad (28)$$

The void fraction is calculated by keeping track of the volume of liquid changing to gas (Eq. 29). The model assumes that the liquid density is a function of temperature but not composition.

$$\frac{d(1-\phi)}{dx} = \frac{1}{\rho_l v_l} \sum_{k=1}^{\# \text{ of liquid species}} \dot{w}_k \quad (29)$$

The steady-state equation for liquid species k (neglecting mass diffusion) is:

$$\frac{d}{dx} \left((1-\phi) \rho_l u_l Y_{l,k} \right) = \dot{w}_k \quad (30)$$

Likewise for the gas species:

$$\frac{d}{dx} \left(\phi \rho_g u_g Y_{g,k} \right) = \dot{w}_k \quad (31)$$

The mass fractions (Y_l and Y_g) are the mass fractions of the liquid in the two-phase region, and the mass fractions of the gases in the bubbles (voids) in the two phase region respectively (i.e. the sum of $Y_{l,k}$ equals 1.0 as does the sum of $Y_{g,k}$). Gas transport and thermodynamic properties are calculated via CHEMKIN⁴¹ and Transport⁴³ subroutines. Liquid properties are mass-averaged and calculated from temperature-

dependent correlations. For the two-phase mixture, heat capacity is mass averaged and thermal conductivity is volume averaged.[§]

Mass is conserved by incorporating:

$$\dot{m} / A_c = \phi \rho_g u_g + (1 - \phi) \rho_l u_l \quad (32)$$

into the subroutine that separates the variables in Eqs. 30 and 31 (ρ_g , ρ_l , u_g , u_l , $Y_{g,k}$ and $Y_{l,k}$). Two more assumptions are necessary before these variables can be separated. By assuming $T_g=T_l$ and u_l equals the surface regression rate (r_b), the mass conservation equation simplifies to $\rho_g u_g = \rho_l u_l = \dot{m} / A_c$. The assumption that u_g is greater than u_l is in qualitative agreement with the conclusion reached by Williams et al.³⁷ discussed in the previous chapter (page 23). The models of Hatch,^{59,60} and Liao⁷⁵ also make this same assumption.

Reaction rates must be handled with caution because of the two-phase interactions. The volumetric species mass production rate (\dot{w}_i) is calculated by:

$$\dot{w}_k = W_k \sum_{i=1}^{\# \text{ of rxns}} \nu_{k,i} q_{i,k} \quad (33)$$

where the definition of the rate-of-progress variable ($q_{i,k}$) depends on the type of reaction. Reactions involving condensed-phase reactants are assumed irreversible. For reactions involving only liquid reactants (fF+gG→products):

$$q = AT^\beta \exp(-E_a/RT) X_F^f X_G^g (1 - \phi) \quad (34)$$

For reactions involving only gas phase reactants, the reactions can be reversible and the rate-of-progress variables are calculated by CHEMKIN subroutines.⁴¹ The rate-of-progress variables are then multiplied by ϕ , the void fraction. Evaporation rates are treated as Liao and Yang:⁷⁵

$$q_{evap} = A_{l-g} \cdot s \left(\frac{1}{4} \sqrt{8RT/\pi W} \right) (pW/RT) \left[\left(\frac{p_{vap}}{p} \right) - X \right] \quad (35)$$

[§] Heat capacity is mass averaged because it has units of energy/mass·K. Thermal conductivity is volume averaged because the area ratio ($Area_g/Area_l$) through which the energy is being conducted is equal to the volume ratio ($\phi/(1-\phi)$). Thermal conductivity has units energy/distance·time·K. By using void fractions, the mass average is numerically equal to the volume average.

where X is the mole fraction of the species (a) in the bubbles if calculating below the interface or (b) in the gas region if calculating at the interface. Following Liau,⁷⁵ the area in Eq. 35 is a function of void fraction:

$$A_{l-g} = \begin{cases} (36\pi n)^{1/3} \phi^{2/3} & \phi < 1/2 \\ (36\pi n)^{1/3} (1-\phi)^{2/3} & \phi > 1/2 \\ 1 & \text{at surface} \end{cases} \quad (36)$$

For reactions involving a gas-phase species (F) attacking a liquid-phase species (G), q is calculated by:

$$q = \text{area} \cdot AT^\beta \exp(-E_a/RT) C_F^f X_G^g \quad (37)$$

The initial boundary conditions for the two-phase region are:

$$\phi = 0, T = T_{melt}$$

$$\tau = \frac{\dot{m}}{\lambda_l W_{propellant}} \left(\Delta H_f \Big|_{T_{melt}} - \Delta H_f \Big|_{T_{init}} \right) \quad (38)$$

and the mass fractions of all species in the liquid and gas phases are zero, except that of the monopropellant which is equal to unity. The quantity $\tau\lambda_l/\dot{m}$ is the energy required to heat the solid propellant from its initial temperature to its melting temperature. The computer program can handle up to four phase transitions and three temperature-dependent heat capacity correlations. The heat of formation of the liquid is calculated by:

$$\Delta H_f \Big|_{T_{melt}} = \Delta H_f \Big|_{T=T_{init}} + \int_{T_{init}}^{T_{melt}} c_p dT + \sum \Delta H_{transition} \quad (39)$$

The system of ordinary differential equations describing the two-phase region (Eqs. 28, 29, 30, and 31) are integrated in x (distance) until a surface condition is reached. The program user may specify one of three conditions which will halt the 2-phase calculations and call the last node the surface. These are: 1) a specified surface temperature, 2) a specified surface void fraction, or 3) for condensed mechanisms involving evaporation, the location where the liquid mass flux times area is equal to the rate of evaporation:

$$(1 - \phi) \rho_l v_l \cdot A_c = q_{evap} \quad (40)$$

Condition 1 can be used when experimentally determined T_s data exist. The model of Prasad and Smooke uses this condition.⁶² Condition 2 can be used with a specified void fraction of 1.0 for propellants that do not have a significant vapor pressure.⁷⁹ Using condition 3, as Liao and Yang,⁷⁵ will give calculated values of T_s and surface void fraction. Once the surface is reached, any remaining liquid is mathematically evaporated (i.e. assumed to vaporize instantaneously). The surface temperature and mass flux fractions serve as boundary conditions for the gas region.

In addition to the surface boundary condition, the model of Prasad et al.⁶² differs from the model presented here in the treatment of decomposition species in the two-phase region. Their model assumes the gas products are dissolved in the liquid, and they neglect bubble formation (or a void fraction) altogether. Therefore, their model is not able to predict the surface void fraction or surface temperature.

Gas Region

The gas region calculations are handled by a modified version of PREMIX⁴⁵ in the "burner-stabilized mode". The equations describing the gas phase are:

$$\begin{aligned} \dot{m} &= \rho u A_c & \rho &= \frac{P\bar{W}}{RT} \\ \dot{m} \frac{dT}{dx} - \frac{1}{c_p} \frac{d}{dx} \left(\lambda A_c \frac{dT}{dx} \right) + \frac{A_c}{c_p} \sum_{k=1}^{kk} \rho Y_k V_k c_{p_k} \frac{dT}{dx} + \frac{A_c}{c_p} \sum_{k=1}^{kk} \dot{w}_k h_k W_k &= 0 & (41) \\ \dot{m} \frac{dY_k}{dx} + \frac{d}{dx} (\rho A_c Y_k V_k) - A_c \dot{w}_k &= 0 \end{aligned}$$

This system of equations is solved using finite difference discretization and Newton's method. The solution is first converged on a coarse grid and then the grid is refined to obtain the resolution desired. All properties are temperature and concentration dependent. Details on the adaptive grid, discretization, the method for solution, and convergence can be found in Ref. 45.

Determination of the Mass Burning Rate

The mass burning rate, \dot{m} , is determined by iteration between the two-phase and gas region calculations. The correct \dot{m} will satisfy the energy balance at the two-phase/gas interface:

$$\lambda_{gl} \left. \frac{dT}{dx} \right|_{s-} + \left[\rho_l v_l (1 - \phi) \Delta H_{vap} \right]_{s-} = \lambda_g \left. \frac{dT}{dx} \right|_{s+} + q_{laser} \quad (42)$$

Equation 42 says that the heat flux from the gas phase flame plus any additional energy from a laser, must equal the heat flux into the condensed phase plus the energy flux required to vaporize any remaining liquid. The solution procedure is as follows (see Figure 11):

1. Specify propellant initial temperature, pressure and an initial guess of \dot{m} .
2. Solve the two-phase region equations.
3. Solve the gas region equations, initially with a coarse grid.
4. Compare left and right sides of Eq. 42. If the heat flux balance error is less than tolerance, go to step 6. If the right side is greater than the left side decrease \dot{m} , else increase \dot{m} . The first time this step is performed, \dot{m} is changed by a small percentage (~3%). On future steps, the next \dot{m} is determined by linear extrapolation based on the previous two \dot{m} 's. If the new \dot{m} is drastically different from the previous \dot{m} ($\geq 30\%$) then a small change in \dot{m} is done to get a better extrapolation.
5. Go to step 2.
6. Refine gas grid if necessary, else go to step 8.
7. Go to Step 4.
8. For evaporation surface definition only: If mass flux is not balanced, go to step 2. Fortunately, by the time the code has reached this point, the mass flux is balanced for most cases. Occasionally one more call to the two-phase and gas region subroutines is required.
9. Problem converged.

In short, \dot{m} is solved by using a "shooting method" for the initial boundary value problem in the two-phase region to give the first-order boundary conditions and match the second-order boundary conditions of the finite-difference boundary value problem in the gas region.

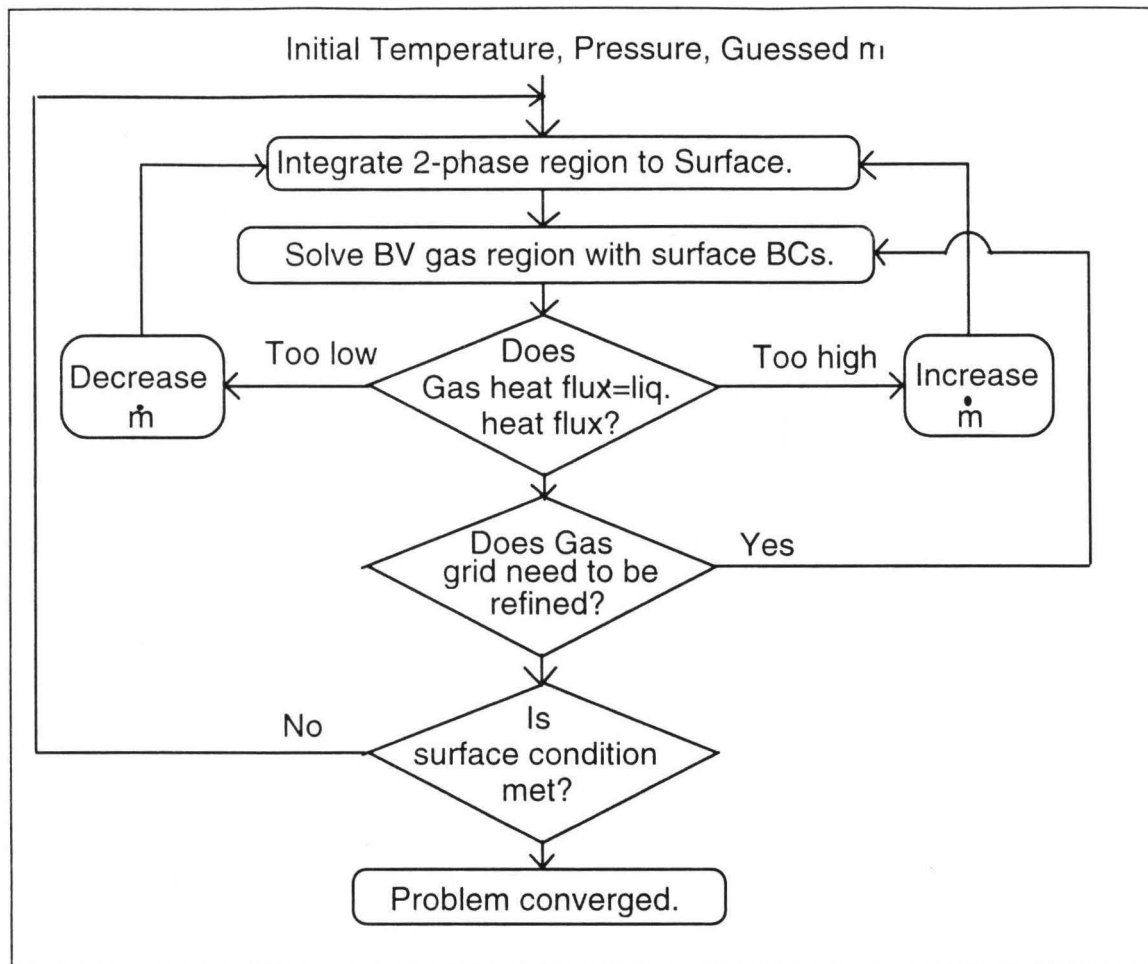


Figure 11: Convergence Scheme for Numerical Model

Model Inputs/Outputs

The objective in developing this model was to maximize the number of calculated combustion characteristics with the constraint that all of the model inputs could be either measured experimentally or estimated with reasonable accuracy. In order to make calculations with the model, the physical conditions, condensed- and gas-phase reaction mechanisms and the thermophysical properties of the original propellant, final combustion products and every intermediate species must be specified. The properties of the solid ingredients can be measured in a laboratory. The thermophysical properties and reaction kinetics for the gas-phase species can be either measured or estimated from *ab initio* calculations. Of all the model inputs, the parameters associated with the liquid phase are the least certain. For the monopropellants modeled in this dissertation, most of the liquid phase properties were extrapolated from measured solid phase properties. Global liquid decomposition mechanisms were developed to correlate with

decomposition studies. The inputs and outputs are summarized in Table 7. The required inputs is discussed in more detail for the individual ingredients.

Table 7: Model Inputs and Outputs

Phase	Input	Comments	Output
Solid	Temperature of Phase Transition	Most of these inputs are used in calculating the boundary conditions of the two-phase region.	Temperature Profile
	ΔH of Phase Transition		
	Density, $c_p(T)$, $\lambda(T)$		
	ΔH_f (@ 298 K)		
	Chemical Composition		
Liquid	T_{melt}		Temperature Profile
	Density, ΔH_f , $c_p(T)$, $\lambda(T)$	Required for each solid or liquid species	Species Concentration Profile
	$P_{vap}(T)$	Required if ingredient tends to vaporize	Void Fraction Profile
	Liquid Decomposition Reaction Mechanism		Percent of original Propellant that evaporates.
			Heat Release from Reaction
			Surface Temperature
Gas	Gas Reaction Mechanism		Temperature Profile (x)
	Thermophysical Properties of every species.	The CHEMKIN database ^{42,43} contains most of this information.	Species Concentration Profiles
	Initial Guess for Temperature and Species Profiles		Heat feedback from gas to liquid region
			Local reaction rates
			Reaction Sensitivity Analysis
			Integral Reaction Flow Analysis
General	Pressure		Surface Regression Rate (r_b)
	Initial Temperature		Sensitivity Analysis with respect to model inputs
	Initial Guess for \dot{m}		Temperature Sensitivity (σ_p)

CHAPTER 5: DECOMPOSITION STUDIES OF RDX AND HMX

The subsequent chapters will describe the modeling of RDX and HMX. As stated in the previous chapter, the reaction mechanisms describing the condensed-phase and gas-phase chemical reactions are required inputs to the model. Many of the model calculations are dependent upon the choice of mechanism and rate constants. In this chapter, the decomposition of RDX and HMX are reviewed. There have been numerous experimental and theoretical studies on the decomposition of these ingredients in all three phases (solid, liquid and gas). Some of the decomposition studies were concerned with slow decomposition that occurs as these monopropellants age, while other studies were performed on conditions which are unrelated to typical propellant combustion (i.e. dissolved in solution or in a vacuum). This chapter discusses those decomposition studies that are most relevant to the self-deflagration conditions that are being modeled. Because of the similarities between RDX and HMX, the decomposition of these nitramines is presented and discussed simultaneously.

The cyclic nitramines RDX (cyclotrimethylenetrinitramine, $C_3H_6N_6O_6$, hexogen) and HMX (cyclotetramethylenetetranitramine, $C_4H_8N_8O_8$, octogen) are very similar molecules. The molecular structure consists of a cyclic chain of $(H_2CNNO_2)_n$ where n equals 3 for RDX and 4 for HMX. (See Figure 12). Decomposition studies of RDX and HMX prior to 1984 have thoroughly been reviewed by Boggs⁹ and Fifer.⁸⁰ Some of the proposed mechanistic steps from these review articles, as well as more recent studies are shown in Table 8.

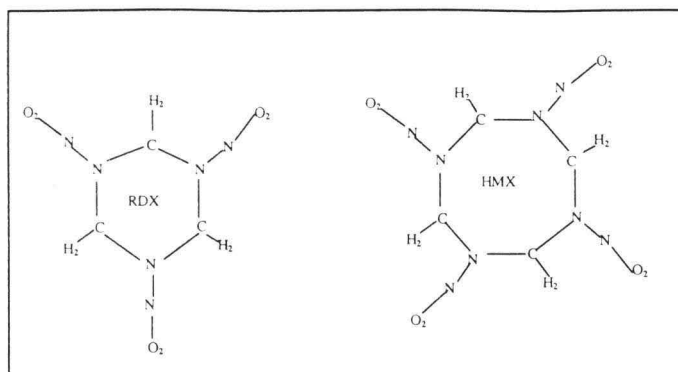
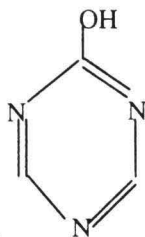


Figure 12: Chemical Structure of RDX and HMX

Table 8: Nitramine Decomposition Mechanisms

Researcher	Mechanism	Comment
Schroeder ^{81,82}	$\text{RDX} \leftrightarrow \text{RDXR}^{**} + \text{NO}_2$	
	$\text{RDXR} \leftrightarrow \text{H}_2\text{CN} + 2\text{H}_2\text{CNNO}_2$	
Farber & Srivastava ⁸³	$\text{HMX} \leftrightarrow 2(\text{H}_2\text{CNNO}_2)_2$	Primary Pathway
	$(\text{H}_2\text{CNNO}_2)_2 \leftrightarrow (\text{H}_2\text{CN})_2\text{NO}_2 + \text{NO}_2$	
	$(\text{H}_2\text{CN})_2\text{NO}_2 \leftrightarrow 2\text{H}_2\text{CN} + \text{NO}_2$	
	$\text{HMX} \leftrightarrow \text{RDX} + \text{H}_2\text{CNNO}_2$	Minor Pathway
Melius ⁴⁸	$\text{RDX} \leftrightarrow \text{RDXR} + \text{NO}_2$	Gas-Phase reactions
	$\text{RDXR} \leftrightarrow \text{RDXRO}^{**}$	
	$\text{RDXRO} \leftrightarrow 2\text{H}_2\text{CNNO}_2 + \text{H}_2\text{CN}$	
	$\text{H}_2\text{CNNO}_2 \leftrightarrow \text{H}_2\text{CN} + \text{NO}_2$	
Behrens ^{84,85}	$\text{RDX} \rightarrow \text{OST}^{\dagger\dagger} + \text{H}_2\text{O} + \text{NO} + \text{NO}_2$	$1.6 \times 10^{19} \exp(-49000 \text{ cal/RT})$ (30%)
	$\text{RDX} \rightarrow \text{NO}_2 + \text{H}_2\text{CN} + 2\text{N}_2\text{O} + 2\text{CH}_2\text{O}$	$3.9 \times 10^{18} \exp(-49000 \text{ cal/RT})$ (10%)
	$\text{RDX} \rightarrow \text{ONDNTA}^{\dagger\dagger} \rightarrow \text{N}_2\text{O} + \text{CH}_2\text{O} + \text{other}$	(30%)
	$\text{RDX} \rightarrow \text{N}_2\text{O} + \text{CH}_2\text{O} + \text{NO}_2 + \text{NH}_2\text{CHO}$	autocatalytic (30%)
	Analogous Pathways for HMX	
Brill ⁴	$\text{RDX} \rightarrow 3\text{CH}_2\text{O} + 3\text{N}_2\text{O}$	$10^{12.9} \exp(-34400 \text{ cal/RT})$
	$\text{RDX} \rightarrow 3\text{HCN} + 3\text{HONO}$	$10^{16.4} \exp(-44100 \text{ cal/RT})$
	$\text{HMX} \rightarrow 4\text{CH}_2\text{O} + 4\text{N}_2\text{O}$	$10^{13.0} \exp(-34000 \text{ cal/RT})$
	$\text{HMX} \rightarrow 4\text{HCN} + 4\text{HONO}$	$10^{16.5} \exp(-44100 \text{ cal/RT})$

** RDXR has the structure of RDX minus a NO₂ group. RDXR is an isomer of RDXRO.



^{††} OST has a structure of

. ONDNTA has the structure of RDX minus one oxygen.

Behrens et al.^{84,85} studied RDX decomposition under very low pressures ($<10^{-6}$ torr) and proposed four competing decomposition paths for RDX. The percentage that each path contributes to the overall decomposition of RDX is listed in Table 8 in parentheses. In subsequent work,⁸⁴ HMX was found to decompose along analogous pathways but his second reaction may become more dominant at higher pressures. Behren's work indicates an N_2O to NO_2 ratio near the surface of approximately 1.3. Rate constants for the first two pathways of RDX have been calculated from their experimental data.⁸⁵

Using IR to measure the concentration of species evolving from small samples of RDX and HMX, Brill⁴ concluded that a global decomposition mechanism consisting of two competing reactions is the most that can be experimentally verified at this time. Brill states that including more mechanistic steps at this point would merely be conjecture. Brill's analysis indicates that the N_2O to NO_2 ratio is approximately 0.75 near the surface for both RDX and HMX.

Litzinger et al. measured the concentration of gaseous species near the surface of burning RDX⁶⁵ and HMX.⁶⁴ Their experiments were performed at one atmosphere with the sample being radiated with 100 W/cm^2 or 400 W/cm^2 heat flux from a CO_2 laser. The heat flux from the laser increases the mass burning rate. The increased mass flux blows the gaseous flame away from the burning surface, thereby enabling them to measure concentrations of intermediate species. Figure 13 shows their measured concentrations of various species at the surface for HMX and RDX. They report significant concentrations of NO , CO , and H_2O , which a simple global mechanism (like Brill's⁴) does not include. Litzinger et al. also measure a significant difference between the surface concentrations of NO_2 and CH_2O for RDX and HMX. The higher CH_2O surface concentration is in qualitative agreement with the observation made by the Hanson-Parr and Parr. Hanson-Parr and Parr⁶⁹ report the surface mole fraction of CH_2O for RDX as 0.01 and 0.08 for HMX under self-deflagration conditions (i.e. no laser).

Both RDX and HMX have significant vapor pressures. Several models are based on the assumption that the primary mechanism by which RDX_{liquid} enters the gas phase is by evaporation rather than through decomposition. Some experiments fail to show the presence of nitramine vapors, but this could be a result of rapid decomposition of the nitramine vapor before it can be detected.⁶⁴ Kraeutle⁸⁶ detected pure HMX condensate on the cover glass of a hot stage after observing the liquefaction of HMX.

Hanson-Parr and Parr⁶⁷ have detected RDX vapor near the surface of a burning propellant using UV-Visible absorption measurements, but estimate that the maximum RDX concentration near the surface is only about 7×10^{16} molecules/cm³. Assuming ideal gas and a temperature of 600 K, this represents a mole fraction of about 0.006. Some models^{49,38} have assumed that RDX predominately transforms from condensed phase to gas phase via evaporation, thereby predicting the mole fraction of RDX at the surface to be approximately 0.15. Though this appears to be a large discrepancy, the models also show that the RDX_{vapor} decomposes to the concentration reported by the Hanson-Parr and Parr by the time it reaches 5 μm above the surface.

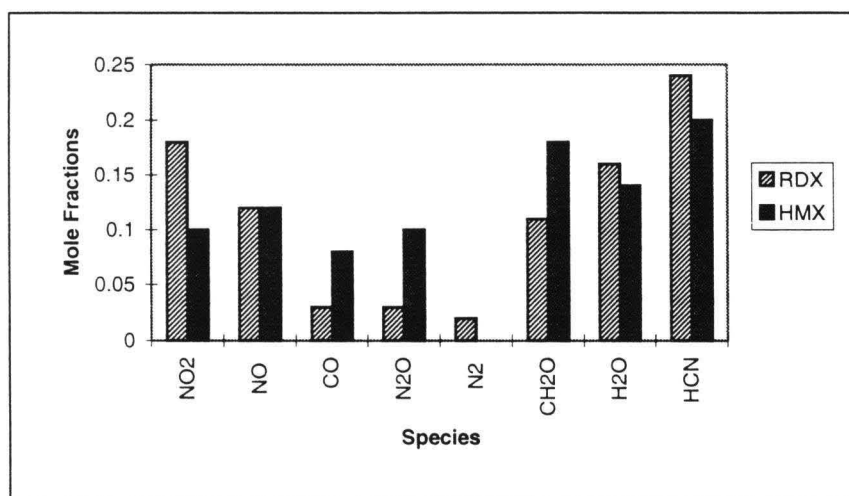


Figure 13: Nitramine Surface Species Concentrations from Litzinger et al.^{63,64}

The general consensus of these studies is that both RDX and HMX predominately decompose to H₂CN (or HCN), NO₂ (or HONO), N₂O and CH₂O. There is some disagreement as to the specific reactions involved in this decomposition. Depending upon the test conditions (laser-flux, low pressure, etc.) other species are detected. Some species may be in relatively high concentration at the surface due to molecular diffusion in the gas phase rather than due to production in the condensed phase. There is enough uncertainty in the condensed-phase and near-surface gas-phase chemistry that using a more detailed condensed phase mechanism is not warranted. Doing so would only add additional and unnecessary degrees-of-freedom.

CHAPTER 6: MODEL CALCULATIONS FOR RDX

RDX was chosen as the monopropellant to model first for several reasons. As mentioned on page 26, Melius⁴⁸ has developed a detailed kinetic mechanism for the gas-phase reactions of RDX which considers the decomposition of RDX_{vapor}. Since the publication of Melius' work, many researchers have collected a variety of very quantitative data about the combustion of pure RDX in an effort to validate and improve his mechanism. As will be shown, this database of experimental results serves to validate the assumptions made in the model.

Properties of RDX

Because most propellants begin rapid decomposition at or near their melting point, the liquid phase properties are very difficult to measure. Often liquid property data must either be estimated or extrapolated from the solid property data. Liquid heat capacity, liquid thermal conductivity and liquid vapor pressure were the least certain properties. A literature search was performed to find values for these properties. The results are shown in Table 9.

Although there is a lot of scatter in the reported heat capacity and density data, the model predictions did not change significantly with variations in these parameters. Only one paper was found that contained experimental thermal conductivity for RDX.⁹⁸ This value was for the solid, and for the temperature range explored, it appeared to be nearly constant. All the other values were given in conjunction with models without referencing their source. Values of thermal conductivity ranged from 1.75×10^{-4} to 7.6×10^{-4} cal/cm·sec·K. Hanson-Parr and Parr⁹² recently reported temperature-dependent values of thermal diffusivity (α)^{‡‡} for RDX between 293 K and 423 K. They cautiously recommend a linear extrapolation for temperatures outside of this range.⁸⁷ Parr also questions Shoemaker's⁹⁸ thermal

conductivity data. Shoemaker made his measurements on pellets of only 80% theoretical mass density (TMD); whereas the samples tested by Hanson-Parr and Parr were 95 to 97% TMD. The voids in Shoemaker's samples could significantly lower his measured thermal conductivity. The voids should not have a large effect on the values of heat capacity. Assuming Shoemaker's values of heat capacity and the thermal diffusivity from Hanson-Parr and Parr are correct, the thermal conductivity can be calculated. (See Figure 14). To enable the model to correctly predict the melt-layer thickness, a value slightly higher than any of these solid thermal conductivities for the liquid phase (8.0×10^{-4} cal/cm·sec·K) was chosen.

Table 9: RDX Property Values Found in the Literature.

Property	Value	Source	Comments
Heat Capacity (cal/g·K)	.0389+.000703T	Shoemaker ⁹⁸	Measured from pressed RDX crystals.
	.269 at 298 K	Parr ⁸⁸	
	.3	Beckstead ⁸⁹	listed for HMX (model)
	0.35	Brewster, ⁹⁰ Williams ³⁶	(model)
	.45 at 473 K	Ben-Reuven ²⁷	
Density (g/cm ³)	1.82	Kubota ¹	
	1.806	Boggs ⁹	
	1.75	Flame Database ³⁵	Value given for pellets made from pressed powder.
Thermal Conductivity (cal/cm sec K)	4.06×10^{-4}	Shoemaker ⁹⁸	Measured from pressed RDX crystals.
	1.75×10^{-4}	Beckstead ⁸⁹	(model)
	3.0×10^{-4}	Parr ⁸⁸	listed for HMX (model)
	5.0×10^{-4}	Brewster ⁶⁶	(model)
Thermal Diffusivity (cm ² /sec)	$\alpha = 0.00142 - 5.72 \times 10^{-6}T + 1.52 \times 10^{-8}T^2$	Hanson-Parr & Parr ⁹²	T in Celcius.
Vapor Pressure (torr)			
$\log_{10}(P) = A - B/T$	A=14.8, B=6799	Rosen ⁹³	(328 K-371 K) sub. pres.
$\log_{10}(P) = A - B/T$	A=11.87, B=5850	Edwards ¹⁰⁰	(384 K-412 K) sub. pres.
$\log_{10}(P) = A - B/T$	A=10.59, B=4433	Rodgers ⁹⁴	(505 K-520 K) vap. pres.
	$P = 10^{14.4} \cdot \exp(-15850/T)$	Maksimov ⁹⁵	(329 K-413 K) sub. pres.
	$P = 10^{16.89} \cdot \exp(-16143/T)$	Cundall ⁹⁶	(343 K-447 K) sub. pres.
	$P = 10^{11.5} \cdot \exp(-12178/T)$	Yang ⁹⁷	Vapor Pressure correlation used in their 1-D RDX model.

$\alpha = \lambda / \rho c_p$, thermal conductivity/density/heat capacity

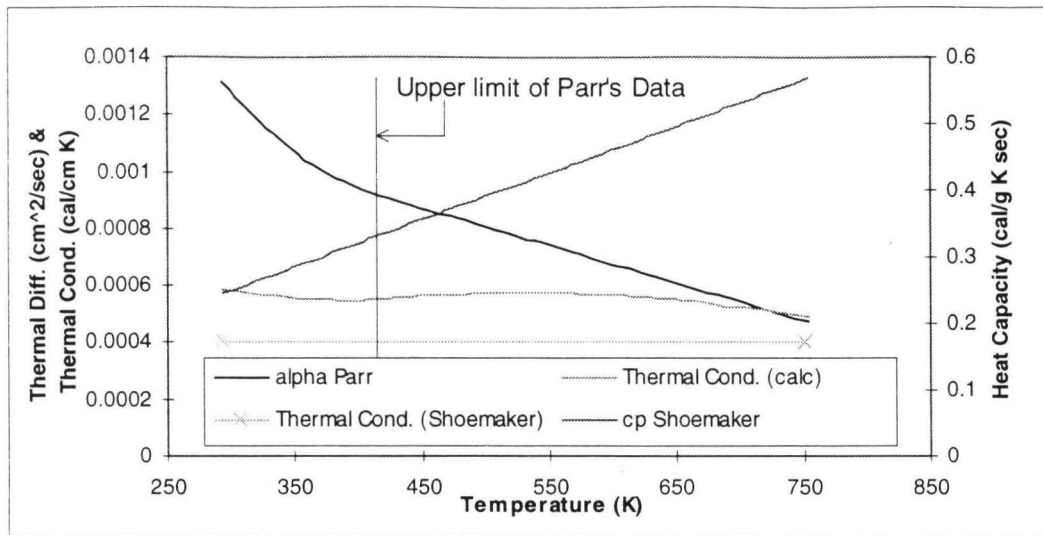


Figure 14: RDX Thermal Conductivity^{98,87}

In attempting to model RDX evaporation, the literature was searched for vapor pressure data. Four different correlations of sublimation pressure and one of vapor pressure were found. (See Figure 15). The vapor pressure attributed to Yang⁷⁵ is an intermediate value used in his model.

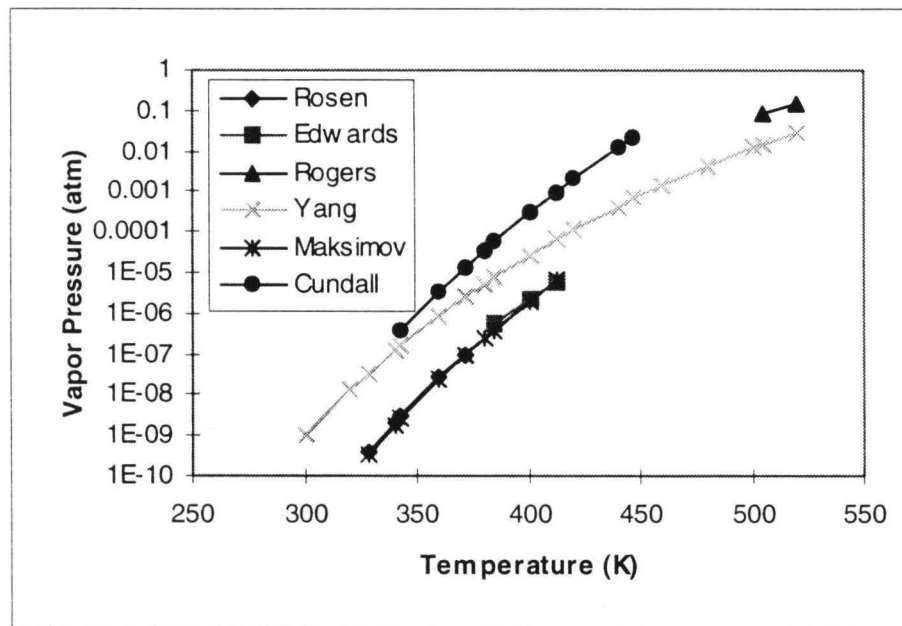


Figure 15: RDX Vapor Pressure Correlations^{93,87,94,95,96,97}

Logically, the vapor pressure data (by Rogers⁹⁴) rather than the sublimation data would seem to be the one to choose since evaporation is being modeled by assuming vapor-liquid equilibrium. Using Rogers' vapor pressure in the calculations did not affect any of the model predictions other than lowering

the surface temperature by 50 to 100 K. The data that gave the most reasonable surface temperature predictions was the sublimation pressure from Edwards.¹⁰⁰ Admittedly, this is an extrapolation of the given pressure correlation beyond the experimental limits. Considering the inaccuracies and assumptions inherent in the evaporation, Edwards' data was chosen. If Rodgers' vapor-pressure correlation is used, the model indicates that less than one percent of the RDX decomposes in the two-phase region. With Edwards' data, up to 25 percent of the RDX is calculated to decompose in the two-phase region.

The thermodynamic and physical properties used to describe the solid and liquid phases of RDX in the subsequent calculations are shown in Table 10.

Table 10: Thermodynamic and Physical Properties of RDX Solid and Liquid Used in Model.

Property	Value	Reference	Comments
ΔH_f RDX _{solid} (298 K)	14.67 kcal/mole	Kubota ¹	
Heat capacity c_p (solid)	.0389+.000703T cal/g K	Shoemaker ⁹⁸	Curve fit of Shoemaker's data.
Thermal Cond. (solid)	4.18×10^{-4} cal/g·K	Shoemaker ⁹⁸	
Solid Density	1.806 g/cm ³	Boggs ⁹	
T_{melt}	478 K	Hall ⁹⁹	
ΔH_{fus}	8.51	Boggs ⁹	
Heat capacity c_p (liquid)	.0389+.000703T cal/gK		Assume same as solid.
Thermal Cond. (liquid)	1.045×10^{-3} cal/cm-s-K		Estimated (see discussion below).
Liquid Density	1.806 g/cm ³		Assume same as solid.
Vapor Pressure	$10^{(11.87-5850/T(K))}$ torr	Edwards ¹⁰⁰	Chosen because it gave the best model results. (see discussion below).

Kinetics of RDX Combustion

There are numerous experimental and theoretical studies on the decomposition of RDX. These were reviewed in Chapter 5. The chemical reaction mechanisms used in the model for the condensed and gas phases are described here.

Liquid RDX Decomposition Mechanism

The liquid-phase decomposition mechanism is shown in Table 11. This mechanism uses the reaction steps and rate constants proposed by Brill⁴ (see Figure 16) with a few modifications. The pre-exponential constants for Reactions 1 and 2 were multiplied by ρ_{RDX} / WT_{RDX} to put the reactions in the right format for the code input. In the analysis of Thynell¹⁰¹ and in the model of Prasad and Smooke,⁶² the

decomposition products of Reactions 1-3 are assumed dissolved in $\text{RDX}_{\text{liquid}}$. In the Davidson-Beckstead⁷⁶ and Liao-Yang⁷⁵ models, these species are treated as gas-phase molecules trapped in the bubbles (modeled as voids). Differences in predictions made by these varying assumptions appear to be minimal.

Table 11: RDX Condensed-Phase Mechanism⁴

Reaction	A	β	E_a (cal/mole)
1. $\text{RDX}(\text{C}) \Rightarrow 3\text{CH}_2\text{O} + 3\text{N}_2\text{O}$ (exothermic)	4.88×10^{11}	0.0	34400
2. $\text{RDX}(\text{C}) \Rightarrow 3\text{H}_2\text{CN} + 3\text{NO}_2$ (endothermic)	6.5×10^{14}	0.0	44100
3. $\text{CH}_2\text{O} + \text{NO}_2 \Rightarrow \text{NO} + \text{CO} + \text{H}_2\text{O}$	802	2.27	13730
4. $\text{RDX}(\text{C}) \Rightarrow \text{RDX}_{\text{vapor}}$ (Evaporation-see description above) Edwards' vapor pressure data			

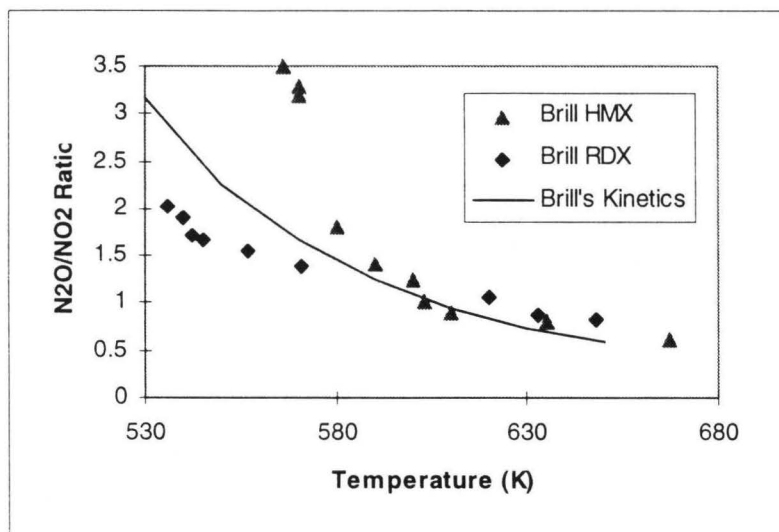


Figure 16: RDX Condensed Phase Kinetics⁴

Gas-Phase Reaction Mechanism

The RDX Yetter (Aug. 1995 version)¹⁰² mechanism of 45 species and 232 reactions was used for the gas-phase mechanism. The full mechanism is listed in the Appendix. As discussed above, Melius⁴⁸ developed the original mechanism and improvements were made by Yetter et al.⁵⁰ Most of the kinetic parameters for the 232 reactions were taken from independent literature sources, many of which are based on experiment. But as noted in the original mechanism file from Yetter, reactions involving H_2CNNO_2 , H_2CN , and HONO need further review. Most of the rate constants for the reactions involving these species and $\text{RDX}_{\text{vapor}}$, RDXR , and RDXRO were estimated by Melius. Other reactions and rate constants appear to have been arbitrarily added by Yetter to force the mechanism to give results similar to experimental

data. Several reactions in the database are preceded by comments such as: “The following two reactions have been added to increase early heat release and reaction rate,” (Reactions 222 and 223) “Pre-exponential factor decreased by 10 relative to Melius,” (Reactions 204 through 209) and “Added to yield N₂ formation during first stage” (Reaction 210). The rate constants associated with reactions involving H₂CNNO₂, H₂CN, and HONO have the most uncertainty. The influence of these reactions is discussed further in the next chapter.

Comparison with Experimental Data

Burning Rate

There are several sources of burning rate data for RDX. Zimmer-Galler,¹⁰³ Glaskova,¹⁰⁴ and Zenin⁷¹ made measurements at T_{init}= 298 K, whereas Boggs et al.³⁴ made measurements for T_{init}= 223 K and T_{init}= 373 K. Zenin's measurements were made with packed powder (20-50 μm diameter) that had a density of 1.66 g/cm³. The TMD^{§§} of RDX is approximately 1.82 g/cm³. The higher burning rates (54% at 1 atm) reported by Zenin can be attributed to the effect of the voids in his samples. Other data reported by Zenin may likewise be biased. Comparisons with the burning rate data are made in Figure 17, Figure 18 and Figure 19. The agreement is very reasonable. The temperature sensitivity (σ_p)^{***} is 0.001 K⁻¹ and is constant with pressure according to the model. The temperature sensitivity is discussed in more detail in conjunction with the HMX model. (See Figure 90 on page 162.)

§§ Theoretical mass density.

*** $\sigma_p = \partial \ln(r_b) / \partial T_{init} |_p$

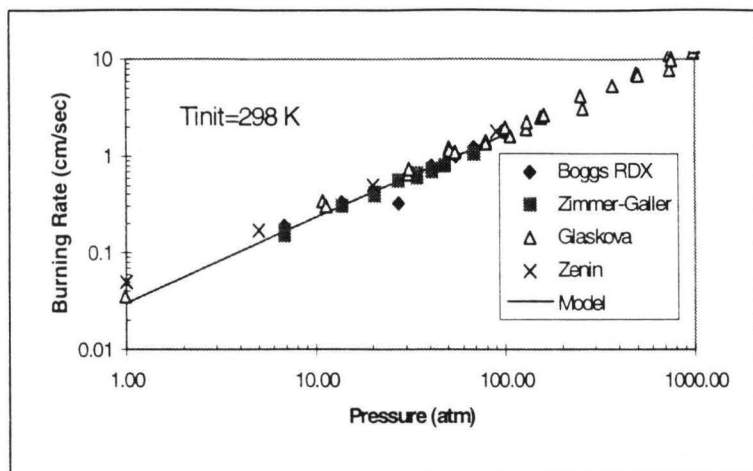


Figure 17: RDX Burning Rate for $T_{init}=298$ K^{34,71,103,104}

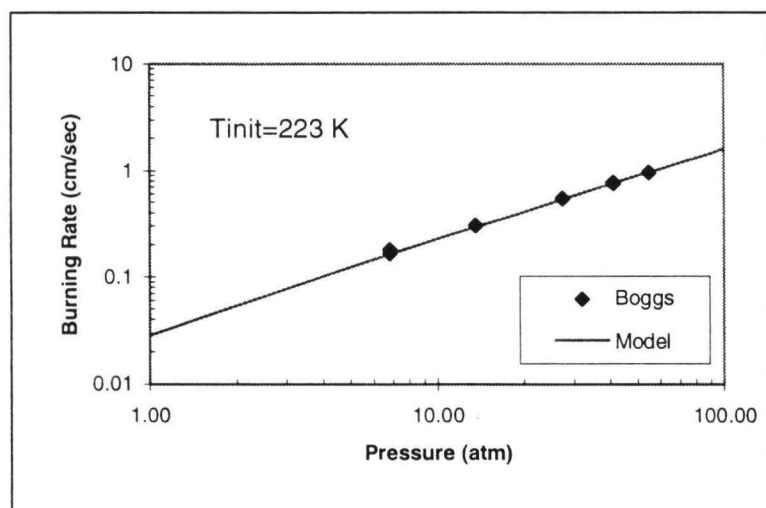


Figure 18: RDX Burning Rate for $T_{init}=223$ K.³⁴

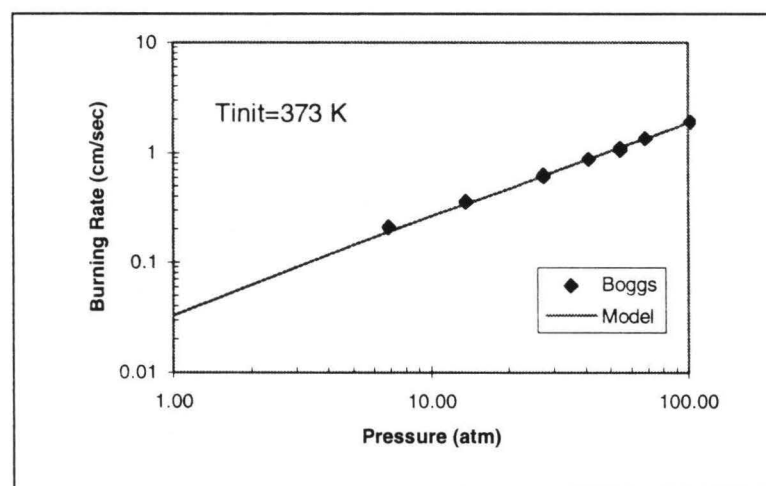


Figure 19: RDX Burning Rate for $T_{init}=373$ K.³⁴

Self-Deflagration Temperature Profiles

There have been several experiments attempting to measure the temperature profile of RDX as a function of distance from the surface. This section discusses only those made under self-deflagration conditions. Temperature profile measurements made under laser-assisted combustion conditions are discussed below. Most of these experiments are performed using small samples of propellant. These measurements are affected by heat loss due to radiation and conduction to surroundings. The model does not consider these losses. Model predictions should correlate most closely to experimental data near the surface where the effect of these heat losses is at a minimum.

Hanson-Parr and Parr⁶⁹ made temperature measurements in self-deflagrating RDX at 1 atm using micro-thermocouples (5 μm) and PLIF.^{†††} Their data are compared to model calculations in Figure 20. The flame temperature as calculated by the model approaches the adiabatic flame temperature. According to Hanson-Parr and Parr, heat loss in the experiment can explain why their data do not reach the adiabatic flame temperature. Near the surface (<.02 cm), the agreement between the data and the calculations made by the model is very reasonable. This would indicate that for this pressure, the calculated heat flux from the gas-phase flame is probably close to that measured by Hanson-Parr and Parr.

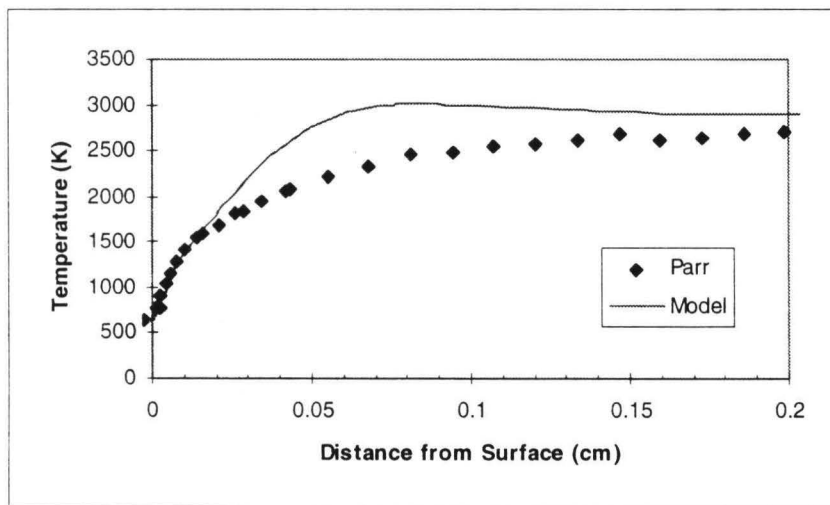


Figure 20: RDX Self-Deflagration Temperature Profile 1 atm (Parr)⁶⁹

^{†††} Planar Laser Induced Fluorescence. Temperatures were determined from the OH rotational band.

Zenin⁷¹ made micro-thermocouple measurements for RDX at 1, 5, 20, and 90 atm. This is from the same data mentioned above (page 52) where the density of the RDX is only 91% of the TMD. His measured burning rates are consistently higher than those predicted by the model. To make use of his data, Zenin's measured mass burning rate was input into the model. Trying to model the effect of the voids in Zenin's samples is beyond the scope of this study. The comparison between Zenin's data and model predictions is shown in Figure 21. At one atmosphere, the agreement near the surface is reasonable but Zenin's measured flame temperature at this pressure is only 1973 K. This is almost 1000 K below the adiabatic flame temperature of 2925 K. For the pressures 5, 20 and 90 atm, the model shows a much steeper temperature gradient near the surface. For these pressures Zenin's final flame temperature (2773 K, 2973 K, and 3073 K) is significantly lower than the theoretical values of 3075 K, 3194 K and 3301 K respectively.^{†††} Some of the error between the model calculations and Zenin's calculations may be related to the voids in his samples.

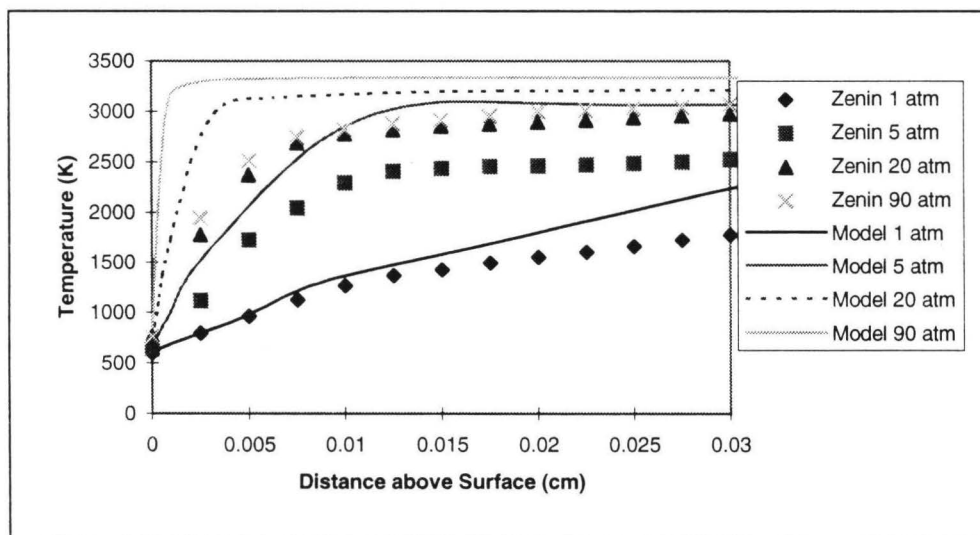


Figure 21: RDX Temperature Profiles at 1, 5, 20 and 90 atm (Zenin).⁷¹

As seen in Figure 22, the model indicates shorter solid pre-heat, melt-layer and gas-phase reaction zones as pressure increases. At high pressures where the temperature gradients are very steep, thermal lag of the thermocouple could become a problem. Based on previous work,¹⁰⁵ Zenin has taken into

^{†††} Calculated by the NASA-Lewis Equilibrium Code.¹¹⁴

account the thermal lag and radiation losses of the thermocouple. A numerical model of Zenin's thermocouple as it passes through the calculated flame was developed. The properties and dimensions of the thermocouple were taken from Ref. 105. This calculation did not give an adequate explanation for the difference between the model and experiment.

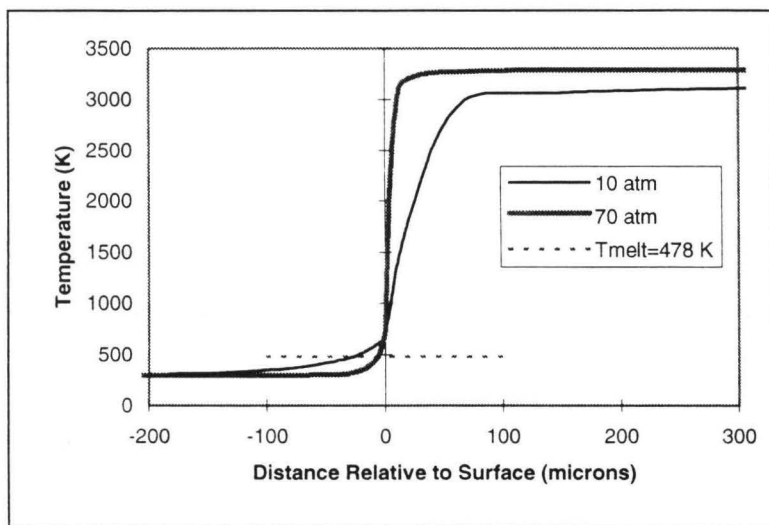


Figure 22: Calculated RDX Temperature Profiles at 10 and 70 atm.

Surface Conditions

From the same data described above, Zenin⁷¹ reported surface temperature and melt-layer thickness as a function of pressure. Brewster⁶⁶ also has made melt-layer thickness measurements. The data are compared with the model calculations in Figure 23 and Figure 24, showing reasonable agreement.

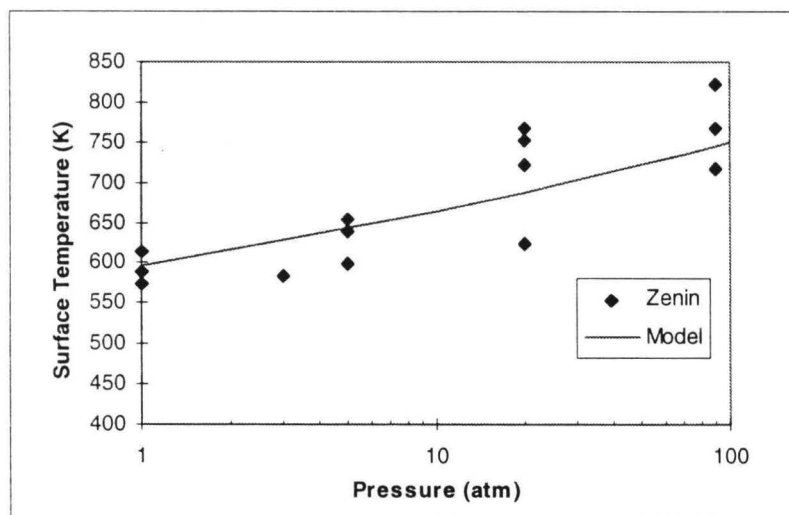


Figure 23: RDX Surface Temperature at 1 to 90 atm (Zenin).⁷¹

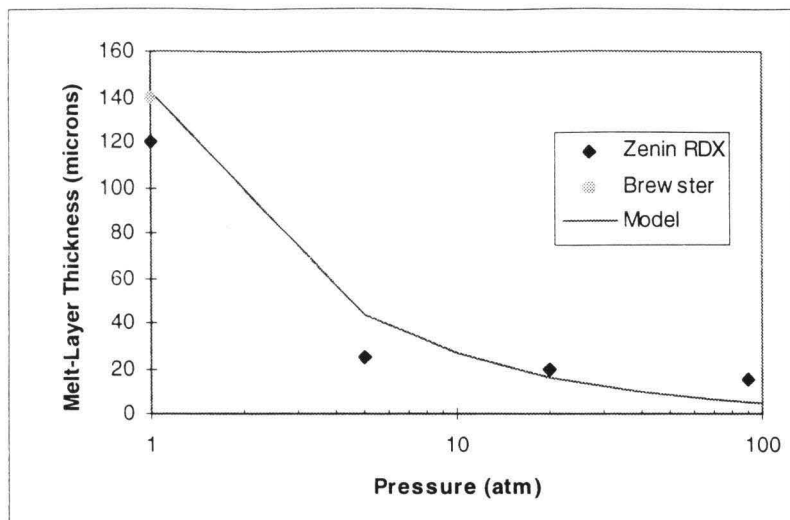


Figure 24: RDX Melt Layer Thickness at 1 to 90 atm (Zenin⁷¹, Brewster⁶⁵)

Species Concentration Profiles

For self-deflagrating RDX, there have been two sets of species concentration data measured. The first was measured by Ermolin et al. in 1986.^{40,106} The data were taken by mass spectrometric sampling at 0.5 atm. Ermolin reports a surface regression rate of 0.025 cm/sec and 1.8 g/cm³ for the sample density. Using these values as inputs to the model, the concentration profiles shown in Figure 25, Figure 26, and Figure 27 were calculated. In Figure 25, the calculated concentration profiles of the intermediates (NO and HCN) decrease, and the calculated concentration profiles of the products (CO and H₂) increase closer to the surface than the measured values. Given that the experimental was performed at 0.5 atm, the agreement is reasonable.

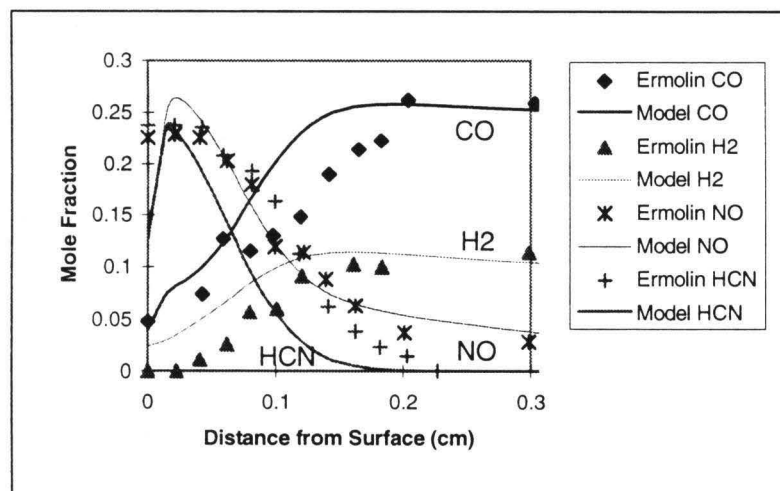


Figure 25: RDX CO, H₂, NO, and HCN Profiles at 0.5 atm (Ermolin)⁴⁰

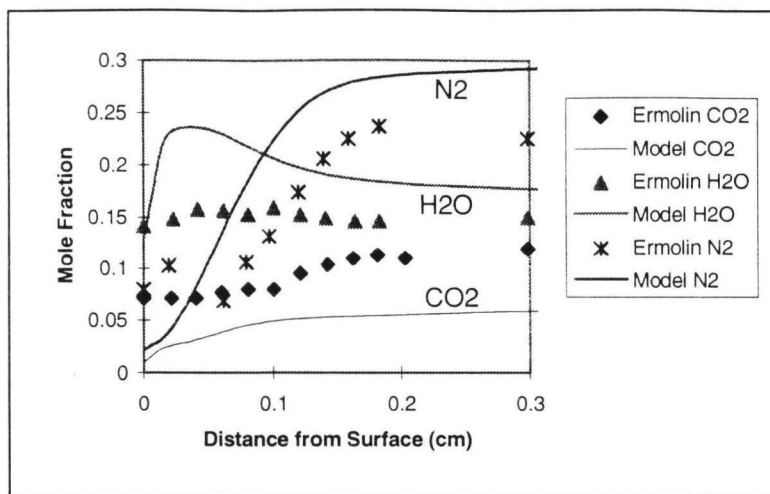


Figure 26: RDX CO₂, H₂O and N₂ Profiles at 0.5 atm (Ermolin).⁴⁰

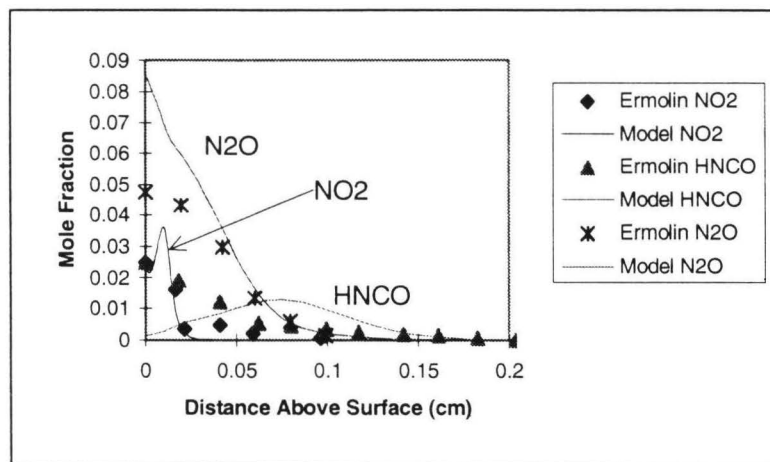


Figure 27: RDX NO₂, HNCO and N₂O Profiles at 0.5 atm (Ermolin).⁴⁰

There are quite large differences between the calculated and measured profiles seen in Figure 26. The predicted values approach the theoretical equilibrium values. The experimental atomic balances in the experimental data are not closed. As seen in Figure 26, approximately 20 percent of the nitrogen is unaccounted for. Such a large error in a mole fraction can greatly effect the other mole fractions. It should be noted that Ermolin reports peak mole fractions of about 0.23 and .025 for NO and NO₂, respectively. Ermolin's peak NO mole fraction is larger than that reported by either Parr⁶⁹ (page 62) or Litzinger^{64,65} (page 70). Thus, the peak concentrations of NO and NO₂ are not well established.

Korobeinichev et al.¹⁰⁶ report mass spectrometry data for RDX at 1 and 2 atm. These data are reported in mass spectral peak intensities rather than mole fractions. To make a comparison with the model, all mole fractions of species for a given molecular mass were summed. For example the mole

fractions of CO, N₂ and H₂CN were added and compared with the scaled signal for mass 28 in Figure 28. Comparisons for molecular weights of 30, 27, and 44 are shown in Figure 29, Figure 30, and Figure 31, respectively. The general location of the main reaction zone at this pressure appears to be located approximately 0.03 cm above the burning surface in both the predicted and measured values. There is a significant difference between the model's predictions and Korobeinichev's measurements for mass 28 below 0.03 cm in Figure 28. According to the mechanism, RDX_{vapor} is decomposing in this region to H₂CNNO₂ which then further decomposes to numerous, smaller species. It is likely that these large, unstable species could continue to decompose in the mass spectrometer probe despite the low pressure (10⁻⁶ torr). Thus, the daughter species (decomposition products) would be detected rather than the mother species (RDX_{vapor} and H₂CNNO₂). This is a possible explanation for the high concentration of low mass species near the surface measured by the experiment but not predicted by the mechanism. Otherwise, the agreement shown in Figure 28 to Figure 31 is very reasonable.

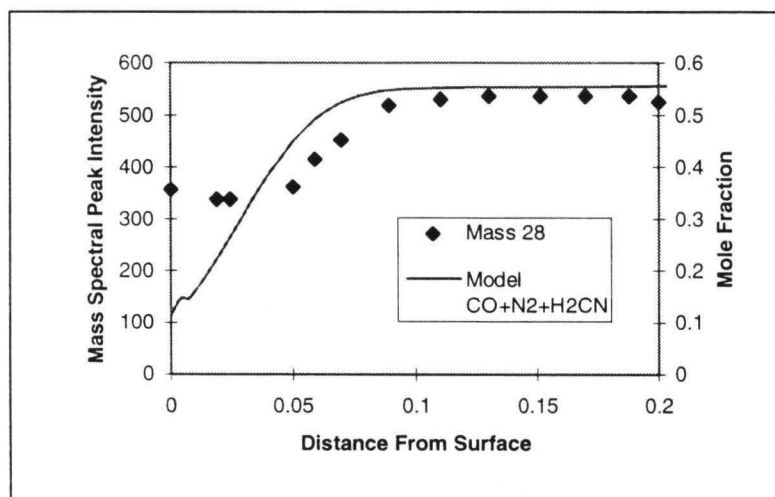


Figure 28: RDX Mass 28 Profile at 1 atm (Korobeinichev).¹⁰⁶

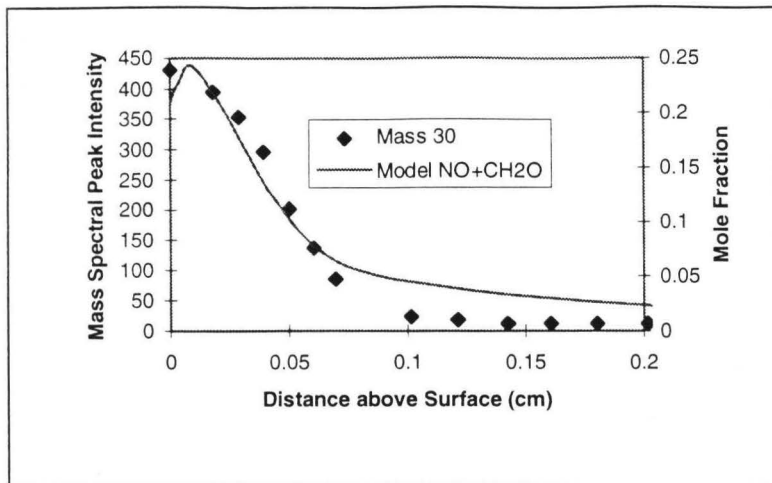


Figure 29: RDX Mass 30 Profile at 1 atm (Korobeinichev).¹⁰⁶

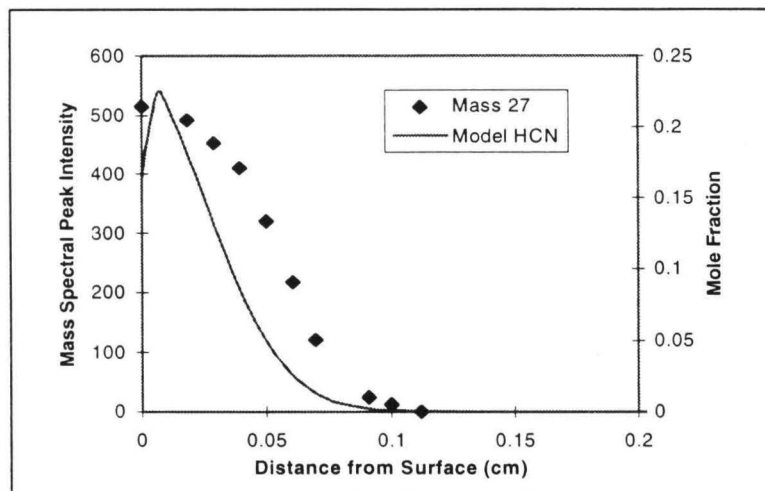


Figure 30: RDX Mass 27 Profile at 1 atm (Korobeinichev).¹⁰⁶

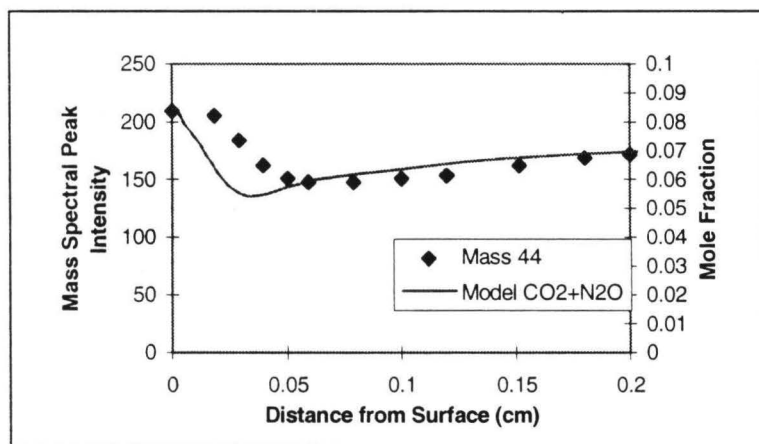


Figure 31: RDX Mass 44 Profile at 1 atm (Korobeinichev).¹⁰⁶

Korobeinichev et al. also made mass spectral measurements for the RDX flame at 2 atm. Again, only mass spectral intensities were reported. At 2 atm, the model indicates that the HCN profile approaches zero at 0.05 cm (Figure 32) compared to 0.1 cm at 1 atm (Figure 30). The experimental data indicate that the concentration profile of mass 27 is nearly independent of pressure, approaching zero by 0.1 cm for both 1 and 2 atm. The agreement between experiment and model for mass 30 is much more reasonable. (See Figure 33). This indicates a possible discrepancy in the experimental data. If the reaction zone for mass 30 moves towards the surface with pressure, it is likely that the reaction zone for other species would show this same trend.

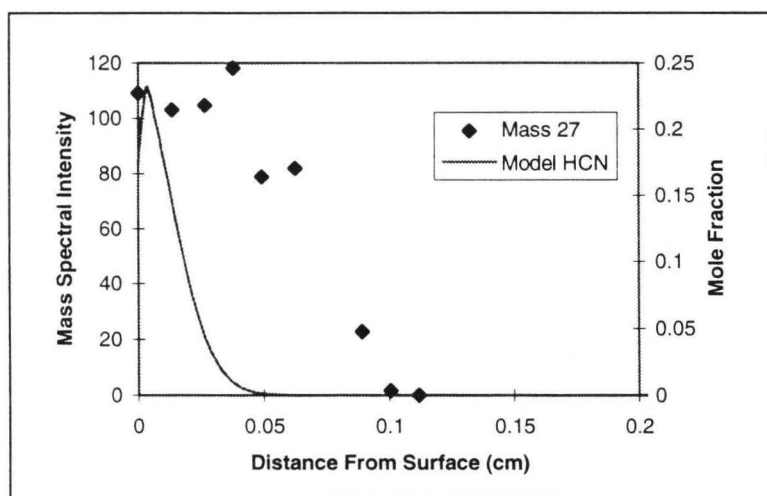


Figure 32: RDX Mass 27 Profile at 2 atm (Korobeinichev).¹⁰⁶

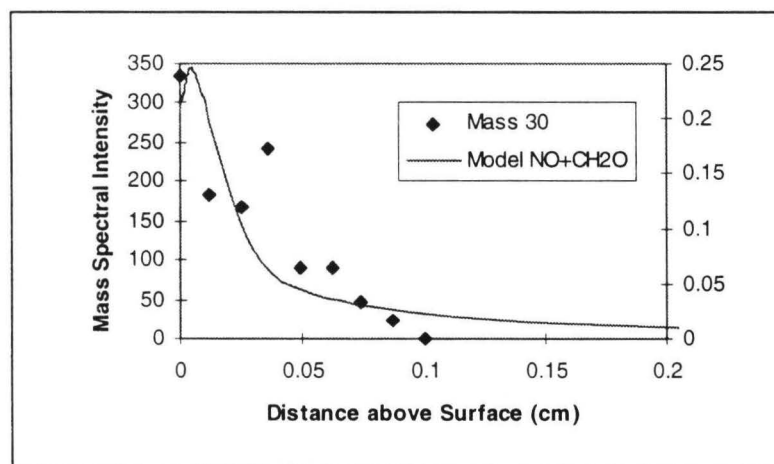


Figure 33: RDX Mass 30 Profile at 2 atm (Korobeinichev).¹⁰⁶

Hanson-Parr and Parr⁶⁹ measured the concentration profiles of CH₂O, HONO, OH, CN, NH, and NO in a self-deflagrating RDX flame at 1.0 atm using UV-Visible absorption and PLIF with a spatial resolution of 4 μm. Concentrations of CH₂O and HONO were less than 1.0 percent. All of the NO₂ reacted too close to the surface to allow its concentration to be measured. The results for OH, NO, CN and NH are shown in Figure 34 and Figure 35. Compared to these data, the model is over-predicting the concentration of NO by approximately 32 percent. The model also appears to be under-predicting the concentration of OH, though the predicted equilibrium value is nearly identical to that calculated by the Nasa-Lewis equilibrium code.¹¹⁴

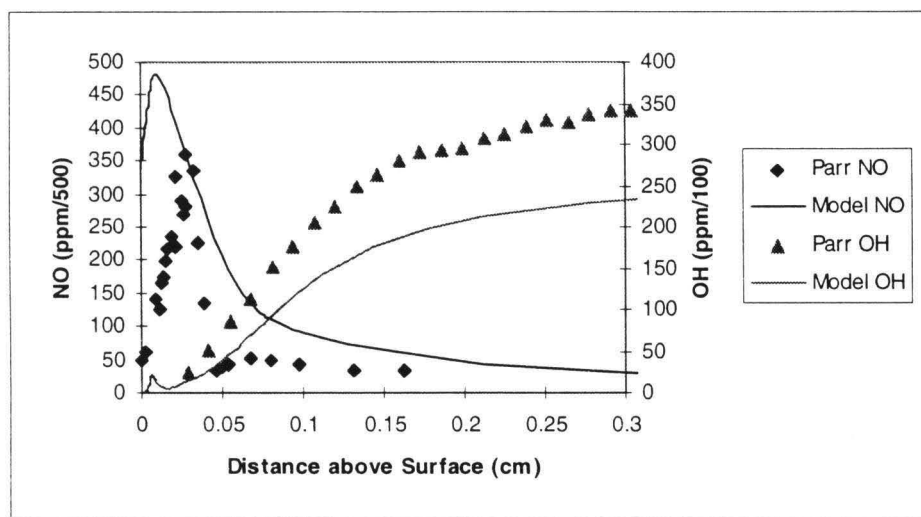


Figure 34: RDX NO and OH Profiles at 1 atm (Parr).⁶⁹

There is much better agreement between the predicted values and the measured values for the radicals CN and NH shown in Figure 35. The agreement in location and magnitude of these peaks is very reasonable. For Ermolin's data, the mass burning rate was input into the model. Hanson-Parr and Parr did not report a burning rate for their samples. The burning rate used in the comparisons made in Figure 34 and Figure 35 was the steady-state value calculated by the model at 1 atm, 0.03 cm/sec.

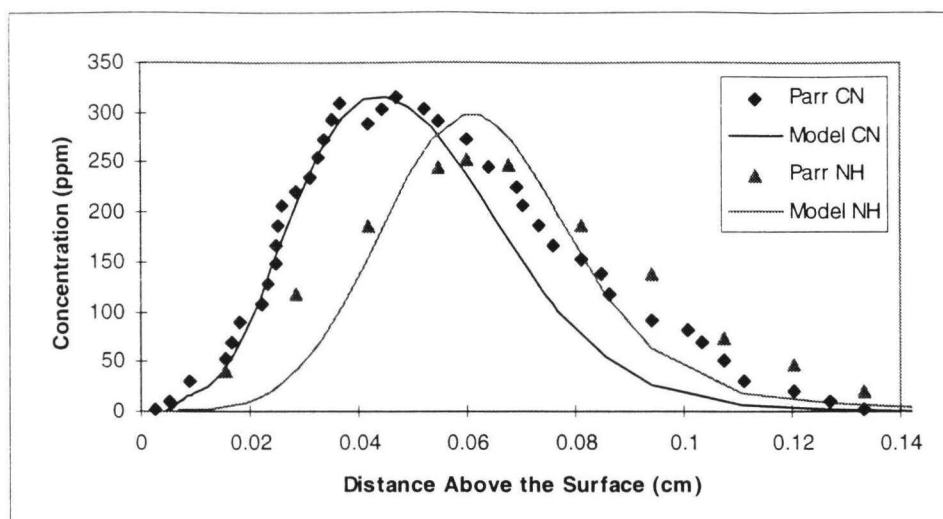


Figure 35: RDX NH and CN Profiles at 1 atm (Parr).⁶⁹

Laser-Assisted Combustion Experiments

Hanson-Parr and Parr⁶⁷ and Litzinger et al.^{64,65} have studied the flame structure of RDX at 1 atm under laser-assisted combustion conditions. By increasing the heat flux to the condensed propellant, the mass burning rate increases. The increased mass flux of gases from the burning surface stretches out the gas-phase flame giving researchers the required spatial resolution to measure species concentration profiles. Hanson-Parr and Parr use UV-visible absorption and Litzinger et al. use a triple quadrupole mass-spectrometer to obtain their data. To compare modeling results with these laser-assisted combustion data, some modifications to the model were necessary.

The laser-assisted experiments are at least two-dimensional because the strands of propellant are surrounded by air, and the laser flux intensity is a function of radius. Most monopropellant models with detailed kinetics are one-dimensional but can be made to approximate the two-dimensional characteristics by: 1) allowing the flame cross-sectional area to expand as a function of distance from the propellant surface and 2) assume an average laser flux for the whole surface. Parr's experiment and how it was modeled are shown in Figure 36. A discussion of how their experiment was modeled follows.

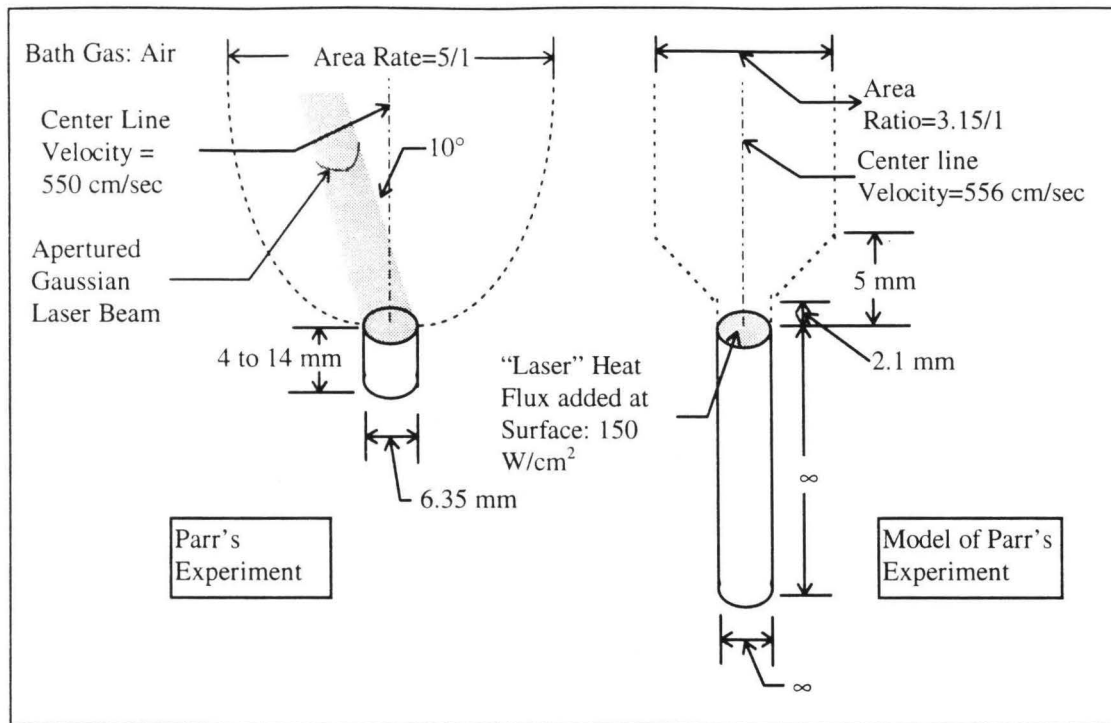


Figure 36: Model of Parrs' Experiment⁶⁷

Hanson-Parr and Parr have quantified the velocity field of the RDX gas flame using particle velocimetry imaging. The following pieces of information were used to determine the area expansion expression:

- 1) The cross-sectional area of the **entire** flame expands by a factor of 5 between the surface and 5 mm above the surface.
- 2) The center line velocity is approximately constant at 550 cm/sec.
- 3) The measured surface regression rate was in the range of 0.06 to 0.09 cm/sec.
- 4) The radial component of the velocity vectors near the centerline was much smaller than those near the edge of the sample. (i.e. The center of the flame may not have expanded as much at the entire flame).
- 5) The length of the measured dark zone is approximately 0.12 cm.
- 6) The experimentally determined temperature profile was used.

The averaged laser flux, location of area expansion, and rate of area expansion were optimized to make the best agreement between the experimental temperature profile and the predicted profile. If the

area were allowed to expand by a factor of five, the calculated centerline velocity would be approximately 125 cm/sec (much lower than 550 cm/sec). For the center line velocity to be approximately 550 cm/sec, the area could only expand by a factor of 3.15. The optimal area expansion correlation was:

$$area = \begin{cases} 1 \text{ cm}^2 & x < .21 \text{ cm} \\ \frac{3.15 - 1}{.5 - .21} \cdot (x - .21) + 1 \text{ cm}^2 & .13 \leq x \leq .5 \text{ cm} \\ 3.15 \text{ cm}^2 & x > .5 \text{ cm} \end{cases} \quad (43)$$

An average laser flux of 150 W/cm² input to the model gave a calculated surface regression rate of 0.086 cm/sec. According to the heat flux-regression rate correlation given by Hanson-Parr and Parr,¹⁰⁷ they would have had to set their laser to 283 W/cm² to get this burning rate. Therefore, according to the model, the propellant surface is receiving only about 50 percent of the peak laser flux. Prasad et al.⁶² make a similar assumption with their model and postulate that this is reasonable due to the Gaussian distribution of the incident laser flux.

There are several aspects of Hanson-Parr and Parr's experiment that are not considered in the model. As seen in Figure 36, they used a small sample of RDX surrounded by air. The one-dimensional model assumes that everything is constant in the radial direction (i.e. an infinitely large plane of RDX). In the experiment, the laser beam passes through the gaseous combustion zone at 10 degrees from the axis. The influence of the laser on the gas-phase and liquid phase reaction chemistry is unknown. In the model, the energy flux from the 'laser' is added to the energy flux from the gas phase flame at the surface. Because of the uncertainty in the area expansion, and non-uniformity of the laser beam, in-depth absorption^{§§§} or gas-phase absorption of the laser flux was not considered.

The measured and modeled temperature profiles are shown in Figure 37. (Note: Hanson-Parr and Parr, after comparing their measurements to calculated temperatures, recently re-analyzed their original data⁶⁷ and have found an alternate interpretation of their results which gives a higher flame temperature.⁶⁹ Previously, their flame temperature was around 2600 K). When considering the differences between the

§§§ For propellants which are not completely opaque, not all of the laser flux is absorbed at the surface, but the absorption is distributed in the liquid and solid volumes.

model and experiment, the agreement for the calculated temperature profile is reasonable. The experimental data now show, and the model predicts, a flame temperature (3050 K) slightly above the adiabatic flame temperature (2925 K) due to the added energy from the laser. Both the model and experiment indicate a “dark zone” or temperature plateau in the RDX under laser-assisted conditions, yet neither indicate such a plateau for self-deflagration. The data indicate this temperature plateau occurs at about 1600 K, but the model predicts a “dark zone” at about 1400 K. This may indicate that the predicted “dark zone” species concentrations are slightly different from those occurring in Hanson-Parr and Parr’s experiment.

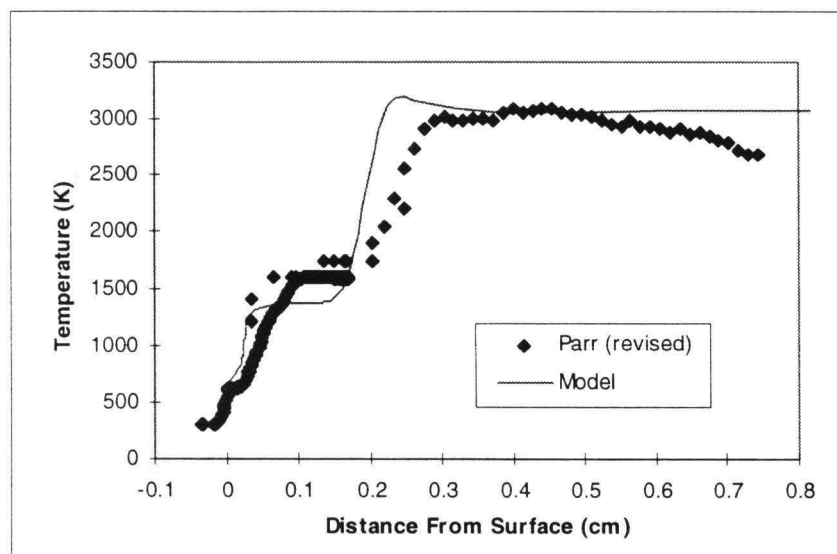


Figure 37: RDX Laser-assisted Temperature Profile at 1 atm (Parr)⁶⁹

The calculated species mole fraction profiles corresponding to the temperature profile shown in Figure 37 are shown in Figure 38. The two-stage flame separated by a “dark zone” is clearly evident. In the primary flame, RDX, CH_2O and N_2O react to form NO, HCN, CO and H_2O . Because of the relatively slow kinetics of NO and HCN, the chemical reactions stall until enough thermal energy is available to overcome the activation energy and ignite the secondary flame. In the secondary flame, NO, HCN, CO and N_2O react to form the equilibrium products N_2 , H_2O , CO, H_2 and CO_2 .

Hanson-Parr and Parr made measurements at several different laser intensities, but scaled all their data in the x direction relative to the location of the CN peak. As seen in Figure 39 and Figure 40,

there is reasonable agreement between the model and the experimental data for location and magnitude for the CN and NH peaks. As shown in Figure 41, there is also reasonable agreement for the location of the rise in the OH profile. Above the mole fraction of 0.035, the model's values and experimental data diverge with the model rising toward the theoretical equilibrium concentration and the experimental values decreasing.

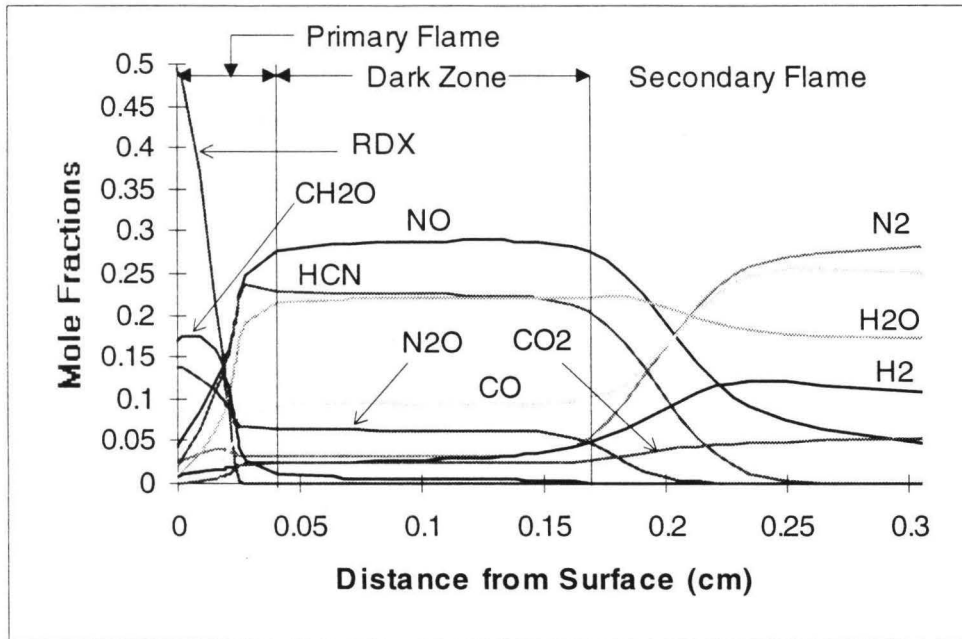


Figure 38: Calculated RDX Laser-assisted Two-Stage Flame Structure at 1 atm.

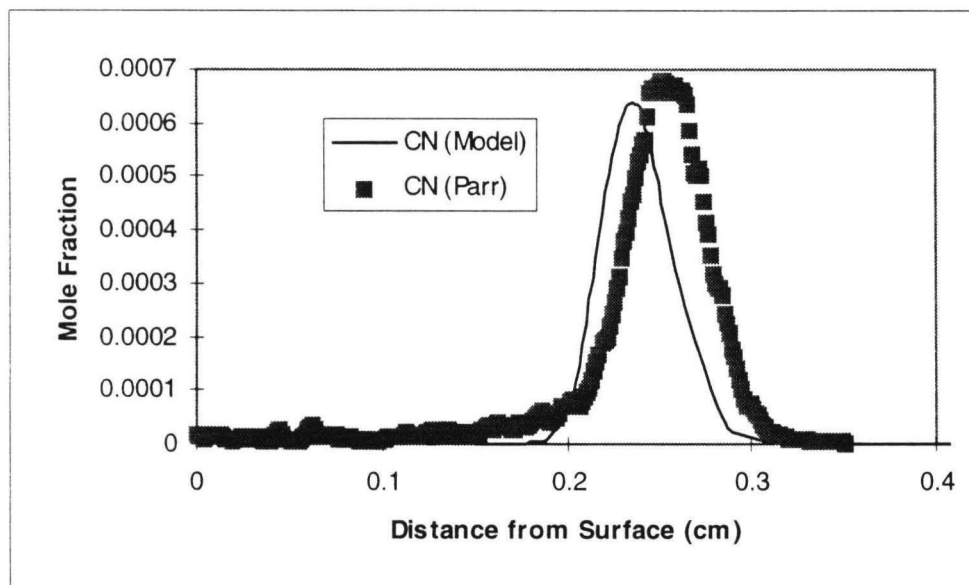


Figure 39: RDX Laser-assisted CN Profile 1 atm (Parr)⁶⁷

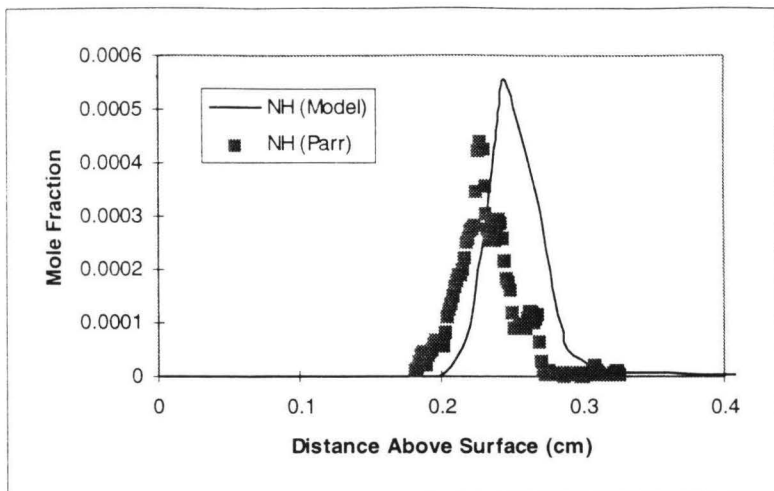


Figure 40: RDX Laser-assisted NH Profile at 1 atm (Parr)⁶⁷

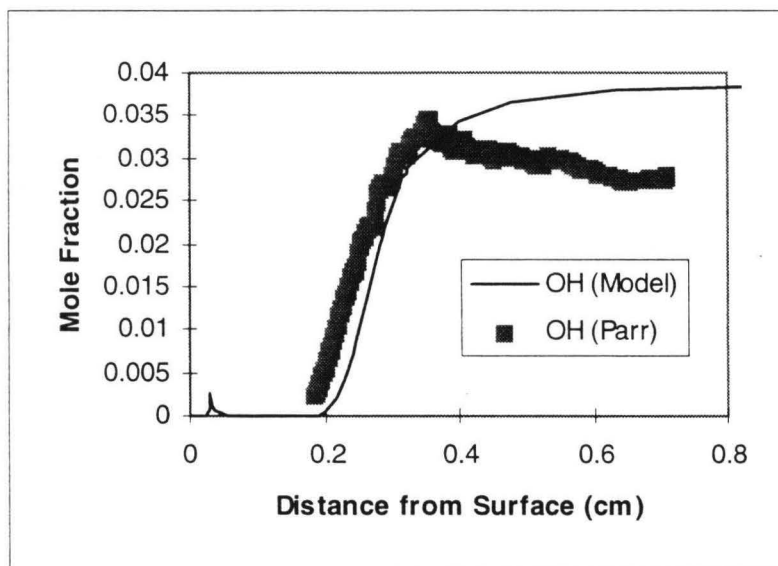


Figure 41: RDX Laser-assisted OH Profile at 1 atm (Parr)⁶⁷

For NO and NO₂, the agreement between the model calculations and the experimental values is poor (See Figure 42). The model is over-predicting the concentration of NO by about 40 percent and under-predicting the concentration of NO₂ by about a factor of 3.5. It should be noted that the experiments indicate that the NO₂ mole fractions decrease with decreasing laser flux. Extrapolating this trend to zero flux gives a scaling factor of 0.29.¹⁰⁸ The fact that the predicted NO₂ appears to be low may not be a problem with the reaction mechanism, but rather with our inability to accurately model the effect of the laser.

Litzinger et al.^{64,65} have also measured the concentration profiles for several species under laser-assisted conditions. Without a laser, the normal heat flux from the gas flame through the surface is approximately 50 W/cm^2 . Their data were taken at two laser intensities (100 W/cm^2 and 400 W/cm^2) and at one atmosphere. The gas-phase part of the model does not converge with a laser flux of 400 W/cm^2 . The model indicates that the advection rate is much higher than the reaction rates and the flame is essentially blown away from the surface. For the 100 W/cm^2 laser intensity, Litzinger reports a surface regression rate of 0.0752 cm/sec . To compare with Litzinger's data, the laser flux in the model was adjusted until the calculated burning rate matched Litzinger's experimental value. For the model, this laser flux is 135 W/cm^2 . The nitrogen-containing species are shown in Figure 43. As Hanson-Parr and Parr's data, the model over-predicts the NO peak concentration by about 30 percent, but there is very reasonable agreement for the NO_2 data.

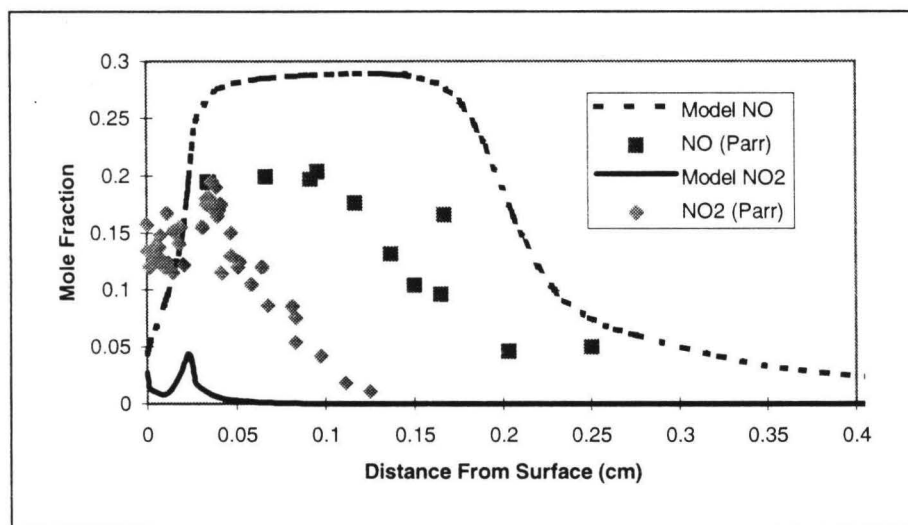


Figure 42: RDX Laser-assisted NO and NO₂ Mole Fractions at 1 atm (Parr)⁶⁷

Table 12 contains a comparison of the measurements of the peak NO and NO₂ concentrations as reported by the various researchers. Compared to Parr's and Litzinger's data, the model is over-predicting the peak concentration of NO. The discrepancy is further investigated in the next chapter (page 76). It is interesting to note that for both Parr's data and the model predictions, the ratio of peak NO to peak NO_{laser} concentrations is 1.17.

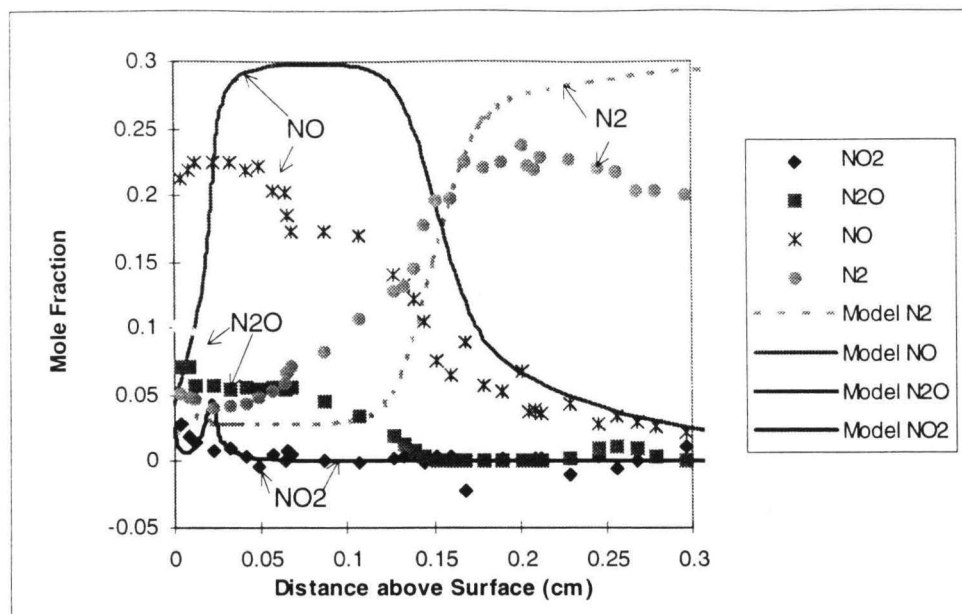


Figure 43: RDX Laser-assisted N-Containing Species Profiles at 1 atm (Litzinger)⁶⁴

Table 12: NO and NO₂ Peak Mole Fractions

Researcher	Conditions	Peak NO Mole Fraction	Peak NO ₂ Mole Fraction
Ermolin ^{40,106}	0.5 atm, no laser	0.23	0.025
Litzinger ^{64,65}	1 atm, 100 W/cm ² laser	0.23	0.03
Parr ⁶⁷	1 atm, 40-500 W/cm ² laser	0.2	0.2
Parr ⁶⁹	1 atm, no laser	0.17	Not measured.
Model	1 atm, 150 W/cm ² laser	0.27	0.05
Model	1 atm, no laser	0.23	0.025

Litzinger measures and the model predicts a peak mole fraction of NO₂ at about 0.03. This is in reasonable agreement with Ermolin’s measurements, but much lower than the value reported by Parr (0.2). As mentioned above, Parr’s NO₂ measurement appears to be a function of laser intensity. For Litzinger, there is no such correlation. It appears that the laser may be causing a systematic error in Parr’s NO₂ measurements.

Figure 44 shows the comparison between Litzinger’s carbon-containing species profiles and those calculated by the model. Near the surface, the model seems to be over-predicting the concentration of CH₂O and under-predicting the concentration of HCN. In the “dark zone”, there is very reasonable agreement between the model and experiment for all carbon-containing species. After the secondary flame the predicted values approach the expected equilibrium values, but Litzinger’s measured values for CO₂

and N_2 (Figure 43) do not. At this distance from the surface, it is likely that the flame is beginning to be diluted by surrounding gases.

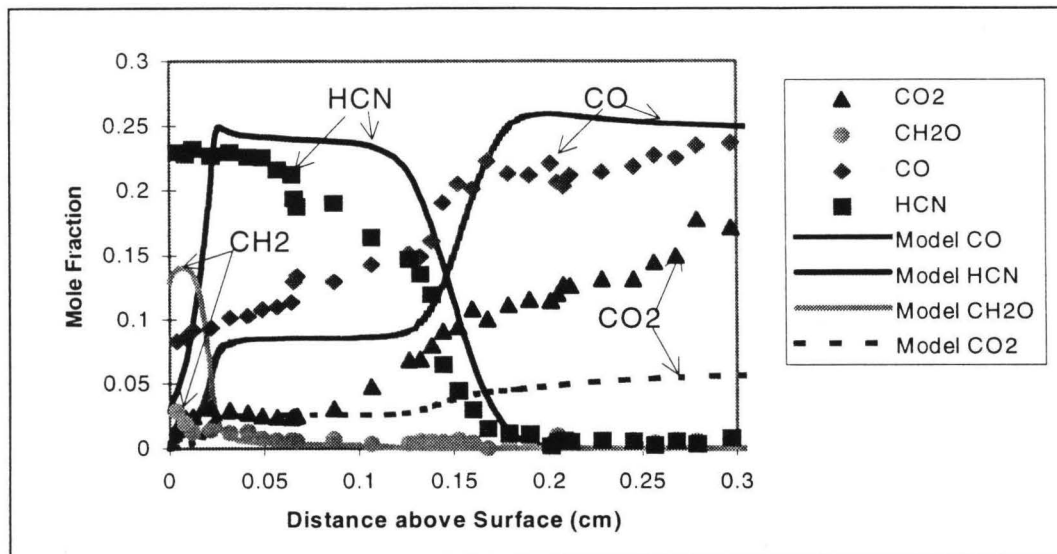


Figure 44: RDX Laser-assisted C-Containing Species Profiles at 1 atm (Litzinger)⁶³

Parr,⁶⁷ Litzinger⁶³ and Brewster⁶⁶ have measured the burning rate of RDX at 1 atm as a function of laser flux intensity. The comparison with the model is shown in Figure 45. The differences in the experimental data likely result from variations in experiment, RDX sample, and how the researchers “define” their laser flux. Hanson-Parr and Parr’s laser beam intensity has a Gaussian distribution, but the tails have been clipped by apertures. They report the peak laser intensity. The diameter of the laser beam of Litzinger et al. was about twice the diameter of their sample. This made their distribution on the RDX sample fairly uniform. By using the appropriate mirrors, integrators, and lenses, Brewster was able to obtain a uniform intensity profile. A uniform intensity profile is assumed in the model, and the agreement with Brewster’s measurements is very reasonable.

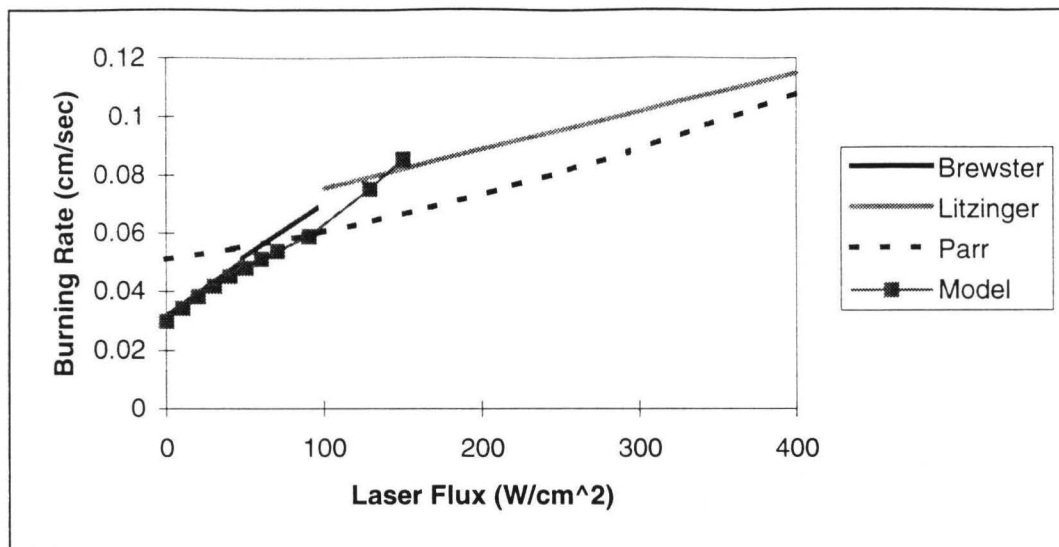


Figure 45: RDX Laser-Assisted Burning Rate at 1 atm (Brewster⁶⁶, Litzinger⁶³, Parr⁶⁷)

Summary of RDX Model Comparison with Experimental Data

Predicted values of burning rate as a function of pressure, initial temperature and laser flux, surface temperature, melt-layer thickness and final-flame temperature all agree very well with the available experiment data. At pressures below 2 atm, the agreement with most species concentration data is reasonable. The most serious discrepancy with experimental data is the NO concentration, where the model, according to experimental data from Parr⁶⁷ and Litzinger,^{63,64} is over-predicting the peak NO mole fraction by 30 to 40 percent. Reasons for this difference are addressed in the next chapter. For NO₂, there is reasonable agreement between the concentration profiles of Ermolin,^{40,106} Litzinger^{63,64} and the model. The data from Hanson-Parr and Parr⁶⁷ are an order of magnitude greater. Hanson-Parr and Parr's measurements appear to be influenced by their laser intensity. For some of the species concentration profiles, there is enough variation between results from the various researchers that it is uncertain whether the model and the experiments have the greatest error.

CHAPTER 7: ANALYSIS AND REDUCTION OF THE MELIUS-YETTER RDX MECHANISM

Introduction

As seen in Chapter 6, calculations made by the model using the Melius-Yetter⁵⁰ mechanism were shown to correlate very reasonably with experimentally determined burning rate, surface and flame temperature, melt-layer thickness, and species concentration profiles. Models by Yang⁷⁵ and Smooke⁶² show similar results when using this mechanism. Most of the chemical reactions in the mechanism were originally studied for the combustion of hydrocarbons. Most of the reactions added or modified by Melius⁴⁸ and Yetter⁵⁰ involve those species specific to nitramine chemistry. Because many of the model calculations are strongly influenced by the gas phase reactions (see Chapter 8), this chapter is an analysis of the Melius-Yetter RDX mechanism. The main reaction paths are identified and discrepancies in species concentrations profiles noted in the previous chapter are investigated. The analysis is extended to the development of skeletal and global mechanisms.

Integral Reaction Flow Analysis

To identify the main reaction paths, every reaction rate was integrated in volume (area of flame \times length of numerical domain) and its contribution to the overall production or destruction of a species was compared with the other reactions (the integral reaction flow analysis). The results for RDX at 20 atmospheres are summarized in Figure 46.

From Figure 46 the following observations can be made:

- Approximately 88% of the RDX evaporates (12% decomposes) from $\text{RDX}_{\text{liquid}}$.
- $\text{RDX}_{\text{vapor}}$ predominately decomposes to H_2CNNO_2 via a couple of intermediates.
- After H_2CNNO_2 decomposes, the RDX decomposition can be summarized by two paths:
 $\text{N}_2\text{O}-\text{CH}_2\text{O}$ (20%) and $\text{NO}_2-\text{H}_2\text{CN}$ (79%).
- $\text{H}_2\text{CN}\rightarrow\text{HCN}\rightarrow\text{HNC}\rightarrow\text{HNCO}\rightarrow\text{CO}$ produces approximately 56% of CO.
- Additional CO comes from $\text{CH}_2\text{O}\rightarrow\text{HCO}\rightarrow\text{CO}$ and $\text{H}_2\text{CN}\rightarrow\text{HCN}\rightarrow\text{NCO}\rightarrow\text{CO}$.
- $\text{NO}_2\rightarrow\text{NO}\rightarrow\text{N}_2$ produces approximately 45% of the N_2 .
- $\text{NO}_2\rightarrow\text{NO}\rightarrow\text{N}_2\text{O}\rightarrow\text{N}_2$ produces approximately 35% of the N_2 .
- Approximately 70% of the H_2 and 11% of the N_2 comes from reactions between small species like H, NH_2 , N, etc.

Explanations for Discrepancies in Species Profiles

In Chapter 6, it was noted that most of the calculated species profiles are in reasonable agreement with experimental data. Possible explanations for the noted discrepancies can be given based on the data presented in Figure 46, comments accompanying the Melius-Yetter⁵⁰ mechanism, and literature searches for the appropriate reaction rate constants. Yetter notes in the mechanism that the reactions involving the species H_2CNNO_2 , HONO, and H_2CN need further review. Additionally, reactions involving the species $\text{RDX}_{\text{vapor}}$, RDXR, and RDXRO are highly uncertain as they were originally estimated by Melius⁴⁸ based on BAC-MP4 calculations without any experimental data.

CH_2O

Near the burning surface (See Figure 44, page 71) the model is over-predicting the concentration of CH_2O by over a factor of four. As seen in Figure 46, CH_2O is produced from the decomposition reactions of H_2CNNO_2 and in particular the reactions listed in Table 13. Reactions 222 and 223 were preceded by the comment "The following two reactions have been added to increase early heat release and reaction rate." It appears that, in reality, the ratio of H_2CNNO_2 decomposing to H_2CN and NO_2 , to

H₂CNNO₂ decomposing to CH₂O and N₂O is greater than what the Melius-Yetter mechanism indicates. As is shown in Figure 63 (page 96), Reaction 221 strongly influences the burning rate, yet the burning rate agrees very well with experimental data. Thus, there appears to be a minor cancellation of errors in the mechanism.

Table 13: Reactions Producing CH₂O

Reaction Number	Reaction	Percent contribution to the overall production of CH ₂ O
221	H ₂ CNNO ₂ +H ₂ O<=>CH ₂ O+N ₂ O+H ₂ O	53.6
223	H ₂ CNNO ₂ +N ₂ O<=>CH ₂ O+2N ₂ O	12.2
217	H ₂ CNO+NO ₂ <=>CH ₂ O+2NO	12.0
226	H ₂ CNNO ₂ +OH<=>CH ₂ O+N ₂ O+OH	11.8
222	H ₂ CNNO ₂ +NO ₂ <=>CH ₂ O+N ₂ O+NO ₂	5.7
22	CH ₂ O+M<=>HCO+H+M	4.6

NO

The largest discrepancies in species concentration profiles involves the nitrogen chemistry and in particular the concentration profiles of NO and NO₂. The model shows reasonable agreement with the NO₂ concentration measured by Litzinger^{64,65} and Ermolin,⁴⁰ but is low by a factor of four compared to Parr's data. (See Table 12, page 70.) Parr's measured concentration of NO₂ appears to be a function of laser flux.⁶⁷ Given this conflict in the experimental data, the discrepancy in the concentration of NO₂ will not be investigated.

The experimental data do consistently indicate that the model is over-predicting the concentration of NO. Several possible explanations and solutions were investigated. The reactions contributing the most to the production of NO (as determined from the integral reaction flow analysis) are shown in Table 14. The rate constants used for these reactions agree well with those found in the literature.¹⁰⁹

Table 14: Reactions Producing NO

Reaction Number	Reaction	Percent contribution to the overall production of NO
61	$\text{NO}_2 + \text{H} \rightleftharpoons \text{NO} + \text{OH}$	63.1
115	$\text{HNO} + \text{NO}_2 \rightleftharpoons \text{HONO} + \text{NO}$	9.1
78	$\text{NH} + \text{NO} \rightleftharpoons \text{N}_2\text{O} + \text{H}$	6.2
112	$\text{HNO} + \text{OH} \rightleftharpoons \text{H}_2\text{O} + \text{NO}$	5.5
91	$\text{NH}_2 + \text{NO} \rightleftharpoons \text{N}_2 + \text{H}_2\text{O}$	5.1
111	$\text{HNO} + \text{H} \rightleftharpoons \text{H}_2 + \text{NO}$	3.5
217	$\text{H}_2\text{CNO} + \text{NO}_2 \rightleftharpoons \text{CH}_2\text{O} + 2\text{NO}$	2.1
65	$\text{NO}_2 + \text{HCO} \rightleftharpoons \text{H} + \text{CO}_2 + \text{NO}$	1.8
168	$\text{NCO} + \text{OH} \rightleftharpoons \text{NO} + \text{CO} + \text{H}$	1.0

The reactions leading to the destruction of NO are listed in Table 15. Except for Reaction 56 all of the rate constants agree well with those found in the literature.¹⁰⁹ Yetter's calculated rate for Reaction 56 is low by approximately four orders of magnitude compared to 22 values found in the NIST Kinetic Data Base.¹⁰⁹ As seen in Figure 46, NO reacts to HONO which reacts to form NO₂. Increasing this rate constant by four orders of magnitude did not change the peak concentration of NO by a significant amount.

Table 15: Reactions Destroying NO

Reaction Number	Reaction	Percent contribution to the overall destruction of NO
77	$\text{NH} + \text{NO} \rightleftharpoons \text{N}_2\text{O} + \text{H}$	21.2
46	$\text{N} + \text{NO} \rightleftharpoons \text{N}_2 + \text{O}$	17.0
90	$\text{NH}_2 + \text{NO} \rightleftharpoons \text{N}_2 + \text{H}_2\text{O}$	9.8
79	$\text{NH} + \text{NO} \rightleftharpoons \text{N}_2 + \text{OH}$	8.5
58	$\text{NO} + \text{HCO} \rightleftharpoons \text{HNO} + \text{CO}$	7.2
56	$\text{NO} + \text{OH} (+\text{M}) \rightleftharpoons \text{HONO} (+\text{M})$	6.0
92	$\text{NH}_2 + \text{NO} \rightleftharpoons \text{N}_2\text{O} + \text{H}_2$	5.5
205	$\text{H}_2\text{CN} + \text{NO} \rightleftharpoons \text{HCN} + \text{HNO}$	5.0
89	$\text{NH}_2 + \text{NO} \rightleftharpoons \text{NNH} + \text{OH}$	5.0
42	$\text{N} + \text{OH} \rightleftharpoons \text{NO} + \text{H}$	4.2
55	$\text{NO} + \text{H} (+\text{M}) \rightleftharpoons \text{HNO} (+\text{M})$	3.7
174	$\text{NCO} + \text{NO} \rightleftharpoons \text{CO}_2 + \text{N}_2$	2.8
173	$\text{NCO} + \text{NO} \rightleftharpoons \text{N}_2\text{O} + \text{CO}$	2.2

The reactions affecting the concentration of NO were further investigated by measuring the sensitivity of the concentration of NO with respect to each gas-phase reaction. Figure 47 is a plot of the

normalized sensitivity coefficients (s) as a function of distance from the surface for the top 15 most sensitive reactions. Normalized sensitivity coefficients for this analysis are defined as:

$$s = \frac{A_i}{\max(X_{NO})} \frac{\partial X_{NO}}{\partial A_i} \quad (44)$$

where A_i is the pre-exponential rate constant of reaction i . Because X_{NO} changes with distance from the surface so does s . (This is calculated as described in the PREMIX manual.⁴⁵ For further discussion of sensitivity analysis please refer to the next chapter.) The NIST Kinetic Database¹⁰⁹ and a recent study by Lin et al.¹¹⁰ were searched for each of the reactions shown in Figure 47. There was very reasonable agreement between most of the rate constants used by Yetter and those found in this limited literature search. However, no comparisons could be made for the following reactions:

- 210: $\text{H}_2\text{CN} + \text{N}_2\text{O} = \text{H}_2\text{CNO} + \text{N}_2$
- 221: $\text{H}_2\text{CNNO}_2 + \text{H}_2\text{O} = \text{CH}_2\text{O} + \text{N}_2\text{O} + \text{H}_2$
- 103: $\text{NNH} + \text{O} = \text{N}_2\text{O} + \text{H}$
- 227: $\text{RDX} (+\text{M}) = \text{RDXR} + \text{NO}_2 (+\text{M})$

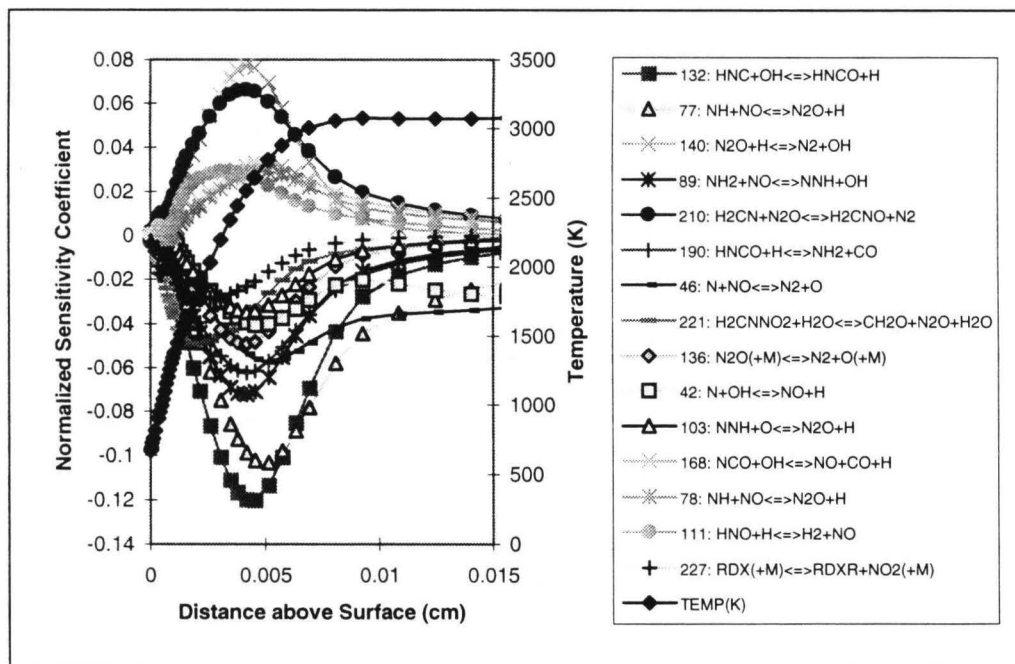


Figure 47: NO Sensitivity Analysis for RDX at 10 atm.

Each of the pre-exponential rate constants for these four reactions was changed by an order of magnitude in the direction necessary to lower the concentration of predicted NO, as determined from Figure 47. (e.g. decreasing the rate of Reaction 210 will decrease NO concentration.) Individually changing the rate constants had little effect on the concentration of NO, yet when all four rate constants were changed simultaneously by an order of magnitude, the calculated peak NO mole fraction was 0.20 compared to 0.24 with the original rate constants. However, these four reactions also affect the burning rate to a significant degree. (See Figure 63, page 96). With these changes, the burning rate changed from 0.2383 cm/sec to 0.3253 cm/sec, an increase of 36 percent. Compared to the NO concentration, the value for burning rate is known with relative certainty to be approximately 0.24 cm/sec. Either the experimental values of the concentration of NO are low or other reactions are at fault. The latter is more likely.

After studying Figure 46 and several sensitivity plots similar to Figure 47, it was concluded that the reason that the model was over-predicting the concentration of NO was likely the result of the combinations of reactions describing the interactions between NO₂, NO, HNO, HONO, HCO and H₂CN. Based on this analysis, the pre-exponential factors of the reactions listed in Table 16 were changed as indicated, and the peak NO mole fraction changed from 0.24 to 0.19. This value is in better agreement with measured values by Parr⁶⁷ and Litzinger.⁶⁴ (See Table 12, page 70). Comparisons between the model using modifications to the Melius-Yetter mechanism outlined in Table 16 and previous results, are shown in Figure 48 and Figure 49. There is much better agreement for NO. These modifications increased and moved the peak concentrations of CN and NH closer to the surface. The shift of the location of the peak may indicate a slight difference in the experimental and calculated burning rate. Unlike the changes to the four reactions above, these adjustments caused insignificant changes in predicted values of burning rate, surface temperature, final flame temperature, and melt-layer thickness for pressures between 1 and 100 atm. Most of the rate constants associated with these reactions (Table 16) have a high degree of uncertainty. It should not be assumed that these adjustments are justifiable from a chemical standpoint, but they may indicate a general location of the problem.

Table 16: Proposed Modifications to Melius-Yetter to Reduce Peak NO Concentration

Reaction Number	Reaction	Original Pre-Exponential Factor (A)	Change by Factor
56	$\text{NO} + \text{OH} + \text{M} \rightleftharpoons \text{HONO} + \text{M}$.155E12	$\times 10000$
58	$\text{NO} + \text{HCO} \rightleftharpoons \text{HNO} + \text{CO}$	7.23E12	$\times 10$
115	$\text{HNO} + \text{NO}_2 \rightleftharpoons \text{HONO} + \text{NO}$	6.02E11	+100
205	$\text{H}_2\text{CN} + \text{NO} \rightleftharpoons \text{HCN} + \text{HNO}$	1.0E14	$\times 100$
206	$\text{H}_2\text{CN} + \text{NO}_2 \rightleftharpoons \text{HCN} + \text{HONO}$	1.0E11	+100
207	$\text{H}_2\text{CN} + \text{NO}_2 \rightleftharpoons \text{H}_2\text{CNO} + \text{NO}$	1.0e12	+100
210	$\text{H}_2\text{CN} + \text{N}_2\text{O} \rightleftharpoons \text{H}_2\text{CNO} + \text{N}_2$	1.0E12	$\times 100$
216	$\text{H}_2\text{CNO} + \text{NO}_2 \rightleftharpoons \text{HCNO} + \text{HONO}$	1.0E12	+100
217	$\text{H}_2\text{CNO} + \text{NO}_2 \rightleftharpoons \text{CH}_2\text{O} + 2\text{NO}$	1.0E12	+100
218	$\text{H}_2\text{CNO} + \text{HNO} \rightleftharpoons \text{H}_2\text{CN} + \text{HONO}$	1.0E12	$\times 100$

(Modifications to rate constants of Reactions 56 and 58 are justifiable according to NIST database. The other rate constants are uncertain and the corresponding reactions were not found in the NIST database.)

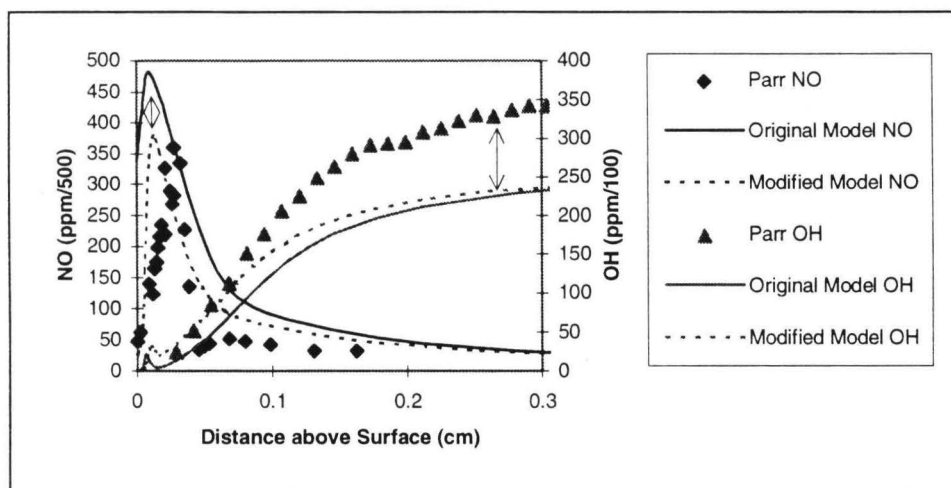


Figure 48: Modified Melius-Yetter NO and OH Concentration Profiles at 1 atm (Parr).⁶⁹

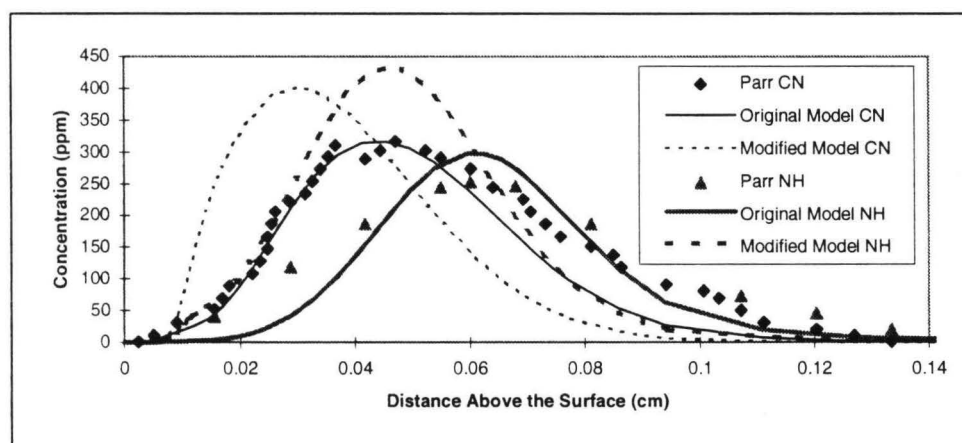


Figure 49: Modified Melius-Yetter NH and CN Concentration Profiles at 1 atm (Parr).⁶⁹

Mechanism Reduction

It is desirable to reduce the size of the gas-phase mechanism for two reasons: 1) by eliminating many of the lesser important reactions the key reaction paths are more easily identified and studied; and 2) for multi-dimensional and/or time-dependent models, CPU time can be reduced greatly by eliminating species and reactions. A reduced mechanism does have drawbacks, such as a reduced range of applicability and a loss of accuracy. In the literature, many reduced mechanisms have been developed to match one parameter (usually laminar flame speed) at one pressure (usually one atmosphere). Such a reduction may be useful for the first reason listed above but may not be applicable in more general modeling such as the effect of pressure oscillations on the combustion of a composite propellant. Two methods used to significantly reduce a mechanism for RDX deflagration that maintain accuracy of predictions over a wide range of applicability are described. One method is used to develop a skeletal mechanism and the other to develop a global mechanism. Both mechanisms are CHEMKIN⁴¹ compatible. It is hoped that these mechanisms can be used in future work in more complex models where reducing CPU time becomes necessary.

Background

PREMIX uses finite differencing to turn the differential equations (Eqs. 14-16) into non-linear algebraic equations, and then uses an adaptive-gridding and Newton's method to solve for the temperature and species concentration profiles. In solving the problem, much of the time is spent generating the Jacobian matrix. The size of the Jacobian can be significantly reduced by eliminating the number of species or nodes. Because the Jacobian matrix is banded, the amount of memory units it requires in PREMIX is $(6 \cdot kk^2 + 22 \cdot kk + 20) \cdot jj$ where kk is the number of species and jj is the number of nodes. Reducing the number of nodes reduces the resolution and accuracy of the solution. Likewise, by eliminating species, one not only loses those species concentration profiles, but also the effect those species have on other species and the entire solution. Since the size of the Jacobian is related to the number of species squared, great reductions in CPU time can be achieved by eliminating species. The remainder of the time is used in function calls, inverting the Jacobian, and solving, which can also be

significantly reduced by eliminating species. The number of reactions has little effect on CPU time when compared to the effect of the number of species.

There are many ways of reducing the number of species and number of reactions in a large elementary-step reaction mechanism.¹¹¹ Several of these methods are briefly described in the Appendix.

Skeletal Mechanism

In the reduction of the number of species, the unmodified August 1995 version of the Melius-Yetter RDX mechanism was the starting point and the standard for comparison. Key reaction paths were identified from the integral flow reaction analysis shown in Figure 46. A few species (RDXR, RDXRO, H₂COHNNO₂) can be dropped immediately by combining a few reactions (replacing reactions in Table 17 with those in Table 18). These changes did not have a significant effect on model predictions.

Table 17: Full Molecular RDX Decomposition****

#	Reactions to be replaced:	A	Ea (cal/mole)
1	RDX(+M)=RDXR+NO2(+M)	2.00E+16	4.500E+04
	Low Parameters	1.57E+17	2.800E+04
2	RDX+H=RDXR+HONO	1.00E+13	5.000E+03
3	RDX+OH=>2H2CNNO2+H2COHNNO2	1.0E13	5.000E+03
4	H2COHNNO2=>HCN+NO2+H2O	1.00E+16	0.000E+00
5	RDXR(+M)=>RDXRO(+M)	1.0E16	2.300E+04
	Low Parameters	7.69E+16	1.800E+04
6	RDXRO(+M)=>2H2CNNO2+H2CN(+M)	1.00E+16	2.300E+04
	Low Parameters	7.69E+16	1.800E+04

Table 18: Skeletal Molecular RDX Decomposition****

#	Replaced by:	A	Ea (cal/mole)
1,5,6	RDX(+M)=2H2CNNO2+H2CN+NO2(+M)	2.0E+16	4.500E+04
	Low Parameters	1.57E+17	2.800E+04
2,5,6	RDX+H=2H2CNNO2+H2CN+HONO	1.0E+13	5.000E+03
3	RDX+OH=>3H2CNNO2+OH	1.0E13	5.000E+03

The mechanism was further reduced using the integral reaction flow analysis. The process was automated by using the following algorithm:

- I. Choose one or more species as the important initial species.

**** Low parameters are rate constants for pressure-dependent fall-off reactions using the Lindemann expression.⁴¹

- II. Add other important species
 - A. For each important species:
 - 1. Integrate the contribution of every reaction to the destruction of an important species from the surface to the end of the flame.
 - 2. Find which reaction contributes the most to the destruction of that species.
 - 3. Mark every species that is involved in any reaction that contributes more than X ($0 < X < 1$) times the contribution of the maximum reaction (determined in II.A.2) as important.
 - B. If any new species are marked as important go to step II.A.
- III. Delete all unimportant species.
- IV. Delete all reactions involving species deleted in step III.
- V. Run calculations and compare with full mechanism.

Once all the unimportant species and the reactions that involve these species have been identified and removed from the mechanism, all other reactions are kept. Starting with RDX as important and $X=0.4$, the algorithm began tracing the decomposition of RDX towards final products. H_2CNNO_2 , NO_2 and H_2CN were the first species added in step II.A.3. This was followed by HCN, NO, H, and OH. (This can be followed on the Integral Flow Analysis in Figure 46.) The process was continued until the final equilibrium species were reached. According to this method, CH_2O is not important in the gas phase but must be considered because it is being produced by the condensed phase decomposition mechanism. To try to reduce the number of species even further, the reaction $\text{RDX}_{\text{liquid}} \rightarrow 3\text{CH}_2\text{O} + 3\text{N}_2\text{O}$ was dropped from the condensed phase decomposition reaction. This path represented only 4.6% of the RDX decomposition compared to over 88% evaporating and 7.3% going to NO_2 and H_2CN . By eliminating CH_2O , HCO could also be dropped. By dropping CH_2O , essentially all of the $\text{RDX}_{\text{vapor}}$ decomposes to H_2CN and NO_2 through H_2CNNO_2 . To eliminate H_2CNNO_2 the reactions in Table 18 were replaced by the reaction in Table 19.

Table 19: Global Molecular RDX Decomposition

Reaction	A	Ea (cal/mole)
$\text{RDX}(+\text{M})=3\text{H}_2\text{CN}+3\text{NO}_2(+\text{M})$	1.3E12	4.500E+04
Low Parameters	1.57E+17	2.800E+04

Essentially, the initial $\text{RDX}_{\text{vapor}}$ decomposition has been represented by one global reaction, and by so doing, four additional species were eliminated. Running the above algorithm with $X=100\%$ resulted in a mechanism of 18 species involved in 39 reactions. The following species were dropped: O_2 , HO_2 , H_2O_2 , CH_2O , HCO , NH_3 , NNH , HNO , CN , C_2N_2 , NCN , N , HONO , NCO , CNO , HOCN , HCNO , NO_3 , HNO_3 , H_2CNH , H_2CNO , H_2CNNO , H_2CNNO_2 , RDXR , RDXRO , $\text{H}_2\text{COHNNO}_2$, and Ar . This mechanism is referred to as S18-39 in the subsequent discussion. It is listed in the Appendix and diagrammed in Figure 50.

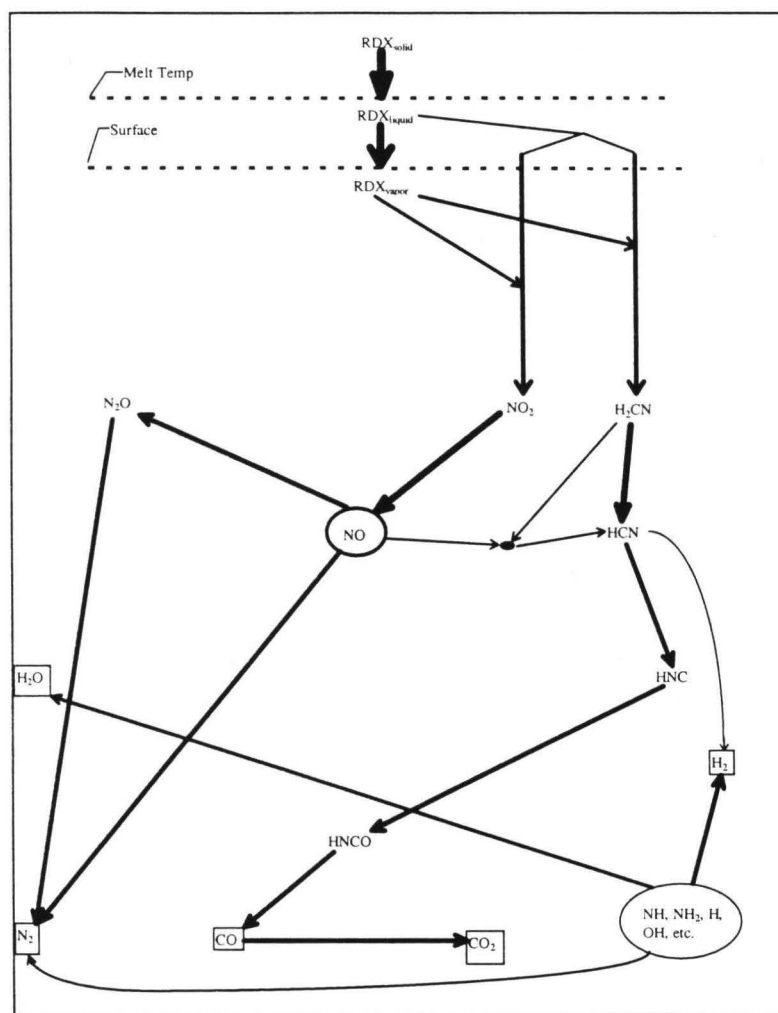


Figure 50: Skeletal RDX Mechanism S18-39.

Several other reduced mechanisms were developed and tested in this process. The smallest mechanism that retained CH_2O and gave reasonable results used the skeletal decomposition of RDX in Table 18 and involved 23 species in 83 reactions (S23-83). Results obtained using S23-83 did not differ greatly from those obtained using S18-39. Comparisons of S18-39 with F45-232 (the original Yetter-Melius Mechanism⁵⁰) and with experimental data are made below.

For nitramine mechanisms, Anderson et al.¹¹² have been working on a reduced mechanism for the dark zone region. They are modeling the system as a batch reactor. Their detailed kinetic mechanism is composed of 185 elementary reactions and 41 species. From this a skeletal mechanism (18 species, 24 reactions) was developed using reaction path analysis and sensitivity analysis. By applying the QSSA to 8 species, a global mechanism (7 species and 3 reactions) was developed. The criteria used in judging their reduced mechanism were ignition delays for pressures between 1 and 30 atmospheres and for initial temperatures between 1000 and 1800 K. Sixteen of the 18 species and 20 of the 24 reactions from Anderson's skeletal mechanism¹¹² are also in S18-39.

Global Mechanism

The objective in developing the global mechanism was to include the minimum number of species and reactions that would enable the model to predict the correct burning rate and approximate final product concentrations over a range of pressures. Another requirement was that the global reaction mechanism had to be written in CHEMKIN⁴¹ format to be compatible with existing computer models. The mechanism was developed by proposing a few reaction steps and then optimizing the kinetic parameters so that the model would predict the correct burning rate and final species concentrations. (i.e., the fitted kinetic method). At this level of global reaction mechanism, the detail in the chemistry that is possible with the full or skeletal mechanisms is lost.

Table 20 contains a global mechanism developed for RDX. This mechanism can be summarized by reactant (RDX)→intermediate (H_2CNNO_2)→final products (CO, NO, H_2 , H_2O , CO_2 , O, OH). There are 9 species involved in 6 reactions. The rate constants for the first 5 reactions were determined by optimization. Reaction 5 is the reverse of reaction 4. The last reaction comes from Tsang and Hampson¹¹³

and is used without modification. Two more species (OH and H) can be eliminated by excluding the final reaction, but as will be shown, the dissociation of water must be considered to have better agreement with the adiabatic flame temperature (See Figure 54, page 88). In this discussion, the global mechanism with 7 species and five reactions (H and OH eliminated) is referred to as G7-5, and likewise the global mechanism with 9 species and six reactions is referred to as G9-6.

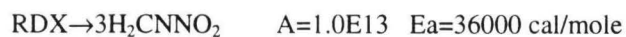
Table 20: RDX Gas-Phase Global Mechanism

	Reaction	A	B	Activation Energy (cal/mole)
1	RDX+M=>3H2CNNO2+M	2.1E11	0	25000
2	H2CNNO2=N2+CO+H2O	3.0E9	0	35000
3	H2CNNO2=H2+CO2+N2	1.0E9	0	35000
4	CO2+H2=>CO+H2O	7.5E9	0	10000
5	CO+H2O=>CO2+H2	8.5E8	0	10000
6	OH+H+M=H2O+M	2.21E22	-2	0.000
	H2/2.500/ H2O/1.200E01/ CO/1.900/ O2/3.800/			(Third body efficiencies for rxn 6)

In the full mechanism, RDX was assumed to decompose in the condensed phase via two competing pathways:



By including these decomposition pathways four additional species must be added to the gas phase mechanism. To avoid this, these reactions were replaced by:



In either case, the transition from condensed phase to gas phase for RDX appears to be dominated by evaporation. The model calculates the net evaporation rate in the same manner as when using the full mechanism. All other model inputs (thermophysical properties of RDX) are the same as those listed in Table 10 on page 50.

Comparison of Reduced Mechanisms with Experiment and Full Mechanism Calculations

The skeletal and reduced mechanisms show reasonable agreement with experimentally determined burning rate data as a function of pressure (Figure 51), surface temperature data (Figure 52), melt-layer thickness data (Figure 53), adiabatic flame temperature data (Figure 54) and adiabatic flame

species concentrations (Figure 55). On a log-log plot the agreement in burning rate looks reasonable, but S18-39 does under-predict this characteristic at 80 atmospheres by 12%. S18-39 has a slightly higher surface temperature and melt-layer thickness because of the different liquid decomposition mechanism. Although all of the major final flame species concentrations show reasonable agreement with theoretical values, the global mechanisms do not accurately reproduce the adiabatic flame temperature because of the missing minor species. Adding global reaction 6 of Table 20 (the dissociation of water) to G7-5 (to make G9-6) reduces the error significantly but increases the number of species by two (OH and H).

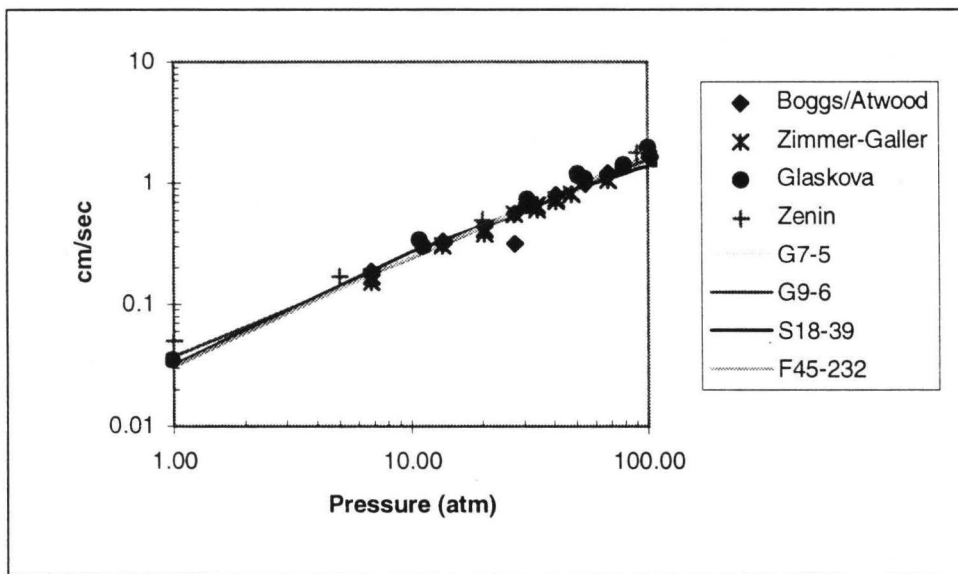


Figure 51: RDX Calculated Burning Rate using Reduced Mechanisms^{34,71,103,104}

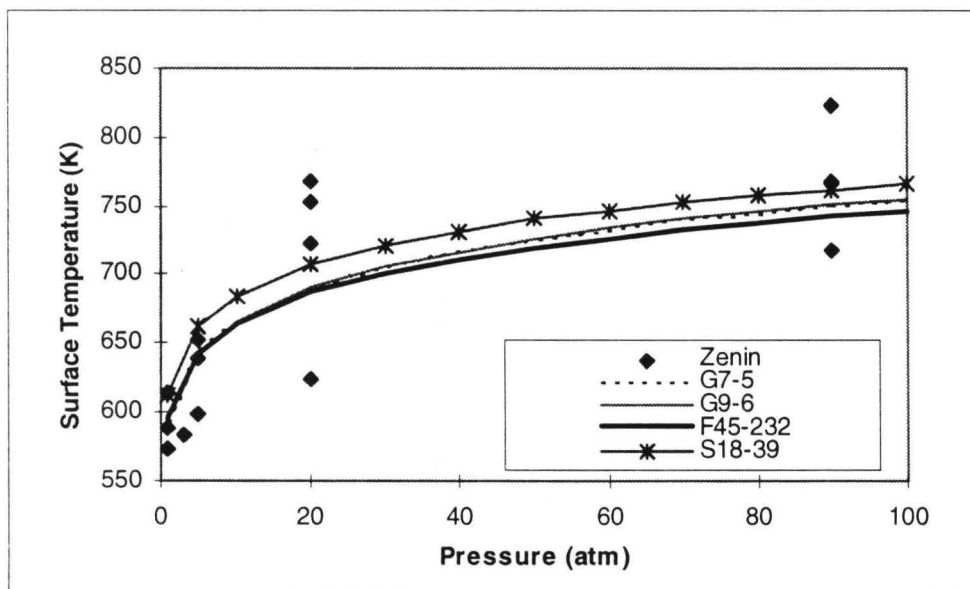


Figure 52: RDX Calculated Surface Temperature using Reduced Mechanisms⁷¹

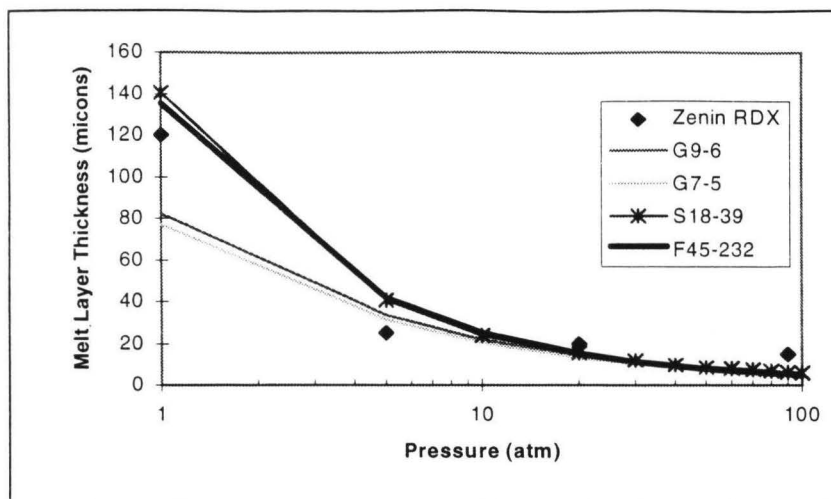


Figure 53: RDX Calculated Melt Layer Thickness using Reduced Mechanism⁷¹

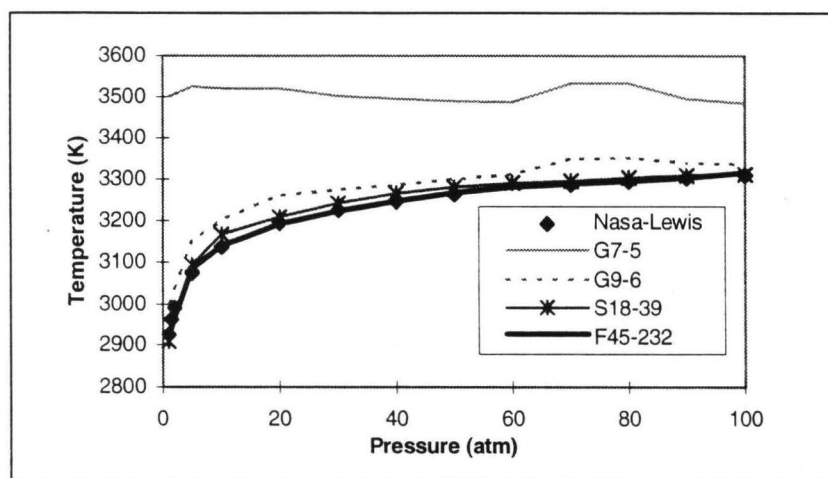


Figure 54: Calculated Adiabatic Flame Temperature using Reduced Mechanisms¹¹⁴

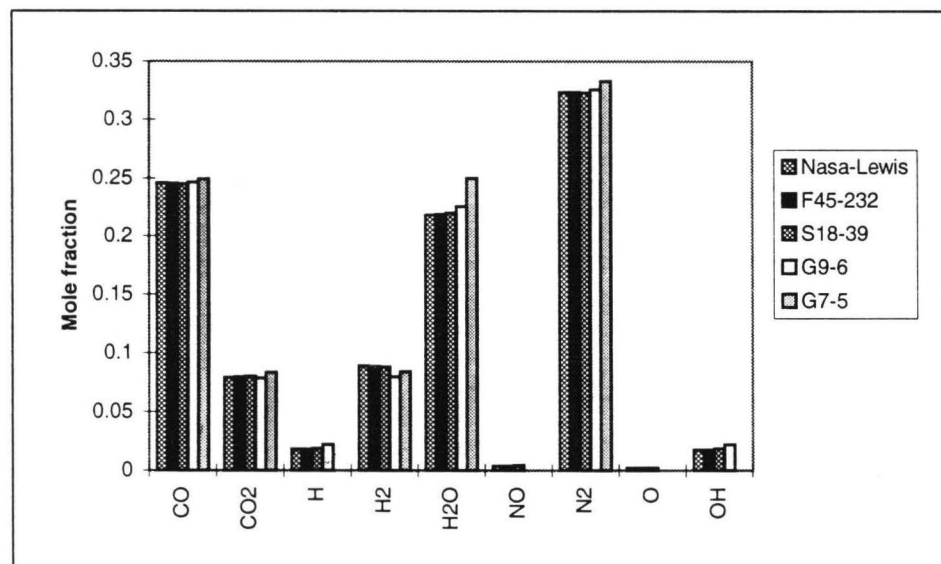


Figure 55: RDX Adiabatic Flame Species Concentrations at 20 atm.

Figure 56 shows the calculated temperature profiles for the full, skeletal and one of the global mechanisms. The heat feedback from the gaseous flame is higher for G9-6 but the condensed phase mechanism is different, requiring a different flux to achieve the balance. The more global the mechanism, the less accurate the predictions.

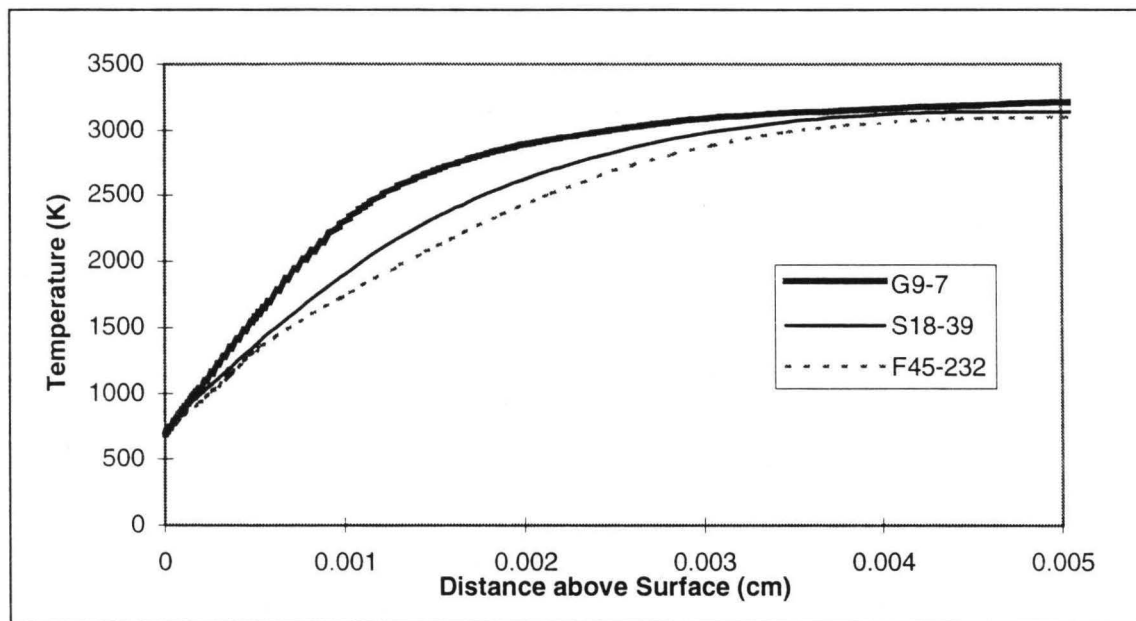


Figure 56: Calculated Temperature Profiles using Reduced Mechanisms at 20 atm.

Concentration profiles of some of the major species as calculated using the F45-232 and S18-39 mechanisms at 20 atmospheres are compared in Figure 57, Figure 58 and Figure 59. In Figure 57, the concentration profiles for NO, H₂O, CO show reasonable agreement. The concentration profile for RDX_{vapor} is different because the reactions involving RDXR, RDXRO, and H₂CNNO₂ were replaced by the single reaction in Table 19. Figure 59 shows significant differences in the profiles of N₂O, NO₂ and CH₂O. Again S18-39 does not include CH₂O. S18-39 does not produce the initial concentration of N₂O as calculated by the F45-232 because of the exclusion of the N₂O production in the condensed phase and the exclusion of the reactions of H₂CNNO₂ going to CH₂O and N₂O.

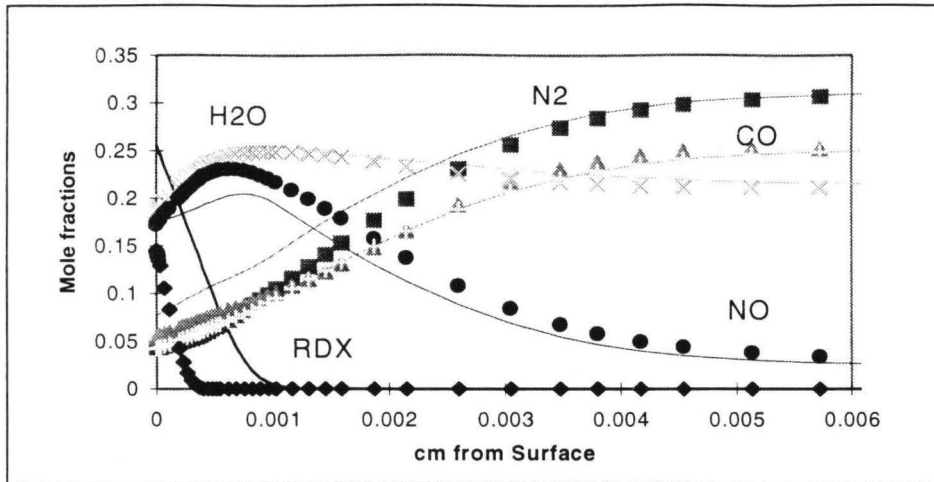


Figure 57: H₂, N₂, CO, RDX Concentration Profiles (Symbols=F45-232, Line=S18-39)

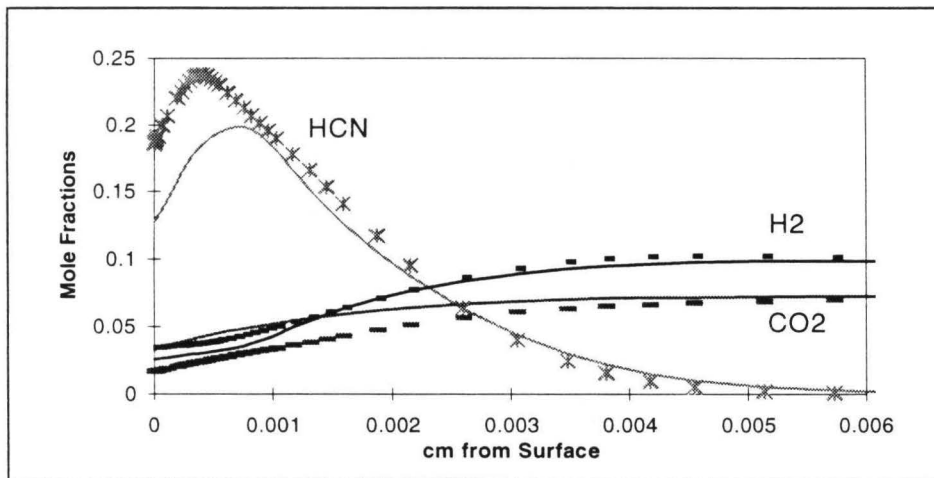


Figure 58: HCN, H₂, CO₂ Concentration Profiles (Symbol=F45-232, Line=S18-39)

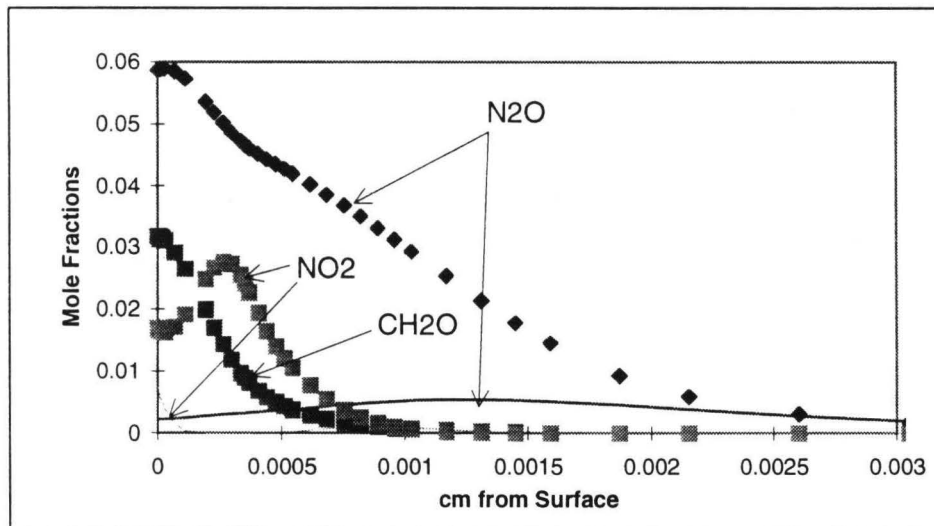


Figure 59: N₂O, NO₂ and CH₂O Concentration Profiles (Symbols=F45-232, Line=S19-39)

CPU Time Savings

One of the main purposes of this study was to find a reduced mechanism that would offer significant savings in CPU time and reasonably reproduce most of the results of the full mechanism. For the sake of comparison in CPU time, a standard test was performed using a number of mechanisms. In PREMIX,⁴⁵ the CPU time can be divided in three categories: function calls, Jacobian generation, and solving. The standard test for each mechanism is the sum of the CPU time for 16 function calls, one Jacobian generation, and 15 solutions normalized for 100 nodes. The results are shown in Figure 60. A power-law fit of the time with respect to the number of species gives an exponent of 2.1. By cutting the number of species in half, CPU time is reduced by more than a factor of 4. The increase in speed relative to the F45-232 mechanism is shown in Figure 61. When using a skeletal or global mechanism one must consider the tradeoffs. S18-39 is 7.5 times faster than the full mechanism, but ignores the CH₂O path. G7-5 is 44 times faster but does not provide much information about the species profiles.

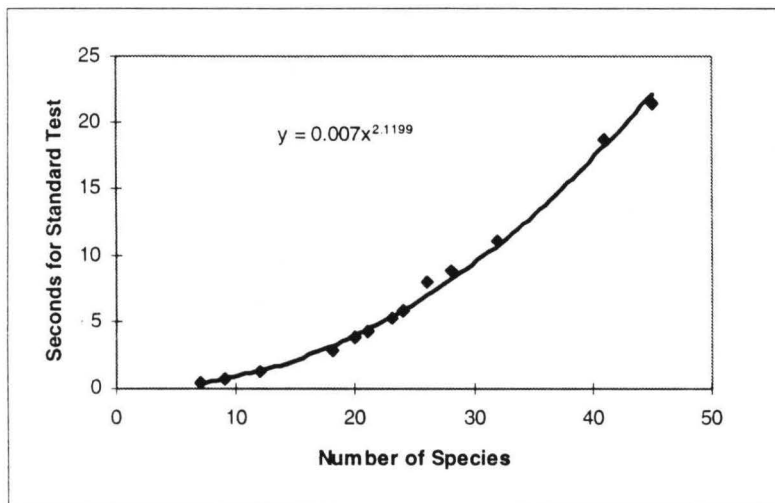


Figure 60: CPU Time for Standard Test

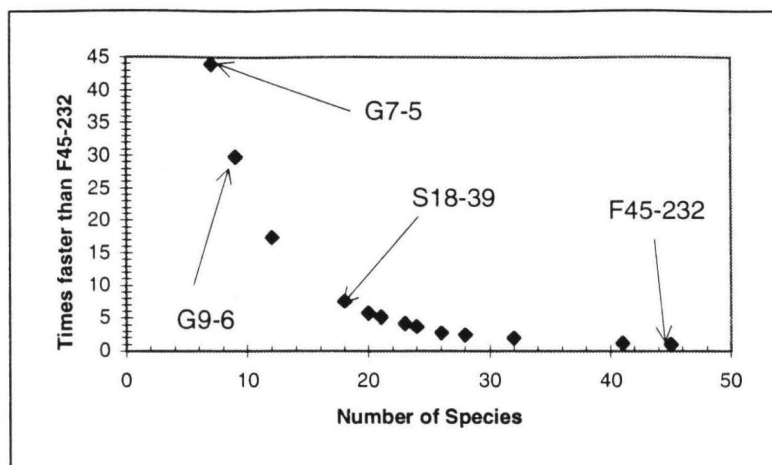


Figure 61: Increase in Speed by Dropping Species.

Conclusions

The Melius-Yetter RDX gas-phase mechanism⁵⁰ has evolved over several years. Most of the reactions that are in common with hydrocarbon combustion have been studied extensively and are well known. For species unique to the RDX flame, reactions have been postulated and rate constants have been estimated. In the development of the mechanism, some of these reactions and rate constants have been adjusted (optimized) so that the full mechanism would match the experimental data. As shown in the previous chapter, there is very reasonable agreement for most of the available data. There is a discrepancy between model calculations and experimental data for the concentration profile of NO. Rate constants for several reactions with a high degree of uncertainty were adjusted to produce better agreement between the model and experimental data for the NO concentration profile.

Using the integral reaction flow analysis method, the Melius-Yetter RDX mechanism (45 species and 232 reactions)⁵⁰ was reduced to 18 species and 39 reactions (S18-39). For typical PREMIX⁴⁵ calculations, the skeletal mechanism is about 7.5 time faster than the full mechanism. Using optimization of the kinetic parameters, two global mechanisms (9 species, 6 reactions, and 7 species, 5 reactions) were developed (G9-6, G7-5) which are about 29.7 and 44.5 times faster, respectively, than the full mechanism. Often reduced mechanisms have a narrow range of applicability. However, the skeletal and global mechanisms presented here reasonably reproduce the burning rate, surface temperature, final flame temperatures, and final product concentrations from 1 to 100 atmospheres. The errors introduced by using

these reduced mechanisms are tabulated in Table 21 for 20 and 70 atm. (Species errors are not shown for 70 atm because they are similar to those at 20 atm.) For several of the major species, the skeletal mechanism reasonably reproduces the concentration profiles calculated by the full mechanism. It is hoped that these mechanisms not only indicate the dominant reaction paths for RDX but will also find use in models which require reductions in CPU time.

Table 21: Comparison of Calculations using Full, Skeletal and Global Mechanisms at 20 and 70 atm.

Pressure	Mechanism	F45-232	S18-39	G9-6	G7-5	
	Times Faster than F45-232	1	7.5	29.7	44.5	
20 atm	Calculation	Value	Percent Deviation from F45-232			
	Burning Rate (cm/sec)	0.4061	10.7%	6.7%	3.3%	
	Surface Temperature (K)	687	2.9%	0.5%	0.3%	
	Melt Thickness (microns)	11	40.5%	25.6%	18.0%	
	Flame Temperature (K)	3173	1.1%	2.8%	11.0%	
	Adiabatic Flame Species	NASA Lewis Mole Fraction	Percent Deviation from NASA Lewis Value			
	N2	0.323	0.0%	-0.1%	0.7%	3.0%
	CO	0.246	-0.2%	-0.5%	0.2%	1.3%
	H2O	0.218	0.2%	0.7%	3.1%	14.4%
	H2	0.089	-0.3%	-1.1%	-10.4%	-5.2%
	CO2	0.079	0.4%	1.1%	-0.4%	5.4%
	H	0.018	-0.4%	3.6%	20.0%	-100.0%
	OH	0.018	-0.2%	6.4%	24.3%	-100.0%
	NO	0.004	0.7%	12.0%	-100.0%	-100.0%
	O	0.002	-0.7%	10.8%	-100.0%	-100.0%
	O2	0.002	0.1%	-100.0%	-100.0%	-100.0%
70 atm	Calculation	Value	Percent Deviation from F45-232			
	Burning Rate (cm/sec)	1.1944	-7.7%	0.7%	-1.4%	
	Surface Temperature (K)	733	2.7%	1.0%	1.0%	
	Flame Temperature (K)	3269	0.8%	2.5%	8.0%	
	Melt Thickness (microns)	4.4	65.0%	38.3%	29.3%	

CHAPTER 8: SENSITIVITY ANALYSIS OF RDX/HMX MODEL

In analyzing experimental data, researchers want to know not only the numerical value of their measurement but what factors influence that value. For example, an experiment can be designed to measure the effect of pressure on burning rate. Some factors are beyond the control of an experiment (e.g., the vapor pressure of RDX) and experimentally determining their influence on measured quantities can be impossible. In numerical models, one may calculate the influence of a model input on a model output by simply perturbing the input by a small amount and measuring the effect on the calculated output. In numerical models, unlike in an experiment, it is easy to change the vapor pressure and calculate the resulting change in burning rate. However, this calculated effect is accurate in terms of the model but may not correspond to reality. There is no guarantee that using the model for sensitivity analysis or making calculations for conditions where there are no experimental data will correspond to actual physical processes. The amount of confidence that may be placed on such calculations depends upon the underlying equations of the model and how well the model correlates with the available experimental data.

Sensitivity analysis can also be useful in identifying possible weaknesses in the model inputs. For example, if the model under-predicts the melt-layer thickness and sensitivity analysis indicates that thermal conductivity is a controlling factor, the literature could be searched, or experiments could be suggested to verify the value of thermal conductivity.

In order to measure the influence of a particular input (A) on an output (B), derivatives are calculated. To make comparisons between the effects of several model inputs, normalized sensitivity coefficients are used. They are defined as:

$$s = \frac{A}{B} \frac{\partial B}{\partial A} \quad (45)$$

and can be interpreted as: 'a 1% increase in *A* results in *s*% change in *B*.' (The value of *s* can be either positive or negative.) In this section, the sensitivity analysis of RDX at 10 atm ($T_{\text{init}}=298$ K) is presented. Because of the similarity between RDX and HMX, and similarity in model sensitivities, the corresponding analysis for HMX will not be presented. The analysis presented here is used in the next chapter in identifying the reasons for the similarities and differences in the combustion of RDX and HMX.

Factors Affecting the Burning Rate

The normalized sensitivity coefficients of factors affecting the mass burning rate are shown in Figure 62. The initial temperature, pressure and heat of formation define the enthalpy of the system and have significant effects. As enthalpy increases (by either T_{init} , pressure, or ΔH_f) the mass burning rate increases. The normalized sensitivity coefficient of burning rate with respect to pressure is 0.82, which is approximately the pressure exponent in correlating the burning rate data with $r_b=aP^n$. The vapor pressure correlation has relatively little effect on the burning rate. In the original model developed by Melius,⁴⁹ the burning rate was determined by an evaporation expression. In the model presented here, although 91.5% of the RDX is calculated to evaporate at 10 atm, the burning rate is most sensitive to factors that influence the energy balance at the surface. These factors include the heat feedback from the gas region and the two liquid decomposition reactions (Table 11, page 51).^{††††} Both reactions positively influence the burning rate, but the calculated burning rate is most sensitive to the exothermic reaction, $\text{RDX(C)} \rightarrow 3\text{CH}_2\text{O} + 3\text{N}_2\text{O}$.

To identify which gas-phase reactions are affecting the calculated burning rate, sensitivity coefficients were calculated by perturbing the \log_{10} of the pre-exponential factor of each gas phase reaction by 10 percent. The reactions having the greatest sensitivity coefficients at 10 atm are shown in Figure 63. As is discussed in the next chapter, reaction 223 is removed from the HMX mechanism to force better agreement between experimental and calculated burning rate data.

^{††††} In Figure 62 and the following figures of sensitivity coefficients, the analysis is calculated with respect to \log_{10} of the pre-exponential rate constants. By doing this, the relative uncertainty of the rate constants more closely correlates with the uncertainty of the other parameters ($c_{p,\text{solid}}$, ΔH_f , etc.)

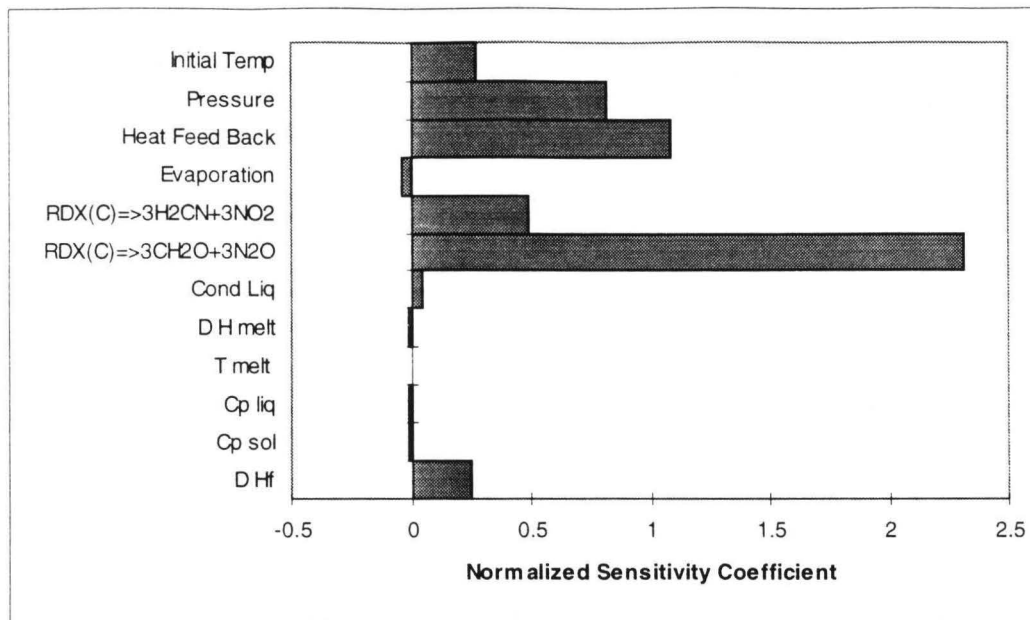


Figure 62: RDX Burning Rate Sensitivity at 10 atm, T_{init}=298.
 (Sensitivity coefficients for reactions were calculated with respect to log₁₀ of the reaction rate pre-factor.)

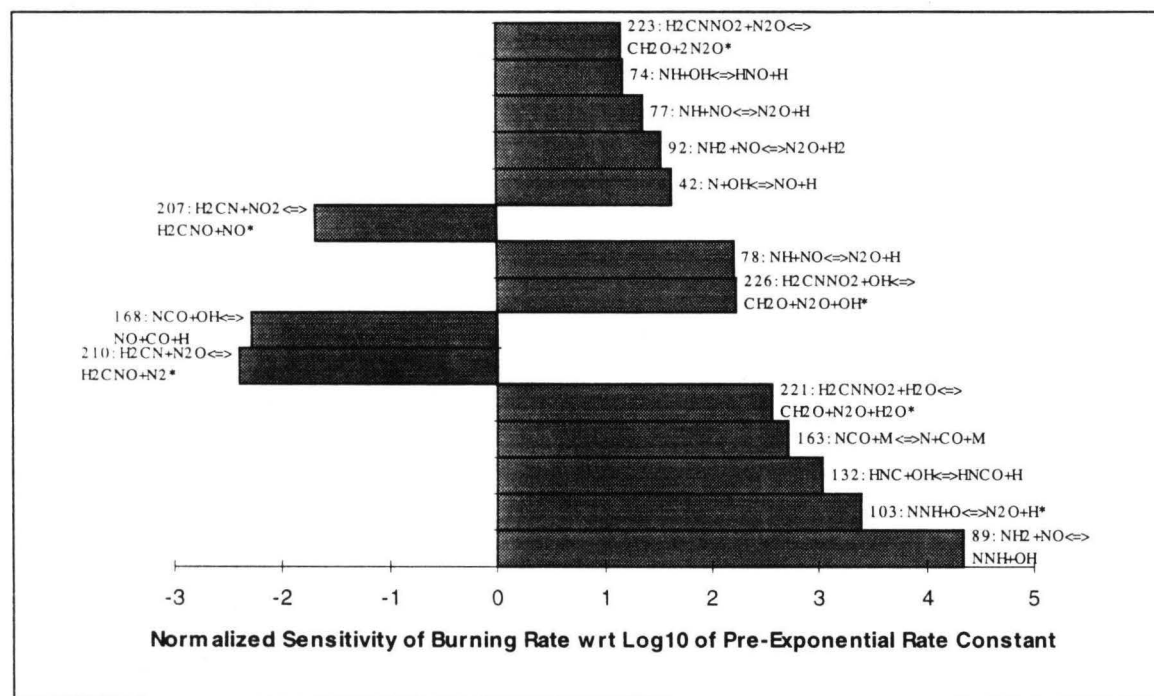


Figure 63: Top Reactions Influencing Burning Rate of RDX at 10 atm.††††

†††† The rate constants of reactions marked with an asterisk (*) are very uncertain.

Factors Affecting Temperature Sensitivity (σ_p)

In Chapter 6 (page 53), the burning rate at initial temperatures of 223 K, 298 K, and 373 K was presented. This change in burning rate with respect to initial temperature is referred to as *temperature sensitivity* (σ_p). In the stability analysis of propellants, temperature sensitivity is a very important parameter and is defined as:

$$\sigma_p = \left. \frac{\partial \ln(r_b)}{\partial T_{init}} \right|_p \quad (46)$$

The sensitivity analysis of σ_p involves taking derivatives of a derivative (i.e. substitute Eq.46 for B in eq. 45). The magnitudes of the sensitivity coefficients shown in Figure 64 are somewhat uncertain because of numerical noise in the model. Of the factors shown in Figure 64, only the solid heat capacity appears to have a significant effect on σ_p . The only place where the initial temperature is used in the model is in eq. 39 (page 38) where it serves as a boundary for the integration of the solid heat capacity.

This model assumes that the liquid- and gas-phase mechanisms do not change with initial temperature. As seen in Figure 62, the heat flux from the gas flame and the condensed-phase reactions strongly influence the burning rate. If these factors do change with initial temperature, they would affect the temperature sensitivity. Temperature sensitivity is discussed further in the Appendix.

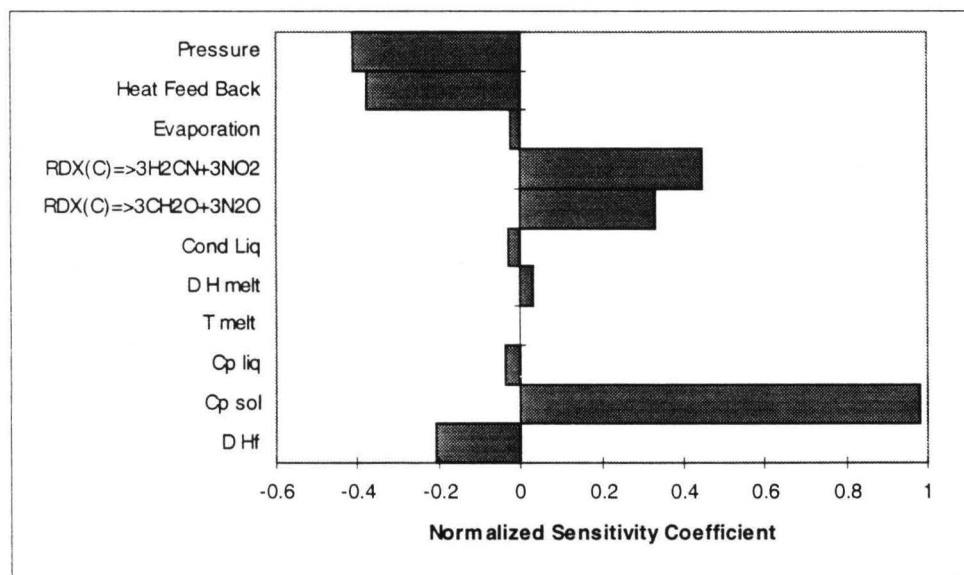


Figure 64: RDX σ_p Sensitivity at 10 atm.

(Sensitivity coefficients for reactions were calculated with respect to \log_{10} of the reaction rate pre-factor)

Factors Affecting the Final Flame Temperature

For a constant enthalpy system, the final flame temperature (or adiabatic flame temperature) should only be a function of the enthalpy of the material entering the system and the pressure of the system. As seen in Figure 65, the final flame temperature is most sensitive to these parameters. The other parameters ($c_{p, \text{solid}}$, $c_{p, \text{liquid}}$, etc.) do not have a significant effect on the final flame temperature. The non-zero sensitivity coefficients for these parameters result from numerical noise in the model. The flame temperature is dependent upon certain gas-phase reactions, namely those which establish the equilibrium between final product concentrations, and those which lead to the final products. (See Figure 66.)

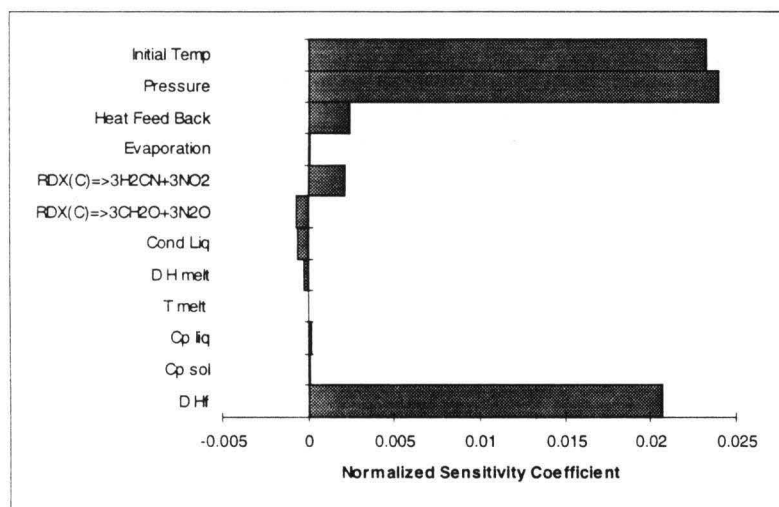


Figure 65: RDX Final Flame Temperature Sensitivity at 10 atm.
(Sensitivity coefficients for reactions were calculated with respect to \log_{10} of the reaction rate pre-factor)

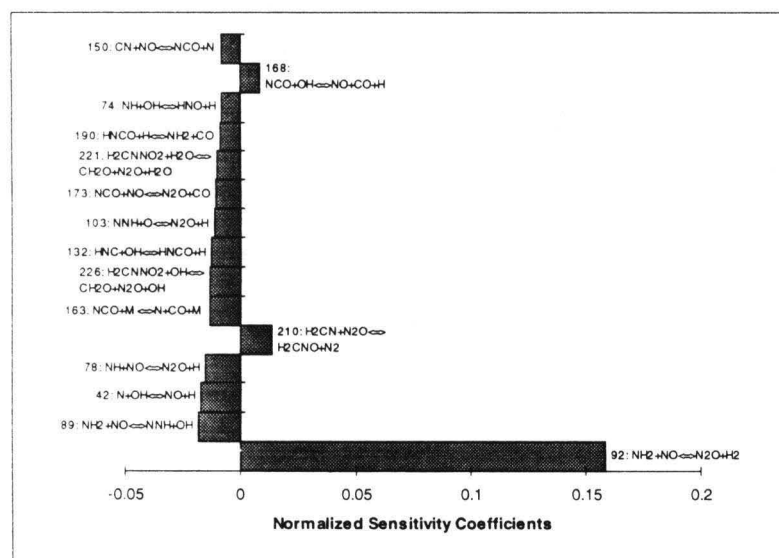


Figure 66: Top Reactions Influencing Final Flame Temperature of RDX at 10 atm.

Factors Affecting the Surface Temperature

The factors affecting the calculated surface temperature are shown in Figure 67. The two liquid decomposition reactions and the vapor pressure correlation (labeled as 'Evaporation' in Figure 67) are the dominating factors in determining the surface temperature once system pressure has been fixed. The surface temperature is relatively insensitive to the other physical properties of RDX. The gas phase reactions have relatively little influence on the surface temperature.

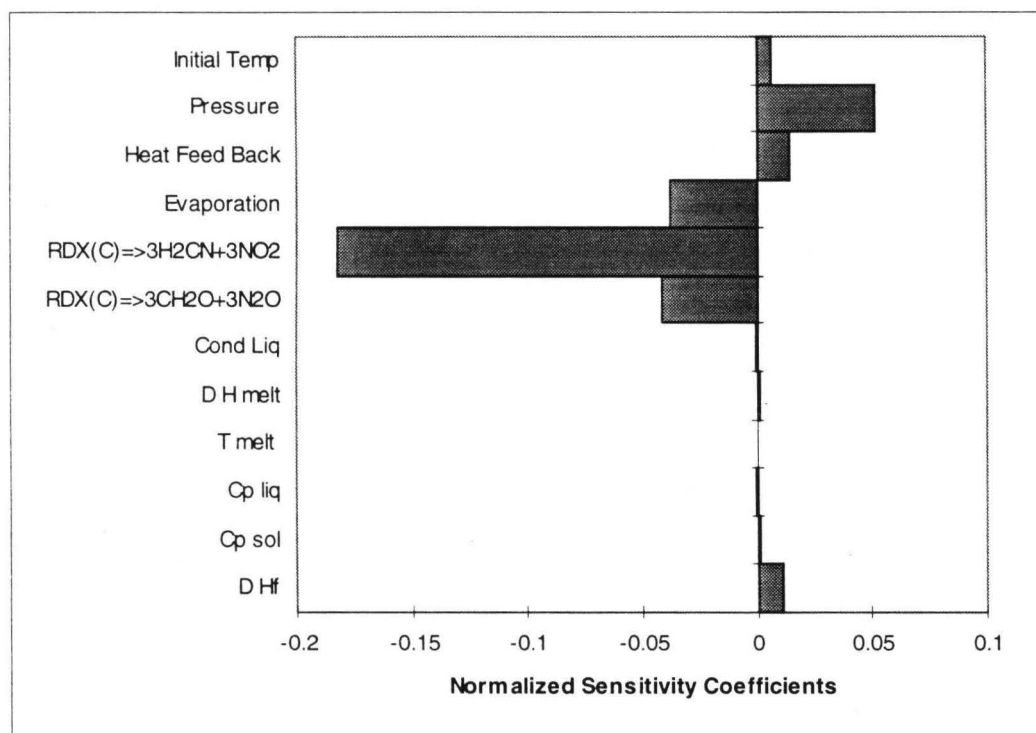


Figure 67: RDX Surface Temperature Sensitivity at 10 atm.

(Sensitivity coefficients for reactions were calculated with respect to \log_{10} of the reaction rate pre-factor.)

Factors Affecting the Melt-Layer Thickness

The melt-layer thickness is largely a function of the melt temperature. (See Figure 68.) The melt-layer thickness is the distance from the solid-liquid interface (defined at T_{melt}) to the liquid-gas interface. The other boundary of the melt layer is largely controlled by the liquid decomposition reactions (Figure 67). The liquid thermal conductivity also has a strong influence on the melt-layer thickness. Originally in the RDX model, Shoemaker's thermal conductivity⁹⁸ for the solid phase was used for the thermal conductivity of the liquid. With Shoemaker's value the model calculated a very thin melt layer compared to the Zenin's experimental data⁷¹ (See Figure 24, page 57). A value of 0.0008 cal/cm-K-sec (~twice

Shoemaker's value) was used in the model to obtain reasonable predictions of melt layer thickness. Using the analysis on page 49, a value for the solid thermal conductivity of 0.0006 cal/cm-K-sec can be calculated from recent thermal-diffusivity data from Hanson-Parr.⁸⁷ This value supports the conclusion based on model calculations that Shoemaker's thermal conductivity values are too low.

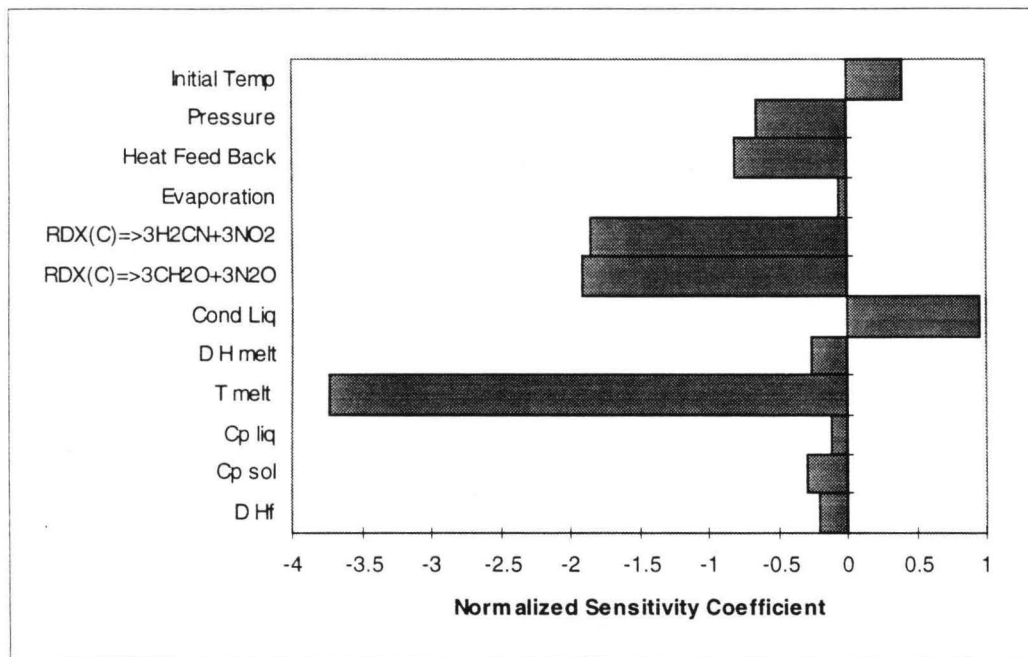


Figure 68: RDX Melt-Layer Thickness Sensitivity at 10 atm.
 (Sensitivity coefficients for reactions were calculated with respect to \log_{10} of the reaction rate pre-factor.)

Summary

Sensitivity calculations can be made for numerous model predictions. In the previous chapter, sensitivity analysis was used to identify which reactions affect the concentration of NO across the length of the flame. In this chapter, sensitivity calculations were made with respect to burning rate, temperature sensitivity, flame temperature, surface temperature, and melt-layer thickness. Burning rate is largely determined by the liquid-phase decomposition reactions and heat feedback from the gas-phase flame. Temperature sensitivity (σ_p) is influenced by the solid heat capacity. The surface temperature is strongly controlled by the vapor pressure correlation. At low pressures, the melt-layer thickness is influenced by the melting temperature, but at higher pressures the heat feedback from the gas-phase flame dominates this prediction. These results are used in the next chapter to explain observed similarities and differences in the combustion characteristics of RDX and HMX.

CHAPTER 9: THE HMX MODEL WITH COMPARISONS TO THE RDX MODEL

Introduction

Because of the similarities between RDX and HMX, much of the work in developing and analyzing the RDX model could be easily extrapolated to the HMX model. In this chapter, the alterations in the model inputs that were necessary to model HMX are described, but the main theme of this chapter is the discussion of the similarities and differences in the combustion characteristics of HMX and RDX. Many of the explanations are based on the sensitivity analysis presented in the previous chapter.

Observed Differences in the Combustion of HMX and RDX

As observed by Hanson-Parr and Parr,⁶⁹ HMX has a much taller flame standoff distance (~3-4 mm) than RDX (0.5 mm) at atmospheric pressure under self-deflagration conditions. They note that the peak formaldehyde mole fraction for HMX is about 8% compared to 1% for RDX. The HMX flame is also not as stable as the RDX flame at these low pressures. This is substantiated by Zarko,¹¹⁵ who observed an oscillating combustion rate for HMX at 1 atm. The magnitude of these oscillations increased with initial temperature. Under laser-assisted combustion conditions, Hanson-Parr and Parr also observed that there is a spray of fuel droplets being ejected from the surface of both RDX and HMX. Without a laser flux, the number density of fuel droplets is smaller (not quantified) for HMX and not detectable for RDX. They also note that the fuel spray interferes with some of their measurements. From these observations, it appears that HMX decomposes via slightly different paths than RDX, at least at low pressures (below 10 atm). At higher pressures there are not sufficient data to support this observation.

Properties of RDX and HMX

Boggs,⁹ Ben-Reuven,¹¹⁶ and Fifer⁸⁰ have each done extensive literature reviews on the properties, mechanisms and combustion characteristics of RDX and HMX. The thermophysical properties of RDX

and HMX used in the model are listed in Table 22. In several respects these monopropellants are very similar. Not only are their elemental compositions identical but their heats of formation on a mass basis are very comparable. For these two reasons their adiabatic flame temperatures and final product concentrations (constant enthalpy and pressure calculation) are nearly identical. There are, however, a few significant differences. $\text{HMX}_{\text{solid}}$ can exist in four phases (β , α , and δ ; γ is unstable) whereas no solid-solid phase transitions have been observed in RDX. RDX melts around 478 K, and HMX melts anywhere between 520-554 K depending upon the solid phase. There is some disagreement as to the melting temperature of HMX because of rapid decomposition beginning at or slightly below the melting point.⁹

The vapor pressure of RDX is approximately four orders of magnitude higher than that of HMX. (See Figure 69.) Most of the literature values are actually sublimation pressure data but, for lack of anything better, sublimation pressure correlations are used in the model for both RDX and HMX. (The choice of properties for RDX is discussed on page 48).

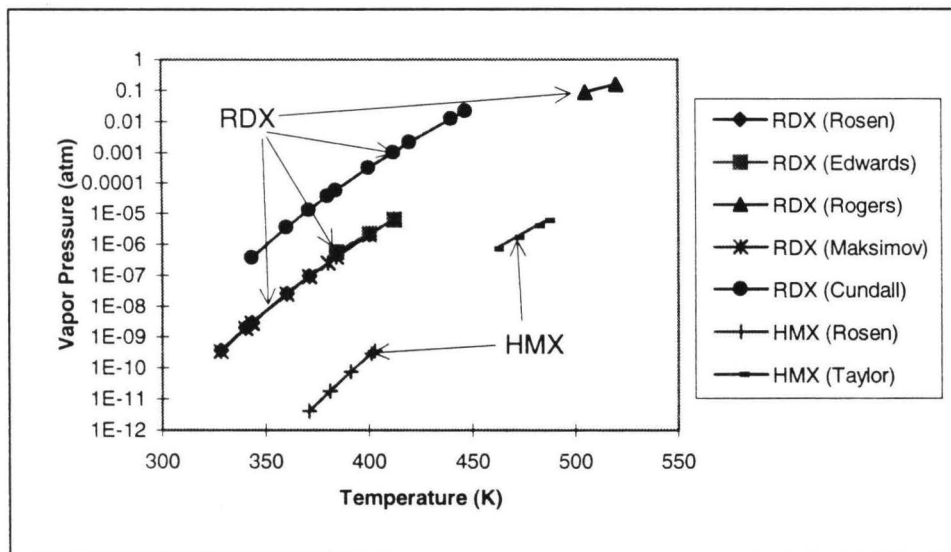


Figure 69: Sublimation Pressures of RDX and HMX^{93,94,95,96,100,120}

Table 22: Thermophysical Properties of RDX and HMX

Property	HMX				RDX	
Chemical Structure	$C_4H_8N_8O_8 (H_2CNNO_2)_4$				$C_3H_6N_6O_6 (H_2CNNO_2)_3$	
$\Delta H_{\text{formation}}$ (@ 298 K)	17.9 kcal/mole (60.4 cal/g) ¹				14.69 kcal/mole (66.1 cal/g) ¹	
Molecular Weight g/mole	296.2				222.1	
Phase	β	α	δ	Liquid	Solid	Liquid
Density (g/cc)	1.90 ¹¹⁷	1.87 ¹¹⁷	1.78 ¹¹⁷	1.9 §§§§	1.806 g/cc ⁹	1.806 g/cc ^{§§§§}
$\Delta H_{\text{transition}}$ kcal/mole	.45 ^{*****}	1.9 ⁹⁹	11.4 ++++		8.52 ⁹⁹	
Transition Temp. (K)	388.5 ¹¹⁸	439 ¹¹⁸	554.5 ¹¹⁸			
Melting Temperature (K)	520 ¹¹⁸	530 ¹¹⁸	554.5 ¹¹⁸		478 ⁹⁹	
β -HMX ¹¹⁹ and RDX _{solid} ⁹⁸ $c_p(T)$ cal/g-K	$c_p(T) = 5.5404 \times 10^{-2} + 6.2531 \times 10^{-4}T$				$c_p(T) = 3.8933 \times 10^{-2} + 7.0300 \times 10^{-4}T$	
α -HMX $c_p(T)$ cal/g-K ++++	$c_p(T) = 5.5404 \times 10^{-2} + 6.2531 \times 10^{-4}T$					
δ -HMX $c_p(T)$ cal/g-K ¹¹⁹	$c_p(T) = 1.2028 \times 10^{-1} + 4.8997 \times 10^{-4}T$					
Liquid $c_p(T)$ cal/g-K ^{§§§§}	$c_p(T) = 1.2028 \times 10^{-1} + 4.8997 \times 10^{-4}T$				$c_p(T) = 3.8933 \times 10^{-2} + 7.0300 \times 10^{-4}T$	
Thermal Cond. (solid) ⁹⁸	0.00036 cal/cm-K-sec				.0004 cal/cm-K-sec	
Thermal Cond. (solid) ^{§§§§}	0.0006 cal/cm-K-sec				0.0006 cal/cm-K-sec	
Thermal Conductivity (liq) ^{*****}	0.0008 cal/cm-K-sec				0.0008 cal/cm-K-sec	
Vapor Pressure ⁺⁺⁺⁺⁺	$10^{(14.73-8296/T(K))}$ torr ¹²⁰				$10^{(11.87-5850/T(K))}$ torr ¹⁰⁰	

§§§§ Assumed to be the same as in the solid phase.

***** Hall⁹⁹ reports a ΔH for the β - δ transition of 2.35 kcal/mole and 1.9 kcal/mole for the α - δ transition.

We estimated the ΔH for the β - α transition as 2.35-1.9=0.45 kcal/mole.

++++ Assumed to be the same as RDX on a mass basis.

++++ Assumed to be the same as β -HMX.

§§§§ Value back calculated using Parr's thermal diffusivity and Shoemaker's heat capacity. See Figure 14, page 49.

***** No thermal conductivity values were found in the literature for the liquid phase. These values were chosen so that the model would correlate well with Zenin's melt-layer thickness data.⁷¹

++++ These values are actually sublimation pressures.

Because no thermal conductivity data for the nitramines in the liquid phase could be found in the literature, we chose 0.0008 cal/cm-K-sec for both RDX and HMX to allow better correlation between the model and experimental data. (See page 49.)

Kinetic Mechanisms

Condensed-Phase Mechanism

Two competing paths as proposed by Brill⁴ (see Figure 16, page 51) are used in the model for the liquid decomposition mechanism of RDX and HMX. (See Table 23.) The liquid decomposition mechanisms for RDX and HMX are essentially the same.††††† Many of the similarities in the combustion of these two monopropellants can be attributed to the similarity of their decomposition paths.

Table 23: Condensed Phase Decomposition Mechanisms of RDX and HMX.⁴

Reaction	A(HMX) s ⁻¹	A(RDX) s ⁻¹	Activation Energy cal/mole
RDX(HMX)→3(4)CH ₂ O+3(4)N ₂ O	10 ^{13.0}	10 ^{12.9}	34,400
RDX(HMX)→3(4)H ₂ CN+3(4)NO ₂	10 ^{16.5}	10 ^{16.4}	44,100

Gas Mechanism

The gas phase mechanism used for RDX is the Melius-Yetter mechanism from August, 1995.⁵⁰ For HMX, a few stoichiometric coefficients were modified in the RDX mechanism to handle the additional H₂CNNO₂ group in HMX. No rate constants were changed. As is explained below, Reactions 222 and 223 were dropped from the HMX mechanism but were retained in the RDX mechanism. All differences in the two mechanisms are noted in Table 24.

The thermodynamic properties of HMX_{vapor} were estimated to be the same as those of RDX_{vapor} on a mass basis. The properties of species HMXR and HMXRO were estimated to have the same difference on a mole basis from HMX_{vapor} as the difference between RDX_{vapor} and RDXR and RDXRO respectively.§§§§§

††††† In the numerical model, the pre-exponential factors are multiplied by $\rho_{\text{RDX}}/W_{\text{T RDX}}$ to be compatible with the units used in the code.

§§§§§ RDXR is RDX minus a NO₂ group. RDXRO is an isomer of RDXR.

Table 24: Differences in the Gas-Phase Mechanisms of RDX and HMX.

Reactions Unique to RDX Mechanism:	A	β	E_a (cal/gmole)
222. $H_2C_2N_2O_2 + NO_2 = CH_2O + N_2O + NO_2$	1.00E+11	0.00	2000.0
223. $H_2C_2N_2O_2 + N_2O = CH_2O + N_2O + N_2O$	1.00E+11	0.00	2000.0
227. $RDX(+M) = RDXR + NO_2(+M)$	2.00E+16	0.00	45000.0
Low pressure limit:	0.15700E+18	0.00000E+00	0.28000E+05
228. $RDX + H = RDXR + HONO$	1.00E+13	0.00	5000.0
229. $RDX + OH = >2H_2C_2N_2O_2 + H_2COHNO_2$	1.00E+13	0.00	5000.0
230. $H_2COHNO_2 = >HCN + NO_2 + H_2O$	1.00E+16	0.00	0.0
231. $RDXR(+M) = >RDXRO(+M)$	1.00E+16	0.00	23000.0
Low pressure limit:	0.76900E+17	0.00000E+00	0.18000E+05
232. $RDXRO(+M) = >2H_2C_2N_2O_2 + H_2CN(+M)$	1.00E+16	0.00	23000.0
Low pressure limit:	0.76900E+17	0.00000E+00	0.18000E+05
Reactions Unique to HMX Mechanism:			
225. $HMX(+M) = HMXR + NO_2(+M)$	2.00E+16	0.00	45000.0
Low pressure limit:	0.15700E+18	0.00000E+00	0.28000E+05
226. $HMX + H = HMXR + HONO$	1.00E+13	0.00	5000.0
227. $HMX + OH = >3H_2C_2N_2O_2 + H_2COHNO_2$	1.00E+13	0.00	5000.0
228. $H_2COHNO_2 = >HCN + NO_2 + H_2O$	1.00E+16	0.00	0.0
229. $HMXR(+M) = >HMXRO(+M)$	1.00E+16	0.00	23000.0
Low pressure limit:	0.76900E+17	0.00000E+00	0.18000E+05
230. $HMXRO(+M) = >3H_2C_2N_2O_2 + H_2CN(+M)$	1.00E+16	0.00	23000.0
Low pressure limit:	0.76900E+17	0.00000E+00	0.18000E+05

Comparisons with Experimental Data

There is a larger variety of experimental data available for model comparison for RDX than for HMX. Where applicable, data for HMX and RDX along with model predictions for both monopropellants are shown in the same figure.

Burning Rate

Figure 70 is a plot of burning rate as a function of pressure (at $T_{init}=298K$) for both RDX and HMX as calculated by the model and measured from a variety of experimental sources.^{34,71,103,104} RDX and HMX appear to have almost identical burning rate curves. However, on close examination of the data below 100 atmospheres and for initial temperatures of 223 K and 373 K, some differences become apparent. (See Figure 71 and Figure 72.)

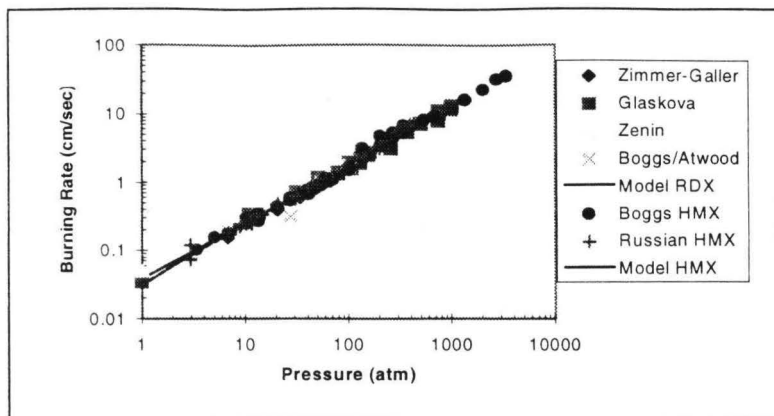


Figure 70: HMX and RDX Burning Rate Data ($T_{init}=298\text{ K}$).^{34,35,71,103,104}

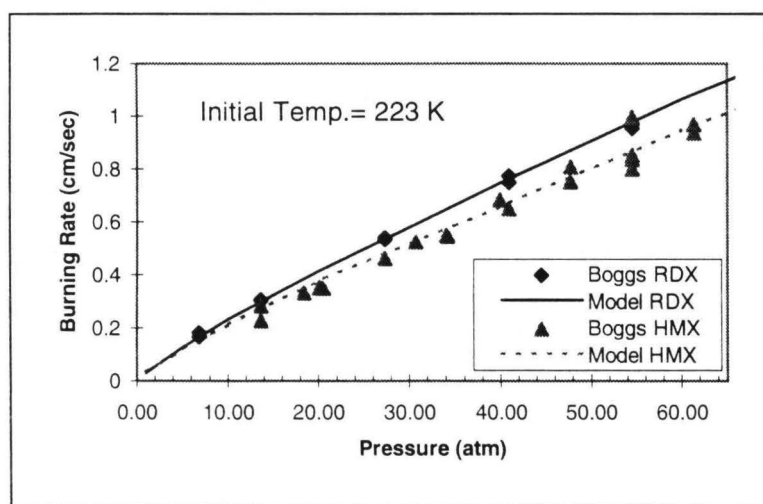


Figure 71: HMX and RDX Burning Rate Data ($T_{init}=223\text{ K}$).³⁴

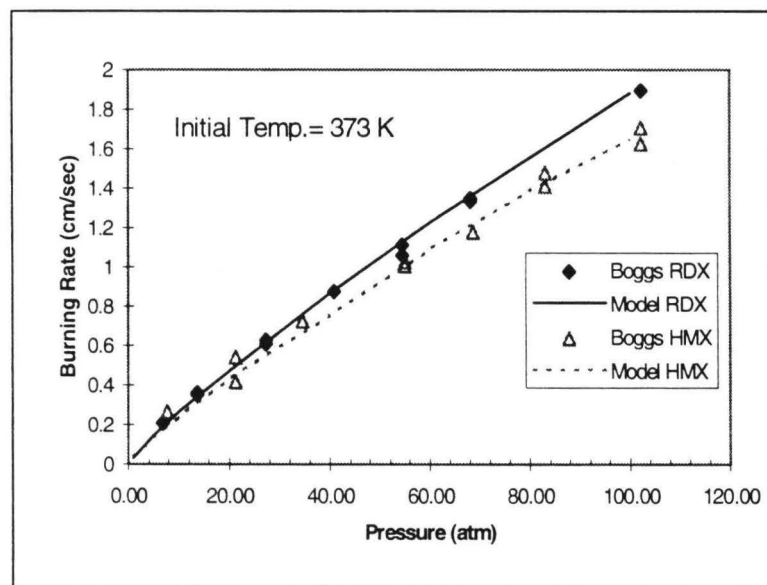


Figure 72: HMX and RDX Burning Rate Data ($T_{init}=373\text{ K}$).³⁴

As seen in both the experimental data and model calculations, RDX has a higher burning rate for this pressure range and for these initial temperatures. Initially, the HMX model predicted essentially the same burning rate curve as for RDX and did not indicate this observed difference. Sensitivity analysis for both HMX and RDX (See Figure 63, page 96) indicated that the burning rate at high pressures was somewhat sensitive to Reaction 223:



After removing Reactions 222 and 223 from the gas-phase mechanism of HMX, the calculated burning rate showed better agreement with the experimental data. It should be noted that in the RDX mechanism, these two reactions were preceded by the comment that the H_2CNNO_2 chemistry needs further study and that these reactions were added “to increase the early heat release reaction rate.” Sensitivity analysis for both RDX and HMX indicates that the burning rate is largely determined by the heat feedback from the gas region and is not a strong function of vapor pressure or melting temperature (Figure 62, page 96). The similarity in the burning rate curves (Figure 70) can be explained by the similarity in the reaction chemistry, and the small differences (Figure 71 and Figure 72) are likely due to differences in the initial vapor decomposition steps, but not necessarily the two steps that were removed from the HMX mechanism (Reactions 222 and 223).

Temperature Sensitivity

For HMX there are burning rate data for a variety of initial temperatures (173, 198, 223, 248, 273, 298, 373, 423 K). The data (symbols) and corresponding model predictions (lines) are shown in Figure 73. The agreement is reasonable for all initial temperatures over the pressure range except for the circled data.

As observed by Parr⁶⁹ and Zarko,¹¹⁵ HMX combustion is unstable near atmospheric pressure and this instability increases with initial temperature. It is possible that in this region ($P < 20$ atm, $T_{\text{init}} > 298\text{K}$), a phenomenon not considered in the model is occurring, such as changes in the decomposition paths in the condensed phases or liquid droplets spraying from the surface. Changes in reaction pathways with initial temperature could result from solid-phase transitions. One may force agreement between the model

and the experimental burning rate data by increasing the rate of the exothermic $\text{HMX}_{\text{liquid}}$ decomposition pathway ($\text{HMX} \rightarrow 3\text{CH}_2\text{O} + 3\text{N}_2\text{O}$) for only these conditions. However, this was not done. A discussion of transformation of the burning rate data presented in Figure 73 into σ_p is included in the Appendix.

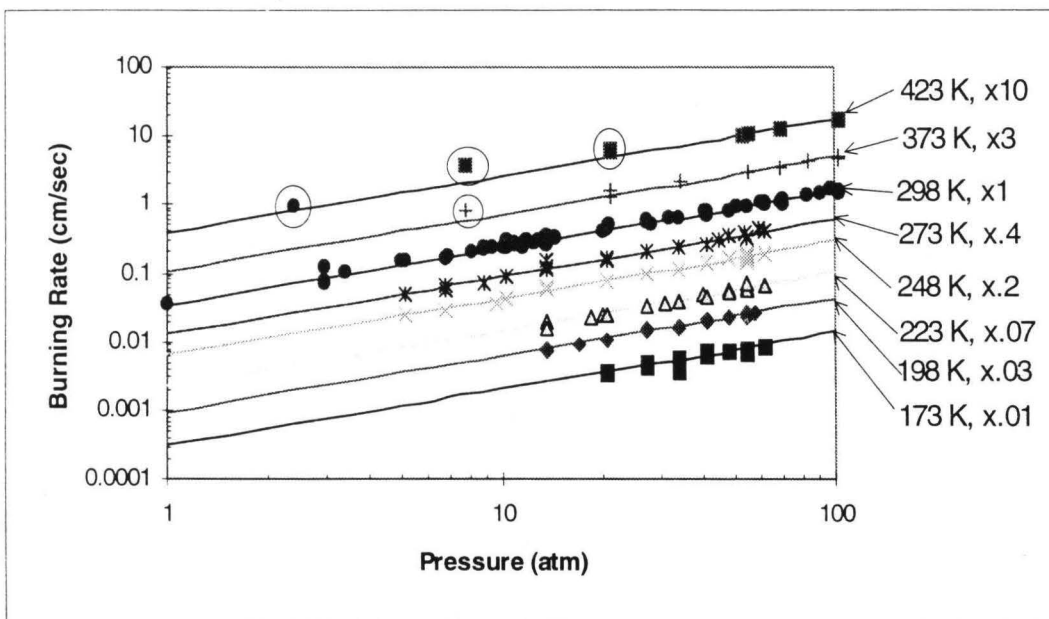


Figure 73: HMX Temperature Sensitivity (173 K to 423 K)³⁴

Adiabatic Flame Temperature

The adiabatic flame temperature and species concentrations, as calculated by the model for both HMX and RDX, are essentially identical and agree well with predictions made by the NASA-Lewis equilibrium code¹¹⁴ (constant enthalpy and pressure calculations). One would expect similar results for HMX and RDX given the similar heats of formation and chemical compositions.

Surface Temperature

Zenin⁷¹ recently reported measurements of surface temperature of RDX and HMX. These data, along with model calculations, are shown in Figure 74. Sensitivity analysis indicates that the surface temperature is strongly affected by the liquid decomposition reactions and the vapor pressure. (See Figure 67, page 99.) The liquid decomposition reactions are similar for these two monopropellants. However, RDX has a higher vapor pressure than HMX, evaporates more readily, and therefore has a lower surface

temperature. For both RDX and HMX, the model indicates that evaporation is the dominant path for converting the condensed phase to the gas phase. This agrees well with assumptions made in the development of other models.^{38,49,62} Figure 75 shows that the percent of the original nitramine that evaporates increases with pressure. This is contrary to Zenin's⁷¹ model based on his experimental data.

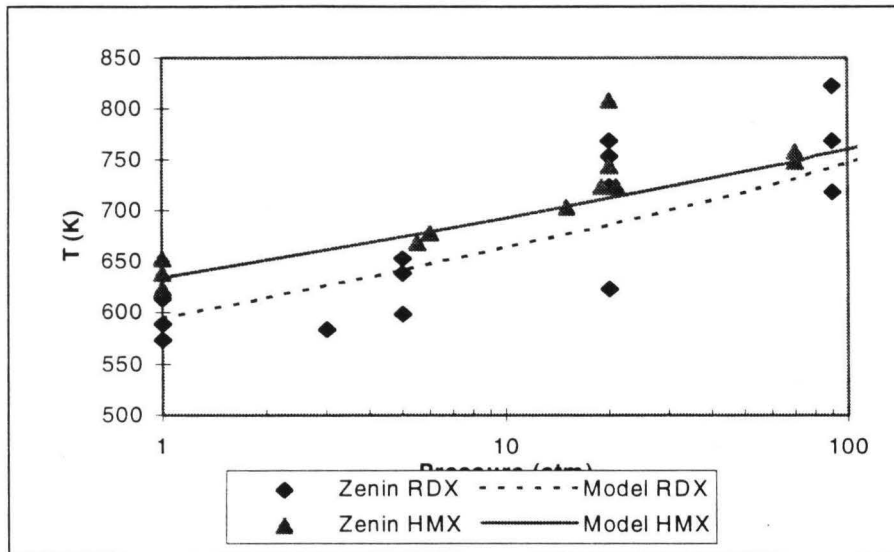


Figure 74: RDX and HMX Surface Temperature⁷¹

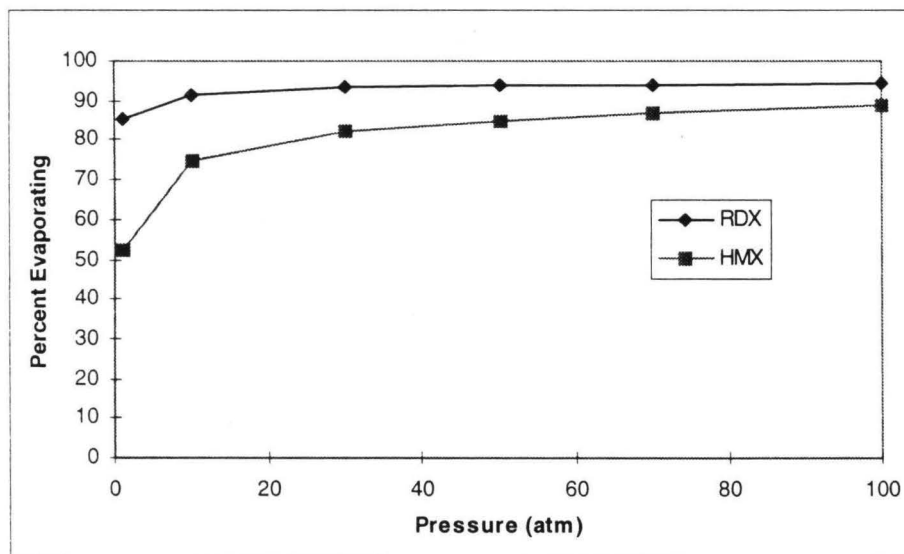


Figure 75: Calculated Percent of RDX and HMX Evaporating

Melt-Layer Thickness

Melt-layer thickness data are shown in Figure 76. Sensitivity analysis indicates that the melt-layer thickness is a function of the melting temperature, liquid thermal conductivity and heat feed back from the gas region. (See Figure 68, page 100) The melt layer of RDX is thicker than that of HMX at low pressures because RDX melts at a lower temperature. The only free input parameter***** that was adjusted in the modeling of these two nitramines was the thermal conductivity of the liquid. This parameter was used to scale the calculated melt-layer thickness to match Zenin's data.⁷¹ None of the other calculations were significantly affected by the magnitude of the liquid thermal conductivity.

As pressure increases, so does the heat feedback from the gas region. Above 10 atm, the effect of the melting temperature and liquid thermal conductivity on melt-layer thickness is not as significant as that of the heat feed back from the gas region. This can be seen in the converging of both the data and model calculations as pressure increases. Brewster⁶⁶ observed experimentally that the melt-layer thickness of RDX increases with added laser flux, but the model shows the opposite trend. This discrepancy may be attributed to in-depth absorption of the laser beam in the melt layer. The model assumes that all of the laser energy is absorbed at the surface.

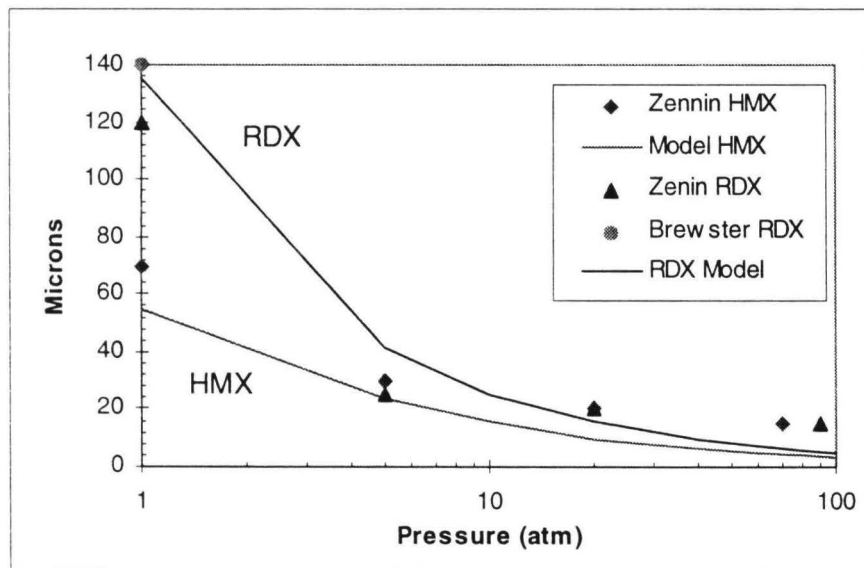


Figure 76: RDX and HMX Melt-Layer Thickness

***** No experimentally determined value for the liquid thermal conductivity was found in the literature. All other model inputs were taken from experimental data as shown in Table 22.

Experimental Data Unique to HMX

Because of the unstable nature of the combustion of HMX near atmospheric pressure, there have been considerably fewer experiments to study the flame structure reported for HMX compared to RDX. Hanson-Parr and Parr have made some measurements for the self-deflagration flame structure at one atmosphere but the data were difficult to reproduce and no temperature profile could be extracted from their data.⁶⁹ Therefore, they reported their measured species concentrations in molecules/cm³. The comparison of model calculations with the data of Hanson-Parr and Parr is shown in Figure 77. The comparison is very poor as the model predicts a much shorter flame. Hanson-Parr and Parr make the following comment about their data: “This quasi-unstable 3D fluid dynamic flame stabilization may lead to poor comparison with models which are 1D only, i.e. the flame liftoff height in the experiments is a sensitive function of the 3D nature caused by the sample size. 1D models may show a shorter flame or one that totally blows off.” Hanson-Parr and Parr also report the location of the CN peak for HMX from 1 to 12 atm.¹²¹ The results are shown in Figure 78, and again the model predicts a much shorter flame.

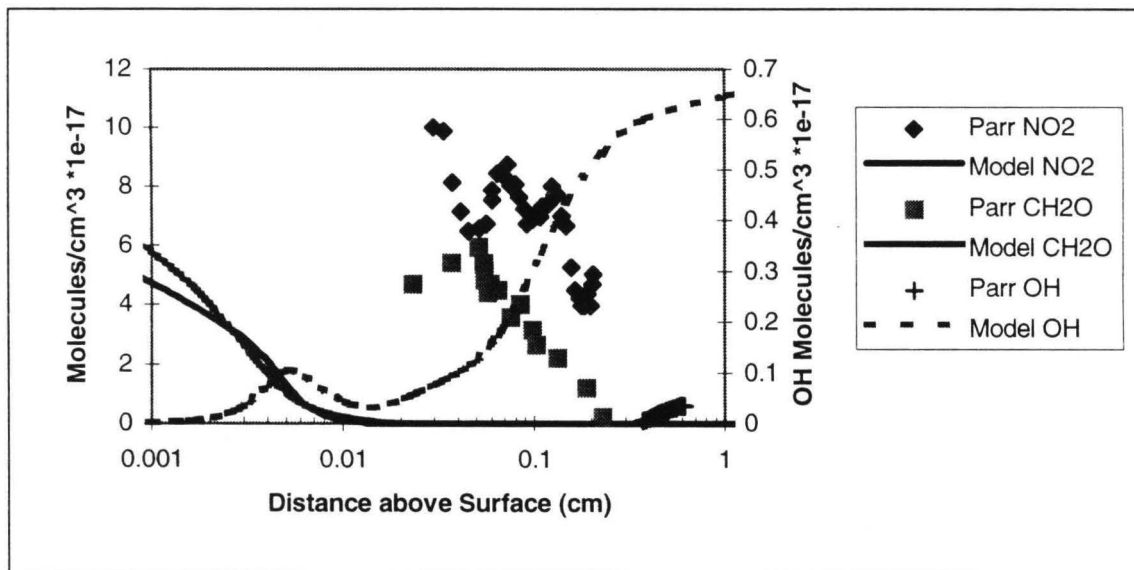


Figure 77: HMX Self-Deflagration Species Profiles at 1 atm (Parr).⁶⁹

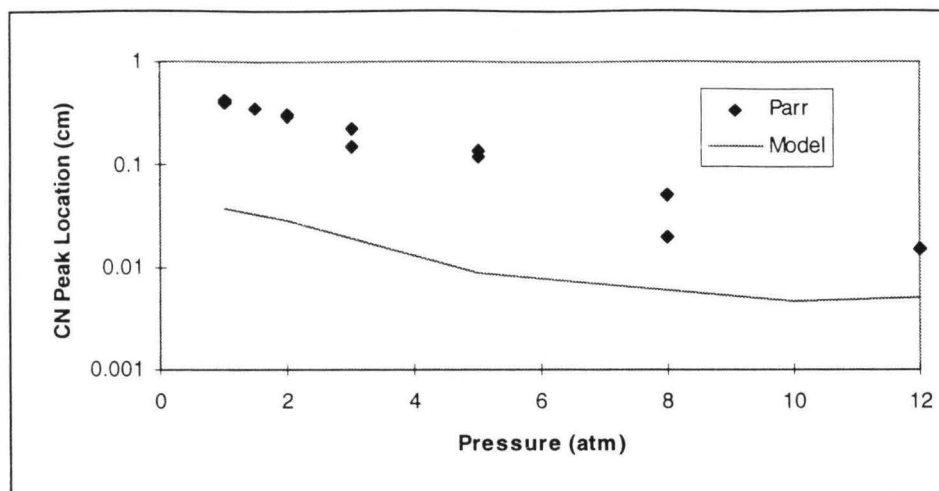


Figure 78: HMX CN Peak Location at 1 to 12 atm (Parr).¹²¹

All of the reactions occurring in the combustion of RDX and HMX should be identical except those describing the initial decomposition of RDX (liquid and vapor) and HMX (liquid and vapor). These differences can likely be attributed to the un-modeled phenomena of initial-temperature dependent decomposition mechanisms and the ejection of liquid droplets from the burning surface. At high pressures (greater than 20 atm, typical of rocket motor conditions) the flame thickness decreases and the influence of the different decomposition reactions is not as significant as at 1 atm.

Summary

In this chapter, the alterations to the RDX model necessary to model HMX are described. Where possible, calculations for RDX and HMX combustion are compared with experimental data. The observed similarities and differences in the combustion characteristics are explained using the results from the sensitivity analysis presented in the previous chapter. These conclusions are summarized in Table 25. Additionally, based on observations of Parr⁶⁹ and Zarko¹¹⁵ as well as model calculations, it appears that the initial decomposition steps of HMX in the liquid and vapor phases are likely to be pressure and initial-temperature dependent and differ from those of RDX. These differences can explain some of the discrepancies between the model and experimental data below 20 atm. Further experimental investigation into the combustion characteristics of HMX at low pressures are necessary to verify these hypotheses.

Table 25: Reasons for the Similarities and Differences in HMX and RDX Combustion

Combustion Characteristic	Strong Function of:	Factors of little influence	Explanation
Burning Rate	Liquid and gas reaction chemistry. $\uparrow q_{\text{gas}} \rightarrow r_b \uparrow$	Vapor pressure, T_{melt}	The similarity of the RDX and HMX reaction chemistry explains the similar burning rate curves. Minor differences appear to be related to the first few decomposition steps in the gas phase.
Temperature Sensitivity	Solid heat capacity. $\uparrow c_p \rightarrow \sigma_p \uparrow$ $\uparrow Q_s \rightarrow \sigma_p \uparrow$	Vapor pressure, T_{melt} , liquid decomposition mechanism, gas reactions.	The model predicts that RDX and HMX have essentially the same σ_p , yet experimental data could indicate the σ_p of HMX is higher at low pressure. This could be caused by a shift in the decomposition mechanism of HMX below 20 atm.
Surface Temperature	Vapor Pressure $\uparrow P_{\text{vap}} \rightarrow T_s \downarrow$		RDX has a higher vapor pressure therefore a lower surface temperature than HMX.
Adiabatic Flame Conditions	ΔH_f , P, T_{init}	Evaporation, reactions, c_p of solid and liquid.	RDX and HMX have similar ΔH_f and identical elemental ratio between C, N, O, and H.
Melt Layer Thickness (P<10 atm)	Melting Temp, Liquid thermal conductivity $\uparrow T_{\text{melt}} \rightarrow L_{\text{melt}} \downarrow$ $\uparrow \lambda_{\text{liq}} \rightarrow L_{\text{melt}} \uparrow$	Heat capacity.	The melting temperature of RDX (478 K) is lower than HMX (520-554 K). The RDX melt layer is thicker than that of HMX at pressures below 10 atm.
Melt Layer Thickness (P>10 atm)	Heat feed back from the gas phase flame. $\uparrow q_{\text{gas}} \rightarrow L_{\text{melt}} \downarrow$	Melting Temp, liquid thermal conductivity, etc.	Above 10 atmospheres, experimental data and model predictions show very little difference in the melt-layer thickness of RDX and HMX. This is due to the similarity in the heat feed back from the gas region.

CHAPTER 10: PRELIMINARY MODELING OF GAP

Introduction

Up to this point, this dissertation has focused on the modeling of two very similar monopropellants, RDX and HMX. To test the model's range of applicability, a very dissimilar energetic material, GAP, was chosen. GAP (glycidyl azide polymer) is an energetic material of interest in the rocket industry because of its high burning rate (~1 cm/sec at 40 atmospheres) and relatively low pressure exponent (~0.5). As seen in the chemical formula $(C_3H_5ON_3)_n$, GAP is very deficient in the oxygen needed for complete combustion.

Numerous researchers have worked on the development of HMX and RDX models since the early 1970's. These nitramines have received a lot of attention in recent years and the agreement between experimental data and model calculations is very reasonable.^{76,62} This is the first attempt at modeling the combustion of GAP using detailed chemistry. As such, the level of understanding and modeling of GAP is much more elementary than that of the nitramines. This chapter describes initial efforts at putting together the pieces of the GAP combustion puzzle. Not all the pieces fit together because of differences in experiments, experimental error, and interpretation of results. It is hoped that in attempting to develop a model of GAP, missing key information is identified to guide future experiments.

There are quite a few differences between GAP and the nitramines. RDX and HMX are crystalline, whereas GAP is a polymer. The calculated adiabatic flame temperatures at one atmosphere are about 2925 K for the nitramines and 1387 K for GAP.¹¹⁴ According to the modeling of RDX and HMX, evaporation appears to be the dominant means of converting the nitramines from condensed to gas phase, where most of the decomposition occurs. Evaporation is not likely to be significant for GAP and condensed-phase decomposition appears to dominate the combustion characteristics.

chromatograph for pressures ranging from 6.8 to 68 atmospheres. This temperature is about 300 degrees above the surface temperatures for self-deflagrating GAP reported by Kubota.¹²⁴ The investigators were able to measure quantitatively the concentrations of the species listed above, but their elemental balances are not closed. They can only account for 58% of the carbon, yet have too much oxygen (136%) and too much nitrogen (121%). Their results indicate that the decomposition product concentrations are fairly insensitive to pressure.

Brill and Chen¹³⁰ have used fast thermolysis/FTIR to study the decomposition of GAP at one atmosphere. This method involves using a very thin sample painted onto a metal tip. The tip is electrically heated, and the concentrations of the IR-active species are measured. Because of the inability to detect non-IR active species like N₂ and H₂, their reported species concentrations are not absolute but relative. In an earlier work, Brill and Oyumi¹³⁰ heated a thin sample of GAP spread between two KBr plates under low and high heating rates. Measurements were taken between 1 and 1000 psi. Like Flanagan, their results also show that concentrations of decomposition products are fairly insensitive to pressure.

Haas et al.,¹²⁹ studied GAP decomposition at extremely low pressures (10⁻² torr) under laser-assisted combustion conditions. Gaseous species (N₂, CO, C₂H₄, HCN, CH₄, and C₂H₂) were measured by gas chromatography and mass spectrometry. In addition to gaseous species, they also observed that approximately 37% of the original GAP was converted to a powder whose composition was approximately C₉H₁₃N₃O₂. They estimate error bounds on their reported species concentrations to be 25 to 30%.

The mole fractions reported from each of the four studies are shown in Figure 79. Because the concentrations reported by Brill et al. are relative, the data from each group are scaled by dividing by the reported mole fraction of CO. (See Figure 80.) Though the experimental conditions differ greatly from one group to another, some general observations can be made. There appears to be better agreement between the results of Haas and Flanagan than with those of Brill. Brill reports significant concentrations of NH₃ and CH₂O but the other groups do not. Likewise Brill reports higher concentrations of HCN but no C₂H₄.

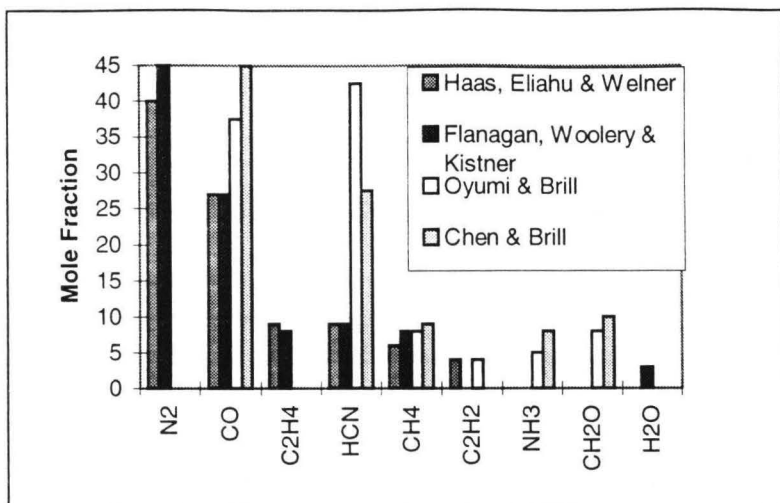


Figure 79: Reported Mole Fractions for GAP Decomposition

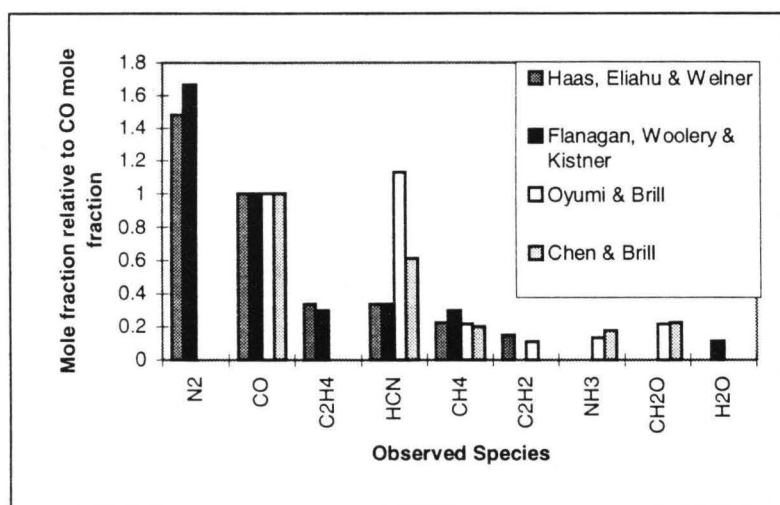


Figure 80: Comparison of Species from Decomposition Studies

Kubota makes the statement, “The results showed that 24% solidified carbon was formed on the burning surface.”¹²⁴ It is unclear how he reached this conclusion. Lengelle reports a carbon residue on the burning surface of GAP interfering with thermocouple measurements.¹²³ Likewise, Yuan¹²⁷ observed carbonaceous residues on the burning surface. The NASA-Lewis equilibrium program¹¹⁴ predicts approximately 29 mole percent solid carbon in the final products but Flanagan¹³² did not see solid carbon and suggested that the equilibrium program be run again, this time preventing the formation of solid carbon. It should be noted that Flanagan only accounted for 58% of the carbon in his elemental mass balances.¹²⁸ When suppressing solid carbon formation, the equilibrium code predicted concentrations of benzene and naphthalene (~2 mole percent for each) in the final flame (See Figure 81). Haas et al.¹²⁹

reference Mishra¹³³ et al., as observing benzene, pyrole and furan. Benzene and similar molecules are precursors to soot formation, but whether soot, solid carbon and/or aromatic molecules are formed at all during the combustion of GAP is not clear. This question needs to be answered because 24% C_{solid} or 2 mole percent benzene is very significant on a mass basis.

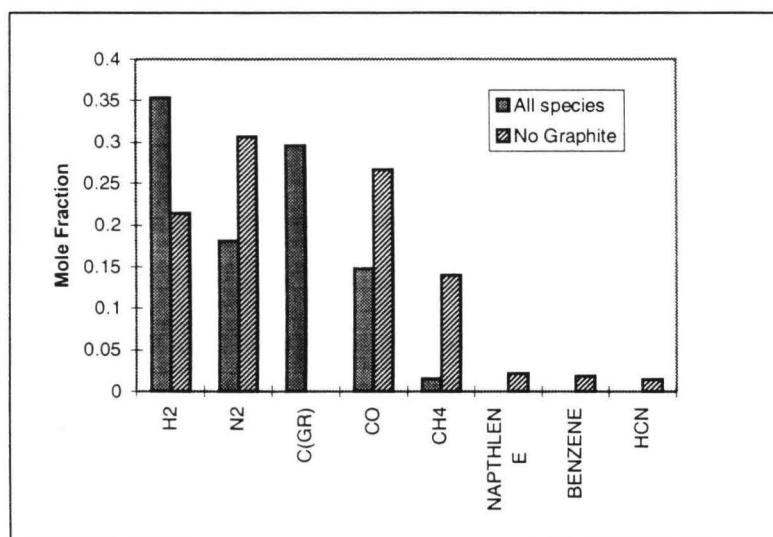
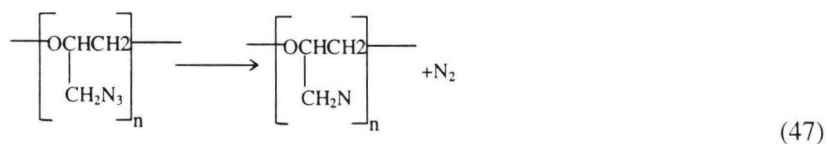


Figure 81: NASA-Lewis¹¹⁴ Calculated GAP Equilibrium Products at 40 atm

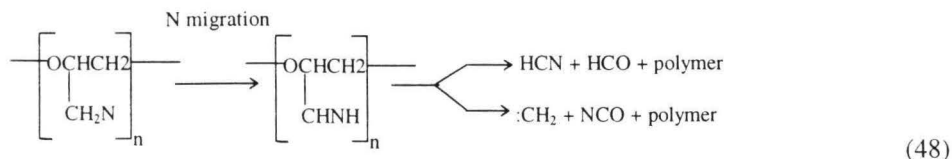
Despite the variance in the studies, there is a general consensus on the first decomposition step—the breaking off of N₂ from the azide to form the nitrene^{130,129,124,134,135}:



Kubota¹²⁴ says that H₂ is released with the N₂ in the exothermic step (164 kcal/mole). Flanagan¹²⁸ gives the heat release as ~80 kcal/mole. The activation energy for the above reaction has been measured by several investigators as approximately 41 kcal/mole.^{123,124,134,135}

Further decomposition of the nitrene is less well understood. Dhar and Singh¹³⁶ say the next step is the release of H₂ (Kubota¹²⁴ included this in the first step) with a heat of reaction of 140 to 170 kcal/mole. Kubota says that the nitrene decomposition produces H₂, C_{solid} and other gaseous products.¹³⁷ Brill and Chen¹³⁰ believe that the nitrene decomposes via two paths. They speculate that the dominant step leads to the formation of HCN while the lesser step involves the migration of H to form NH₃. None of

the other researchers report detecting NH₃. Haas et al.¹²⁹ also propose two similar decomposition paths for the nitrene:



The first path mainly leads to HCN, CO and methane and the second path leads to ethylene, acetylene and CO. They note that the second path could also produce NH₃ though it was not observed in their experiments.

The condensed phase reactions of GAP appear to be very complex and poorly understood. Species evolving from the surface could range from solid carbon to naphthalene and from stable species like N₂ to reactive species like CH₂ and monatomic nitrogen.¹²⁹ At the level of our current understanding, a global decomposition mechanism for GAP is probably all that is justifiable in a numerical model.

Combustion Characteristics of GAP

GAP has some interesting combustion characteristics, but again there is considerable disagreement in the literature. For example the pressure exponent of GAP has been reported to be 0.28¹³⁷, 0.44¹²², 0.52¹²³, 0.63¹²⁷, and 0.692.¹³⁸ Reported temperature sensitivities range from 0.002¹³⁹ to 0.01¹²² (1/K). These large variations in combustion characteristics can likely be attributed to variations in the preparation process of the GAP. For example, Flanagan et al. noted that the temperature sensitivity of GAP is very much a function of which curing agent is used.¹³⁹ To make reliable comparisons between experiment and models it is necessary to know the chemical composition, heat of formation and heat capacity of the GAP that was used in the experiment. **Unfortunately, this information is not included in most of the publications.** The reported combustion characteristics are compared below with model results.

Modeling

There are some significant differences in applying the combustion model to a polymer rather than a crystalline substance. For RDX and HMX, the two-phase zone begins at the melt temperature. But for GAP, only one reference to a molten layer on the surface was found in the literature, and being a polymer, a distinct melting temperature is not expected.¹²⁷ For GAP, the two-phase zone starts at some temperature above the initial temperature and below a temperature where decomposition is occurring at any significant rate. As long as this criterion is observed the choice of temperature to start this region had insignificant effects on model predictions. Evaporation is another significant difference in modeling GAP and the nitramines. For RDX and HMX, evaporation was the dominant path of conversion of condensed phase material to gas phase, according to the model. For GAP, being a polymer, evaporation is likely to be insignificant. For the nitramines, evaporation helped determine the boundary between the two-phase zone and the gas-flame zone (the surface of the burning propellant). For GAP, the surface is defined as the point where 99.999% of the condensed phase material has disappeared due to decomposition into gaseous species. Because of the linear relationship between concentration of the condensed species and the decomposition rates, the exact solution is asymptotic to 100%. To avoid this problem, a number very close to 100% was chosen. Finally, most of the chemical reactions occurring in the combustion of the nitramines are occurring in the gas flame, but for GAP, much of the heat release occurs in the two-phase region.

The condensed-phase decomposition mechanism of RDX and HMX used in the model is very simple. Most of the original propellant was assumed to evaporate with a fraction decomposing into four relatively stable species (NO_2 , HCN , N_2O and CH_2O). For GAP, numerous species with a wide range of stability have been detected coming off of the surface. Many of the major species detected are already near their thermodynamic equilibrium concentrations (N_2 and CO). This causes two problems. The first problem is developing a condensed phase decomposition mechanism that accurately reproduces the species observed in the decomposition studies. The second problem involves the calculation of the burning rate. Because the gas-phase flame of GAP is so weak and the burning rate of GAP is so high (about 2.5

times higher than RDX/HMX at 10 atm,⁺⁺⁺⁺⁺) the gas-phase reactions are blown away from the surface. Experimentally this is observed as a weak flame detached from the surface. At near atmospheric pressures, several researchers report that GAP self extinguishes.^{132,129} The model shows that convection carries the gases away from the surface before they can react to a significant degree. This leads to difficulty in numerical convergence of the gas-flame zone and in the calculation of the burning rate.

The propellant properties listed in Table 27 were used in the model. Ten units of the monomer chemical composition, taken from Ref. 123, were used to simulate the polymer (GAP10). Other values were taken from the sources as referenced in the table. The gas-phase reaction mechanism was developed by assembling the Melius-Yetter⁵⁰ gas phase mechanism for RDX, Cohen's¹⁴⁰ AP mechanism and the GRI hydrocarbon mechanism.¹⁴¹ Of the resulting mechanism, some species which would not be present were eliminated (like RDX, chlorine-containing species, etc.). The result was a mechanism containing 58 species involved in 292 reactions. This mechanism is probably much more complicated than is necessary, but at this point, the GAP model is not established well enough to reduce the mechanism.

Table 27: GAP Properties used in Model

Chemical Composition	C ₃₃ H ₅₆ O ₁₁ N ₂₆ (GAP10)	Heat of Formation (@298)	0.28 Kcal/g ¹²⁶
Heat Capacity	0.3845 kcal/g K ¹²⁴	Thermal Conductivity	3.5E-4 cal/cm-s-K ¹²³
Density	1.3 g/cm ³		

Many different global decomposition mechanisms were tried for the condensed phase. As expected, the predicted combustion characteristics are largely controlled by the condensed-phase reactions. The various mechanisms were developed by setting the burning rate at 40 atmospheres to 1.96 cm/sec (as reported in experiment¹²⁶), and adjusting the species being produced and the pre-exponential rate constants until the heat fluxes at the interface between regions two and three matched. Then a series of runs were performed to see how the predictions compared to experimental data at other initial temperatures and pressures. Three of the mechanisms that were tried are shown in Table 28. Each mechanism has four steps and for ease of comparison, steps are listed together rather than in individual mechanisms. The differences in rate constants between mechanisms for each step are minor.

⁺⁺⁺⁺⁺ Based on GAP burning rate data from Kubota¹³⁷ and the data presented in Figure 70, page 106.

Table 28: Proposed Condensed-phase Reaction Mechanisms for GAP

Step	Mech	Reactant	Products																	Log(A)	Ea			
			GAPR10	N ₂	H ₂	C(S)	CO	HCN	H ₂ CN	CN	CH ₄	C ₆ H ₆	C ₂ H ₄	C ₂ H ₂	CH ₂ O	NH ₃	H ₂ O	CH ₂	CNO			CH ₂ CO	C ₂ H ₃	C
1	A	GAP10	1	8																			15.7	41.5
	B	GAP10	1	8																			14.9	41.5
	C	GAP10	1	8																			14.9	41.5
2	A	GAPR10	2	21	14	11	6			2													11.0	25
	B	GAPR10	2	15	2	11	6			2	2												11.0	25
	C	GAPR10	1	17		11	2		6	2	1		3										11.0	25
3	A	GAPR10	2		11							4		11	6						3		10.3	25
	B	GAPR10	2		9						1	1	2	11	6			1					10.3	25
	C	GAPR10	2		6		2					3	4	11	4								10.0	25
4	A	GAPR10		9	5				1				1		2	1	8	7	3	2			10.6	25
	B	GAPR10		4		3	2				1	2		1	2	1	11	6					10.6	25
	C	GAPR10		4	10		9	2			1	4	3	2									10.6	25

(GAP10 is 10 units of polymer backbone structure, GAPR10 is GAP10 minus 8N₂. Activation energy units are kcal/mole. The activation energy for Step 1 was measured by Lengelle et al.¹²³ Numbers represent stoichiometric coefficients. For example, Step 1 in Mech A is GAP10→1GAPR10+8N₂.)

The species mole flux fractions coming off of the surface as calculated by each of the three mechanisms, are compared in Figure 82. The mole fractions shown are scaled by the mole fraction of CO. Thus Figure 82 can easily be compared to scaled experimental values shown in Figure 80. In Mechanism A, it is assumed that much of the carbon goes to C_{solid} as reported by Kubota.¹²⁴ Mechanisms A and B both produce significant amounts of the very reactive species CH₂. Because the formation of CH₂ requires significant energy (high temperatures), Litzinger recommended that it be dropped from our decomposition mechanism.¹⁴² Finally, both mechanisms A and B produce CNO. In Haas's proposed mechanism (Eq. 47 and 48 above), NCO (not CNO) is produced, but according to Flanagan it is unlikely that many nitrogen-oxygen bonds (like in CNO) are being formed in the condensed phase because of the lack of oxygen.¹³² In developing mechanism C, the objective was to avoid species like CNO, C_{solid} and CH₂.

The key differences in these three mechanisms are summarized in Table 29. Comparisons with experimental data and model predictions using each mechanism are made below.

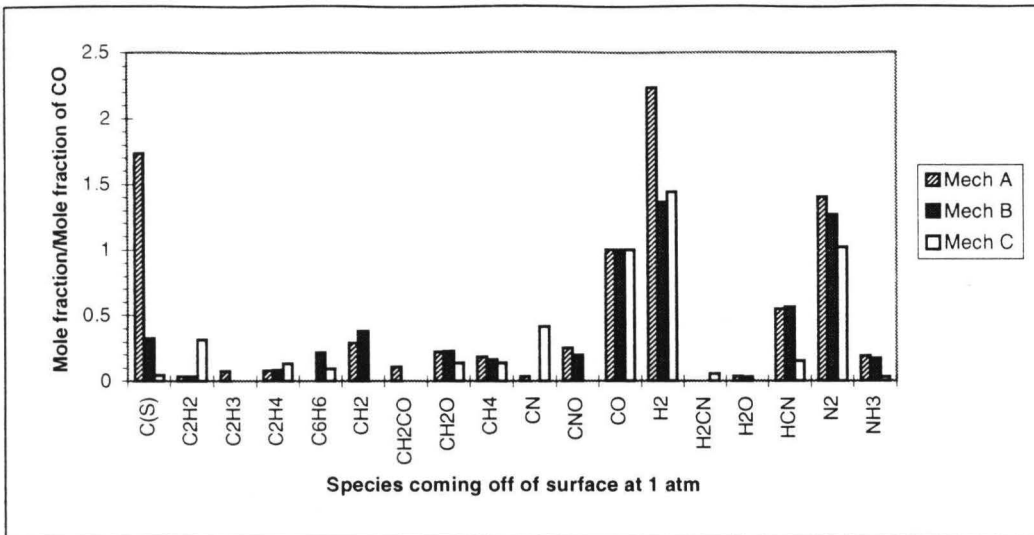


Figure 82: Comparison of Condensed Phase Decomposition Products

Table 29: Key Characteristics of Three Proposed GAP Mechanisms

Mechanism	Differences in Species Production	Differences in Calculated Results
A	Large Concentrations of H ₂ , C _{solid} , and CH ₂ . Significant amounts of CNO.	Lower surface temperature (by about 50 K) than other two mechanisms.
B	Same as Mechanism A, but with much of the H ₂ and C _{solid} in benzene (C ₆ H ₆)	Reasonable agreement with burning rate, T _s , and T _f data.
C	Very little C _{solid} and no CH ₂ or CNO. Large amounts of CN.	Essentially no gas-phase flame. Adiabatic Flame Temperature ~800 K.

Comparison with Experimental Data

Because of the lack of a definitive mechanism, mechanisms A, B and C were each optimized to give approximately the correct burning rate at 40 atmospheres. There remains enough uncertainty in the condensed-phase mechanism that attempting to do further optimization at this point would only force-fit the model with possibly unrealistic parameters.

Burning Rate

The calculated burning rate as a function of pressure is compared to experimental data in Figure 83. The agreement is reasonable for this stage of modeling. The difference in pressure exponent between the mechanisms results from differences in species available for reaction near the surface.

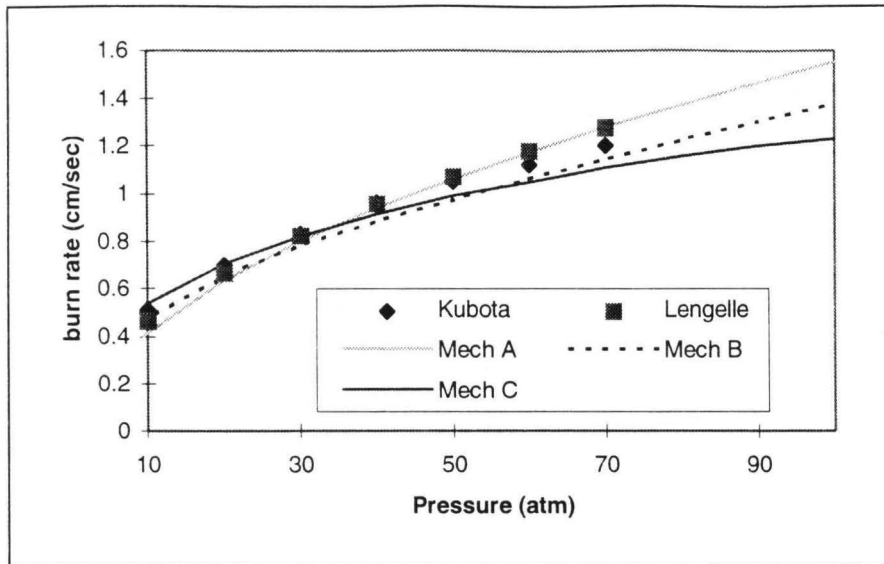


Figure 83: GAP Burning Rate with Pressure.

As seen in Figure 84, the burning rate of GAP is very sensitive to initial temperature. Only the predictions using Mechanism A are shown to simplify the figure. Calculations using the other two mechanisms are similar. For GAP, the calculated and experimental value of σ_p is approximately 0.01 K^{-1} . This is ten times the value for RDX. This difference is discussed in the Appendix.

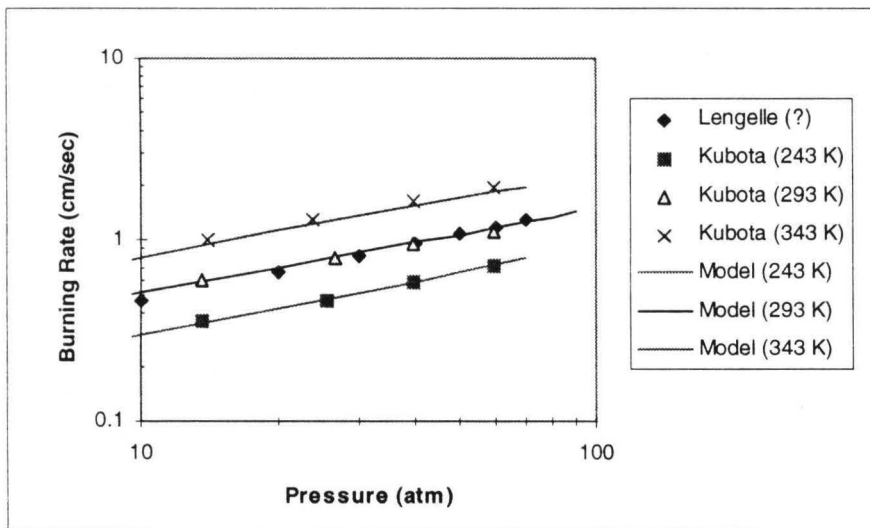


Figure 84: GAP Temperature Sensitivity of Burning Rate (Mechanism A)

Surface Temperature

Kubota¹²⁴ measured the surface temperature of GAP at pressures less than 10 atm (see Figure 85). Mechanism A under-predicts the surface temperature by about 50 K. All three mechanisms under-predict Lengelle's¹²³ reported value of 800 K at about 40 atm. More experimental data are needed.

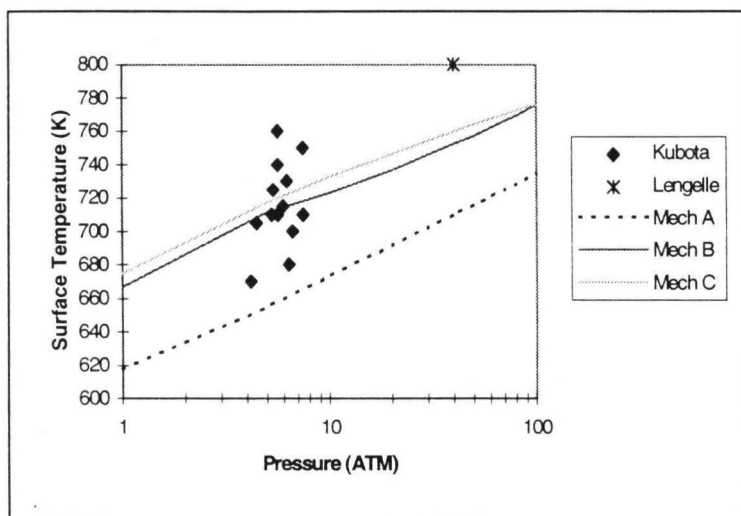


Figure 85: GAP Surface Temperature with Pressure.

Final Flame Temperature

Figure 86 shows the adiabatic flame temperature compared to that calculated by the NASA-Lewis equilibrium program.¹¹⁴ In the numerical model, enthalpy is conserved. The heat of formation of the mixture of final flame products is equal to the heat of formation of the original un-reacted GAP. The fact that the model's flame temperature does not match that calculated by the NASA-Lewis equilibrium code indicates the combustion of GAP does not go to completion (in the model). Lengelle¹²³ reports an experimental flame temperature as "(?) 1300 K" at ~40 atm. This indicates that the reactions in the experiment do not go to completion. Mechanisms A and B come much closer to thermal-equilibrium than does mechanism C. In fact, calculations made using mechanism C show only about a 100 K increase above the surface temperature. At present, no one has reported experimentally-determined, measured final products of the combustion of GAP.

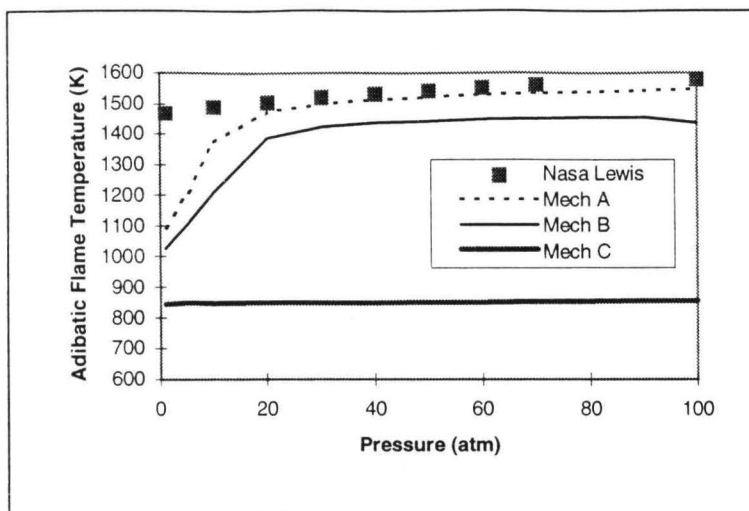
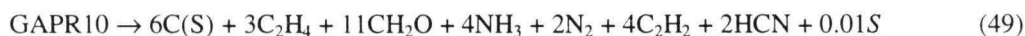


Figure 86: GAP Adiabatic Flame Temperature

Sensitivity Analysis

In developing the condensed phase decomposition mechanisms, both the species being produced and the rate constants were varied to aid in the numerical convergence of the burning rate at 40 atm. To determine the effect that the production of a particular species has on the combustion characteristics as calculated by the model, a small amount of each gaseous species was generated in one of the decomposition reaction mechanisms. For example, starting with mechanism C, Reaction 2 was perturbed to:



where S represents each species, one at a time. This, of course, violates the mass and energy balances to a small degree but provides some useful information. For a particular species, this sensitivity analysis indicates whether its production increases or decreases the burning rate. This analysis also provides similar information relative to the surface temperature, flame temperature, and other combustion characteristics as necessary. This type of sensitivity analysis will vary with the base mechanism. The presence and concentration of other species affects the influence a particular species has on these characteristics. Table 30 summarizes these results at 40 atm for mechanism C.

Table 30: Sensitivity to Production of Species Analysis (Mechanism C, GAP)

	Ranking	Surface Temperature	Flame Temperature	Burning Rate
Strongly Decreases	1	CO ₂	CO ₂	HO ₂
	2	H ₂ O	H ₂ O	O ₂
	3	CH ₃ OH	CH ₃ OH	CO ₂
	4	H ₂ O ₂	C ₂ H ₆	H ₂ O
	5	HNO ₃	CH ₂ O	OH
	6	CH ₂ O	CH ₄	O
	7	CO	CO	CH ₃ OH
	8	HNCO	CH ₂ CO	CH ₃ O
	9	CH ₄	C ₆ H ₆	H ₂ O ₂
	10	C ₂ H ₆	NH ₃	CH ₂ O
↑ Decreases	10	C ₂ H ₃	O ₂	CN
	9	C ₂ N ₂	N ₂ O	H ₂ CN
	8	NH	HNO ₃	C ₆ H ₆
	7	CH ₂	HONO	HCNO
	6	CNO	NO ₂	H ₂ CNO
	5	CH ₂ (S)	NO	C ₂ H ₂
	4	CN	HNO	H ₂ CNNO
	3	NCN	NO ₃	C ₂ N ₂
	2	N	H ₂ O ₂	NCN
	1	CH	H ₂ CNO	CNO
Increases ↓				
Strongly Increases				

According to the results in Table 30, if the decomposition of GAP produces species with nitrogen-oxygen bonds, the final flame temperature and burning rate are higher. On the other hand, if the solid-phase decomposition of GAP produces final products like CO₂ and H₂O, the flame temperature, surface temperature and burning rate are lower. Producing radicals like CH, N, NCN and CN tends to increase the surface temperature. All three mechanisms give approximately the same burning rate at 40 atm, but this analysis does explain why the calculated adiabatic flame temperatures using mechanisms A and B are higher than those of mechanism C. Both A and B produce CNO in the condensed phase. Though not listed in Table 30, CNO ranks as number 12 in increasing the flame temperature, and does contain a nitrogen-oxygen bond. This analysis can also explain why the surface temperature of mechanism A is low compared to both experimental data and the model results using the other two mechanisms. The reason appears to be the high production rate of H₂ (See Figure 82). Again, H₂ is not listed in the top ten species for decreasing the surface temperature for mechanism C but is ranked number eight when the sensitivity calculations are run using mechanism A. This type of analysis is very useful in trying to understand the complex decomposition of GAP. Currently there is not a well-defined

decomposition mechanism but as one evolves, this type of analysis can guide researchers as to what species could be being produced or which species' thermodynamic properties need review. Once most of the uncertainty in the model has been resolved by experiment, this type of analysis could be useful in identifying ways of modifying the combustion of a propellant by altering its chemistry.

Conclusion

Our lack of understanding of the combustion of GAP is significant. There are few property values for GAP in the literature that are well known. Most values reported in the literature appear to have been estimated. Several research groups have done significant studies on the decomposition of GAP, but the various groups arrive at very different conclusions. Some report large amounts of solid carbon while others say that they did not see any. Some measure significant amounts of NH_3 and CH_2O while others report small amounts of CH_2O and no NH_3 . One researcher reports seeing aromatic molecules. These differences could stem from differences in the preparation of the polymer or from differences in experimental technique. The method of preparation can affect the chemical composition, the heat of formation, and the physical properties, but these critical experimental data have not been reported. There are also very significant differences in the reported burning rate, temperature sensitivity and other combustion characteristics in the literature.

In summary, the following information (in approximate order of importance) needs to be clarified:

- Chemical composition and heat of formation of the GAP being tested (i.e., what has been added to the GAP, in what percentage, and what are its properties).
- Quantitative concentrations of the decomposition products of GAP (including possibly very reactive species).
- Verify and quantify the presence of C_{solid} , benzene, NH_3 etc.
- Precise burning rate as a function of pressure and initial temperature.
- The final flame temperature.
- The final combustion products of GAP.

- Surface temperature.
- Temperature profile.

The purpose of this study has not been to force the model to fit the data. Rather, predictions were made to indicate what further experimental data are required to eliminate some of the degrees of freedom currently in our model. A type of sensitivity analysis of model predictions with respect to the production of various species in the decomposition mechanism of GAP has been used to identify possible alternatives to the reported decomposition products. From this analysis, species containing nitrogen-oxygen bonds will increase the final flame temperature and burning rate, though the formation of such bonds appears unlikely in GAP combustion. Once most of the uncertainty in the model has been resolved by experiment, this type of analysis could be useful in identifying ways of modifying the combustion of a propellant by altering its chemistry.

CHAPTER 11: SUMMARY AND CONCLUSIONS

Summary of Work

A one-dimensional, steady-state numerical model using detailed reaction kinetics has been developed and applied to RDX, HMX and GAP. The nitramines (RDX and HMX) are very similar propellants. They are crystalline in structure and have significant vapor pressures. For RDX and HMX, most of the decomposition occurs in the gas phase. GAP is considerably different from the nitramines. It is a polymer and has a very weak gas-phase flame. Most of the decomposition of GAP occurs in the condensed phases. Despite the differences between the nitramines and GAP, the model predictions of burning rate, temperature sensitivity, surface temperature, and flame temperature, correlate reasonably for these three monopropellants with most of the available experimental data.

For the nitramines, there are also species-concentration-profile data. For most measured species, the model predictions agree well with experimental data. The largest discrepancy occurs for the NO concentration. Model calculations indicate that the weakness probably occurs due to the relatively uncertain rate constants for several reactions involving NO, NO₂, HNO, HONO, HCO and H₂CN.

Sensitivity analysis of the model was used to explain the similarities and differences in the combustion characteristics of RDX and HMX. According to the model, the similarity in liquid- and gas-phase reactions can explain the similarities in burning rate. The model also indicates that the higher vapor pressure of RDX is the reason why the surface temperature of RDX is lower than that of HMX. The melt layer of RDX is thicker than that of HMX at pressures below 20 atm because of the lower melting point. Above 20 atm, this difference in melt-layer thickness is reduced due to increasing effect and similarity of the gas-phase reactions.

For RDX, computation times were reduced by over a factor seven by using a skeletal gas-phase reaction mechanism. The full mechanism consists of 45 species in 232 reactions. The skeletal mechanism

has only 18 species in 39 reactions. Calculations of burning rate, temperature profiles and most species concentration profiles using the reduced mechanism were not significantly different from those using the full mechanism. A global mechanism (9 species in 6 reactions) was also developed. Using the global mechanism, the model could still accurately predict burning rate, surface temperature, final flame temperature, and final species concentrations between 1 and 100 atm. The CPU time were reduced by nearly a factor of 30.

For the nitramines, the only model input which did not come from an independent source was the liquid thermal conductivity. In other words, there was essentially only one degree of freedom. The choice of liquid thermal conductivity had a significant effect on only the melt-layer thickness. For GAP, most of the required model inputs and data for model validation have not been well quantified. For this reason, there remains considerable freedom in the choice of input parameters and description of reaction mechanisms. Further experimental studies of GAP are necessary.

Originality of Work

In the introduction of this dissertation, the nature of the contract under which this research was funded was explained. There has been a considerable amount of communication between the different modeling groups, as well as communication between those developing models and those performing experiments. The combustion model that has been developed as part of my research is a compilation of ideas from several researchers. The gas-phase sub-model is an adaptation of the PREMIX code developed at Sandia.⁴⁵ The treatment of the void fraction in the two-phase region is similar to BenRueven's²⁶ treatment in 1975 and Hatch's⁵⁹ in 1987. The relationship between the liquid velocity and the gas velocity in the two-phase region was based upon work of Margolis et al.³⁷ The evaporation sub-model came from Liao and Yang.⁷⁵ The RDX gas-phase mechanism came from Yetter et al.⁵⁰ The liquid-decomposition mechanism was based on experimental work by Brill et al.⁴ Parr et al.,⁸⁷ Shoemaker et al.,⁹⁸ Kubota et al.¹ and others provided thermophysical properties for the monopropellants. Parr et al.,^{67,68,69} Litzinger et al.,^{64,65} Boggs et al.,³⁴ Zenin et al.,⁷¹ and numerous others provided various experimental data to validate

the model. The interactions between these numerous researchers has resulted in unprecedented agreement between experimental and predicted results.

As I have been developing this model over the past four years, two other groups (Liau and Yang⁷⁵ at PSU, and Prasad and Smooke⁶² at Yale) also developed similar models for RDX. There are differences between the models, but these differences do not seem to significantly affect the predicted values. The differences and similarities in these three models are shown in Table 31. Excluding the common use of CHEMKIN subroutines⁴¹ and PREMIX,⁴⁵ each of the codes was written independently from the others. With all the cross-communication it is somewhat difficult to distinguish original contributions. The original aspects of my work are discussed in the following subsections.

Table 31: Comparison of RDX Multi-Phase Models of BYU, PSU and Yale.

Characteristic	BYU	PSU ⁷⁵	Yale ⁶²
Solid Reactions	None	None	None
Liquid Diffusion	Neglected	Neglected	Neglected
Two-Phase Region	Void Fraction	Void Fraction	All gas-phase species are absorbed in the liquid. No voids considered.
Liquid Decomposition Reactions	Brill ⁴	Thynell ¹⁰¹	Brill ⁴
Evaporation	Calculated using vapor pressure correlation at void/liquid interface and at surface.	Calculated using vapor pressure correlation at void/liquid interface and at surface.	By definition, all liquid moving through the plane of the surface evaporates.
Surface Temperature	Calculated	Calculated	Input, Calculated (?)
Gas Phase	PREMIX	PREMIX	PREMIX
Gas-Phase Mechanism	Melius-Yetter ⁵⁰	Melius-Yetter ⁵⁰	Melius-Yetter ⁵⁰
Solution Method	Iteration between initial value problem in two-phase region and boundary value problem in gas region. Solid phase is incorporated as a boundary condition in two-phase calculations. Burning rate (r_b) determined by matching heat flux at surface.	Iteration between the boundary value problem in the condensed-phases region and the boundary value problem in gas region to converge on r_b and T_s .	Solid, liquid and gas regions solved simultaneously as a boundary value problem using the mechanics of the PREMIX code. Artificial boundary conditions $T(x=0)=T_s$ or $X_{RDX}(x=\text{large distance from surface})=0$ used to specify the system of equations.

RDX Modeling

Other than the development of the code, my contribution in the development of the RDX model has been the study of the effect of model inputs on predicted values. This sensitivity analysis has led me to question several of the thermophysical property values reported in the literature. This careful evaluation of these model inputs has reduced some of the uncertainty in RDX modeling. The modifications to the Melius-Yetter⁵⁰ mechanism with regards to the peak NO concentration is unique (page 76). The development of the reduced mechanism in Chapter 7 is also unique.

HMX Modeling

The extension of the RDX model to HMX and the identification of the reasons behind the similarities and differences in the combustion of these two monopropellants is unique. Williams³⁸ identified some of these reasons using a model based on an erroneous assumption. Smooke¹⁴³ recently extended his RDX model to HMX but has mainly been interested in the influence of real gas behavior above 100 atm.

GAP Modeling

This work represents the first attempt at modeling the combustion of GAP with detailed kinetics. Though this model has not been refined to the extent of the nitramine models, this work has identified several key questions that must be answered before further refining of the model can take place. The sensitivity analysis with respect to the generation of decomposition products in the condensed phase is unique.

Development of Modeling Tools

Much of the significance of this work has been the development of several tools (computer programs) for the modeling of propellants. These modeling tools are already being used by other graduate

students and a professor^{#####} in developing models of other propellants. A brief description of the capabilities of these codes is given here. The complete listing of the source codes is too long to be placed in the Appendix.

Phase3: The 1D, SS Propellant Combustion Code

Phase3 (for solid, liquid and gas) is the name of the solid homogeneous propellant combustion model. It is a menu-driven program, designed for user interaction, though it does have the ability to run in batch mode. The underlying equations and numerical convergence techniques are discussed in Chapter 4. Some of the features of Phase3 are outlined here.

Standard Calculations

Given the thermophysical properties of the propellant, intermediates and final products, reaction mechanisms, pressure and initial temperature, the model will predict the burning rate, temperature profile, species concentration profile, void fraction profile, melt layer thickness, surface temperature, heat flux from the gas flame to the surface, and heat release due to reaction in the condensed phase. These represent the basic model outputs. The program can easily be set up to perform repeated calculations at many pressures and initial temperatures automatically. When the code is having difficulty converging, adjustments in convergence methods and parameters are automatically made. All output is written to a semi-colon delimited text file which can easily be read into most spreadsheet programs for further analysis.

Sensitivity Analysis

One of the most useful aspects of Phase3 is the automatic sensitivity analysis. The code can perturb almost every model input and measure the effect on many model predictions. This is useful in identifying weaknesses in the model, uncertainty in model inputs and explaining the differences between

Dr. Masafumi Tanaka, a visiting professor at BYU from the National Defense Academy (Aug 1995-Aug 1996).

various ingredients. An option in the code allows the user to test the effects of changing combinations of variables at the same time. The sensitivity analysis of the original PREMIX⁴⁵ code has been greatly expanded so as to give the sensitivity coefficients for not only temperature but for each species concentration with respect to each reaction and the heat of formation of each species. A separate code, OPENSENS automatically analyzes and sorts the sensitivity output from PHASE3. The output from OPENSENS is also semi-colon delimited text.

Reduced Mechanisms

Several subroutines are included in Phase3 to aid the user in developing reduced mechanisms. These subroutines perform the integral reaction flow analysis, automatically drop unimportant reactions and species from the calculations (according to the algorithm described on page 82) and will generate CHEMKIN-compatible files containing the reduced mechanism. Restart files for the new mechanisms can be generated from converged cases.

Mechanism Manager

In the literature, there are numerous compilations of detailed kinetic mechanisms. For a given system, different researchers can use significantly different mechanisms. Mechanism Manager is a menu-driven database program that reads in multiple CHEMKIN files, performs sorts and comparisons and will generate new reaction sets based on criteria that the user specifies.

Foundation for Future Work

The tools that have been developed as part of this dissertation provide the ground work for future research. Phase3 and the Mechanism Manager provide researchers the ability to explore many options in physical parameters and reaction mechanisms with relatively small amounts of development time. The RDX and HMX models have been fairly well validated with numerous comparisons with experimental data. This level of modeling will serve as a standard for future models.

Modeling of Other Propellants

As shown with GAP, Phase3 can be used to model monopropellants other than the nitramines. This code has also been used to model ammonium perchlorate (AP).⁷⁹ Further refinement of the AP model continues at BYU by other graduate students. In addition to monopropellants, the code will accept multi-ingredient propellants with the assumption that they are perfectly mixed.

Extension to Multi-Dimensional and Unsteady Models

The development and refinement of steady-state combustion models is necessary before extending such models to multi-dimensions or unsteady conditions. Often these multi-dimensional models require excessive amounts of CPU time. The 1D-SS model can be used to explore simplifying assumptions (such as reduced mechanisms) which could then be incorporated into the more complex models.

Publications

During the past four years, I was the primary author of five journal articles and a significant contributor as a co-author to another paper. I have also been an active participant at several conferences and workshops. A brief summary of these papers is given here:

Peer-Reviewed

“A Three-Phase Model of HMX Combustion” (*Proceedings of the 26th International Symposium on Combustion*, 1996)¹⁴⁴ contains much of the work presented in Chapter 9.

“Improvements to RDX Combustion Modeling”⁷⁶ (To be published in the *Journal of Propulsion and Power*, May 1997) describes the assumptions of the model and contains information similar to that presented in Chapters 4, 5 and 6.

“A Comparison of Solid Monopropellant Combustion Modeling” (*4th International Symposium on Special Topics on Chemical Propulsion*, Stockholm, Sweden May, 1996),¹⁴⁵ of which I was a co-author, contains much of the literature review in Chapter 3 and many of the calculations presented in Chapters 6 and 9.

JANNAF

“Reasons for the Similarities and Differences in the Combustion of RDX and HMX” (33rd JANNAF Combustion Meeting, Nov. 1996)¹⁴⁶ contains more of the work in Chapter 9.

“A Reduced Mechanism for RDX Combustion” (33rd JANNAF Combustion Meeting, Nov. 1996)¹⁴⁷ discusses the skeletal and global mechanisms reported in Chapter 7.

“A Model and Mechanism for the Combustion of GAP” (33rd JANNAF Combustion Meeting, Nov. 1996)¹⁴⁸ contains most of the information presented in Chapter 10.

In an hour and a half presentation, I discussed my modeling of RDX and HMX at the JANNAF Combustion Subcommittee Workshop, “Flame Structure and Combustion Modeling of HMX and RDX” with several researchers§§§§§§§§ working in this area. The results from the work shop should be published in this year’s JANNAF proceedings.

§§§§§§§§ Q. Brewster, M. Smooke, J. Finlinson, R. Geisler, S. Son.

REFERENCES

¹Kubota, N., "Survey of Rocket Propellants and Their Combustion Characteristics," *Fundamentals of Solid-Propellant Combustion*, edited by K. Kuo and M. Summerfield, Vol. 90, Progress in Astronautics and Aeronautics, AIAA, New York, 1984, pp. 1-47.

²An example is the work of Tim and Donna Parr. See other endnotes to their numerous publications in this list of references.

³Melius, C. F. and Binkley, J. S., "Thermochemistry of the decomposition of Nitramines in the Gas Phase," *Proceedings of the 21st Symposium (Int) on Combustion*, The Combustion Institute, 1986, pp. 1953-1963.

⁴Brill, T. B., "Multiphase Chemistry Considerations at the Surface of Burning Nitramine Monopropellants," *Journal of Propulsion and Power*, Vol. 11, No. 4, 1995, pp. 740-751.

⁵Behrens, R. Jr., and Bulusu, S. N., "Thermal Decomposition of Energetic Materials 3&4," *Journal of Physical Chemistry*, Vol. 96, No. 22, 1992, pp. 8877-8897.

⁶Boyer, E., Lu, Y. C. and Kuo, K. K., "Characterization of Condensed-Phase Chemical Reactions of RDX and Nitramine-Based Propellants," *32nd JANNAF Combustion Meeting*, CPIA # 638, Vol. 1, 1995, pp. 173-183.

⁷Beckstead, M., Branch, M., Brill, T., Litzinger, T., Smooke, M., and Yang, V., "Nonsteady Combustion Mechanisms of Advanced Solid Propellants," Proposal to DOD University Research Initiative and AFOSR, University of Colorado at Boulder, July 1, 1992.

⁸Beckstead, M. W., "Solid Propellant Combustion Mechanisms and Flame Structure," *Pure and Appl. Chem.*, Vol. 65, No. 2, 1993, pp. 297-307.

⁹Boggs, T. L. "Thermal Behavior of RDX and HMX," *Fundamentals of Solid-Propellant Combustion*, edited by K. Kuo and M. Summerfield, Vol. 90, Progress in Astronautics and Aeronautics, AIAA, New York, 1984, pp. 121-176.

¹⁰Kuo, K. K. and Lu, Y. C., "Modeling of Physicochemical Processes of Burning RDX Monopropellants," *30th JANNAF Combustion Meeting*, CPIA # 606, Vol. II, 1993, pp. 235-257.

¹¹Wilson, S. J., Fetherolf, B. L., Brown, P. W. and Kuo, K. K., "Surface Microstructure Resulting from Laser-Induced Pyrolysis and Combustion of M43 and XM39," *30th JANNAF Combustion Meeting*, CPIA #606, Vol. II, 1993, pp.167-181

¹²Ermolin, N. E., Korobeinichev, O. P., Tereshchenko, A. G. and Fomin, V. M., "Kinetic Calculations and Mechanism Definition for Reactions in an Ammonium Perchlorate Flame," *Fizika Goreniya i Vzryva*, Vol 18. No. 2, 1982, pp. 61-70.

-
- ¹³Beckstead, M. W., Derr, R. L. and Price, C. F., "Model of Composite Solid-Propellant Combustion Based on Multiple Flames," *AIAA Journal* Vol. 8, No. 12, 1970, pp. 2200-2207.
- ¹⁴Kuo, K. K., Principles of Combustion, John Wiley & Sons, 1986, pp. 163-209.
- ¹⁵Beckstead, M. W. and McCarty, K. P., "Calculated Combustion Characteristics of Nitramine Monopropellants," *13th JANNAF Combustion Meeting*, Vol. I, 1976, pp. 58-67.
- ¹⁶Beckstead, M. W., "Model For Double-Base Propellant Combustion," *AIAA Journal*, Vol 18, No. 8, 1980, pp. 980-985.
- ¹⁷Cohen, N., "Review of Composite Propellant Burning rate Modeling," *AIAA Journal*, Vol. 18, No. 3, 1980, pp. 277-293.
- ¹⁸Beckstead, M. W., Derr, R. L. and Price, C. F., "The Combustion of Solid Monopropellants and Composite Propellants," *13th Symposium on Combustion*, The Combustion Institute, 1971, pp. 1047-1056.
- ¹⁹Guirao, C. and Williams, F. A., "A Model for Ammonium Perchlorate Deflagration between 20 and 100 atm," *AIAA Journal*, Vol. 9, No. 7, 1971 pp. 1345-1356
- ²⁰Beckstead, M. W., "A Model for Solid Propellant Combustion," *18th Symposium (Int) on Combustion*, The Combustion Institute, 1981, pp. 175-185.
- ²¹Beckstead, M. W. and McCarty, K. P., "Modeling Calculations for HMX Composite Propellants," *AIAA Journal*, Vol. 20, No. 1, 1982, pp. 106-115.
- ²²Mitani, T. and Williams, F. A., "A Model for the Deflagration of Nitramines," *21st Symposium (Int) on Combustion*, The Combustion Institute, 1986, pp. 1965-1974.
- ²³Beckstead, M. W., "Modeling AN, AP, HMX, and Double Base Monopropellants," *26th JANNAF Combustion Meeting*, CPIA # 529, Vol. 4, 1989, pp. 255-268.
- ²⁴Cor, J. and Renie, J., "A Continuous Surface Regression Model for the Combustion of Composite Solid Propellants," *Western States Section of the Combustion Institute*, Report 87-17, 1987.
- ²⁵Glick, R. L., "Distribution Functions for Statistical Analysis of Monodispersed Composite Solid Propellant Combustion," *AIAA Journal*, Vol. 14, 1976, pp. 1631-1633.
- ²⁶BenReuven, M., Caveny, L., Vichnevetsky, R., and Summerfield, M., "Flame Zone and Sub-Surface Reaction Model for Deflagrating RDX," *16th Symposium (Int.) on Combustion*, The Combustion Institute, 1976, pp. 1223-1233.
- ²⁷BenReuven, M. and Caveny, L., "HMX Deflagration and Flame Characterization," *Report AFRPL-TR-79-94*, Thiokol Corporation, Huntsville AL, Vol. II, Oct. 1980.
- ²⁸Cohen, N., Lo, G. and Crowley, J., "Model and Chemistry of HMX Combustion," *AIAA Journal*, Vol. 23, No. 2, 1985, pp. 276-282.

²⁹Ermolin, N. E., Korobeinichev, O. P., Tereshchenko, A. G. and Fomin, V. M., "Simulation of Kinetics and Chemical Reaction Mechanism of Ammonium Perchlorate Burning," *Sov. J. Chem. Phys.*, Vol. 1(12), 1984, pp. 2872-2883.

³⁰Bizot, A. and Beckstead, M., "A Model for Double Base Propellant Combustion," *22nd Symposium (Int.) on Combustion*, The Combustion Institute, 1988, pp. 1827-1834.

³¹Bizot, A. and Beckstead, M., "A Model for HMX Propellant Combustion," *Flame Structure*, (edited by O. P. Korobeinichev) Vol. 1, 1991, pp. 230-235.

³²Roh, T., Tseng, I., and Yang, V., "Effects of Acoustic Oscillations on Flame Dynamics of Homogeneous Propellants in Rocket Motors," *Journal of Propulsion and Power*, Vol. 11. No. 4, 1995, pp. 640- 650.

³³ Mitani, T., and Williams, F. A., " A Model for the Deflagration of Nitramines," SAND86-8230, Dec. 1986.

³⁴ Boggs, T. L., Atwood, A. I., Curran, P. O., Parr, T. P., Hanson-Parr, D., Paull, D., Wiknich, J., and Price, C. F., "The Pressure and Temperature Sensitivity of Burning Rates of Solid Propellant Ingredients," Naval Air Warfare Center, China Lake, CA, To have been presented in Beijing, personal communication, 1995.

³⁵Fogelzang, A. E., "Combustion of Explosives and Propellants Database," Version 2.43, Moscow, Russia, 1994.

³⁶ Li, S. C., Williams, F. A., and Margolis, S. B., "Effects of Two-Phase Flow in a Model for Nitramine Deflagration," *Combustion and Flame*, Vol. 80, 1990, pp. 329-349.

³⁷ Margolis, S., Williams, F. and Armstrong, R., "Influences of Two-Phase Flow in the Deflagration of Homogeneous Solids," *Combustion and Flame*, Vol. 67, 1987, pp. 249-258.

³⁸ Li, S. C., and Williams, F. A., "Nitramine Deflagration: Reduced Chemical Mechanism for Primary Flame Facilitating Simplified Asymptotic Analysis," *Journal of Propulsion and Power*, Vol. 12, No. 2, 1996, pp. 302-309.

³⁹ Korobeinichev, O., Orlov, V., Shifon, N., "Mass-Spectrometric Study of the Chemical Structures of Flames of Perchloric Acid in Lean and Rich Mixtures with Methane," *Fizika Goreniya i Vzryva*, Vol. 18, No. 5, 1982, pp. 77-83.

⁴⁰Ermolin, N. E., Korobeinichev, O. P., Kuibida, L. V. and Fomin, V. M., "Study of the Kinetics and Mechanism of Chemical Reactions in Hexogen Flames," *Fizika Goreniya i Vzryva*, Vol. 22, No. 5, 1986, pp. 54-64.

⁴¹Kee, R. J., Rupley, F. M., Miller, J. A., "Chemkin-II: A Fortran Chemical Kinetics Package for the Analysis of Gas Phase Chemical Kinetics," Sandia Report SAND89-8009B•UC-706, Jan 1993.

⁴²Kee, R. J., Rupley, F. M., and Miller, J. A., "The Chemkin Thermodynamic Data Base," Sandia Report SAND87-8215B•UC-4, Feb 1992.

⁴³Kee, R. J., Dixon-Lewis, G., Warnatz, J., Coltrin, M. E., and Miller, J. A., "A Fortran Computer code Package for the evaluation of Gas-Phase Multicomponent Transport Properties," Sandia Report SAND86-8246•UC-401, Jul. 1992.

⁴⁴Coltrin, M. E., Kee, R. J. and Rupley, F. M., "Surface Chemkin (Version 4.0): A Fortran Package for Analyzing Heterogeneous Chemical Kinetics at a Solid-Surface-Gas-Phase Interface," Sandia Report SAND90-8003B•UC-401, Jul 1991.

⁴⁵Kee, R. J., Grcar, J. F., Smooke, M. D. and Miller, J. A., "A Fortran Program for Modeling Steady Laminar One-Dimensional Premixed Flames," Sandia Report SAND85-8240•UC-401, Apr 1992.

⁴⁶Glarborg, P., Kee, R. J., Grcar, J. F., and Miller, J. A., "PSR: A Fortran Program for Modeling Well-Stirred Reactors," Sandia Report SAND86-8209•UC-4, Feb 1992.

⁴⁷Melius, C. F. and Binkley J. S., "Thermochemistry of the Decomposition of Nitramines in the Gas Phase," *21st Symposium (Int) on Combustion*, The Combustion Institute, 1986, pp. 1953-1963.

⁴⁸Melius, C. F., "Thermochemical Modeling: I. Application to Decomposition of Energetic Materials," *Chemistry and Physics of Energetic Materials*, Edited by S. N. Bulusu, 1990, pp. 21-49.

⁴⁹Melius, C. F., "Thermochemical Modeling: II. Application to Ignition and Combustion of Energetic Materials," *Chemistry and Physics of Energetic Materials*, Edited by S. N. Bulusu, 1990, pp. 51-78.

⁵⁰Yetter, R. A., Dryer, F. L., Allen, M. T., Gatto, J. L., "Development of Gas-Phase Reaction Mechanism for Nitramine Combustion," *Journal of Propulsion and Power*, Vol. 11, No. 4, 1995, pp. 683-697.

⁵¹Lin, M. C., Mebel, A. M. and Morokuma, K., "Theoretical Study of the Gas-Phase Structure, Thermochemistry, and Decomposition Mechanisms of NH_4NO_2 and $\text{N}_2\text{H}_4(\text{NO}_2)_2$," *Journal of Physical Chemistry*, 1995.

⁵²Politzer, P. Lane, P., Grice, M., Concha, M., and Redfern, P., "Comparative Computational Analysis of some Nitramine and Diflouramine Structures, Dissociation Energies and Heats of Formation," *Journal of Molecular Structure*, Vol. 338, 1995, pp. 249-256.

⁵³Yetter, Personal Communication. Aug 1995.

⁵⁴Cohen, N. "A Review of Kinetic Models for High Temperature Gas Phase Decomposition of Ammonium Perchlorate," *Aerospace Report No. ATR-92(9558)-3*, The Aerospace Corporation. Sep. 1992.

⁵⁵Pearson, G. and Jacobs, P., "Mechanism of the Decomposition of Ammonium Perchlorate," Rocket Propulsion Establishment, Ministry of Technology, London, RPE Tech. Report 69/6, 1969.

⁵⁶Sahu, H., Sheshadri, T. and Jain, V., "Novel Kinetic Scheme for Ammonium Perchlorate Gas Phase," *J. Phys. Chem.* Vol. 94, 1990, pp. 294-295.

⁵⁷Ermolin, N., Korobeinichev, O., Tereshchenko, A., Fomin, V., "Kinetic Calculations and Mechanism Definition for Reactions in an Ammonium Perchlorate Flame," *Fizika Goreniya i Vzryva*, Vol 18, No. 2, 1982, pp. 61-70.

⁵⁸ Narahari, H. K, Mukunda, H. S. and Jain, V. K, "A Model for Combustion Monopropellants (AP) with Complex Gas Kinetics," *20th Symposium (Int.) on Combustion*, The Combustion Institute, 1984, pp. 2073-2082.

⁵⁹ Hatch, R. L., "Chemical Kinetics Combustion Model of the NG/Binder System," *23rd JANNAF Combustion Meeting*, CPIA #457, Vol. I, 1986, pp. 157-165.

⁶⁰ Hatch, R. L., "Chemical Kinetics Modeling of HMX Combustion," *24th JANNAF Combustion Meeting*, CPIA # 476, Vol. I, 1987, pp. 383-391.

⁶¹Anderson, W. R., Ilincic, N. and Meagher, N. E., "Detailed and Reduced Chemical Mechanisms for the Dark Zones of Double Base and Nitramine Propellants in the Intermediate Temperature Regime," *32nd JANNAF Combustion Meeting*, CPIA # 638, Vol. I, 1995, pp. 197-214.

⁶²Prasad, K., Yetter, R., and Smooke, M., "An Eigenvalue Method for Computing the Burning Rates of RDX Propellants," *32nd JANNAF Combustion Meeting*, CPIA # 638, Vol. 1, 1995, pp. 69-84.

⁶³Fetherolf, B. L., and Litzinger, T. A., "Chemical Structure of the Gas Phase Above Deflagrating RDX: Comparison of Experimental Measurements and Model Predictions," *30th JANNAF Combustion Meeting*, CPIA # 606, Vol. II, 1993, pp. 15-30.

⁶⁴Tang, C., Lee, Y. and Litzinger, T., "A Study of Gas-Phase Processes During the Deflagration of RDX Composite Propellants Using Triple Quadrupole Mass Spectrometer," *31st JANNAF Combustion Meeting*, CPIA # 620, Vol. II, 1994, pp. 307-316.

⁶⁵Lee, Y., Tang, C., Kudva, G., Litzinger, T., "The Near-Surface Gas-Phase Structure of RDX During CO₂ Laser-Assisted Combustion," *32nd JANNAF Combustion Meeting*, CPIA #638, Vol. I, 1995, pp. 107-118.

⁶⁶Brewster, M., and Schroeder, T., "Experimental Study of Steady and Unsteady Combustion of RDX," *32nd JANNAF Combustion Meeting*, CPIA #638, Vol. I, 1995, pp. 85-94.

⁶⁷Hanson-Parr, D., and Parr, T., "RDX Laser-Assisted Flame Structure," *31st JANNAF Combustion Meeting*, CPIA #620, Vol. II, 1994, pp.407-423.

⁶⁸Hanson-Parr, D., and Parr, T., "RDX Flame Structure," *25th Symposium (Int) on Combustion*, The Combustion Institute, 1994, pp. 1635-1643.

⁶⁹Parr, T., and Hanson-Parr, D., "RDX, HMX, and XM39 Self-Deflagration Flame Structure," *32nd JANNAF Combustion Meeting*, CPIA # 631, Vol. I, 1995, pp. 429-438.

⁷⁰Ritchie, S. J., Thynell, S. T., and Kuo, K., "Modeling and Experiments of Laser-Induced Ignition of Nitramine Propellants," *32nd JANNAF Combustion Meeting*, CPIA #638, Vol. I, 1995, pp. 185-196.

⁷¹Zenin, A., "HMX and RDX: Combustion Mechanism and Influence on Modern Double Base Propellant Combustion," *Journal of Propulsion and Power*, Vol. 11, No. 4, 1995, pp. 752-758.

⁷²Korobeinichev, O., Kuibida, L., and Madirvaev, V., "Investigation of the Chemical Structure of the HMX Flame," *Fizika Goreniya i Vzryva*, Vol. 20, No. 3, 1983, pp. 43-46.

⁷³Parr, T., and Hanson-Parr, D., "HNF Diffusion Flame Structure," *32nd JANNAF Combustion Meeting*, CPIA # 631, Vol. I, 1995, pp. 339-346.

⁷⁴Tang, C., Lee, Y., Kudva, G., and Litzinger, T., "A Study of the Gas Phase Chemical Structure During CO₂ Laser Assisted Combustion of HMX," *32nd JANNAF Combustion Meeting*, CPIA #638, Vol. I, 1995, pp. 119-130.

⁷⁵Liau, Y. and Yang, V., "Analysis of RDX Monopropellant Combustion with Two-Phase Subsurface Reactions," *Journal of Propulsion and Power*, Vol. 11, No. 4, 1995, pp. 729-739.

⁷⁶Davidson, J. and Beckstead, M., "Improvements in RDX Combustion Modeling," *32nd JANNAF Combustion Meeting*, CPIA # 638, Vol. I, 1995, pp. 41-56. (See also: AIAA No. 96-0885, *34th Aerospace Sciences Meeting*, Jan. 1996.) To be published in *Journal of Propulsion and Power*.

⁷⁷Laxton, J. A., Kuo, K. K., and Lu, Y. C., "Modeling and Numerical Simulation of Physicochemical Processes Occurring in the Two-Phase Foam Layer of Burning RDX," *32nd JANNAF Combustion Meeting*, CPIA #638, Vol. I, 1995, pp. 95-106.

⁷⁸Brown, P. N., Hindmarsh, A. C., and Byrne, G. D., "DVIDE" Computer Subroutine Package for Solving Ordinary Differential Equations, Aug. 31, 1991.

⁷⁹Tanaka, M., and Beckstead, M. W., "A Three Phase Combustion Model of Ammonium Perchlorate," AIAA 96-2888, *32nd Joint Propulsion Conference*, Lake Buena Vista, FL., July, 1996.

⁸⁰Fifer, Robert A., "Chemistry of Nitrate Ester and Nitramine Propellants," *Fundamentals of Solid-Propellant Combustion*, edited by K. Kuo and M. Summerfield, Vol. 90, Progress in Astronautics and Aeronautics, AIAA, New York, 1984, pp. 177-237.

⁸¹Schroeder, M., "Critical Analysis of Nitramine Decomposition Data: Activation Energies and Frequency Factors for RDX and HMX Decomposition," *17th JANNAF Combustion Meeting*, CPIA #329, Vol. II, 1980, pp. 493-508.

⁸²Schroeder, M., "Critical Analysis of Nitramine Decomposition Data: Product Distributions from HMX and RDX Decomposition," *18th JANNAF Combustion Meeting*, CPIA #347, Vol. II, 1981, pp. 395-411.

⁸³Farber, M. and Srivastava, R. O., "Thermal Decomposition of HMX," *16th JANNAF Combustion Meeting*, CPIA #308, 1979, pp. 59-71.

⁸⁴Behrens, R., and Bulusu, S., "Thermal Decomposition of HMX, Mononitroso-RDX, TNCHP and KC in the Liquid Phase: Results from Simultaneous Thermogravimetry Modulated Beam Mass Spectrometry Measurements," *29th JANNAF Combustion Meeting*, CPIA #593, Vol. II, 1992, pp.283-293.

⁸⁵ Erickson, K., Behrens R., and Bulusu, S., "Development of Rate Expressions for the Thermal Decomposition of RDX," *29th JANNAF Combustion Meeting*, CPIA #593, Vol. II, 1992, pp. 295-305.

⁸⁶ Kraeutle, K. J., "The Thermal Decomposition of HMX: Effect of Experimental Conditions and of Additives," *18th JANNAF Combustion Meeting*, CPIA #347, Vol. II, 1981, pp. 383-394.

⁸⁷ Parr, T, "Thermal Diffusivity Fits," Personal Communication, Dec 3, 1996.

⁸⁸ Parr, Tim, (Fax sent to M. Smooke and V. Yang and forwarded to M. W. Beckstead) July 1995.

⁸⁹ Beckstead, M. W., "Modeling AN, AP, HMX, and Double Base Monopropellants," *26th JANNAF Combustion Meeting*, CPIA #524, Vol. 4, 1989, pp. 255-268.

⁹⁰ Brewster, M. Q., Zebrowski, M. A., Schroeder, T. B., and Son, S.F., "Unsteady Combustion Modeling of Energetic Solids," AIAA Paper 95-2859, Jul. 1995.

⁹¹ Beckstead, M. W., "A Propellant Ignition Code for Motor Applications," *31st JANNAF Combustion Meeting*, CPIA #620, Vol. II, 1994, pp. 163-180.

⁹² Hanson-Parr, D., and Parr, T., "CDL Thermal Diffusivities of Propellants Ingredients," Reported at MURI meeting, Monterey, CA, Nov. 1996.

⁹³ Rosen, J. M. and Dickinson, C., "Vapor Pressures and Heats of Sublimation of Some High Melting Organic Explosives", *Journal of Chemical and Engineering Data*, Vol. 14, No. 1, 1969, pp. 120-124.

⁹⁴ Rogers, R. N., "Determination of Condensed Phase Kinetic Constants", Note, *Thermochimica Acta*, No. 9, 1974, pp. 444-446.

⁹⁵ Maksimov, Yu. Ya, Apal'kova, V.N., Braverman, O.V. and Solov'ev, A. I., "Kinetics of Thermal Decomposition of Cyclotrimethylenetrinitramine and Cyclotetramethylene-Tetranitramine in Gas Phase," *Russian Journal of Physical Chemistry*, Vol. 59, 1985, pp. 201-204.

⁹⁶ Cundall, R. B., Palmer, T. F., and Wood, C. E. C., "Vapour Pressure Measurements of Some Organic Explosives," *Journal of the Chemical Society, Faraday Transactions I*, Vol. 74, 1978, pp. 1339-1345.

⁹⁷ Yang, Vigor, Personal Communication. July 1994.

⁹⁸ Shoemaker, R. L., Stark, J. A., and Taylor, R. E., "Thermophysical Properties of Propellants," *High Temperatures-High Pressures, ETPC Proceedings* Vol. 17, 1985, pp. 429-435.

⁹⁹ Hall, P. G. , "Thermal Decomposition and Phase Transitions in Solid Nitramines," *Trans. Faraday. Society*, Vol. 67 (part2), 1971, pp.556-562.

¹⁰⁰ Edwards, G., "The Vapour Pressure of Cyclo-Trimethylene-Trinitramine (Cyclonite) and Pentaerythritol-Tetranitrate:," *Trans. Faraday Society*, Vol. 49, 1953, pp. 152-154.

-
- ¹⁰¹ Thynell, S., Gongwer, P., and Brill, T., "Modeling of Thermal Response of Filament used in T-Jump Experiment," *31st JANNAF Combustion Meeting*, CPIA #620, Vol. II, 1994, pp. 221-232.
- ¹⁰² Yetter, R. Personal communication. See Reference 50.
- ¹⁰³ Zimmer-Galler, R., "Correlations Between Deflagration Characteristics and Surface Properties of Nitramine-Based Propellants," *AIAA J.*, Vol. 6, No. 11, 1968, pp. 2107-2110.
- ¹⁰⁴ Glaskova, A. P., Rozantsev, E. G., Boblev, V. K. and Skripko, L. A., "Effect of the Chemical Structure of the Inhibitor on the Combustion of RDX," *Combustion, Explosion & Shock Waves*, No. 4, 1970, pp. 584-585.
- ¹⁰⁵ Zenin, A., "Topics of Discussions," Copies of overheads presented at BYU. In the possession of Dr. Merrill Beckstead, BYU, 1994.
- ¹⁰⁶ Korobeinichev, O.P., Kuibida, L. V., Paletsky, A. A. and Chernov, A. A., "Study of Solid Propellant Flame Structure by Mass-Spectrometric Sampling," *Combust. Sci Tech.*, Vol. 113-114, 1996, pp. 557-571.
- ¹⁰⁷ Parr, Tim, Personal Communication, Aug. 24, 1995.
- ¹⁰⁸ Parr, Tim, Personal Communication, Sept 26, 1995.
- ¹⁰⁹ Westley, F., Herron, J., Hampson, R., Mallard, W., "NIST Chemical Kinetics Database," Version 4.0, U.S. Department of Commerce, Apr. 1992.
- ¹¹⁰ Park, J., and Lin, M.C., "Mass-Spectrometric Measurements of Product Branching Probabilities in the $\text{NH}_2 + \text{NO}_x$ ($x=1,2$) Reactions," St. Petersburg, 1996.
- ¹¹¹ Tomlin, A. S., Turanyi, T., and Pilling, M. J., "Mathematical Tools for the Construction, Investigation and Reduction of Combustion Mechanisms," *Oxidation Kinetics and Autoignition of Hydrocarbons*, Edited by M. J. Pilling, Elsevier (in press). Summary downloaded from "<http://chem.leeds.ac.uk/Combustion/Combustion.html>"
- ¹¹² Ilincic, N., Anderson, W. R., and Seshadri, K. "Development of a Reduced Mechanism for the Double Base Propellant Dark Zone," *34th Aerospace Sciences Meeting, and Exhibit*, AIAA Report No. 96-0649, Jan. 15-18, 1996.
- ¹¹³ Tsang, W., Hampson, R., "Chemical Kinetic Database for Combustion Chemistry. Part I. Methane and Related Compounds," *J. Phys. Chem. Ref. Data*, Vol. 15, 1986, p. 1087.
- ¹¹⁴ McBride, B. J., and Gordon, S., "Computer Program for Calculation of Complex Chemical Equilibrium Compositions and Applications," *NASA Ref. Pub. 1311*, June 1996.
- ¹¹⁵ Zarko, V. Progress Report presented at MURI meeting, Reno, NV, Jan. 9, 1997.
- ¹¹⁶ Ben-Reuven, M. "Nitramine Monopropellant Deflagration an General Nonsteady Reacting Rocket Chamber Flows," Ph.D. Dissertation at Princeton University, 1980.
- ¹¹⁷ McCrone, W. C., "Cyclotetramethylene Tetranitramine HMX," *Analytical Chemistry*, Vol. 22, 1950, pp. 1225-1226. (As referenced by Boggs⁹)

-
- ¹¹⁸ Teetsov, A., and McCrone, W., "The Microscopical Study of Polymorph Stability Diagrams," *The Microscope*, Vol. 15, No. 1, 1965, pp. 13-29. (As referenced by Ben-Reuven.¹¹⁶)
- ¹¹⁹ Koshigoe, L., Shoemaker, R., and Taylor, R., "Specific Heat of HMX," *AIAA Journal*, Vol. 22, No. 11, 1984, pp. 1600-1601.
- ¹²⁰ Taylor, J., and Crookes, R., "Vapour Pressure and Enthalpy of Sublimation of 1, 3, 5, 7, Tetranitro-1, 3, 5, 7-tetra-aracylo-octane (HMX)." *Journal of the Chemical Society, Faraday Transactions I*, Vol. 3, 1976, pp. 723-729. (As referenced by Ben-Reuven¹¹⁶.)
- ¹²¹ Parr, T. and Hanson-Parr, D., "Solid Propellant Flame Structure," *Decomposition, Combustion, And Detonation Chemistry of Energetic Materials*, Edited by T. Brill, T. Russell, W. Tauo, and R. Wardle) *Materials Research Society*, Vol. 418, 1996, pp. 207-129.
- ¹²² Kubota, N. and Sonobe, T., "Combustion Mechanism of Azide Polymer." *Propellants, Explosives, Pyrotechnics* Vol. 13, 1988, pp. 172-177.
- ¹²³ Lengelle, G., Fourest, B., Godon, J. C., and Guin C., "Condensed Phase Behavior and Ablation Rate of Fuels for Hybrid Propulsion," *29th Joint Propulsion Conference*, AIAA 93-2413, June 28-30, 1993.
- ¹²⁴ Kubota, N. and Sonobe, T., "Combustion of GAP Propellants," *Comb. And Detonation Phenomena, 19th International Annual Conference of ICT*, Germany, 1988, pp. 21 to 2-12.
- ¹²⁵ Kubota, N. and Sonobe, T., "Burning Rate Catalysis of Azide/Nitramine Propellants," *23rd Symposium (International) on Combustion*, The Combustion Institute, 1990, pp. 1331-1337.
- ¹²⁶ Frankel, M. B., Grant, L. R., and Flanagan, J. E., "Historical Development of Glycidyl Azide Polymer," *Journal of Propulsion and Power*, Vol. 8, No. 3, 1992, pp. 560-563.
- ¹²⁷ Yuan, L.Y., Liu, T. K, and Cheng, S. S., "The Combustion Characteristics of GAP Gumstock Propellants," AIAA 96-3235, *Joint Propulsion Conference*, July, 1996.
- ¹²⁸ Flanagan, J., Woolery, D. and Kistner, R., "Fundamental Studies of Azide Decomposition and Combustion," AFRPL TR-96-094, Dec. 1986.
- ¹²⁹ Haas, Y., Eliahu, Yeshadyahu, B., and Welner, S., "Infrared Laser-Induced Decomposition of GAP," *Combustion and Flame*, Vol. 96, 1994, pp. 212-220.
- ¹³⁰ Chen, J. K., and Brill, T. B., "Thermal Decomposition of Energetic Materials 54. Kinetics and Near-Surface Products of Azide Polymers AMMO, BAMO and GAP in Simulated Combustion," *Combustion and Flame*, Vol. 87, 1991. pp. 157-168.
- ¹³¹ Oyumi, Y. and Brill, T. B., "Thermal Decomposition of Energetic Materials 12. Infrared Spectral and Rapid Thermolysis Studies of Azide-Containing Monomers and Polymers," *Combustion and Flame*, Vol. 65, 1986, pp. 127-135.
- ¹³² Flanagan, Joseph, Personal communication with M. W. Beckstead July, 1996.
- ¹³³ Mishra, I., Juneau, S. P. and Groom, T., *1984 JANNAF Propulsion Meeting*, CPIA #390, 1984, pp. 118-132.

¹³⁴ Farber, M., Harris, S. P. and Srivastava, R. D., "Mass Spectrometric Kinetic Studies on Several Azido Polymers," *Combustion and Flame*, Vol. 55, 1984, pp. 203-311.

¹³⁵ Goshgarian, B. B., "The Mechanism of Nitramine and Advanced Propellant Ingredient Initial Thermochemical Decomposition," AFRPL-TR-82-040, 1982.

¹³⁶ Dhar, S. S., and Singh, H., "Burnrate & Catalysis Behavior of GAP based CMDB Propellants," *Joint Propulsion Conference*, AIAA 95-2586, Jul. 10-12, 1995.

¹³⁷ Kubota, N., Sonobe, T., Yamamoto, A., and Shimizu, H., "Burning Rate Characteristics of GAP Propellants," *J. Propulsion and Power*, Vol. 6, No. 6, 1990, pp. 686-689.

¹³⁸ Simmons, R. L., "Unusual Combustion Behavior of Nitramines and Azides," *4th International Symposium on Special Topics on Chemical Propulsion*, Stockholm, Sweden May, 1996.

¹³⁹ Flanagan, J., Woolery, D., and Kistner, R., "Combustion Behavior of Azide Polymers," CPIA #432, Vol. II, *22nd JANNAF Combustion Meeting*, 1985, pp. 31-40.

¹⁴⁰ Cohen, N., "A Review of Kinetic Models for the High Temperature Gas Phase Decomposition of Ammonium Perchlorate," *Aerospace Report No. AFT-92(9558)-3*, 1992, pp. 1-36.

¹⁴¹ Frenklach, M., Bowman, T., Smith, G., and Gardiner, B., "GRI-MECH 1.2," Downloaded from "http://euler.Berkeley.EDU/gri_mech/index.html"

¹⁴² Litzinger, Tom, Personal Communication, 15 Jul, 1996.

¹⁴³ Prasad, K., Smooke, M., Tanoff, M., Yetter, R., "Modeling the deflagration of HMX at High Pressures," *33rd JANNAF Combustion Meeting*, Nov. 1996.

¹⁴⁴ Davidson, J. and Beckstead, M., "A Three-Phase Model for HMX Combustion," *Proceedings of the 26th International Symposium on Combustion*, The Combustion Institute, Jul-Aug. 1996.

¹⁴⁵ Beckstead, M., Davidson, J., and Jing, Q., "A Comparison of Solid Monopropellant Combustion and Modeling," *4th International Symposium on Special Topics on Chemical Propulsion*, Stockholm, Sweden May, 1996.

¹⁴⁶ Davidson, J., Beckstead, M. and Jing, Q., "Reasons for the Similarities and Differences in the Combustion of RDX and HMX," *33rd JANNAF Combustion Meeting*, CPIA, 1996.

¹⁴⁷ Davidson, J., Beckstead, M., and Jeppson, M. "A Reduced Mechanism for RDX Combustion" *33rd JANNAF Combustion Meeting*, CPIA, Nov. 1996.

¹⁴⁸ Davidson, J. and Beckstead, M., "A Model and Mechanism for the Combustion of GAP," *33rd JANNAF Combustion Meeting*, Nov. 1996.

¹⁴⁹ Warnatz, J., Maas, U. and Dibble, R. W., Combustion: Physical and Chemical Fundamentals, Modeling and Simulation, Experiments, Pollutant Formation, Springer, New York 1996.

¹⁵⁰ Schmidt, D., Segatz, J., Riedel, U., Warnatz, J., and Maas, U., "Simulation of Laminar Methane-Air Flames using Automatically Simplified Chemical Kinetics," *Combust. Sci. Tech.*, Vols. 113-114, 1996, pp. 3-16.

¹⁵¹ T. Turanyi, "Application of Repro-Modelling for the Reduction of Combustion Mechanisms," *Proceedings of the 25th Symp. (Int.) on Combustion*, The Combustion Institute, 1995, pp. 948-955.

¹⁵² Pilling, M. J., Turányi, T., Hughes, K. J., "Combustion Simulations in the Dainton Laboratory at the School of Chemistry," Downloaded from "<http://chem.leeds.ac.uk/Combustion/Combustion.html>", October 9, 1996.

APPENDIX: THE MELIUS-YETTER RDX GAS-PHASE MECHANISM

CHEMKIN INTERPRETER OUTPUT: CHEMKIN-II Version 3.1 Feb. 1993
DOUBLE PRECISION

```

-----
ELEMENTS      ATOMIC
CONSIDERED   WEIGHT
-----
  1.  AR      39.9480
  2.  C       12.0112
  3.  H       1.00797
  4.  N       14.0067
  5.  O       15.9994
-----

```

```

-----
C
P H
H A
A R
SPECIES      S G MOLECULAR TEMPERATURE   ELEMENT COUNT
CONSIDERED   E E WEIGHT     LOW     HIGH     AR C H N O
-----
  1.  AR      G 0  39.94800  300.0 5000.0  1  0  0  0  0
  2.  H2      G 0   2.01594  300.0 5000.0  0  0  2  0  0
  3.  O2      G 0  31.99880  300.0 5000.0  0  0  0  0  2
  4.  H2O     G 0  18.01534  300.0 5000.0  0  0  2  0  1
  5.  O       G 0  15.99940  300.0 5000.0  0  0  0  0  1
  6.  H       G 0   1.00797  300.0 5000.0  0  0  1  0  0
  7.  OH      G 0  17.00737  300.0 5000.0  0  0  1  0  1
  8.  HO2     G 0  33.00677  200.0 3500.0  0  0  1  0  2
  9.  H2O2    G 0  34.01474  300.0 5000.0  0  0  2  0  2
 10.  CH2O    G 0  30.02649  300.0 5000.0  0  1  2  0  1
 11.  HCO     G 0  29.01852  300.0 5000.0  0  1  1  0  1
 12.  CO      G 0  28.01055  300.0 5000.0  0  1  0  0  1
 13.  CO2     G 0  44.00995  300.0 5000.0  0  1  0  0  2
 14.  N       G 0  14.00670  200.0 6000.0  0  0  0  1  0
 15.  N2      G 0  28.01340  300.0 5000.0  0  0  0  2  0
 16.  NO      G 0  30.00610  200.0 6000.0  0  0  0  1  1
 17.  NO2     G 0  46.00550  200.0 6000.0  0  0  0  1  2
 18.  NH      G 0  15.01467  200.0 6000.0  0  0  1  1  0
 19.  NH2     G 0  16.02264  200.0 6000.0  0  0  2  1  0
 20.  NH3     G 0  17.03061  200.0 6000.0  0  0  3  1  0
 21.  NNH     G 0  29.02137  200.0 6000.0  0  0  1  2  0
 22.  HNO     G 0  31.01407  200.0 6000.0  0  0  1  1  1
 23.  HONO    G 0  47.01347  300.0 5000.0  0  0  1  1  2
 24.  HCN     G 0  27.02582  200.0 6000.0  0  1  1  1  0
 25.  N2O     G 0  44.01280  200.0 6000.0  0  0  0  2  1
 26.  CN      G 0  26.01785  200.0 6000.0  0  1  0  1  0
 27.  C2N2    G 0  52.03570  300.0 5000.0  0  2  0  2  0
 28.  NCN     G 0  40.02455  300.0 4000.0  0  1  0  2  0
 29.  NCO     G 0  42.01725  200.0 6000.0  0  1  0  1  1
 30.  CNO     G 0  42.01725  300.0 4000.0  0  1  0  1  1
 31.  HNCO    G 0  43.02522  300.0 5000.0  0  1  1  1  1
 32.  HOCN    G 0  43.02522  300.0 5000.0  0  1  1  1  1
 33.  HCNO    G 0  43.02522  300.0 5000.0  0  1  1  1  1
 34.  NO3     G 0  62.00490  300.0 5000.0  0  0  0  1  3
 35.  HNO3    G 0  63.01287  300.0 5000.0  0  0  1  1  3
 36.  H2CN    G 0  28.03379  300.0 4000.0  0  1  2  1  0
 37.  H2CNH   G 0  29.04176  300.0 4000.0  0  1  3  1  0
 38.  H2CNO   G 0  44.03319  300.0 4000.0  0  1  2  1  1
 39.  H2CNNO  G 0  58.03989  300.0 4000.0  0  1  2  2  1
 40.  H2CNNO2 G 0  74.03929  300.0 4000.0  0  1  2  2  2
-----

```

41. RDX	G 0 222.11787	300.0	4000.0	0	3	6	6	6
42. RDXR	G 0 176.11237	300.0	4000.0	0	3	6	5	4
43. RDXRO	G 0 176.11237	300.0	4000.0	0	3	6	5	4
44. HNC	G 0 27.02582	300.0	5000.0	0	1	1	1	0
45. H2COHNO2	G 0 91.04666	300.0	4000.0	0	1	3	2	3

REACTIONS CONSIDERED				(k = A T**b exp(-E/RT))		
				A	b	E
1. H2+M=H+H+M				4.57E+19	-1.40	104000.0
	H2	Enhanced by	2.500E+00			
	H2O	Enhanced by	1.200E+01			
	CO	Enhanced by	1.900E+00			
	CO2	Enhanced by	3.800E+00			
2. O+H2O=OH+OH				2.97E+06	2.02	13400.0
3. O+H2=H+OH				5.06E+04	2.67	6290.0
4. O+O+M=O2+M				6.17E+15	-0.50	0.0
	H2	Enhanced by	2.500E+00			
	H2O	Enhanced by	1.200E+01			
	CO	Enhanced by	1.900E+00			
	CO2	Enhanced by	3.800E+00			
5. H+O2=O+OH				1.94E+14	0.00	16440.0
6. H+O2(+M)=HO2(+M)				4.52E+13	0.00	0.0
	Low pressure limit:	0.67000E+20	-0.14200E+01	0.00000E+00		
	TROE centering:	0.10000E+01	0.10000E-89	0.10000E+91		
	H2	Enhanced by	2.500E+00			
	H2O	Enhanced by	1.200E+01			
	CO	Enhanced by	1.900E+00			
	CO2	Enhanced by	3.800E+00			
7. H+O+M=OH+M				4.72E+18	-1.00	0.0
	H2	Enhanced by	2.500E+00			
	H2O	Enhanced by	1.200E+01			
	CO	Enhanced by	1.900E+00			
	CO2	Enhanced by	3.800E+00			
8. OH+H2=H2O+H				2.16E+08	1.51	3430.0
9. OH+H+M=H2O+M				2.21E+22	-2.00	0.0
	H2	Enhanced by	2.500E+00			
	H2O	Enhanced by	1.200E+01			
	CO	Enhanced by	1.900E+00			
	CO2	Enhanced by	3.800E+00			
10. HO2+O=O2+OH				1.75E+13	0.00	-397.0
11. HO2+H=H2+O2				6.62E+13	0.00	2130.0
12. HO2+H=OH+OH				1.69E+14	0.00	874.0
13. HO2+OH=H2O+O2				1.90E+16	-1.00	0.0
14. HO2+HO2=H2O2+O2				4.20E+14	0.00	11980.0
	Declared duplicate reaction...					
15. HO2+HO2=H2O2+O2				1.30E+11	0.00	-1629.0
	Declared duplicate reaction...					
16. H2O2(+M)=OH+OH(+M)				2.95E+14	0.00	48460.0
	Low pressure limit:	0.12000E+18	0.00000E+00	0.45500E+05		
	TROE centering:	0.50000E+00	0.10000E-89	0.10000E+91		
17. H2O2+O=OH+HO2				9.64E+06	2.00	3970.0
18. H2O2+H=H2O+OH				1.00E+13	0.00	3590.0
19. H2O2+H=HO2+H2				4.82E+13	0.00	7950.0
20. H2O2+OH=H2O+HO2				1.00E+12	0.00	0.0
	Declared duplicate reaction...					
21. H2O2+OH=H2O+HO2				5.80E+14	0.00	9557.0
	Declared duplicate reaction...					
22. CH2O+M=HCO+H+M				1.63E+33	-4.10	92550.0
23. CH2O+M=H2+CO+M				8.25E+15	0.00	69540.0
	AR	Enhanced by	1.000E+00			
24. CH2O+O2=HCO+HO2				2.05E+13	0.00	38920.0
25. CH2O+O=HCO+OH				1.81E+13	0.00	3078.0
26. CH2O+H=HCO+H2				1.26E+08	1.62	2163.0
27. CH2O+OH=HCO+H2O				3.43E+09	1.18	-447.0
28. CH2O+HO2=HCO+H2O2				1.99E+12	0.00	11660.0
29. HCO+M=H+CO+M				1.85E+17	-1.00	17000.0
	H2	Enhanced by	1.890E+00			
	H2O	Enhanced by	1.200E+01			
	CO	Enhanced by	1.900E+00			

	CO2	Enhanced by	3.800E+00			
30.	HCO+O2=CO+HO2			7.58E+12	0.00	406.0
31.	HCO+O=CO+OH			3.00E+13	0.00	0.0
32.	HCO+O=CO2+H			3.00E+13	0.00	0.0
33.	HCO+H=CO+H2			7.23E+13	0.00	0.0
34.	HCO+OH=CO+H2O			3.00E+13	0.00	0.0
35.	HCO+HO2=CO2+OH+H			3.00E+13	0.00	0.0
36.	CO+O(+M)=CO2(+M)			1.80E+10	0.00	2380.0
	Low pressure limit:	0.13500E+25	-0.27880E+01	0.41910E+04		
	TROE centering:	0.10000E+01	0.10000E-89	0.10000E+91		
	N2	Enhanced by	1.330E+00			
	H2	Enhanced by	2.500E+00			
	H2O	Enhanced by	1.200E+01			
	CO	Enhanced by	1.900E+00			
	CO2	Enhanced by	3.800E+00			
37.	CO+O2=CO2+O			2.53E+12	0.00	47700.0
38.	CO+OH=CO2+H			1.50E+07	1.30	-765.0
39.	CO+HO2=CO2+OH			5.80E+13	0.00	22930.0
40.	N+H2=H+NH			1.60E+14	0.00	25140.0
41.	N+O2=NO+O			6.40E+09	1.00	6280.0
42.	N+OH=NO+H			3.80E+13	0.00	0.0
43.	N+HO2=NH+O2			1.00E+13	0.00	2000.0
44.	N+HO2=NO+OH			1.00E+13	0.00	2000.0
45.	N+CO2=NO+CO			1.90E+11	0.00	3400.0
46.	N+NO=N2+O			3.27E+12	0.30	0.0
47.	N+NO2=NO+NO			4.00E+12	0.00	0.0
48.	N+NO2=N2O+O			5.00E+12	0.00	0.0
49.	N+NO2=N2+O2			1.00E+12	0.00	0.0
50.	N+HNO=NH+NO			1.00E+13	0.00	2000.0
51.	N+HNO=N2O+H			5.00E+10	0.50	3000.0
52.	N+N2O=N2+NO			1.00E+13	0.00	19870.0
53.	NO+M=N+O+M			9.64E+14	0.00	148400.0
	N2	Enhanced by	1.500E+00			
	CO2	Enhanced by	2.500E+00			
54.	NO+O(+M)=NO2(+M)			1.30E+15	-0.75	0.0
	Low pressure limit:	0.47200E+25	-0.28700E+01	0.15510E+04		
	TROE centering:	0.95700E+00	0.10000E-89	0.83320E+04		
55.	NO+H(+M)=HNO(+M)			1.52E+15	-0.41	0.0
	Low pressure limit:	0.89600E+20	-0.13200E+01	0.73520E+03		
	TROE centering:	0.82000E+00	0.10000E-89	0.10000E+91		
56.	NO+OH(+M)=HONO(+M)			1.99E+12	-0.05	-721.0
	Low pressure limit:	0.50800E+24	-0.25100E+01	-0.67560E+02		
	TROE centering:	0.62000E+00	0.10000E-89	0.10000E+91		
	H2O	Enhanced by	5.000E+00			
57.	HO2+NO=NO2+OH			2.11E+12	0.00	-479.0
58.	NO+HCO=HNO+CO			7.23E+12	0.00	0.0
59.	NO2+O=O2+NO			3.91E+12	0.00	-238.0
60.	NO2+O(+M)=NO3(+M)			1.33E+13	0.00	0.0
	Low pressure limit:	0.14900E+29	-0.40800E+01	0.24670E+04		
	TROE centering:	0.82600E+00	0.10000E-89	0.31910E+04		
61.	NO2+H=NO+OH			3.50E+14	0.00	1500.0
62.	NO2+OH(+M)=HNO3(+M)			2.41E+13	0.00	0.0
	Low pressure limit:	0.64200E+33	-0.54900E+01	0.23500E+04		
	TROE centering:	0.83700E+00	0.10000E-89	0.16570E+04		
63.	NO2+CH2O=HONO+HCO			8.02E+02	2.77	13730.0
64.	NO2+HCO=CO+HONO			1.24E+23	-3.29	2354.0
65.	NO2+HCO=H+CO2+NO			8.39E+15	-0.75	1927.0
66.	NO2+CO=CO2+NO			9.03E+13	0.00	33780.0
67.	NO2+NO2=NO3+NO			9.64E+09	0.73	20920.0
68.	NO2+NO2=2NO+O2			1.63E+12	0.00	26120.0
69.	NH+M=N+H+M			2.65E+14	0.00	75510.0
70.	NH+O2=HNO+O			3.89E+13	0.00	17890.0
71.	NH+O2=NO+OH			7.60E+10	0.00	1530.0
72.	NH+O=NO+H			5.50E+13	0.00	0.0
73.	NH+O=N+OH			3.72E+13	0.00	0.0
74.	NH+OH=HNO+H			2.00E+13	0.00	0.0
75.	NH+OH=N+H2O			5.00E+11	0.50	2000.0
76.	NH+N=N2+H			3.00E+13	0.00	0.0
77.	NH+NO=N2O+H			2.94E+14	-0.40	0.0
	Declared duplicate reaction...					
78.	NH+NO=N2O+H			-2.16E+13	-0.23	0.0
	Declared duplicate reaction...					
79.	NH+NO=N2+OH			2.16E+13	-0.23	0.0
80.	NH+NO2=NO+HNO			1.00E+11	0.50	4000.0
81.	NH+NO2=N2O+OH			1.00E+13	0.00	0.0

82.	NH+NH=N2+H+H	5.10E+13	0.00	0.0
83.	NH2+O2=HNO+OH	1.78E+12	0.00	14900.0
84.	NH2+O=HNO+H	6.63E+14	-0.50	0.0
85.	NH2+O=NH+OH	6.75E+12	0.00	0.0
86.	NH2+H=NH+H2	6.92E+13	0.00	3650.0
87.	NH2+OH=NH+H2O	4.00E+06	2.00	1000.0
88.	NH2+N=N2+2H	7.20E+13	0.00	0.0
89.	NH2+NO=NNH+OH	2.80E+13	-0.55	0.0
90.	NH2+NO=N2+H2O	1.30E+16	-1.25	0.0
	Declared duplicate reaction...			
91.	NH2+NO=N2+H2O	-2.80E+13	-0.55	0.0
	Declared duplicate reaction...			
92.	NH2+NO=N2O+H2	5.00E+13	0.00	24640.0
93.	NH2+NO=HNO+NH	1.00E+13	0.00	40000.0
94.	NH2+NO2=N2O+H2O	3.28E+18	-2.20	0.0
95.	NH3+M=NH2+H+M	2.20E+16	0.00	93470.0
96.	NH3+O=NH2+OH	9.40E+06	1.94	6460.0
97.	NH3+H=NH2+H2	6.40E+05	2.39	10170.0
98.	NH3+OH=NH2+H2O	2.04E+06	2.04	566.0
99.	NH3+HO2=NH2+H2O2	3.00E+11	0.00	22000.0
100.	NH2+HO2=NH3+O2	1.00E+13	0.00	0.0
101.	NH2+NH2=NH3+NH	5.00E+13	0.00	10000.0
102.	NNH+M=N2+H+M	1.00E+14	0.00	3000.0
103.	NNH+O=N2O+H	1.00E+14	0.00	0.0
104.	NNH+H=N2+H2	1.00E+14	0.00	0.0
105.	NNH+OH=N2+H2O	5.00E+13	0.00	0.0
106.	NNH+NO=N2+HNO	5.00E+13	0.00	0.0
107.	NNH+NH=N2+NH2	5.00E+13	0.00	0.0
108.	NNH+NH2=N2+NH3	5.00E+13	0.00	0.0
109.	HNO+O2=NO+HO2	1.00E+13	0.00	25000.0
110.	HNO+O=OH+NO	1.81E+13	0.00	0.0
111.	HNO+H=H2+NO	1.81E+13	0.00	993.5
112.	HNO+OH=H2O+NO	1.00E+13	0.00	993.5
113.	HNO+HCO=CH2O+NO	6.02E+11	0.00	1987.0
114.	HNO+NO=N2O+OH	2.00E+12	0.00	26000.0
115.	HNO+NO2=HONO+NO	6.02E+11	0.00	1987.0
116.	HNO+NH2=NO+NH3	2.00E+13	0.00	1000.0
117.	HNO+HNO=H2O+N2O	8.51E+08	0.00	3080.0
118.	HONO+O=OH+NO2	1.20E+13	0.00	5961.0
119.	HONO+H=H2+NO2	1.20E+13	0.00	7352.0
120.	HONO+OH=H2O+NO2	1.26E+10	1.00	135.1
121.	HCN(+M)=H+CN(+M)	8.30E+17	-0.93	123800.0
	Low pressure limit: 0.35700E+27 -0.26000E+01	0.12490E+06		
	TROE centering: 0.95700E+00 0.10000E-89	0.83320E+04		
122.	HCN+O=CN+OH	2.70E+09	1.58	29200.0
123.	HCN+O=NH+CO	3.45E+03	2.64	4980.0
124.	HCN+O=NCO+H	1.38E+04	2.64	4980.0
125.	HCN+OH=H2O+CN	3.90E+06	1.83	10290.0
126.	HCN+OH=H+HOCN	5.85E+04	2.40	12500.0
127.	HCN+OH=H+HNCO	1.98E-03	4.00	1000.0
128.	HCN+OH=NH2+CO	7.83E-04	4.00	4000.0
129.	HCN=HNC	2.06E+14	-1.11	43710.0
130.	HNC+O=NH+CO	2.89E+12	0.00	0.0
131.	HNC+O=H+NCO	1.60E+01	3.08	-224.0
132.	HNC+OH=HNCO+H	2.80E+13	0.00	3700.0
133.	HNC+OH=CN+H2O	1.50E+12	0.00	7680.0
134.	HNC+NO2=HNCO+NO	1.00E+12	0.00	32000.0
135.	HNC+CN=C2N2+H	1.00E+13	0.00	0.0
136.	N2O(+M)=N2+O(+M)	7.91E+10	0.00	56020.0
	Low pressure limit: 0.91300E+15 0.00000E+00	0.57690E+05		
	H2O Enhanced by	7.500E+00		
	NO Enhanced by	2.000E+00		
	CO Enhanced by	2.000E+00		
	CO2 Enhanced by	3.000E+00		
	HCN Enhanced by	3.000E+00		
137.	N2O+O=O2+N2	1.00E+14	0.00	28000.0
138.	N2O+O=2NO	1.00E+14	0.00	28000.0
139.	N2O+H=N2+OH	2.53E+10	0.00	4550.0
	Declared duplicate reaction...			
140.	N2O+H=N2+OH	2.23E+14	0.00	16750.0
	Declared duplicate reaction...			
141.	N2O+OH=HO2+N2	2.00E+12	0.00	40000.0
142.	N2O+CO=N2+CO2	5.01E+13	0.00	44000.0
143.	CN+H2=H+HCN	5.50E+02	3.18	-223.0
144.	CN+O2=NCO+O	7.50E+12	0.00	-389.0

145.	CN+O=CO+N	1.80E+13	0.00	0.0
146.	CN+OH=NCO+H	4.22E+13	0.00	0.0
147.	CN+CH2O=HCN+HCO	4.22E+13	0.00	0.0
148.	CN+HCO=HCN+CO	6.02E+13	0.00	0.0
149.	CN+CO2=CO+NCO	3.67E+06	2.16	26900.0
150.	CN+NO=NCO+N	9.64E+13	0.00	42120.0
151.	CN+NO2=NCO+NO	1.59E+13	0.00	-1133.0
152.	CN+HNO=HCN+NO	1.81E+13	0.00	0.0
153.	CN+HONO=HCN+NO2	1.20E+13	0.00	0.0
154.	CN+HCN=H+C2N2	1.21E+07	1.71	1530.0
155.	CN+N2O=NCN+NO	3.85E+03	2.60	3696.0
156.	CN+CN(+M)=C2N2(+M)	5.66E+12	0.00	0.0
	Low pressure limit:	0.34200E+26	-0.26100E+01	0.00000E+00
	TROE centering:	0.50000E+00	0.10000E-89	0.10000E+91
157.	C2N2+O=NCO+CN	4.57E+12	0.00	8880.0
158.	C2N2+OH=HOCN+CN	1.86E+11	0.00	2900.0
159.	NCN+O2=NO+NCO	1.00E+14	0.00	0.0
160.	NCN+O=CN+NO	1.00E+14	0.00	0.0
161.	NCN+H=HCN+N	1.00E+14	0.00	0.0
162.	NCN+OH=HCN+NO	5.00E+13	0.00	0.0
163.	NCO+M=N+CO+M	3.10E+16	-0.50	48300.0
	N2	Enhanced by	1.500E+00	
164.	NCO+H2=HNCO+H	7.60E+02	3.00	4000.0
165.	NCO+O2=NO+CO2	2.00E+12	0.00	20000.0
166.	NCO+O=CO+NO	2.00E+13	0.00	0.0
167.	NCO+H=NH+CO	5.36E+13	0.00	0.0
168.	NCO+OH=NO+CO+H	1.00E+13	0.00	0.0
169.	NCO+OH=NO+HCO	5.00E+12	0.00	15000.0
170.	NCO+CH2O=HNCO+HCO	6.02E+12	0.00	0.0
171.	NCO+HCO=HNCO+CO	3.61E+13	0.00	0.0
172.	NCO+N=N2+CO	2.00E+13	0.00	0.0
173.	NCO+NO=N2O+CO	6.20E+17	-1.73	763.0
174.	NCO+NO=CO2+N2	7.80E+17	-1.73	763.0
175.	NCO+NO2=CO+2NO	1.39E+13	0.00	0.0
176.	NCO+NO2=CO2+N2O	4.17E+12	0.00	0.0
177.	NCO+HNO=HNCO+NO	1.81E+13	0.00	0.0
178.	NCO+HONO=HNCO+NO2	3.61E+12	0.00	0.0
179.	NCO+N2O=N2+NO+CO	9.03E+13	0.00	27820.0
180.	NCO+CN=NCN+CO	1.81E+13	0.00	0.0
181.	NCO+NCO=N2+2CO	1.00E+13	0.00	0.0
182.	CNO+O=CO+NO	1.00E+13	0.00	0.0
183.	CNO+NO2=CO+2NO	1.00E+13	0.00	0.0
184.	CNO+N2O=N2+CO+NO	1.00E+12	0.00	15000.0
185.	HNCO(+M)=NH+CO(+M)	6.00E+13	0.00	99800.0
	Low pressure limit:	0.21700E+29	-0.31000E+01	0.10190E+06
	TROE centering:	0.93800E+00	0.10000E-89	0.33040E+04
186.	HNCO+O2=HNO+CO2	1.00E+12	0.00	35000.0
187.	HNCO+O=CO2+NH	9.64E+07	1.41	8524.0
188.	HNCO+O=OH+NCO	6.67E-04	4.55	1780.0
189.	HNCO+O=HNO+CO	1.58E+08	1.57	44300.0
190.	HNCO+H=NH2+CO	2.20E+07	1.70	3800.0
191.	HNCO+OH=H2O+NCO	6.38E+05	2.00	2563.0
192.	HNCO+HO2=NCO+H2O2	3.00E+11	0.00	29000.0
193.	HNCO+NH=NH2+NCO	3.00E+13	0.00	23700.0
194.	HNCO+NH2=NH3+NCO	5.00E+12	0.00	6200.0
195.	HNCO+CN=HCN+NCO	1.51E+13	0.00	0.0
196.	HCNO+O=HCO+NO	1.00E+12	0.00	9000.0
197.	HCNO+OH=HCO+HNO	1.00E+13	0.00	5000.0
198.	HCNO+OH=CNO+H2O	1.00E+12	0.00	2000.0
199.	HCNO+CN=HCN+CNO	1.00E+12	0.00	2000.0
200.	HOCN+O=NCO+OH	1.50E+04	2.64	4000.0
201.	HOCN+H=HNCO+H	2.00E+07	2.00	2000.0
202.	HOCN+OH=NCO+H2O	6.40E+05	2.00	2560.0
203.	H2CN+M=HCN+H+M	5.30E+16	0.00	29000.0
204.	H2CN+CH2O=H2CNH+HCO	1.00E+11	0.00	14000.0
205.	H2CN+NO=HCN+HNO	1.00E+11	0.00	3000.0
206.	H2CN+NO2=HCN+HONO	1.00E+11	0.00	1000.0
207.	H2CN+NO2=H2CNO+NO	1.00E+11	0.00	3000.0
208.	H2CN+HNO=H2CNH+NO	1.00E+11	0.00	4000.0
209.	H2CN+HONO=H2CNH+NO2	1.00E+11	0.00	12000.0
210.	H2CN+N2O=H2CNO+N2	1.00E+11	0.00	3000.0
211.	H2CNH+OH=H2CN+H2O	1.00E+13	0.00	0.0
212.	H2CNH+CN=H2CN+HCN	1.00E+13	0.00	0.0
213.	H2CNO+M=HCNO+H	1.00E+16	0.00	50000.0
214.	H2CNO+OH=HCNO+H2O	1.00E+13	0.00	0.0

215.	H2CNO+NO=HCNO+HNO			1.00E+12	0.00	25000.0
216.	H2CNO+NO2=HCNO+HONO			1.00E+12	0.00	2000.0
217.	H2CNO+NO2=CH2O+NO+NO			1.00E+12	0.00	0.0
218.	H2CNO+HNO=H2CN+HONO			1.00E+12	0.00	2000.0
219.	H2CNNO(+M)=H2CN+NO(+M)			1.00E+16	0.00	2000.0
	Low pressure limit:	0.76900E+17	0.000000E+00	0.15000E+05		
220.	H2CNNO2(+M)=H2CN+NO2(+M)			1.00E+16	0.00	31000.0
	Low pressure limit:	0.20000E+16	0.000000E+00	0.26000E+05		
221.	H2CNNO2+H2O=CH2O+N2O+H2O			1.00E+11	0.00	2000.0
222.	H2CNNO2+NO2=CH2O+N2O+NO2			1.00E+11	0.00	2000.0
223.	H2CNNO2+N2O=CH2O+N2O+N2O			1.00E+11	0.00	2000.0
224.	H2CNNO2+H=H2CN+HONO			1.00E+12	0.00	5000.0
225.	H2CNNO2+OH=HCN+NO2+H2O			1.00E+13	0.00	3000.0
226.	H2CNNO2+OH=CH2O+N2O+OH			1.00E+13	0.00	0.0
227.	RDX(+M)=RDXR+NO2(+M)			2.00E+16	0.00	45000.0
	Low pressure limit:	0.15700E+18	0.000000E+00	0.28000E+05		
228.	RDX+H=RDXR+HONO			1.00E+13	0.00	5000.0
229.	RDX+OH=>2H2CNNO2+H2COHNO2			1.00E+13	0.00	5000.0
230.	H2COHNO2=>HCN+NO2+H2O			1.00E+16	0.00	0.0
231.	RDXR(+M)=>RDXRO(+M)			1.00E+16	0.00	23000.0
	Low pressure limit:	0.76900E+17	0.000000E+00	0.18000E+05		
232.	RDXRO(+M)=>2H2CNNO2+H2CN(+M)			1.00E+16	0.00	23000.0
	Low pressure limit:	0.76900E+17	0.000000E+00	0.18000E+05		

NOTE: A units mole-cm-sec-K, E units cal/mole

APPENDIX: DESCRIPTION OF MECHANISM REDUCTION METHODS

To organize this discussion, the mechanism reduction methods are grouped in three categories: 1) reaction flow (or rate of production) analysis; 2) time scale analysis methods; and 3) fitted reduction.

Reaction Flow Analysis

Reaction flow analysis¹⁴⁹ is generally the first step in reducing a mechanism. Reactions are compared on the basis of their contribution to the rate of production (or consumption) of a particular species. This method is useful in identifying redundant species and eliminating reactions that do not significantly contribute to the main reaction paths. Two types of reaction flow analysis are mentioned here. The integral reaction flow analysis (applied to RDX on page 73) considers the overall contribution of a reaction to each species by integrating its rate of production (or consumption) in x (distance) for 1-dimensional, steady-state systems, or in time for time-dependent homogeneous systems. The local reaction flow analysis examines the contribution to the production (or consumption) of a species by each reaction at specific times or distances; hence, it is more strict than the integral reaction flow analysis. A reaction is considered unimportant if its maximum rate for each species (at all nodes) is less than ϵ times the maximum rate of all reactions for each species.

Time-Scale Analysis

Time-scale analysis methods such as the quasi-steady-state approximation (QSSA)¹¹¹ and the partial equilibrium approximation¹⁴⁹ have been very successful in reducing mechanisms. To apply the QSSA, QSSA species must first be identified. Then, algebraic equations must be solved for the concentration of the QSSA species as functions of the concentrations of the non-QSSA species and forward and reverse rate constants. Solving the QSSA equations numerically will drastically reduce CPU

time savings. However, for large mechanisms the algebraic manipulation can be very challenging. Using the QSSA with many of the existing CHEMKIN⁴¹-based models would require rewriting several of the subroutines.

The partial equilibrium approximation infers that certain reactions are at equilibrium, and concentrations of intermediates are solved by setting forward and reverse rates equal to each other. This assumption is usually only valid at high temperatures (~ 1600 K).¹⁴⁹ The intrinsic low-dimensional manifold (ILDM) method¹⁵⁰ is also based in the analysis of time scales. (See Ref.'s 149 and 150 for details.) The number of independent variables (enthalpy, pressure, species mass fractions) are reduced by lumping the variables into rate-of-progress variables. This method is very robust and can be automated where the user specifies only the desired degrees of freedom and the composition of the manifolds is then calculated.¹⁵⁰

Fitted Kinetic Mechanisms

The development of fitted kinetic mechanisms involves proposing a reaction scheme and then optimizing the kinetic parameters and concentration exponents to match either kinetic data or results produced by a detailed kinetic mechanism.¹¹¹ Fitted kinetic mechanisms can offer significant savings in CPU time, but often at the sacrifice of real chemistry. The rate expressions used in fitting kinetic mechanisms can take the Arrhenius form, polynomials or any imaginable function. Using polynomial functions fitted to results taken from a detailed mechanism is referred to as the repro-modeling approach.^{151,152} All of the methods that use time scale analysis or fitted kinetic mechanisms which are not elementary in form would require rewriting of existing CHEMKIN⁴¹-based models.

APPENDIX: SKELETAL RDX MECHANISM S18-39

CHEMKIN INTERPRETER OUTPUT: CHEMKIN-II Version 3.1 Feb. 1993
DOUBLE PRECISION

```

-----
ELEMENTS      ATOMIC
CONSIDERED    WEIGHT
-----
  1.  AR      39.9480
  2.   C      12.0112
  3.   H       1.00797
  4.   N      14.0067
  5.   O      15.9994
-----
    
```

```

-----
C
P H
H A
A R
S G MOLECULAR TEMPERATURE  ELEMENT COUNT
CONSIDERED  E E WEIGHT      LOW      HIGH      AR C  H  N  O
-----
  1.  H2      G 0   2.01594  300.0 5000.0  0  0  2  0  0
  2.  H2O     G 0  18.01534  300.0 5000.0  0  0  2  0  1
  3.   O      G 0  15.99940  300.0 5000.0  0  0  0  0  1
  4.   H      G 0   1.00797  300.0 5000.0  0  0  1  0  0
  5.  OH      G 0  17.00737  300.0 5000.0  0  0  1  0  1
  6.  CO      G 0  28.01055  300.0 5000.0  0  1  0  0  1
  7.  CO2     G 0  44.00995  300.0 5000.0  0  1  0  0  2
  8.  N2      G 0  28.01340  300.0 5000.0  0  0  0  2  0
  9.  NO      G 0  30.00610  300.0 5000.0  0  0  0  1  1
 10.  NO2     G 0  46.00550  300.0 5000.0  0  0  0  1  2
 11.  NH      G 0  15.01467  300.0 5000.0  0  0  1  1  0
 12.  NH2     G 0  16.02264  300.0 5000.0  0  0  2  1  0
 13.  HCN     G 0  27.02582  300.0 5000.0  0  1  1  1  0
 14.  N2O     G 0  44.01280  300.0 5000.0  0  0  0  2  1
 15.  HNCO    G 0  43.02522  300.0 4000.0  0  1  1  1  1
 16.  H2CN    G 0  28.03379  300.0 4000.0  0  1  2  1  0
 17.  RDX     G 0 222.11787  300.0 4000.0  0  3  6  6  6
 18.  HNC     G 0  27.02582  300.0 5000.0  0  1  1  1  0
-----
    
```

```

REACTANTS CONSIDERED
-----
  1.  O+H2=H+OH      (k = A T**b exp(-E/RT))
  2.  H+O+M=OH+M    A      b      E
                    5.06E+04  2.67  0.6
                    4.72E+18 -1.00  0.0
                    H2      Enhanced by 2.500E+00
                    H2O     Enhanced by 1.200E+01
                    CO      Enhanced by 1.900E+00
                    CO2     Enhanced by 3.800E+00
  3.  OH+H2=H2O+H   2.16E+08  1.51  0.3
  4.  OH+H+M=H2O+M  2.21E+22 -2.00  0.0
                    H2      Enhanced by 2.500E+00
                    H2O     Enhanced by 1.200E+01
                    CO      Enhanced by 1.900E+00
                    CO2     Enhanced by 3.800E+00
  5.  CO+O(+M)=CO2(+M)  1.80E+10  0.00  0.2
    Low pressure limit: 0.13500E+25 -0.27880E+01 0.41910E+04
    
```

TROE centering:	0.10000E+01	0.10000E-89	0.10000E+91			
N2	Enhanced by	1.330E+00				
H2	Enhanced by	2.500E+00				
H2O	Enhanced by	1.200E+01				
CO	Enhanced by	1.900E+00				
CO2	Enhanced by	3.800E+00				
6. CO+OH=CO2+H			1.50E+07	1.30		-0.8
7. NO+O(+M)=NO2(+M)			1.30E+15	-0.75		0.0
Low pressure limit:	0.47200E+25	-0.28700E+01	0.15510E+04			
TROE centering:	0.95700E+00	0.10000E-89	0.83320E+04			
8. NO2+H=NO+OH			1.32E+14	0.00		0.4
9. NO2+CO=CO2+NO			9.03E+13	0.00		0.3
10. NH+O=NO+H			5.50E+13	0.00		0.0
11. NH+NO=N2O+H			2.94E+14	-0.40		0.0
Declared duplicate reaction...						
12. NH+NO=N2O+H			-2.16E+13	-0.23		0.0
Declared duplicate reaction...						
13. NH+NO=N2+OH			2.16E+13	-0.23		0.0
14. NH+NO2=N2O+OH			1.00E+13	0.00		0.0
15. NH+NH=N2+H+H			5.10E+13	0.00		0.0
16. NH2+O=NH+OH			6.75E+12	0.00		0.0
17. NH2+H=NH+H2			6.92E+13	0.00		0.4
18. NH2+OH=NH+H2O			4.00E+06	2.00		0.1
19. NH2+NO=N2+H2O			1.30E+16	-1.25		0.0
Declared duplicate reaction...						
20. NH2+NO=N2+H2O			-2.80E+13	-0.55		0.0
Declared duplicate reaction...						
21. NH2+NO=N2O+H2			5.00E+13	0.00		0.2
22. NH2+NO2=N2O+H2O			3.28E+18	-2.20		0.0
23. HCN+O=NH+CO			3.45E+03	2.64		0.5
24. HCN+OH=H+HNCO			1.98E-03	4.00		0.1
25. HCN+OH=NH2+CO			7.83E-04	4.00		0.4
26. HCN=HNC			2.06E+14	-1.11		0.4
27. HNC+O=NH+CO			2.89E+12	0.00		0.0
28. HNC+OH=HNCO+H			2.80E+13	0.00		0.4
29. HNC+NO2=HNCO+NO			1.00E+12	0.00		0.3
30. N2O(+M)=N2+O(+M)			7.91E+10	0.00		0.6
Low pressure limit:	0.91300E+15	0.00000E+00	0.57690E+05			
H2O	Enhanced by	7.500E+00				
NO	Enhanced by	2.000E+00				
CO	Enhanced by	2.000E+00				
CO2	Enhanced by	3.000E+00				
HCN	Enhanced by	3.000E+00				
31. N2O+O=2NO			1.00E+14	0.00		0.3
32. N2O+H=N2+OH			2.53E+10	0.00		0.5
Declared duplicate reaction...						
33. N2O+H=N2+OH			2.23E+14	0.00		0.2
Declared duplicate reaction...						
34. N2O+CO=N2+CO2			5.01E+13	0.00		0.4
35. HNCO(+M)=NH+CO(+M)			6.00E+13	0.00		1.0
Low pressure limit:	0.21700E+29	-0.31000E+01	0.10190E+06			
TROE centering:	0.93800E+00	0.10000E-89	0.33040E+04			
36. HNCO+O=CO2+NH			9.64E+07	1.41		0.9
37. HNCO+H=NH2+CO			2.20E+07	1.70		0.4
38. H2CN+M=HCN+H+M			5.30E+16	0.00		0.3
39. RDX(+M)=3H2CN+3NO2(+M)			1.30E+12	0.00		0.5
Low pressure limit:	0.15700E+18	0.00000E+00	0.28000E+05			

NOTE: A units mole-cm-sec-K, E units cal/mole

APPENDIX: BURNING RATE SENSITIVITY TO INITIAL TEMPERATURE

The experimental data and model calculations of burning rate as a function of initial temperature and pressure for RDX (page 53), HMX (page 108) and GAP (page 124) are presented in the main body of this dissertation. This appendix is a discussion of the transformation of the data into values of σ_p . In the stability analysis of solid propellants, the change of the natural log of burning rate with respect to initial temperature at a constant pressure***** is referred to as the temperature sensitivity or σ_p . This appendix contains a description of how experimental burning rate data can be converted to values of σ_p . Then, possible discrepancies between the model and experimental data for HMX are explained. Finally, the order-magnitude difference in values of σ_p for RDX and GAP is addressed.

Determining σ_p from Experimental Data

This discussion will use the HMX burning rate data of Boggs et al.³⁴ To generate experimental values of σ_p , ideally one would make measurements at a given pressure for several initial temperatures and then make the appropriate transformation of the data. (For example: At 54.54 atm the slope of the line in Figure 87 is the best estimate of σ_p using this method.) Because of the scatter in the experimental data, determining an accurate derivative can be prone to errors. For the various pressures there are relatively few data points (ranging from 2 to 30). Temperature sensitivity calculated using this method with 95% confidence intervals is shown in Figure 88. As seen by the confidence intervals, there is a very large amount of uncertainty in the value of σ_p , particularly at pressures below 20 atm. The temperature sensitivity below 20 atm is strongly influenced by the circled values in Figure 73 (page 108).

$$***** \sigma_p = \left. \frac{\partial \ln(r_b)}{\partial T_{init}} \right|_p$$

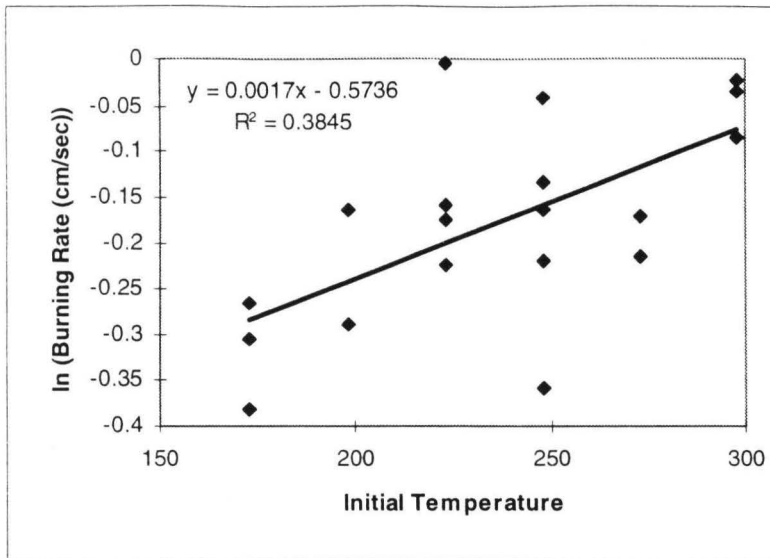


Figure 87: Simple σ_p Analysis (HMX, P=54.53 atm).

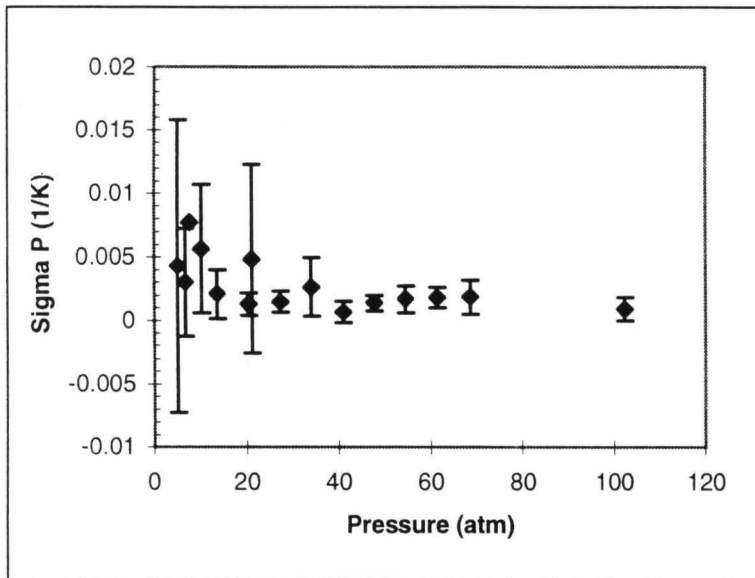


Figure 88: Temperature Sensitivity from Bogg's Data³⁴ using Simple Analysis.

The data can be smoothed (i.e., reduce the effect of the scatter) by fitting the data with an equation or model for a specific initial temperature as a function of pressure. Traditionally, a power fit is used: $r_b = aP^n$. Using the power interpolating function for the data taken at or below an initial temperature of 298 K, and a linear interpolation ($r_b = mP + b$) for data from $T_{init} = 373$ K and 423 K, smoothed data can be generated (symbols in Figure 89) and then transformed to values of σ_p (slope of the lines in

+++++ A linear interpolation correlated the 373 K and 423 K data better than the power fit.

Figure 89). To simplify the figure, 95 percent confidence intervals are not shown for all data. The smoothing equations were not extrapolated more than 3 atmospheres beyond the ranges of the original experimental. Inherent in this analysis is the assumption that σ_p does not change with initial temperature (i.e. straight lines rather than curves in Figure 89). But as seen in Figure 89, the data below 20 atm and above the initial temperature of 298 K may indicate otherwise.

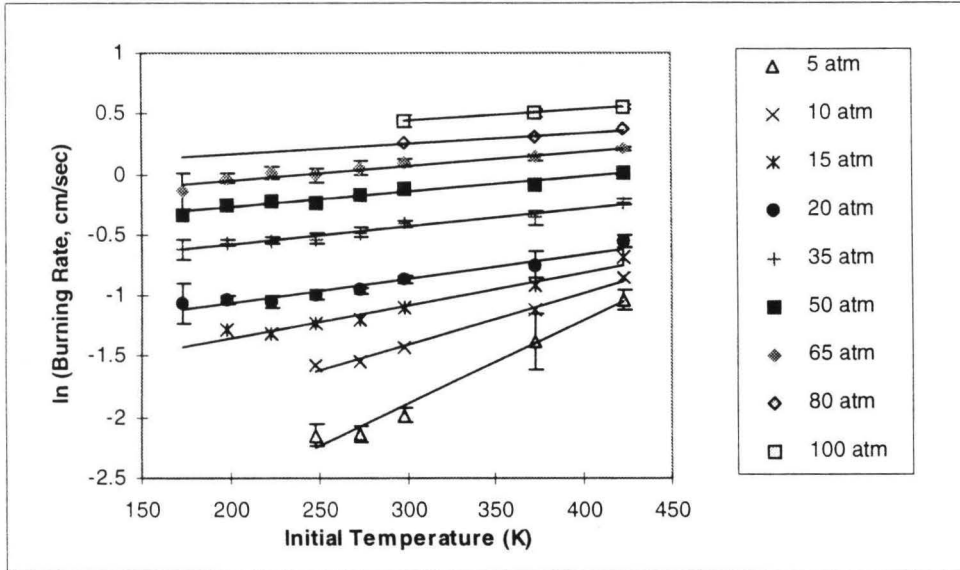


Figure 89: σ_p Calculation from Bogg's Smoothed HMX Data³⁴

Figure 90 contains the smoothed HMX and RDX data from Boggs et al.³⁴ transformed into σ_p values along with predictions made by the model. Additionally, the HMX data were also transformed into σ_p values via a statistical model by fitting all of the data simultaneously. By so doing, the dependence of σ_p on initial temperature as well as accurate confidence intervals were calculated. The development of the statistical model is in the following appendix. The HMX experimental data were analyzed using both methods to demonstrate that σ_p is likely a function of initial temperature at low pressures, and the value of σ_p is very dependent upon how the data are analyzed.

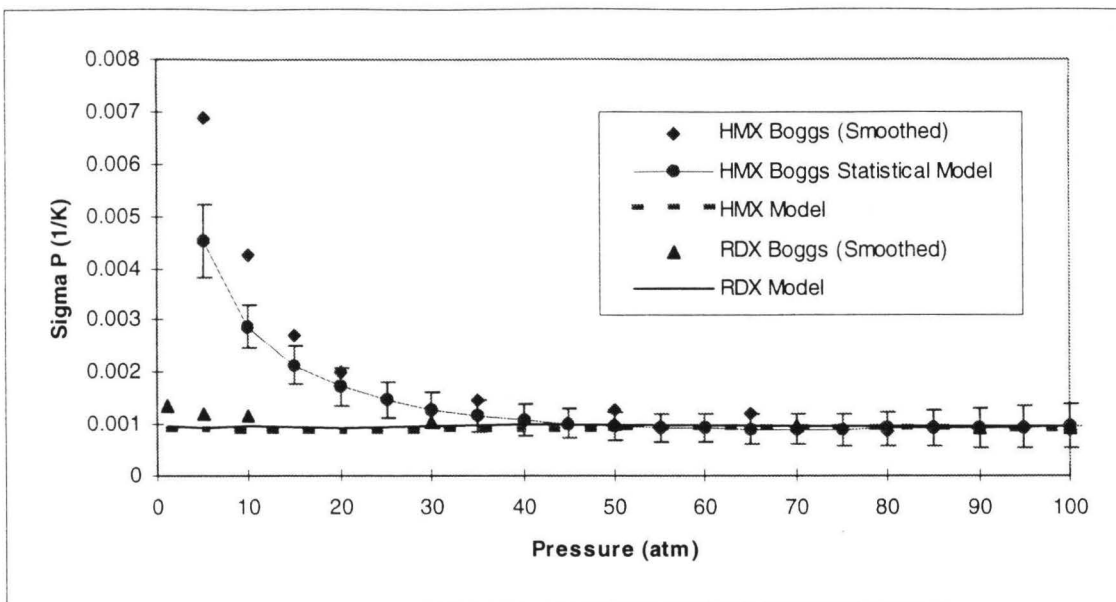


Figure 90: RDX and HMX Temperature Sensitivity (298 K)³⁴

Reconciling Predicted and Calculated Values of σ_p for HMX

The values of σ_p determined from the experimental data are highly uncertain. The apparent increase in temperature sensitivity could indicate a change in reaction mechanism at low pressures (<20 atm) and high initial temperatures (>298 K). Under these conditions, this trend indicates a weakened gaseous flame due to increased exothermic reactions in the condensed phase. The large flame stand-off distance observed by Parr⁶⁹ and the oscillating combustion observed by Zarko¹¹⁵ support this conclusion (see page 101).

According to the model, RDX and HMX have essentially the same temperature sensitivity ($\sim 0.001 \text{ K}^{-1}$). Sensitivity analysis indicates that the heat capacity of the **solid** nitramines affects the temperature sensitivity of the burning rate. (See Figure 64, page 97.) However, increasing the solid heat capacity numerically, increases the predicted values of σ_p by only a small amount. (Approximately a one percent increase in $c_{p,\text{solid}}$ will increase σ_p by one percent. See Figure 64, page 97) Other parameters such as melting temperature, heat of fusion, physical properties of the liquid phase, and condensed-phase and gas-phase reactions appear to have little effect on the σ_p . The effects of solid heat capacity and condensed-phase heat release cannot explain the difference between the predicted and measured values of σ_p below 20 atm. The experimental data indicate that there are real phenomena occurring that are not included in

the model. Possible explanations are an initial-temperature dependent, condensed-phase decomposition mechanism or the effect of “fuel spray” as observed by Hanson-Parr and Parr.⁶⁹ Additional burning rate data for these initial temperatures are desirable to help determine certain values of σ_p below 20 atm.

The Difference in Temperature Sensitivity of RDX and GAP

In Chapter 10, the monopropellant GAP is modeled. Both experimental data and the model (using Mechanisms A, B, or C) indicate the temperature sensitivity of GAP to be approximately 0.01 K^{-1} . This is 10 times the experimental and predicted value of temperature sensitivity of RDX (see Figure 91).

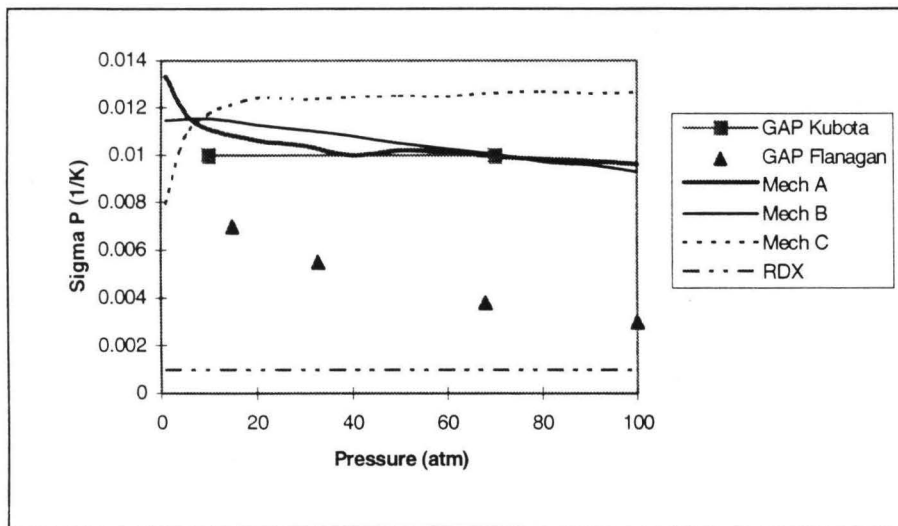


Figure 91: GAP Temperature Sensitivity^{132,137}

As was explained in Chapter 10, there are some significant differences between RDX and GAP. To understand why the model is correctly predicting such large differences in the temperature sensitivity of these two propellants, the various input parameters of RDX were changed to the values used in the GAP model. Changing the solid heat capacity of RDX to that of GAP, only changed the calculated value of σ_p from 0.00095 to 0.0013 K^{-1} . By changing the heat of formation, $c_{p,\text{solid}}$, $c_{p,\text{liquid}}$, and the thermal conductivity to the values of GAP, the calculated σ_p still only increased to 0.0014. When turning off the evaporation of RDX, calculating the surface condition as is done in the GAP model (page 120), and using all of the GAP properties but maintaining the elemental compositions and reaction mechanisms of RDX,

the calculated value of σ_p is only 0.00143 K^{-1} . Using the gas-phase mechanism of GAP^{#####} in the RDX model did not change the temperature sensitivity at all. Differences in these physical or thermodynamic properties cannot explain the observed difference in the temperature sensitivity. There must be an explanation in the gas-phase and/or liquid-phase reaction chemistry.

For GAP, many of the species coming off the surface are near their final equilibrium concentrations. To see the effect of this on RDX (with RDX properties), the exothermic liquid reaction:



was added to the mechanism. Increasing the rate constants for this reaction, had the effect of increasing the heat released in the two-phase region (Q_s) while decreasing the heat release in the gas flame. The effect of Q_s on burning rate and σ_p is shown in Figure 92. Changing the condensed-phase reactions alone cannot account for the difference in calculated values of σ_p for RDX and GAP.

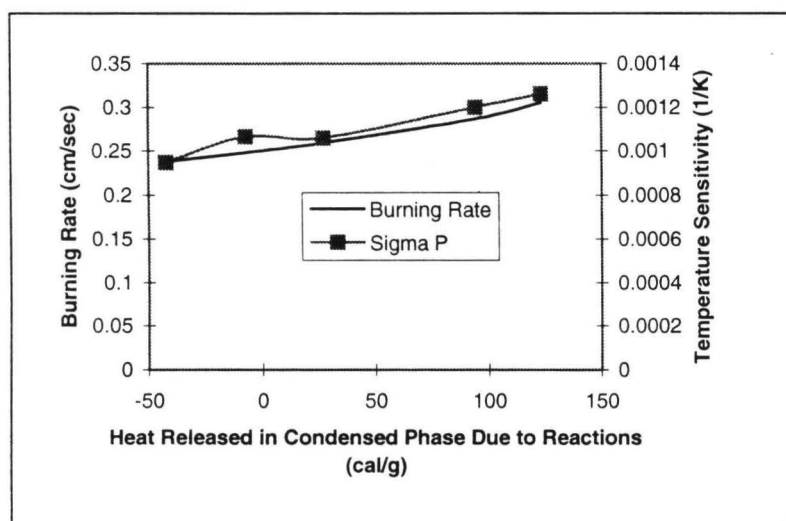


Figure 92: Effect of Q_s on Burning Rate and Temperature Sensitivity (RDX)

The best explanation for the higher σ_p of GAP compared to RDX can be seen in Figure 93. This figure contains the energy flux at both sides of the surface of these propellants as a function of mass burning rate (\dot{m}) and initial temperature. Where the condensed-phase energy flux (solid lines) intersects the gas-phase energy flux (dashed lines), the mass burning rate is converged (see convergence scheme in

The RDX gas-phase mechanism is a subset of the GAP gas-phase mechanism (page 120).

Figure 11, page 41). Decreasing the initial temperature has the effect of shifting the condensed phase energy flux curve higher, but has no effect on the gas-phase energy flux curve. (Increasing pressure will shift the gas-phase curve higher). The slope of the condensed-phase curves is largely determined by the condensed-phase properties and reactions. As seen in Figure 93, the heat flux from the RDX gas-phase to the surface is relatively insensitive to mass-burning rate. (i.e. The RDX gas flame is relatively stable.) The GAP gas-phase flame is very sensitive to mass-burning rate. A small change in initial temperature, shifts the condensed-phase energy flux curve either up or down. Because the gas-phase energy flux curve has nearly the same slope as the condensed-phase curve, the intersection of the curves occurs at a much different \dot{m} . According to the model, GAP has a higher value of σ_p than RDX because the gas-phase flame of GAP is more sensitive \dot{m} .

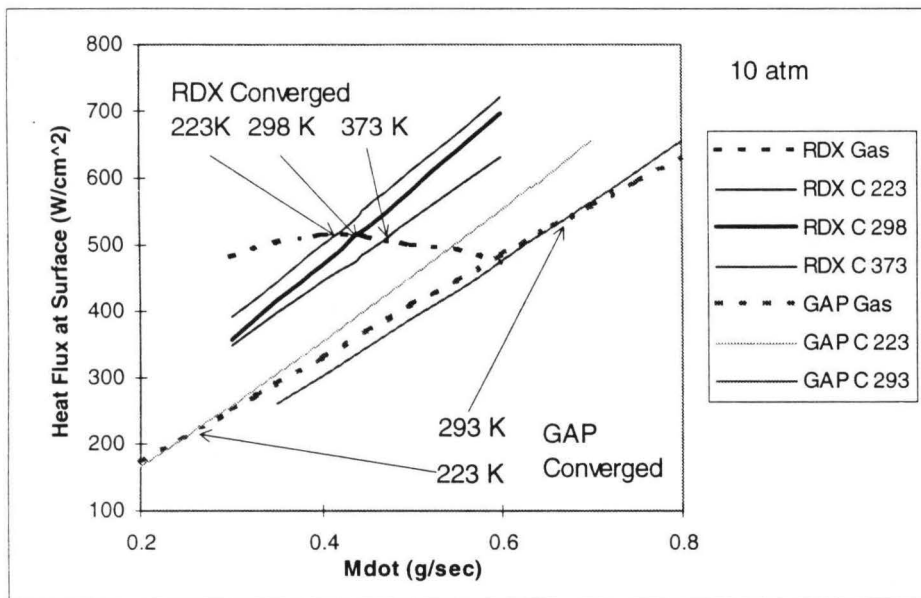


Figure 93: Energy Balance at the Surface of RDX and GAP (10 atm) (C for Condensed)

The follow-up question to the above explanation is, “Why is the gas-phase flame of GAP so sensitive to \dot{m} ?” As noted in Chapter 10, most of the species coming off of the surface of GAP are near their equilibrium concentrations and the GAP flame appears to be kinetically limited. GAP is very fuel rich and has a low adiabatic flame temperature (~1500 K). There is very little energy to be released in the gas-phase of GAP. In contrast, most of the RDX evaporates, regardless of initial temperature or pressure.

The adiabatic flame temperature of RDX is approximately twice that of GAP (~3000 K). Most of the energy is released in the gas-phase of RDX.

Summary

Because the calculation of σ_p involves a derivative, values extracted from experimental data are highly uncertain. The model reasonably correlates most of the original burning rate data as a function of pressure and initial temperature for RDX, HMX and GAP. The largest discrepancy between measured and predicted values occurs for HMX below 20 atm and above the initial temperature 298 K. Under these conditions, one potential reason for this discrepancy could be related to the observation of unstable burning of HMX and liquid fuel spraying from the surface. The model does not consider the spray or changes in decomposition mechanism with initial temperature. Experimental data for HMX indicate that σ_p is considerably higher than 0.002 K^{-1} below 20 atm, but the model predicts a value of 0.001 K^{-1} .

Experimental data and model calculations indicate the temperature sensitivity of GAP (0.01 K^{-1}) is approximately ten times that of RDX (0.001 K^{-1}). While σ_p is sensitive to the solid heat capacity, the minor differences in the value of heat capacity for RDX and GAP do not explain the order-of-magnitude difference in σ_p . The value of σ_p for GAP is much greater than that of RDX because the gas-phase flame of GAP is much more sensitive to small changes in mass burning rate.

APPENDIX: STATISTICAL ANALYSIS OF BOGGS' HMX TEMPERATURE SENSITIVITY DATA

The experimental data from Boggs: (T in K, P in atm, rb or Y in cm/sec)

Tinit=173 K

Tinit=198 K

Tinit=223 K

Tinit=248 K

i = 0, 1.. 13

j = 14, 15.. 30

k = 31, 32.. 49

l = 50, 51.. 68

T _i	P _i	Y _i
173	20.45	0.368
173	20.45	0.338
173	27.27	0.487
173	27.27	0.437
173	34.08	0.563
173	34.08	0.351
173	40.9	0.706
173	40.9	0.668
173	40.9	0.63
173	47.72	0.724
173	54.53	0.767
173	54.53	0.737
173	54.53	0.683
173	61.35	0.853

T _j	P _j	Y _j
198	13.63	0.262
198	13.63	0.246
198	17.04	0.31
198	20.45	0.363
198	20.45	0.353
198	27.27	0.495
198	27.27	0.485
198	27.27	0.467
198	34.08	0.549
198	34.08	0.533
198	40.9	0.686
198	40.9	0.65
198	47.72	0.749
198	47.72	0.742
198	54.53	0.848
198	54.53	0.749
198	57.26	0.874

T _k	P _k	Y _k
223	13.63	0.282
223	13.63	0.227
223	18.4	0.33
223	20.11	0.351
223	20.45	0.348
223	27.27	0.459
223	30.67	0.523
223	34.08	0.551
223	34.08	0.546
223	39.88	0.685
223	40.9	0.65
223	47.72	0.808
223	47.72	0.752
223	54.53	0.853
223	54.53	0.838
223	54.53	0.8
223	54.53	0.996
223	61.35	0.968
223	61.35	0.937

T _l	P _l	Y _l
248	5.11	0.123
248	6.82	0.144
248	9.54	0.185
248	10.22	0.206
248	13.63	0.305
248	13.63	0.277
248	20.45	0.381
248	20.45	0.371
248	27.27	0.467
248	34.08	0.579
248	34.08	0.546
248	40.9	0.732
248	47.72	0.798
248	54.53	0.874
248	54.53	0.848
248	54.53	0.803
248	54.53	0.96
248	54.53	0.698
248	61.35	0.96

Experimental Data Continued...

Tinit=273 K

i = 69, 70.. 92

T _i	P _i	Y _i
273	5.11	0.117
273	6.82	0.169
273	6.82	0.136
273	8.86	0.176
273	10.22	0.225
273	10.22	0.216
273	13.63	0.295
273	13.63	0.282
273	13.63	0.312
273	13.63	0.283
273	20.45	0.411
273	20.45	0.368
273	20.45	0.368
273	27.27	0.521
273	27.27	0.513
273	34.08	0.599
273	40.9	0.63
273	44.99	0.765
273	47.72	0.864
273	53.85	0.927
273	54.53	0.843
273	54.53	0.806
273	59.3	1.097
273	61.35	0.998

Tinit=298 K

j = 93, 94.. 121

T _j	P _j	Y _j
298	3.41	0.1011
298	5.11	0.1524
298	6.82	0.1694
298	6.82	0.1669
298	6.82	0.1626
298	10.22	0.2921
298	10.22	0.2459
298	13.63	0.3404
298	13.63	0.2921
298	13.63	0.2616
298	20.45	0.4445
298	27.27	0.5994
298	27.27	0.5461
298	27.88	0.536
298	34.08	0.655
298	40.9	0.79
298	40.9	0.734
298	40.9	0.686
298	47.72	0.8357
298	48.13	0.841
298	54.53	0.978
298	54.53	0.965
298	54.53	0.917
298	61.35	1.143
298	61.35	1.034
298	69.05	1.1335
298	69.05	1.0921
298	102.25	1.6759
298	102.25	1.4895

Tinit=373 K

k = 122, 123.. 132

T _k	P _k	Y _k
373	7.77	0.264
373	21.13	0.542
373	21.13	0.417
373	34.56	0.725
373	55.08	1.026
373	55.08	1.007
373	68.64	1.1765
373	83.03	1.4802
373	83.03	1.4085
373	102.25	1.707
373	102.25	1.625

Tinit=423 K

l = 133, 134.. 141

T _l	P _l	Y _l
423	7.77	0.389
423	21.13	0.62
423	21.13	0.592
423	52.76	1.026
423	55.42	1.064
423	68.64	1.307
423	68.64	1.275
423	102.25	1.783
423	102.25	1.75

Analysis of Boggs' burning rate data.

Page references come from "Statistics for the Engineering and Computer Sciences." by Mendenhall and Sincich (1984)

number of data points= rows(Y) = 142

ORIGIN = 0 n = 0, 1.. rows(Y) - 1 numpar = 7 k = 0, 1.. numpar - 1

Y is the dependent variable, burning rate.

Transform Y and P by natural log to get better fits.

$$Y_n := \ln(Y_n) \quad P_n := \ln(P_n)$$

$$F(T, P) = \begin{bmatrix} 1 \\ P \\ T \\ P^2 \\ P^2 \cdot T \\ P \cdot T^2 \\ T^3 \end{bmatrix} \quad \begin{array}{l} F \text{ is the array of functions} \\ \text{which will be made into a} \\ \text{linear combination to} \\ \text{represent burn rate as} \\ \text{a function of initial} \\ \text{Temperature and } \ln(P). \end{array}$$

$$dfdt(T, P) = \begin{bmatrix} 0 \\ 0 \\ 1 \\ 0 \\ P^2 \\ 2 \cdot P \cdot T \\ 3 \cdot T^2 \end{bmatrix} \quad \begin{array}{l} dfdf \text{ is the derivative of } F \\ \text{wrt initial } T \text{ holding } P \\ \text{constant.} \end{array}$$

The statistical model:

$$\ln(\text{rb}) = B_0 + B_1 \cdot \ln(P) + B_2 \cdot T + B_3 \cdot \ln(P)^2 + B_4 \cdot \ln(P)^2 \cdot T + B_5 \cdot \ln(P) \cdot T^2 + B_6 \cdot T^3$$

$$X_{n,k} = F(T_n, P_n)_k \quad \text{X matrix as defined on Page 424.}$$

$$a(T, P) = \text{submatrix}(F(T, P), 0, \text{numpar} - 1, 0, 0) \quad \text{Used in calculating confidence intervals (page 446-7)}$$

$$c = (X^T \cdot X)^{-1} \quad \text{Defined on page 429. used here to reduce calculation and notation.}$$

$$B = c \cdot X^T \cdot Y \quad \text{Least squares estimates of the coefficients (B0-B6) of the functions in } F$$

$$\text{rbf}(T, P) = \sum_k F(T, P)_k \cdot B_k \quad \text{Equation representing the least squared estimate of } \ln(\text{rb}) \text{ as a function of initial } T \text{ and } P.$$

$$\text{SSE} = \sum_n (Y_n - \text{rbf}(T_n, P_n))^2 \quad \text{Squared Standard Error (equivalent to definition on Page 430).}$$

$$\text{SSE} = 0.780372$$

$$s = \sqrt{\frac{\text{SSE}}{\text{rows}(Y) - \text{numpar}}} \quad s = 0.07603 \quad \text{Estimate of the standard deviation (Page 430).}$$

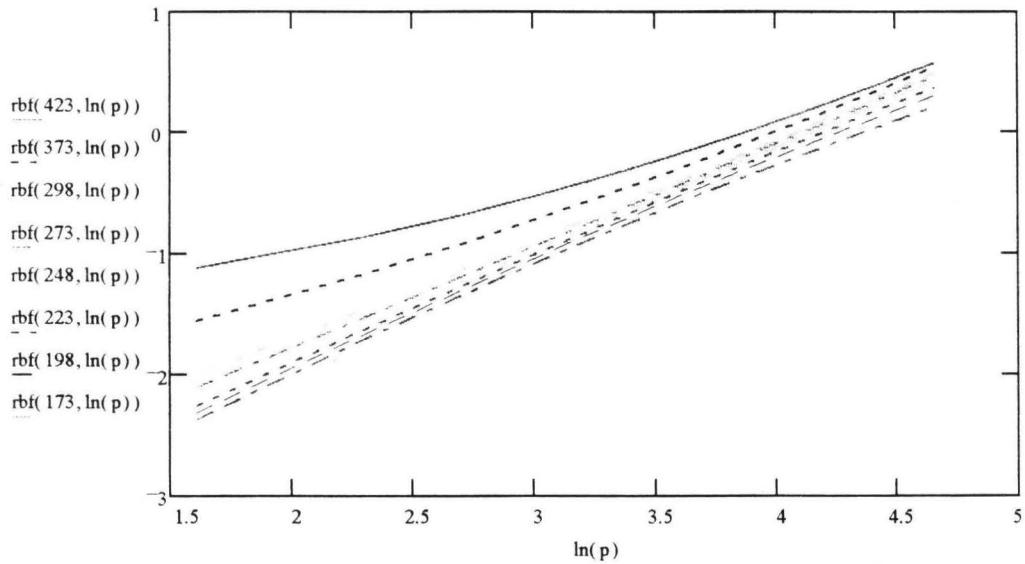
Ttest = qt(.975, rows(Y) - numpar) Ttest = 1.977692 Student's T statistic for 95% confidence

$Be_k = Ttest \cdot s \cdot \sqrt{c_{k,k}}$ +/- values for each of the coefficients in B (Page 432)

$B_{t_k} = \frac{B_k}{s \cdot \sqrt{c_{k,k}}}$ Test statistic for each coefficient Bk: If abs(Btk) > Ttest then that coefficient contributes significantly to the prediction made by the model.

$B = \begin{bmatrix} -4.590512 \\ 1.374139 \\ 0.001886 \\ -0.138044 \\ 5.147192 \cdot 10^{-4} \\ -7.358022 \cdot 10^{-6} \\ 3.136913 \cdot 10^{-8} \end{bmatrix}$	$Be = \begin{bmatrix} 0.341476 \\ 0.253288 \\ 9.647445 \cdot 10^{-4} \\ 0.07308 \\ 2.551439 \cdot 10^{-4} \\ 2.801532 \cdot 10^{-6} \\ 1.097604 \cdot 10^{-8} \end{bmatrix}$	$B_t = \begin{bmatrix} -26.586429 \\ 10.729379 \\ 3.866339 \\ -3.735726 \\ 3.989733 \\ -5.194267 \\ 5.652172 \end{bmatrix}$	<p>Every function in statistical model significantly contributes to the model predictions.</p>
---	--	---	--

Model Predictions p = 5, 10.. 105



95% Confidence intervals for burning rate as a function of pressure and initial temperature.

$t_{95} = qt(0.975, \text{rows}(Y) - \text{numpar})$ Student's T-test value for 95% confidence interval.

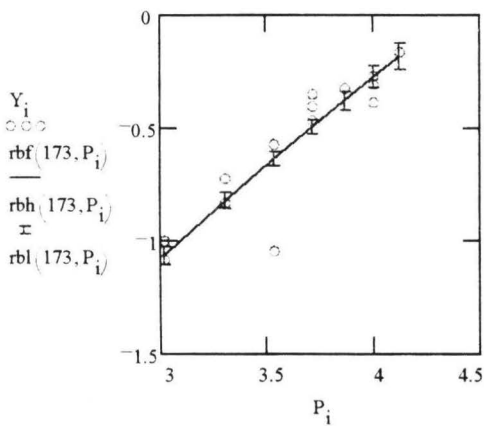
$\text{rbf}_e(T, P) = t_{95} \cdot s \cdot \sqrt{|a(T, P)^T \cdot c \cdot a(T, P)|}$ 95% confidence interval for rb model (Page 447).

$\text{rbh}(T, P) = \text{rbf}(T, P) + \text{rbf}_e(T, P)$ Upper limit on burn rate predictions

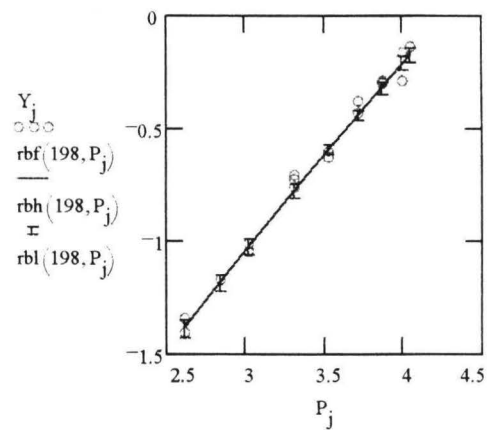
$\text{rbl}(T, P) = \text{rbf}(T, P) - \text{rbf}_e(T, P)$ Lower limit on burn rate predictions

How well does the statistical model correlate the original data?

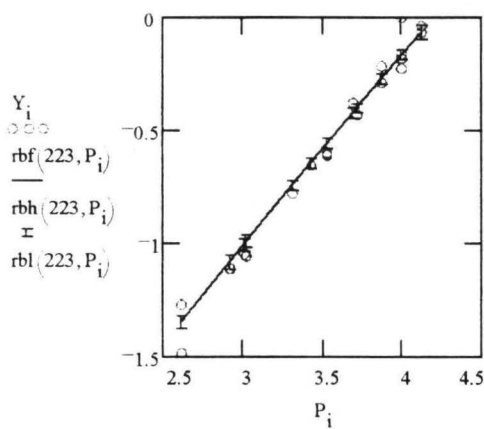
Initial Temp=173 K $i := 0, 1.. 13$



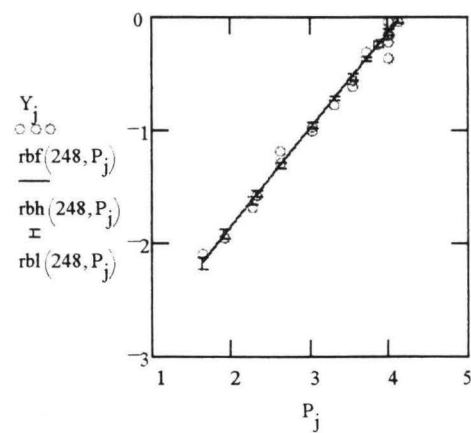
Initial Temp=198 K $j := 14, 15.. 30$



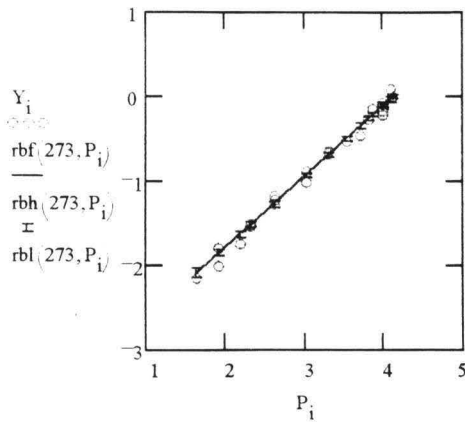
Initial Temp=223 K $i := 31, 32.. 49$



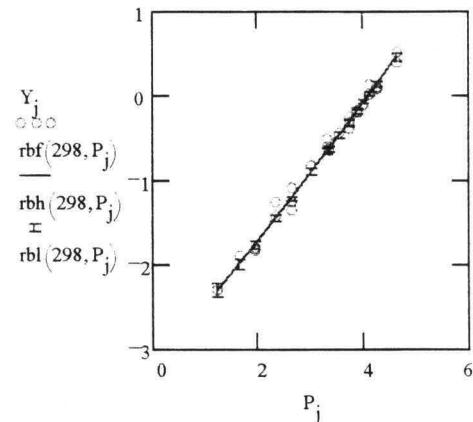
Initial Temp=248 K $j := 50, 51.. 68$



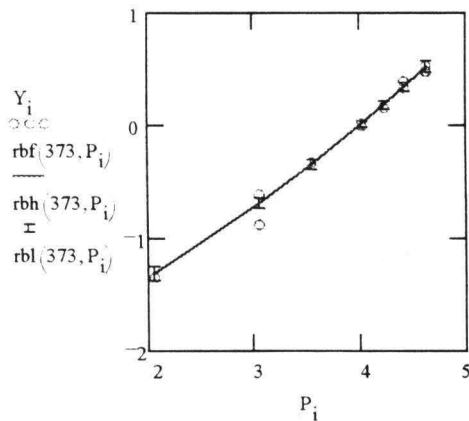
Initial Temp=273 K i := 69, 70.. 92



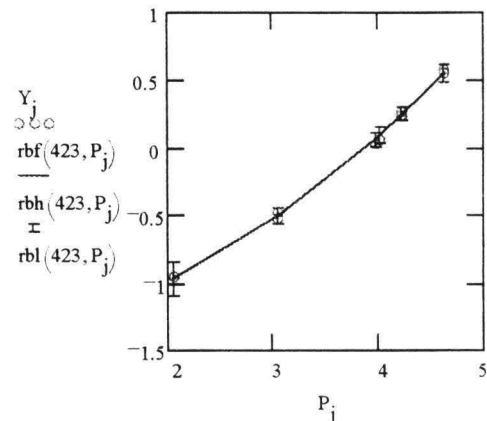
Initial Temp=298 K j := 93, 94.. 121



Initial Temp=373 K i := 122, 123.. 132



Initial Temp=423 K j := 133, 134.. rows(Y) - 1



Now that the Statistical Model fits the experimental data ($R^2=98.5\%$), calculate σ_p .

$$\sigma_p(T, P) := \frac{d}{dT} \ln(\text{rbf}(T, P)) \quad \text{Numerical definition of the temperature sensitivity.}$$

$$\sigma_p(298, \ln(10)) = 0.002874$$

$$\text{dfdts}(T, P) := \text{submatrix}(\text{dfdt}(T, P), 0, \text{numpar} - 1, 0, 0) \quad \text{Submatrix of } dF/dT$$

$$\text{dfdt}_e(T, P) := t_{95} \cdot s \cdot \sqrt{|\text{dfdts}(T, P)^T \cdot c \cdot \text{dfdts}(T, P)|} \quad \text{Error bounds on } dF/dT$$

$$\sigma_p(T, P) := \sum_k B_k \cdot \text{submatrix}(\text{dfdt}(T, P), 0, \text{numpar} - 1, 0, 0)_k \quad \text{Derivative of } \ln(\text{rb}) \text{ wrt initial Temp } (\sigma_p)$$

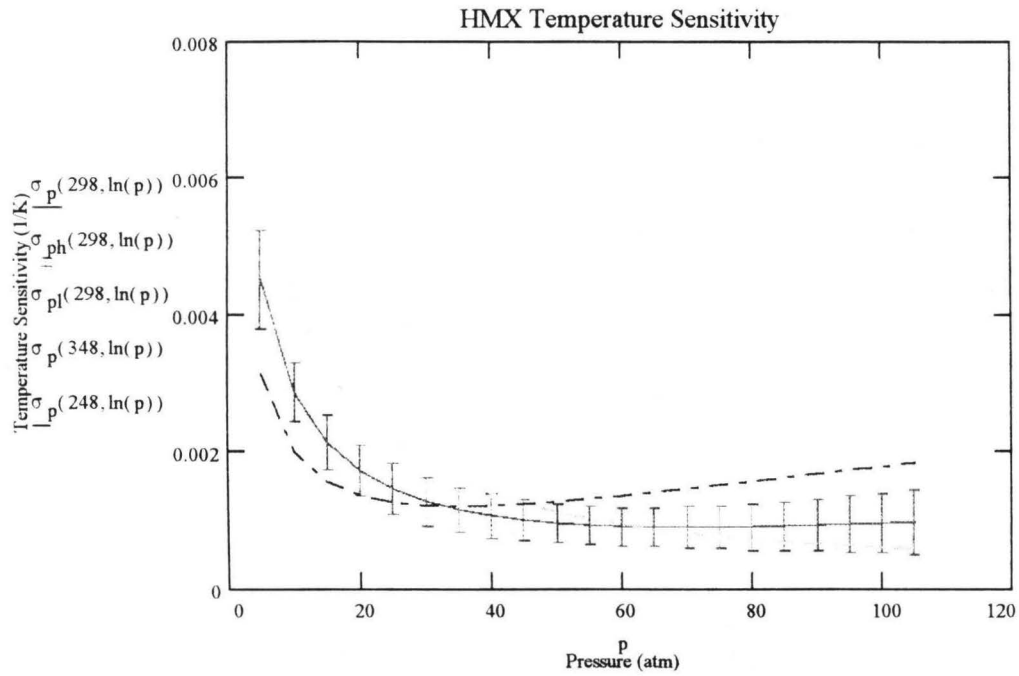
$$\sigma_p(298, \ln(10)) = 0.002874 \quad \text{Answer agrees with numerical derivative above.}$$

$$\sigma_{pe}(T,P) = dfdt_e(T,P) \quad \text{Error bounds on } \sigma_p.$$

$$\sigma_{pl}(T,P) = \sigma_p(T,P) - \sigma_{pe}(T,P) \quad \text{Lower limit (95\% confidence)}$$

$$\sigma_{ph}(T,P) = \sigma_p(T,P) + \sigma_{pe}(T,P) \quad \text{Upper limit (95\% confidence)}$$

Plot of Results



Combustion Modeling of RDX, HMX and GAP with Detailed Kinetics

Jeffrey E. Davidson

Department of Chemical Engineering

Ph.D. Degree, April 1997

ABSTRACT

A one-dimensional, steady-state numerical model of the combustion of homogeneous solid propellant has been developed. The combustion processes is modeled in three regions: solid, two-phase (liquid and gas) and gas. Conservation of energy and mass equations are solved in the two-phase and gas regions and the eigenvalue of the system (the mass burning rate) is converged by matching the heat flux at the interface of these two regions. The chemical reactions of the system are modeled using a global kinetic mechanism in the two-phase region and an elementary kinetic mechanism in the gas region.

The model has been applied to RDX, HMX and GAP. There is very reasonable agreement between experimental data and model predictions for burning rate, temperature sensitivity, surface temperature, adiabatic flame temperature, species concentration profiles and melt-layer thickness. Many of the similarities and differences in the combustion of RDX and HMX are explained from sensitivity analysis results. The combustion characteristics of RDX and HMX are similar because of their similar chemistry. Differences in combustion characteristics arise due to differences in melting temperature, vapor pressure and initial decomposition steps. A reduced mechanism consisting of 18 species and 39 reactions was developed from the Melius-Yetter RDX mechanism (45 species, 232 reactions). This reduced mechanism reproduces most of the predictions of the full mechanism but is 7.5 times faster. Because of lack of concrete thermophysical property data for GAP, the modeling results are preliminary but indicate what type of experimental data is necessary before GAP can be modeled with more certainty.

COMMITTEE APPROVAL:

Merrill W. Beckstead, Committee Chair

John L. Oscarson, Committee Member

Thomas H. Fletcher, Committee Member

Ronald E. Terry, Committee Member

Paul O. Hedman, Committee Member

William G. Pitt, Graduate Coordinator